

**DESIGN AND ANALYSIS OF MINIATURIZED  
SUBSTRATE INTEGRATED WAVEGUIDE  
RECONFIGURABLE FILTERS FOR MM-WAVE  
APPLICATIONS**

*Thesis submitted for the fulfilment of requirements for the degree of*

***DOCTOR OF PHILOSOPHY***

In

***Electronic Engineering***

By

**CLEOPHAS DOUGLAS KUDZAI MUTEPEFE**



**DEPARTMENT OF ELECTRONIC ENGINEERING, HOWARD COLLEGE,  
UNIVERSITY OF KWAZULU-NATAL, DURBAN - 4041  
SOUTH AFRICA.**

**STUDENT NO.: 221117339**

**APRIL 2023**

**DESIGN AND ANALYSIS OF MINIATURIZED  
SUBSTRATE INTEGRATED WAVEGUIDE  
RECONFIGURABLE FILTERS FOR MM-WAVE  
APPLICATIONS**

*Student:*

Mr. Cleophas Douglas Kudzai Mutepfe

*Supervisor:*

Prof. (Dr.) Viranjay M. Srivastava

*This thesis submitted in fulfillment of the requirements  
for the degree of Doctor of Philosophy: Electronic Engineering*

*In*

*Howard College of Agriculture, Engineering & Science*

*University of KwaZulu-Natal, Durban*

*South Africa.*

As the candidate's supervisor, I have approved this thesis for submission.

Signed.....

Date 3<sup>rd</sup> April 2023

Name: Prof. (Dr.) Viranjay M. Srivastava

# Declaration-1

## PLAGIARISM

---

I, Cleophas Douglas Kudzai Mutepfe with Student Number 221117339 with thesis titled *Design and Analysis of Miniaturized Substrate Integrated Waveguide Reconfigurable Filters For Mm-Wave Applications*; hereby declare that:

- i. The research reported in this thesis, except where otherwise indicated, is my original research.
- ii. This thesis has not been submitted for any degree or examination at any other university.
- iii. This thesis does not contain other persons' data, pictures, graphs or other information, unless specifically acknowledged as being sourced from other persons.
- iv. This thesis does not contain other persons' writing, unless specifically acknowledged as being sourced from other researchers. Where other written sources have been quoted, then:
  - a. Their words have been re-written but the general information attributed to them has been referenced.
  - b. Where their exact words have been used, then their writing has been placed inside quotation marks, and referenced.
- v. Where I have reproduced a publication of which I am an author, co-author or editor, I have indicated in detail which part of the publication was actually written by myself alone and have fully referenced such publications.
- vi. This thesis does not contain text, graphics or tables copied and pasted from the Internet, unless specifically acknowledged, and the source being detailed in the thesis and in the References sections.

Cleophas Douglas Kudzai Mutepfe

Date: 3<sup>rd</sup> April 2023

## Declaration-2

## PUBLICATIONS

---

Details of contribution to publications that form part and/or include research presented in this thesis (include publications that have been submitted, *in press* and published and give details of the contributions of each author to the experimental work and writing of each publication). I, Cleophas Douglas Kudzai Mutepfe declare that these publications were a result of my own work presented in this thesis:

### Journals:

1. **Cleophas D. K. Mutepfe** and Viranjay M. Srivastava, “Design of miniaturized half-mode substrate integrated waveguide dual band filter for X and Ku band applications,” *J. of Communications (JCM)*, vol. 18, no. 3, pp. 180-186, March. 2023.  
(DOI: 10.12720/jcm.18.3.180-186) [ETP]
2. **Cleophas D. K. Mutepfe** and Viranjay M. Srivastava, “Design and implementation of graphene-based tunable microwave filter for THz applications,” *Nanomaterials* (nanomaterials), vol. 12, no. 24, article 4443, pp. 1-12, Dec. 2022.  
(DOI: 10.3390/nano12244443) [MDPI]
3. **Cleophas D. K. Mutepfe** and Viranjay M. Srivastava, “Sixth-order cross-coupled filter utilizing half- and eighth-mode substrate integrated waveguide resonators with wide stop-band,” *Int. J. of Microwave and Optical Technology (IJMOT)*, vol. 17, no. 5, pp. 479-486, Sept.2022.  
(ISSN: 1553-0396) [IAMOT]
4. **Cleophas D. K. Mutepfe** and Viranjay M. Srivastava, “Design and analysis of compact 5<sup>th</sup> mode balanced substrate integrated waveguide bandpass filter for 39 GHz,” *Int. J. on Communications Antenna and Propagation (IRECAP)*, vol. 11, no. 6, pp. 401-407, Dec. 2021.  
(DOI: [10.15866/irecap.v11i6.20981](https://doi.org/10.15866/irecap.v11i6.20981)) [Praise Worthy Prize]

5. **Cleophas D. K. Mutepfe** and Viranjay M. Srivastava, “Designing of novel eighth-mode forth-order substrate integrated waveguide band-pass filter with high selectivity,” *J. of Communications (JCM)*, vol. 16, no. 12, pp. 553-558, Dec. 2021.  
(DOI: [10.12720/jcm.16.12.553-558](https://doi.org/10.12720/jcm.16.12.553-558)) [ETP]
  
6. **Cleophas D. K. Mutepfe** and Viranjay M. Srivastava, “An approach to high selectivity substrate integrated waveguide band-pass filter for mm-wave applications,” *Int. J. of Microwave and Optical Technology (IJMOT)*, vol. 15, no. 6, pp. 592-598, Nov. 2020.  
(ISSN: [1553-0396](https://doi.org/10.1553/0396)) [IAMOT]

### Conferences:

7. **Cleophas D. K. Mutepfe** and Viranjay M. Srivastava, “Second order reconfigurable half-mode substrate integrated waveguide dual-band filter: A circuit perspective,” *IEEE 2<sup>nd</sup> Ukrainian Microwave Week (UkrMW-27)*, Ukraine, 14-18 Nov. 2022, pp. 329-332.  
(DOI: [10.1109/UkrMW58013.2022.10037059](https://doi.org/10.1109/UkrMW58013.2022.10037059)) [IEEE Xplore]
  
8. **Cleophas D. K. Mutepfe** and Viranjay M. Srivastava, “Miniaturized substrate integrated waveguide dual-band filter with high common-mode signal suppression,” *43<sup>rd</sup> PhotonIcs and Electromagnetics Research Symposium (PIERS)*, Hangzhou, China, 21-25 Nov. 2021, pp. 1388-1395.  
(DOI: [10.1109/PIERS53385.2021.9694979](https://doi.org/10.1109/PIERS53385.2021.9694979)) [IEEE Xplore]

# DEDICATION

---

To God be the Glory. The Creator of Heaven and Earth

To my late father, who always taught me to be strong, reach for the sky and always aim  
for the BEST.

To my late mother, for the love and words of wisdom you shared with me

To my Wife Brenda and Kids Bradley, Bailey and Brooklyn – (the 3 B's). I wish you  
nothing but the BEST.

To all my siblings.

And to all those who are trying to achieve their dreams but are feeling weak but still  
endeavoring to keep their heads up their shoulders, find strength in the LORD

## PREFACE

---

This work was done by the candidate *Cleophas Douglas Kudzai Mutepe* under the supervision of *Professor (Dr.) Viranjay M. Srivastava* at the Department of Electronic Engineering, Howard College, University of KwaZulu-Natal, Durban, South Africa.

Material emanating from this research work was published in international journals. Some parts were published in International Journal of Microwave and Optical Technology, while some parts in International Journal of Communication, and some parts were published in The International Journal on Communications Antenna and Propagation, some parts in the MDPI nanomaterial journal and as well some parts were published in the Institute of Electrical and Electronics Engineers.

The other work that arose from this research work was also presented at international conferences. Some parts were presented at Photonics & Electromagnetics Research Symposium (PIERS) conference held in Hangzhou, China, and the other part of this research work was presented at a conference held in Ukraine under the title IEEE 2nd Ukrainian Microwave Week (UkrMW).

# ACKNOWLEDGEMENTS

---

First and foremost, I would like to give thanks and praises to our living God, for giving me the strength and courage to embark on this journey. I thank you Lord for not leaving me alone on any part of this journey. You alone, Lord Jesus takes all the Glory.

I would like to whole heartedly thank my supervisor Professor (Dr.) Viranjay M. Srivastava for the guidance and support from day one until the end of this research work. You really know how to bring the best out of your students, and I couldn't have wished for any better supervisor than you. When things seemed impossible and tough you always found a way to make them possible, I really appreciate you Professor and may all you dreams come true. I would also want to thank the University of Kwazulu-Natal and the department of Electrical, Electronic and Computer Engineering for giving me this opportunity to further up my studies and climb a step higher in my career.

I am so appreciative of my family, and in particular my wife Brenda for being there for me during this whole journey of my doctorate studies. You managed to keep me going through all the stresses of work and studies. I really appreciate you may our living God grant you all the wishes and desires of your heart. I am thankful to my kids, for being understanding kids during this time because time was not enough to be with you always during this PhD journey.

To my siblings, I thank you for your prayers. I appreciate the desire you had for me to keep going and achieve this milestone. Special mention goes to my sister Millie Tapiwa for taking over most of the burden of making sure we stayed in school when Dad passed on. Thank you very much for such love and care.

Last but not least I do appreciate everyone who contributed in this research work in one way all the other. I thank you so much may the good Lord bless you abundantly.

# ABSTRACT

---

Microwave filters are an integral part of communication systems. With the advent of new technologies, microwave devices, such as filters, need to have superior performance in terms of power handling, selectivity, size, insertion loss etc. During the past decade, many applications have been added to the communication networks, resulting in communication systems having to operate at high frequencies in the region of THz to achieve the stringent bandwidth requirements. To achieve the requirements of the modern communication system, tunability and reconfigurability have become fundamental requirements to reduce the footprint of communication devices. However, the communication systems that are more prevalent such as planar circuits have either a large footprint or are not able to handle large amounts of power due to radiation leakage.

In this thesis, Substrate Integrated Waveguide (SIW) technology has been employed. The SIW has the same properties as the conventional rectangular waveguide; hence it benefits from the high quality (Q) factor and can handle large powers with small radiation loss. The Half-mode (HMSIW), Quarter-mode (QMSIW), and Eighth-mode (EMSIW) cavity resonators have been designed and used for the miniaturization of the microwave filters. The coupling matrix method was used to implement a filter that uses cross-coupled EMSIW and HMSIW cavity resonators to improve the selectivity of the filter.

Balanced circuit techniques have been used to design the circuits that preserve communication systems integrity whereby the Common Mode (CM) signal was suppressed using Deformed Ground Structure (DGS) and a center conductor patch with meandered line. For the designed dual-band filter, the common mode signal was suppressed to -90 dB and -40 dB for the first and second passband, respectively. The insertion loss observed is 2.8 dB and 1.6 dB for the first and second passband, respectively.

For tunability of the filter, a dual-band filter utilizing triangular HMSIW resonators has been designed and reconfigurability is achieved by perturbing the substrate permittivity by dielectric rods. The dielectric rods' permittivity was changed to achieve tunability in the first instance, and then the rods' diameter changed in the second instance. For the lower-band, frequency is tunable from  $8.1\text{ GHz}$  to  $9.15\text{ GHz}$ , while the upper band is tuned from  $14.61\text{ GHz}$  to  $16.10\text{ GHz}$ . A second order SIW filter with a two layer substrate was then

designed to operate in the THz region. For reconfigurability, Graphene was sandwiched between the Silicon Di-Oxide substrate and the top gold plate of the filter, and the chemical potential of Graphene was then varied by applying a dc bias voltage. With a change in dc voltage the chemical potential of Graphene changes accordingly. From the results, a chemical potential change of 0.1 eV to 0.6 eV brings about a frequency change from 1.289 THz to 1.297 THz.

# **TABLE OF CONTENTS**

DECLARATION 1: PLAGIARISM.....	ii
DECLARATION 2: PUBLICATIONS .....	iii
DEDICATION.....	v
PREFACE .....	vi
ACKNOWLEDGMENTS .....	vii
ABSTRACT .....	viii
TABLE OF CONTENTS .....	x
LIST OF FIGURES .....	xvi
LIST OF TABLES.....	xxi
LIST OF ABBREVIATIONS.....	xxii
Declaration-1 .....	ii
PLAGIARISM .....	ii
PUBLICATIONS.....	iii
ABSTRACT.....	viii
Chapter-1.....	1
INTRODUCTION .....	1
1.1.    Communication System.....	1
1.2.    Background of Filters .....	2
1.3.    Research Motivation.....	3
1.4.    Research Objectives.....	5
1.5.    Research Contributions.....	5
1.6.    Organization of the thesis .....	7
1.7.    Resulting Peer-Reviewed Publications.....	9
Chapter-2.....	12
LITERATURE REVIEW.....	12
2.1.    Introduction.....	12
2.2.    Miniaturization .....	13
2.3.    Multi-band filters .....	15
2.4.    Balanced Filters .....	17

2.5.	Common mode suppression.....	20
2.6.	Reconfigurability of Filters.....	21
2.7.	Graphene Tuning .....	22
2.8.	Filter background theory.....	24
2.8.1	Butterworth (Maximally flat) Approximation .....	25
2.8.2	Chebyshev Approximation .....	26
2.8.3	Elliptic Approximation .....	27
2.9.	Low-pass Filter Prototype Networks .....	28
2.9.1	Maximally Flat Low-pass Filter Prototype .....	29
2.9.2	Chebyshev Low-pass Filter Prototype .....	29
2.9.3	Elliptic Low-pass Filter Prototype.....	30
2.10.	Transformation of the LPF .....	31
2.10.1	Low-pass Filter Transformation .....	32
2.10.2	High-pass Filter Transformation.....	32
2.10.3	Band-pass Filter Transformation .....	33
2.10.4	Band-Stop Filter Transformation.....	34
2.11.	Immittance, Impedance, and Admittance Inverters .....	35
2.11.1	Using Immittance Inverters .....	36
2.11.2	Band-pass Filter Using Immittance Inverters .....	37
2.12.	Chapter Summary .....	40
Chapter-3.....		42
<b>SUBSTRATE INTEGRATED WAVEGUIDE FILTER DESIGN .....</b>		<b>42</b>
3.1.	Rectangular Waveguide.....	42
3.2.	Rectangular Waveguide Cavity Resonators.....	46
3.3.	Substrate Integrated Waveguide .....	47
3.4.	SIW Transitions .....	49
3.4.1	Micro-strip to SIW Transition .....	49
3.4.2	Co-planar waveguide (CPW) to SIW Transition .....	50
3.5.	Losses in SIW .....	51
3.6.	Design of a SIW filter with High selectivity .....	52
3.6.1	Filter Implementation .....	53
3.7.	Results Analysis and Discussion .....	56
3.8.	Chapter Summary .....	59
Chapter-4.....		61
<b>SIW MINIATURIZATION .....</b>		<b>61</b>
4.1.	Introduction.....	61

4.2.	Ridged Substrate Integrated Waveguide.....	61
4.3.	Using Complementary Slip Ring Resonator (CSRR).....	63
4.4.	Bisecting the SIW structure .....	65
4.5.	Miniaturized filter design 1.....	66
4.5.1	Proposed Fourth-Order Filter Design .....	67
4.6.	Results Analysis and Discussions.....	70
4.7.	Proposed miniaturized filter design-2.....	71
4.8.	Results and analysis of second filter design .....	76
4.9	Dual band filter .....	79
4.9.1	Multi-Mode Dual Band Filter Design.....	79
A.	Filter Topology .....	79
B.	Resonator Design.....	80
C.	Realization of the Filter .....	82
4.10	Results and analysis of Dual Band Filter.....	85
4.11.	Chapter Summary .....	87
Chapter-5.....		88
<b>BALANCED FILTERS .....</b>		<b>88</b>
5.1.	Introduction.....	88
5.2.	Propagating Modes .....	89
5.3.	Balanced Filter Design.....	90
5.4.	Results and Analysis of Balanced Filter .....	95
5.5.	Common Mode Suppression Techniques .....	97
5.6.	Common mode suppression filter design process.....	97
5.7.	Common-Mode (CM) Suppression Mechanism.....	99
5.7.1	Dumbbell Structure.....	99
5.7.2	Center conductor patch with meandered line.....	101
5.8.	Results and analysis of filter with Common Mode Suppression.....	103
5.9.	Chapter Summary .....	105
Chapter-6.....		107
<b>RECONFIGURABLE SIW FILTERS.....</b>		<b>107</b>
6.1.	Introduction.....	107
6.2.	Ferromagnetic Materials .....	108
6.3.	Ferroelectric Materials.....	108
6.4.	Semiconductors.....	109
6.5.	Mechanical Systems .....	110
6.6.	Dielectric Rods Tunable Filter.....	111

6.6.1 Dielectric rod tunable filter design .....	111
6.6.2 Reconfigurability of the filter .....	113
6.7. Results and analysis of Filter Tunability .....	114
6.8. Chapter Summary .....	116
Chapter-7.....	118
<b>TERA HERTZ FREQUENCY BAND TUNING USING GRAPHENE .....</b>	<b>118</b>
7.1. Graphene material.....	118
7.2. Graphene Conductivity .....	119
7.3. Graphene Tunable Filter Design.....	121
7.4. Results.....	122
7.5. Effect of Graphene Aspect ratio on the center frequency .....	126
7.6. Discussion of results .....	128
7.7. Chapter Summary .....	129
Chapter-8.....	130
<b>RESULTS AND CONCLUSIONS.....</b>	<b>130</b>
8.1. Introduction.....	130
8.2. Summary of results .....	130
8.3. Conclusions and future work .....	132
<b>REFERENCES.....</b>	<b>133</b>
<b>NOTES.....</b>	<b>152</b>
<b>NOTES.....</b>	<b>153</b>

# LIST OF FIGURES

---

Figure 1.1 General communication system.....	1
Figure 1.2 General communication system (a) Transmitter. (b) Receiver.....	2
Figure 1.3 General overview of the thesis. ....	8
Figure 2.1 Two-port filter network .....	25
Figure 2.2 Butterworth filter response [4].....	26
Figure 2.3 Chebyshev frequency response [5].....	27
Figure 2.4 Elliptic function frequency response. [4].....	28
Figure 2.5 Low-pass filter prototype for all poles with (a) Ladder network (b) Dual network. [4].....	29
Figure 2.6 LPF prototype for the elliptic filter (a) Ladder network and (b) Dual network [4]. ....	31
Figure 2.8 HPF prototype transformation .....	33
Fig. 2.9 BPF prototype transformation .....	34
Figure 2.11 Immittance inverter used to convert (a) inductor to a capacitor, (b) capacitor to an inductor.....	35
(b).....	36
Figure 2.12(a) Immittance inverters (b) The dual .....	36
Figure 2.13 BPF transformation.....	37
Figure 2.14 Transformed filter using J -inverters. ....	38
(a) .....	38
Fig. 2.15(a) Band pass filter using K inverters and distributed resonators (b) Band pass filter using J inverters and distributed resonators. ....	39
Using the K inverters: .....	39
Figure 3.1 Rectangular Waveguide.....	42
Figure 3.2 Field line distribution of lower TE and TM modes [1]. ....	45
Figure 3.3 (a) Field variations for TE <sub>101</sub> and TE <sub>102</sub> and (b) Cavity resonator [1].....	46

Figure 3.4 SIW structure.....	49
Figure 3.5 Microstrip to SIW transition.....	49
Figure 3.6 CPW to SIW transition.....	50
Figure 3.7 CPW-SIW transition with current probe.....	50
Figure 3.8 Illustration of resonators topology.....	53
Figure 3.9 Extraction of the coupling coefficient.....	54
Figure 3.10 Extraction of the external quality factor.....	55
Figure 3.11 Fifth-order SIW filter.....	55
Fig 3.12 Output results of the 5 <sup>th</sup> -order SIW filter.....	56
Figure 3.13 Voltage standing wave ratio (VSWR).....	58
Figure 3.14 SIW filter cut in half.....	58
Figure 3.15 Output results of the half-mode filter.....	59
Figure 3.16 The VSWR in half mode.....	59
Figure 4.1 (a) Ridged waveguide (b) Equivalent circuit.....	62
Figure 4.2 Ridged SIW. (a) 2-D view (b) front view.....	62
Figure 4.3 Ridged SIW with a metal strip.....	63
Figure 4.4 (a) Half mode ridged SIW and (b) Folded Half mode ridged SIW.....	63
Figure 4.5 (a) SRR and (b) Equivalent circuit.....	64
Fig. 4.6 (a) CSRR (b) Equivalent circuit.....	65
Figure 4.7 (a) Full SIW resonator structure (b) HMSIW (c) QMSIW (d) EMSIW (e) SMSIW [162].....	66
Figure 4.8 Electric field distribution of EMSIW resonator (a) First orientation, and (b) second orientation.....	66
Figure 4.9 EMSIW filter topology.....	68
Figure 4.10 Forth order EMSIW filter.....	68
Figure 4.11 Coupling factor extraction.....	69
Figure 4.12 Output results of the proposed filter (a) $S_{11}$ output and (b) Combined $S_{11}$ and $S_{12}$ output.....	70

Figure 4.13	Filter topology. ....	74
Fig. 4.14	Equivalent circuit of the 6 <sup>th</sup> order filter. ....	74
Figure 4.15	Filter implementation. ....	75
Figure 4.16.	Determining the coupling coefficient. ....	75
Figure 4.17	S parameter plot, $S_{11}$ . ....	77
Figure 4.18	S-parameter plot; $S_{11}$ and $S_{21}$ . ....	77
Figure 4.19	The VSWR analysis. ....	78
Figure 4.20	Second-order single-band filter topology. ....	79
Figure 4.21	Second-order dual-band filter topology. ....	80
Figure 4.22	Resonator modes field distribution. ....	81
Figure 4.23	Determination of coupling coefficient using full mode resonator. ....	83
Figure 4.24	Determination of coupling coefficient using half-mode resonator. ....	83
Fig 5.25	Determination of external quality factor. ....	84
Fig. 4.26	Results of dual-band filter utilizing full mode SIW resonators. ....	85
Figure 4.27	Results of dual-band filter utilizing half-mode SIW resonators. ....	85
Figure 5.1	Differential mode transmission lines (a) Two conductors and (b) Three conductors. ....	88
Figure 5.2	Single-ended voltages (a) even mode and (b) odd mode [80]. ....	89
Figure 5.3	Substrate Integrated Waveguide (SIW) resonator. ....	91
Figure 5.4	TE <sub>102</sub> (a) field intensity, and (b) Field pattern. ....	92
Figure 5.5	The DM and CM $S_{12}$ response. ....	92
Figure 5.6	Substrate Integrated Waveguide (SIW) filter. ....	93
Figure 5.7	Coupling coefficient simulation. ....	93
Figure 5.8	External quality factor simulation. ....	94
Figure 5.9	Output results. ....	95
Figure 5.10	Half-mode configuration. ....	95
Figure 5.11	Half-mode configuration output results. ....	96

Figure 5.12	(a) Schematic filter topology, and (b) 3D view of the filter structure. ....	98
Figure 5.13	(a) Top view of the filter, and (b) Bottom view of the filter. ....	98
Figure 5.14	Output from the filter without any suppression mechanism.....	99
Figure 5.15	(a) Dumbbell unit cell geometry, and (b) Dumbbell unit cell equivalent circuit.....	100
Figure 5.16	(a) Dumbbell DGS etched at the bottom surface of the filter, and (b) The top surface of the filter with a view of the DGS at the bottom. ....	101
Figure 5.17	(a) Center patch with meandered loop, (b) Equivalent circuit for common-mode, and (c) Differential-mode.....	102
Figure 5.18	(a) The bottom surface of the filter with conductor patch and meandered loop, and (b) Top surface of the filter with a view of the DGS at the bottom. ....	103
Figure 5.19	Output result of the filter with (a) dumbbell DGS, and (b) conductor patch with meandered loop. ....	104
Fig 6.1	Operation principle of YIG [192] .....	108
Figure 6.2	Illustration of the ferroelectric, paraelectric region, and hysteresis loop [32]. .....	109
Figure 6.3	Varactor diode. ....	110
Figure 6.4	The MEMs components.....	110
Figure 6.5	(a) Line of symmetry to form HMSIW, and (b) Dual band filter.....	112
Figure 6.6	The $S_{11}$ and $S_{21}$ Parameter. ....	113
Figure 6.7	Dielectric rod-filled SIW filter. ....	113
Figure 6.8	Equivalent circuit.....	113
Figure 6.9	Variation of dielectric rod diameter.....	114
Figure 6.10	S-parameter results for $\epsilon=12.94$ .....	115
Figure 6.11	S-parameter results for $\epsilon=11.2$ .....	115
Figure 6.12	S-parameter results for $\epsilon=6.45$ .....	116
Figure 7.1	The lattice structure of Graphene [202].....	118
Figure 7.2	Relationship between chemical potential and center frequency [38]. ....	120

Figure 7.3	Second-order SIW filter 3D image. ....	121
Figure 7.4	Cross-sectional side view of second-order SIW filter. ....	122
Figure 7.5	The S-parameter results. ....	123
Figure 7.6	Group delay. ....	123
Figure 7.6	Current distribution.....	123
Figure 7.8	Impedance plot. ....	124
Figure 7.9	Chemical potential = 0.1 eV. ....	125
Figure 7.10	Chemical potential=0.2 eV. ....	125
Figure 7.11	Chemical potential = 0.4 eV. ....	125
Figure 7.12	Chemical potential = 0.6 eV. ....	126
Figure 7.13	Length and width of graphene. ....	126
Figure 7.14	For $w_1 = 50 \mu\text{m}$ and $z_1 = 100 \mu\text{m}$ . ....	127
Figure 7.15	For $w_1 = 50 \mu\text{m}$ and $z_1 = 300\mu\text{m}$ . ....	127
Figure 7.16	For $w_1 = 100 \mu\text{m}$ and $z_1 = 300\mu\text{m}$ .....	128
Figure 7.17	For $w_1 = 150 \mu\text{m}$ and $z_1 = 100\mu\text{m}$ .....	128

## LIST OF TABLES

---

Table 3.1	Filter dimensions.....	56
Table 3.2	Comparison with the other existing works .....	57
Table 4.1	Design Parameters.....	69
Table 4.2	Comparison of the proposed design with existing work.....	71
Table 4.3	Polynomial normalized coefficients.....	72
Table 4.4	Coupling Matrix.....	73
Table 4.5.	Parameter values .....	76
Table 4.6	Comparison with similar work.....	78
Table 4.7	Filter dimensions.....	84
Table 4.8	Comparison with existing work .....	86
Table 5.1	Comparison with similar work.....	96
Table 5.2	Comparison with similar work for SIW technology.....	105
Table 6.1	Comparison table of tuning technologies [4].....	107
Table 7.1	SIW filter parameters .....	122
Table 7.2	Graphene parameters.....	124

# LIST OF ABBREVIATIONS

---

SIW	Substrate Integrated Waveguide
HMSIW	Half Mode Substrate Integrated Waveguide
QMSIW	Quarter Mode Substrate Integrated Waveguide
EMSIW	Eighth Mode Substrate Integrated Waveguide
5G	Fifth Generation
4G	Fourth Generation
3G	Third Generation
2G	Second Generation
1G	First Generation
3D	Three Dimensional
2D	Two Dimensional
1D	One Dimensional
CM	Common Mode
DGS	Defected Ground Structure
LPF	Low Pass Filter
CPW	Co Planar Waveguide
CSRR	Complementary Split Ring Resonator
HPF	High Pass Filter
BPF	Band Pass Filter
TE	Transverse Electric
TM	Transverse Magnetic

VSWR	Voltage Standing Wave Ratio
SRR	Slip ring Resonator
SMSIW	Sixteenth Mode Substrate Integrated Waveguide
DM	Differential Mode
YIG	Yttrium – Iron- Granite
MEMs	Micro-ElectroMechanical systems
MHz	Mega Hertz
GPS	Global Positioning System
Wi-Fi	Wireless Fidelity
TV	Television
BSF	Band Stop Filter
LC	Inductor Capacitor
PCB	Printed Circuit Board
EBG	Electromagnetic Bandgap
PMC	Perfect Magnetic Conductor
SIR	Stepped Impedance Resonators
UIR	Uniform Impedance Resonators
R-MMR	Ring Multi-Mode Resonator
SI-SRLR	Stepped Impedance Square Ring Loaded Resonators
HTS	High-Temperature Superconducting
SSLR	Symmetric-Stub Loaded Resonator
EGaIn	Eutectic Gallium Indium
FSS	Frequency Selective Surfaces

MIMO	Multiple Input, Multiple Output
GOI	Graphene On Insulator
FBW	Fractional Bandwidth
GCPW	grounded co-planar waveguide
CR	Circular Ring
CMRC	Compact Microstrip Resonant Cell
SRR	Slip ring Resonator
TZ	Transmission zero
RL	Return loss
IL	Insertion Loss
CSRR	Complementary Slip Ring Resonator
HMWSIW	Half Mode Substrate Integrated Waveguide
HM	Half Mode
EM	Eighth Mode
CMRR	Common Mode Rejection Ratio
DBs	Decibels
BST	Barium Strontium Titanate
PCM	Phase change Material
RF	Radio Frequency
SPP	Surface Plasmon Polaritons
DC	Direct Current
LTCC	Low Temperature Co-Fired Ceramic

# Chapter-1

## INTRODUCTION

---

Microwave frequency ranges from  $300\text{ MHz}$  to  $300\text{ GHz}$  on the electromagnetic spectrum. Communication systems can utilize only a part of this spectrum [1], [2]. Hence, the spectrum is subdivided into smaller frequency bands. Several applications utilize these sub-bands of frequency. Applications such as GPS, Wi-Fi, TV, cellular, Bluetooth, and many others are found in these frequency bands [2]. With these different applications accessing the spectrum simultaneously, regulatory bodies need to come in to manage the use and impose standards to be followed to ensure efficient use of the spectrum resource. To guarantee efficient sharing of the spectrum, microwave filters are employed.

The last two decades have seen new communication services grow exponentially, bringing about the need for high-performance microwave devices such as filters [3]. In cellular services, specific and stringent specifications should be applied at the base station and mobile handset to ensure successful communication. To meet such stringent conditions, it has become imperative to develop different devices and develop various development strategies.

### 1.1. Communication System

Figure 1.1 shows the block diagram of a general communication system [4]. The information source consists of signals of both analogue and digital nature that must be transmitted through the transmitter over a communication channel [4]. Conversely, the receiver receives the information and is directed to its destination. Microwave filters can be employed in both the transmitter and receiver sections of the communication system shown in Fig. 1.1. On the transmitter side, the different information signals are separated into their channel by narrowband filters and then transmitted over a single channel using the multiplexer, as shown in Fig. 1.2 (a).

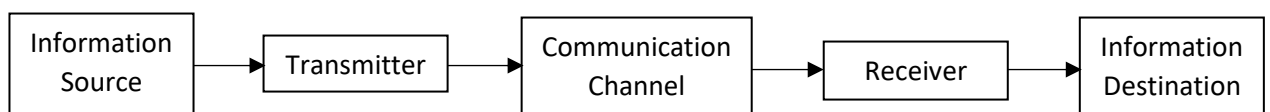


Figure 1.1 General communication system.

The multiplexer consists of several narrowband filters of fractional bandwidth 0.2% to 2 % used to divide the information signal into narrowband channels before transmission. In Fig. 1.2(b), the block diagram of the receiver section is illustrated. When the signal is received, it is split into several channels using narrowband filters before being transmitted to the respective destination. This is done through the use of demultiplexers, whereby filters are used to extract the signals and feed them to their destinations.

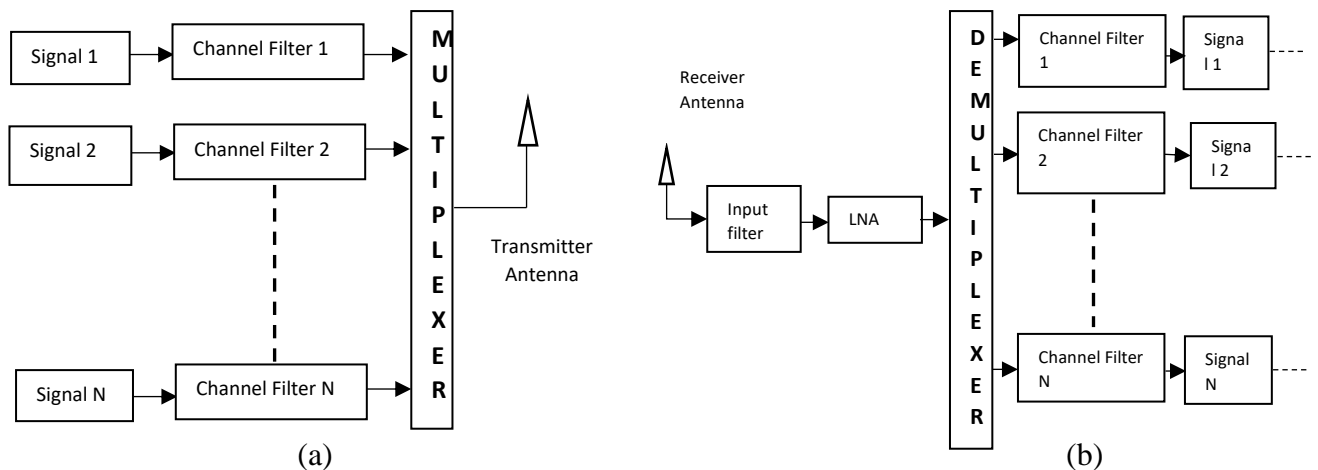


Figure 1.2 General communication system (a) Transmitter. (b) Receiver

## 1.2. Background of Filters

A filter can be defined as a device that passes signals within a specific frequency band and suppresses any other signals that fall out of the frequency band of interest [4]. Different types of filters are used to achieve this definition. They can be classified as (i) Low pass filters (LPF), which pass signals below a particular cut-off frequency, (ii) High pass filters (HPF), used to pass signals that fall above a specific cut-off frequency, (iii) band-Pass Filters (BPF) that passes signals within a specific range of frequencies and (iv) Band-Stop Filters (BSF) used to suppress signals that fall within a certain frequency range [5]. Because of the stringent requirements imposed on the use of the spectrum by regulatory bodies, it is imperative that filters, among other things, should be small in size [6]–[9]. Satellite systems and modern communication systems require small components [10]. The filters should also have high selectivity to avoid interference between adjacent channels. Filters should be simple to design and integrate with other technologies in use. The

tunability of filters is also desirable to minimize components in a communication system. It can be costly to re-install and modify wireless infrastructure hence the need for tunability or reconfigurability.

There are three main methods used in the design of filters:

- i. LC filters. The combination of inductors and capacitors can be used to design low-frequency filters. These filters suffer from high losses and poor Q-factor [5].
- ii. Microstrip filters. In this technology, transmission line sections are used to construct the filters. These filters are easy to fabricate and easily integrated with other circuits. However, they are lossy, tend to operate at low frequencies and possess low Q factors [7].
- iii. Waveguide filters. These structures operate at high frequencies and have high Q-factors [1]. However, they are bulky and difficult to fabricate or integrate with other structures.

From these methods for the development of filters, it can be seen that the quality factor is low for LC and microstrip filters. While providing high efficiency and Q factors, the waveguide structure is bulky and difficult to integrate with other structures, making it challenging to work with. Hence a compromise is needed that trades off the disadvantages of these structures while maintaining an acceptable level of operation.

### **1.3. Research Motivation**

In the 18<sup>th</sup> century, it was proven that electromagnetic waves could transmit information signals wirelessly [11]. Since then, enormous research work has been done to develop communication systems that can efficiently use the electromagnetic spectrum band for wireless transmission of signals. As of 1980, almost every decade has seen new generations of technology emerging, starting from 1<sup>st</sup> generation (1G) up to today, where we are now in the fifth generation (5G) era going into the 6<sup>th</sup> generation (6G) technology. The major driver for the rapid technological change has been the traffic growth that must be added to the communication system. It is estimated that up to 2030, there will be a rapid increase in the number of developing applications that need to be incorporated into the communication system [3, 11]. This requires that communication systems operate at

frequencies in the terahertz frequency band to have wider frequency bandwidth which can cover enormous applications on the communication system [12].

With the requirement for communication systems to operate at very high frequencies [12], the most popular technologies with most systems for filter development will have shortcomings. Planar technology has high radiation losses and low Q-factor in the microwave and terahertz frequency region. The conventional waveguide has a high Q-factor and lowers radiation losses at this frequency range; however, it has the shortcoming of being bulky. Communication systems such as satellites require that devices be as small as possible; hence the rectangular waveguide becomes unsuitable for such systems. The conventional waveguide is also not flexible and difficult to integrate with other components in a communication system. Hence there is a need to come up with miniaturized devices such as filters that can operate at high frequencies with low radiation loss and have high Q-factors for efficient transmission of information signals.

Substrate integrated waveguide (SIW) technology offers a compromise between planar technology and conventional waveguide in the development of microwave devices [13-15]. SIW has the same propagation characteristics as the traditional waveguide and can operate at much higher frequencies as compared to planar filters without incurring much radiation losses and the Q factor is comparably higher [16], [17]. The disadvantages of the conventional waveguide are overcome by the fact that SIW can be easily integrated with other system components and is easy to fabricate using well-established techniques such as PCB design [18]–[20]. To date, it is imperative that SIW devices are miniaturized to fit into modern communication systems.

With the proliferation of many applications in the communication system, the frequency spectrum is going to be further divided into the sub-frequency band. In each band, different applications will be transmitted. Hence, to have an efficient communication system, it will be essential to have tunable filters to select various applications without redesigning, modifying or re-installing the whole system. In this research work, to solve the issue of high radiation losses and poor Q factor at high frequencies, SIW technology is used to design miniaturized devices operating in the microwave frequency range and tunability is implemented using different dielectrics and Graphene because of its excellent electrical properties.

## 1.4. Research Objectives

The main objective of this research is to develop miniaturized, high-selectivity filter devices able to operate at microwave frequencies and above. The filters should have the capability of tunability and reconfigurability to operate at a range of frequencies within the band. To achieve this, the following sub-objectives are perused in this thesis:

- i. Study different technologies for designing filters operating at microwave frequency range and above.
- ii. To propose different filter designs using substrate integrated waveguide technology, which possesses the following characteristics: (a) Small footprint, (b) High selectivity, (c) Low radiation loss, and (d) High Q-factor
- iii. Analyze balanced circuits for noise reduction in filter circuits and design balanced filters with high Common Mode (CM) noise suppression.
- iv. Analyze different techniques used to design tunable or reconfigurable filters at high frequencies.
- v. Design tunable filters that can operate at a wide frequency range.

## 1.5. Research Contributions

Substrate integrated filters have been proposed in the literature [8], [19], [21]–[23]; however, they fall short in selectivity, which leads to not having sharp band edges. This may affect adjacent channels in a communication system where many applications are being transmitted simultaneously. In this thesis, the work presented illustrates the design of high selectivity filters using SIW technology and goes further to reduce the size of the filter by 50% through the use of a half-mode structure of the SIW resonator without degradation in the performance of the filter. To further reduce the size of the filters and increase selectivity, the coupling matrix method was used to design a 6<sup>th</sup>-order filter with cross-coupled SIW resonators. Eighth-mode substrate integrated waveguide resonators were used and a high-order miniaturized structure was achieved.

The use of balanced filters for noise reduction in filter circuits has been demonstrated in literature; however, the common mode signal suppression was limited. Most balanced circuits are single band, developed using planar circuits [24]–[28]. In this research work, two structures have been used for common-mode suppression: a) Dumbbell-shaped

resonators - symmetrically etched on the ground plane of the balanced SIW filter. b) Meandered inductive loops - slotted in the ground plane that behaves as low pass filters. The structures have been designed to preserve the symmetry of the filter and operate at the frequency that is to be suppressed. An extra 5 dBs in CM signal suppression was observed without affecting the differential mode (DM) signal.

This research work has been able to miniaturize the structure of the filter up to 87.5% through the use of eighth-mode SIW (EMSIW) cavity resonators. To avoid complex designs and increased selectivity while at the same time reducing the footprint, a single-layer SIW band-pass filter is designed using the Eighth-Mode Substrate Integrated Waveguide filter cavities. Four of these cavities were carefully placed in topology for the filter to operate as a cross-coupled fourth-order structure, increasing selectivity. Two EMSIW resonators were modified to achieve cross-coupling. The selectivity is increased by the source load coupling, which results in three transmission zeros on both sides of the pass-band.

As the new generations of communication systems keep expanding with applications covering almost the entire earth and near out of space [11], operating at frequencies in the terahertz band is necessary. Tunability of filters becomes imperative as many applications get incorporated into the communication systems. In literature, several methods for tunability have been proposed [29]–[35]; however, most rely on semiconductors, ferromagnetic material and microwave electro-mechanical switches, which are bulky and are only suitable for operational frequencies below  $100\text{ GHz}$  [4]. This thesis presents simple and flexible tuning through dielectric rods on a half-mode dual-band SIW filter employing triangular shape half-mode resonators. Tuning of  $1.05\text{ GHz}$  bandwidth was achieved for the center frequency of the first pass-band, and for the second pass-band, the center frequency was tuned within a bandwidth of  $1.49\text{ GHz}$ . In the literature, limited work has been reported on Graphene material implemented to achieve tunability on substrate integrated waveguides. Most reported work is based on planar technology [36]–[41]. In this thesis, a second-order Graphene-based tuning was presented to cater to the low operational frequencies of many technologies in use, and tuning was achieved in the terahertz region. The operational center frequency of the filter was tuned within the range of  $1.289\text{ THz}$  to  $1.297\text{ THz}$ , which indicates tunability within a bandwidth of  $8\text{ GHz}$ .

## 1.6. Organization of the thesis

This research aims to develop miniaturized tunable microwave filters that operate at high frequencies. As such, in this chapter, chapter 1, the theory and background of microwave communication systems and filters are presented. Figure 1.3 illustrates the general overview of the thesis.

In chapter 2, the literature review is presented. The need for miniaturization has been explored with the existing fieldwork. Previous work done in terms of balanced filters, multi-band filters, and filter tunability is investigated as well. In addition, it also presents the theory and background of microwave filter design. The frequency response approximation of the ideal filter has been realized using the Butterworth (maximally flat), Chebyshev and Elliptic functions. Low-pass filter prototypes are presented in terms of the normalized parameters and the transformation from the low-pass filter prototype to real-life filters is presented. Admittance and impedance inverters are also presented in this chapter.

Chapter 3 presents the detailed design of substrate integrated waveguide filters. Firstly, the conventional rectangular waveguide has been investigated and its relationship with the substrate integrated waveguide is established. The SIW resonators and ways to interconnect the SIW structure with other technologies have been explored. Losses that occur in SIW structures are also studied in this chapter, and the mathematical models are presented. Finally, the proposed high-selectivity SIW band-pass filter has been presented.

In chapter 4, the work on filter miniaturization has been presented. Different methods and ways used to reduce the filter footprint have been analyzed. Half-mode and Eighth mode substrate integrated waveguide resonators are used to design miniaturized filters.

Chapter 5 deals with the theory behind balanced filters as a way to maintain high integrity within communication systems. Topologies for differential and common mode transmission lines have been presented. The possible propagating modes in the transmission lines are investigated. The basic principles of balanced filter design are explained. A dual-band balanced filter has been proposed as well in this chapter. Common mode suppression techniques are also presented. A filter design using a dumbbell defected ground structure and another one utilizing a center conductor with the meandered loop are demonstrated for effective common mode suppression.

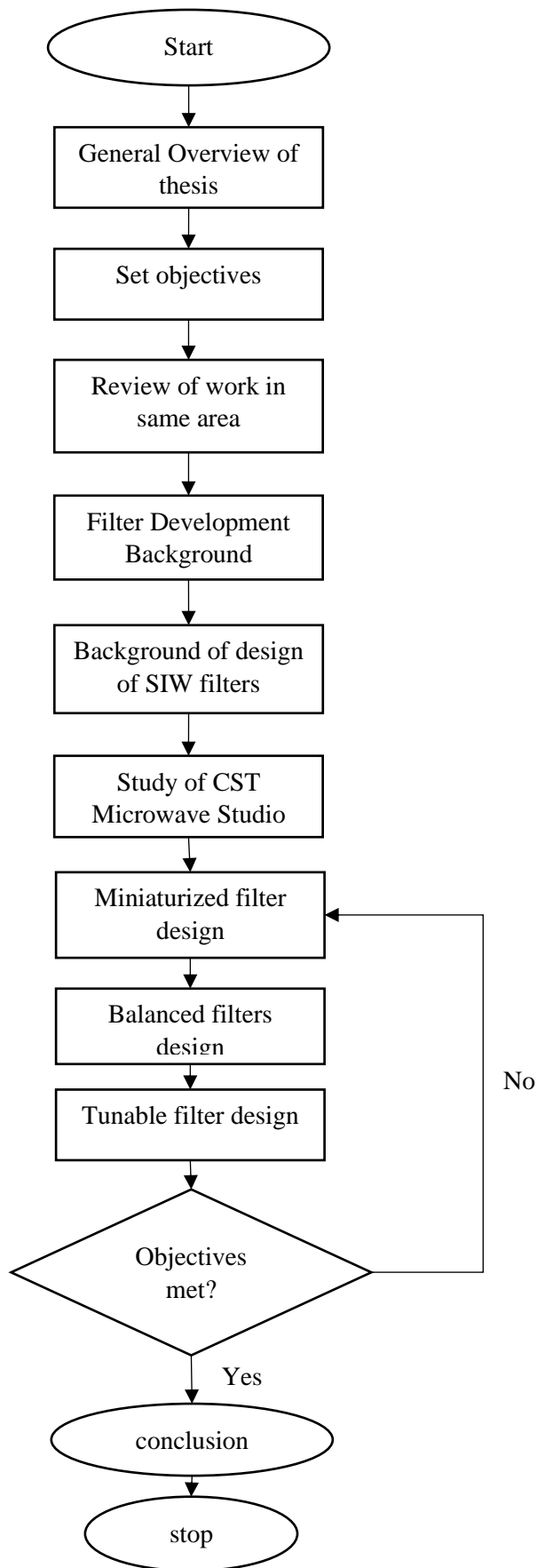


Figure 1.3 General overview of the thesis.

In chapter 6, the need for reconfigurability or tunability has been analyzed. Different ways to achieve tunability are presented with their advantages and disadvantages. The need for Graphene to substitute conventional tuning methods to avoid high radiation losses at high frequencies has been discussed. Two designs for implementing tunable filters are presented. The first used dielectric rods of different permittivities and the second was implemented by changing the chemical potential of Graphene to achieve tunability.

In chapter 7, the tunability of filters at THz range has been realized. Graphene material is discussed, its suitability for frequency tuning in the THz region has been analyzed, and the theory behind its electrical conductivity is presented. The chemical potential of Graphene is varied by the external voltage, and in turn, this changes the center frequency. The aspect ratio of Graphene was also altered in pursuit of frequency reconfigurability.

Finally, Chapter 8 presents the summary of this work, the conclusion of the work, and future recommendations on more work to be done are given.

## 1.7. Resulting Peer-Reviewed Publications

### Journals:

1. **Cleophas D. K. Mutepfe** and Viranjay M. Srivastava, "Design of miniaturized half-mode substrate integrated waveguide dual band filter for X and Ku band applications," *J. of Communications (JCM)*, vol. 18, no. 3, pp. 180-186, March. 2023.  
(DOI: 10.12720/jcm.18.3.180-186) [ETP]
2. **Cleophas D. K. Mutepfe** and Viranjay M. Srivastava, "Design and implementation of graphene-based tunable microwave filter for THz applications," *Nanomaterials* (nanomaterials), vol. 12, no. 24, article 4443, pp. 1-12, Dec. 2022.  
(DOI: 10.3390/nano12244443) [MDPI]
3. **Cleophas D. K. Mutepfe** and Viranjay M. Srivastava, "Sixth-order cross-coupled filter utilizing half- and eighth-mode substrate integrated waveguide resonators with

wide stop-band,” *Int. J. of Microwave and Optical Technology (IJMOT)*, vol. 17, no. 5, pp. 479-486, Sept.2022.  
(ISSN: 1553-0396) **[IAMOT]**

4. **Cleophas D. K. Mutepfe** and Viranjay M. Srivastava, “Design and analysis of compact 5<sup>th</sup> mode balanced substrate integrated waveguide bandpass filter for 39 GHz,” *Int. J. on Communications Antenna and Propagation (IRECAP)*, vol. 11, no. 6, pp. 401-407, Dec. 2021.  
(DOI: [10.15866/irecap.v11i6.20981](https://doi.org/10.15866/irecap.v11i6.20981)) **[Praise Worthy Prize]**
  
5. **Cleophas D. K. Mutepfe** and Viranjay M. Srivastava, “Designing of novel eighth-mode forth-order substrate integrated waveguide band-pass filter with high selectivity,” *J. of Communications (JCM)*, vol. 16, no. 12, pp. 553-558, Dec. 2021.  
(DOI: [10.12720/jcm.16.12.553-558](https://doi.org/10.12720/jcm.16.12.553-558)) **[ETP]**
  
6. **Cleophas D. K. Mutepfe** and Viranjay M. Srivastava, “An approach to high selectivity substrate integrated waveguide band-pass filter for mm-wave applications,” *Int. J. of Microwave and Optical Technology (IJMOT)*, vol. 15, no. 6, pp. 592-598, Nov. 2020.  
(ISSN: [1553-0396](https://doi.org/10.1553-0396)) **[IAMOT]**

## Conferences:

7. **Cleophas D. K. Mutepfe** and Viranjay M. Srivastava, “Second order reconfigurable half-mode substrate integrated waveguide dual-band filter: A circuit perspective,” *IEEE 2<sup>nd</sup> Ukrainian Microwave Week (UkrMW-27)*, Ukraine, 14-18 Nov. 2022, pp. 329-332.  
(DOI: [10.1109/UkrMW58013.2022.10037059](https://doi.org/10.1109/UkrMW58013.2022.10037059)) **[IEEE Xplore]**
  
8. **Cleophas D. K. Mutepfe** and Viranjay M. Srivastava, “Miniaturized substrate integrated waveguide dual-band filter with high common-mode signal suppression,”

*43<sup>rd</sup> PhotonIcs and Electromagnetics Research Symposium (PIERS)*, Hangzhou, China, 21-25 Nov. 2021, pp. 1388-1395.

(DOI: [10.1109/PIERS53385.2021.9694979](https://doi.org/10.1109/PIERS53385.2021.9694979))

*[IEEE Xplore]*

## Chapter-2

# LITERATURE REVIEW

---

### 2.1. Introduction

For the past decade, SIW technology has seen a steep jump in its usage, and research work has seen a tremendous increase as well [21, 42–45]. SIW technology is a compromise between the well-established rectangular waveguide and planar technology. Rectangular waveguides can handle high powers, exhibit tremendously lower losses, and have high Q factors but have the disadvantage of large size [7]. On the other hand, planar technology devices have smaller sizes than rectangular waveguides but have less power handling capabilities, lower Q factors, and higher insertion losses. The SIW trades in the middle of the two mentioned structures above [8]. The SIW size is smaller than that of the conventional rectangular waveguide. It is easier to integrate with other microwave components but has higher losses and less power handling capability than the rectangular waveguide [16], [17]. The SIW is larger than equivalent planar structures but can handle higher powers and operate at higher frequencies than planar structures. Various principles that guide the design of rectangular waveguides also apply to the SIW, and the characteristics such as field patterns and dissipation properties are similar [14, 15]. Numerous works have been carried out in the field of SIW technology.

*Devika et. al.* [46] have designed a SIW filter operating at 2.4 GHz and a separate one operating at 5 GHz. Three vias achieved filtering action inside the cavity to perturb the magnetic field. *Gopinath and Lal* [47] used a combination of circular and rectangular SIW cavities to develop a BPF to operate in the Ku band. *Khan and Mandal* [18] used the higher-order TE<sub>301</sub> resonators and their high unloaded Q-factor to implement a 3-pole SIW filter. A midline feeding scheme provided transmission zeros with bypass coupling and the transmission zeros were placed at the band edges to realize high selectivity.

*Moitra et. al.* [15] achieved a SIW BPF using an I-shaped electromagnetic bandgap structure (EBG) slots. The SIW BPF was then bent up to 150° to achieve miniaturization. *Martin et. al.* [48] proposed a fourth-order SIW BPF for K to E band applications through the use of inductive iris coupling. *Moitra et. al.* [49] have used circular ring, split rings, and inductive posts to design a BPF. High isolation was achieved using an array of these

structures; however, the selectivity was still appreciably low. In most work, low-order filters are designed, and this work seeks to work on high-order SIW filters.

## 2.2. Miniaturization

In the existing literature, various research works have been reported towards reducing the size and increasing the selectivity of these devices. *Ho and Tang* [50] have used a multi-layer structure to design a triple-band filter. Two miniaturized SIW cavities were stacked vertically, and the middle layer was designed with three identical patches formed by evenly trisecting a circular patch. The small size was achieved; however, since this is a multi-layer topology, it becomes complicated to design. *Salim et. al.* [51] have achieved miniaturization by etching out a complimentary folded ring resonator with a meander line slot to the layer of the filter. The size of the structure was reduced. However, the selectivity was not as good on both sides of the pass-band as there were few transmission zeros. *Xie et. al.* [52] have presented a third-order miniaturized SIW filter using a half-mode fan-shaped resonator operating at a center frequency of  $1\text{ GHz}$ . A metalized via located on the center of the circle and a semicircular ring slot etched along the circumference were used to realize the half-mode resonance.

*Wang and Dong* [53] have presented a miniaturized mm-wave band-pass filter. This Miniaturization was achieved through the use of stepped impedance slot resonators. The center frequency could also be varied by adjusting the stepped impedance size; however, the selectivity was not high on the higher side of the pass-band. *Delmonte et. al.* [7] have presented a miniaturized filter based on a modified quarter-mode SIW resonator. Metal vias were added to shield the open boundary of the quarter mode resonator to minimize high radiation leakage. QMSIW cavity was reported in which to avoid radiation losses, the classical QMSIW cavity was modified by adding a line of vias to shield the open boundary. To preserve the virtual magnetic wall, a slot was etched on the top and bottom metal surfaces; however, the losses were still high, and selectivity was not so good.

Eighth-mode SIW resonators were used for miniaturization in various existing research. *Li et. al.* [54] have presented a multi-layered SIW band-pass filter operating around  $2.8\text{ GHz}$ , utilizing four vertically stacked resonators. The cross-coupling of the load and source increased the selectivity of the filter; however, the multi-layer technique complicates the design. *Li et. al.* [55] presented a balanced, dual-band filter utilizing quarter-mode and

eighth-mode SIW cavities. The quarter model was implemented on a single-layer substrate but had lower selectivity, while the eighth-mode filter was a fourth-order filter and had high selectivity; however, being implemented on a multi-layer made the design complex. *Guo et al.* [56] designed a miniaturized filter using the eighth-mode resonator loaded with a stub-capacitor, also used for center frequency tuning. The filter had a small footprint, but the selectivity was poor, especially on the upper side of the pass-band. *Lu and Zhu* [57] have used quarter-mode and eighth-mode resonators to achieve a third-order SIW filter operating at a center frequency of  $3.66\text{ GHz}$ . Metallic vias were used to shield the open boundaries of the eighth mode structure together with slots etched on the top metallic surface. The final filter had low selectivity on the higher frequency side of the pass-band. *Nie and Hong* [58] have used the eighth-mode SIW cavity for size reduction. Slots are also etched on the surface of the filter to lower the dominant frequency of the eighth mode cavity; however, the output shows poor selectivity, especially on the lower side of the pass-band.

From the above reviews, in many instances, work done so far in miniaturization using different modes of the SIW use only one or two resonators on a single substrate; this implies lower-order filters, which result in poor selectivity. In work that was done using more cavities for operation at higher order for higher selectivity, multiple layers were used, which results in complicated designs [54, 55, 59]. *Troudi and Osman* [60] have reported a half-mode structure used in a cross-coupled band-pass filter. An irregular impedance technique is used to miniaturize the physical size of the conventional Complementary Slip Ring Resonator (CSRR). The filter exhibited two transmission zeros on the lower and upper sides of the pass-band. The structure was loaded with an elliptical complementary split-ring resonator with an irregular impedance for miniaturization. The filter operated at  $6.876\text{ GHz}$  and had a size of  $41.48\text{ mm}^2$ . However, the filter suffers poor selectivity. *Zhu et al.* [61] have presented a dual-mode band-pass filter from half-mode SIW cavities. The  $\text{TE}_{102}$  and  $\text{TE}_{301}$  modes were used as the resonant modes, while  $\text{TE}_{101}$  was used as the non-resonating mode. An additional via and a slot line were used to perturb the  $\text{TE}_{103}$  and  $\text{TE}_{102}$  modes. A two-pole HMSIW filter with an asymmetrical response and a four-pole HMSIW were reported. The filter operated at  $10\text{ GHz}$  and has a size of  $1.75\lambda_g^2$ , where  $\lambda_g$ , is the guided wavelength. *Nosrati et al.* [62] have presented a capacitively coupled SIW filter. This work uses a planar gap-coupled structure as a substitute for the conventional inductive aperture coupling. Two open-circuited studs are used to capacitively couple two SIW resonators. This resulted in a miniaturized filter operating at  $1.8\text{ GHz}$  and having a size of  $0.2 \times 0.2\lambda_g^2$ .

*Dong et al.* [63] have presented a seventh-order filter with three layers to achieve high selectivity. The first layer realized a Perfect Magnetic Conductor (PMC) using periodic plates and metallic patches. The middle layer generated the gap layer, while etched slots were formed to operate as resonators in the third layer. The filter operated at about  $17\text{ GHz}$  and had a reported wide stop-band. *Grine et. al.* [64] have implemented a double-layer filter using sixteenth-mode SIW resonators with defective ground structures in the middle metal layer. This produced four transmission zeros on both sides of the pass-band, increasing selectivity. Two deformed ground structures of different lengths were used for coupling. The filter operated at around  $11\text{ GHz}$ .

### **2.3. Multi-Band Filters**

With the technological improvement, modern and advanced communication systems are needed to handle the demands of technological advancement. Microwave components must have high-performance capabilities and be more compact [65]. This paves the way for the development of smaller communication devices. To achieve this, multi-band filters have been developed to concentrate the hardware needed to perform specific tasks in a smaller area. In literature, several methods have been employed to develop multi-band filters. For example:

- Having different single-band filters and combining them into one multi-band filter. Zhang and Zhu [66] have designed a dual-band filter with a controllable in-band ripple factor and isolation between the dual pass-band. In that work, two multi-mode resonators with short-circuited stubs were connected in parallel to form the dual-band filter. Shen et. al. [67] have designed a tri-band filter with controllable frequency and bandwidth using composite right and left-handed resonators. Three different filters operating at distinct frequencies are built and combined to create a triple-band filter. Zhang and Zhu [68] have designed a tri-band band-pass filter based on  $\lambda/4$  resonators. The first and third pass-band was achieved by coupling two dual-band  $\lambda/4$  Stepped Impedance Resonators (SIRs). And the second pass-band was realized by two coupled  $\lambda/4$  Uniform Impedance Resonators (UIRs). Zhang et. al. [69] have realized a quad-band filter using two resonators. The first was an eight-mode resonator operating at the first, second, and third pass-band. The second resonator was a short-end stub-loaded resonator, forming the

third pass-band. This method of designing multi-band filters had the problem of large size and matching circuits needed on the input and output ports.

- Having a wideband filter and dividing it into different sub-bands. The coupling matrix synthesis technique can achieve this by inserting transmission zeros within the band. Shakib et. al. [70] have designed a triple-band filter using SIW half-mode resonators. An iterative optimization technique was used based on full-wave simulation. Transmission zeros were placed within the width of the band-pass filter, and the polynomial Eq.s were solved. Tsai et. al. [71] have designed a low-temperature co-fired ceramic structure that was used to design a triple-band laminated waveguide filter. Two of the three pass-bands were assigned adjacently by using a split-type dual-band response by inserting transmission zeros in the middle of a single pass-band. A four-pole elliptic response achieves the third band. Esmaeili and Bornemann [72] have presented a triple pass-band filter consisting of six cascaded singlets. Four of six transmission zeros were placed within the pass-band, thereby producing three pass-bands.
- Using a multi-mode resonator. The multi-mode resonator can generate the desired modes and when the proper input-output coupling is implemented, a multi-band filter can be designed as required. Gao et. al. [73] have designed a multi-stub loaded resonator with eight resonance modes for the tri-band filter. Four modes form the highest band and the other two bands were realized by two modes. The frequencies of the three pass-bands can be controlled by adjusting the modes. Li et. al. [74] have used a Ring Multi-Mode Resonator (R-MMR) and a pair of parallel coupled lines to design a tri-band band-pass filter. Since the R-MMR was symmetric, its resonant characteristics can be analyzed using the odd and even mode analysis method. Three degenerate modes were perturbed to separate them into six resonant modes, and the tri-band filter was designed using these six modes. Ren et. al. [75] have used four modes of Stepped Impedance Square Ring Loaded Resonators (SI-SRLRs) to design multi-band filters with controllable frequency separation between the common mode and differential mode. By the addition of two more open-circuited stubs to the square ring of the SI-SRLR, a six-mode SI-SRLR was obtained. A tri-band filter was then obtained by coupling these two six-mode resonators. Ren et. al. [76] have designed multi-band High-Temperature Superconducting (HTS) filters using multi-mode SRLRs. The SRLR had four resonant modes. Two open transmission lines were then attached to both sides of the ring of the

SRLR of one wavelength. *Xie et. al.* [77] have used a triple-mode resonator to design a triplexer. Centered cross-shaped metalized vias holes perturb the cavity to modify the field distribution and mode frequencies.

From these literature reviews, most technologies used to design multi-band filters include R-MMR, SI-SRLRs, stub-loaded resonators [73–76], etc. However, these technologies mostly operate at lower frequencies, and they are bulky. To operate at higher frequencies, substrate integrated waveguide technology can be employed. With the properties of SIW technology, high Q factor and high power handling capability filters can be developed. SIW technology has characteristics similar to the conventional rectangular waveguide [78].

## **2.4. Balanced Filters**

Balanced communication circuits have the advantage of noise suppression. There is a need for high noise immunity in communication systems and it is always a good idea to use such circuits. This is because the balanced circuits can suppress Common-Mode (CM) signals on their input and provide passage to differential signals. In many cases, noise appears on the input as a common signal; hence can then be effectively suppressed using balanced circuits. Balanced- or Differential-Mode (DM) signals are transmitted as complementary pairs with equal amplitude but opposite in-phase signals [79, 80]. An adequately designed balanced filter offers low electromagnetic interference, high immunity to electromagnetic noise, low cross talk, high out-of-band rejection ratio, and high selectivity [79, 80].

In microwave engineering, it is very important to preserve communication integrity. The transmitted signal must not be changed in shape and form by any means and should be isolated from noise interference as much as possible. One way to reduce noise is using balanced filter circuits [81]. Unlike single-ended circuits, balanced circuits are immune to electromagnetic interference, suffer low cross-talk, and have high immunity to environmental noise [80]. Noise appears on the input as a Common-Mode (CM) signal and can be effectively suppressed using balanced circuits. Balanced circuits have the ability to suppress the common-mode signal and allow the Differential-Mode (DM) signal to pass through.

Much work has been done in the literature involving balanced filter circuits. Most balanced filter circuits have been implemented using planar circuits [81–84]. Cervantes and Chavez [81] have presented a balanced filter based on two closed-loop transmission lines. One had a characteristic impedance of  $50 \Omega$  and the other had a characteristic impedance of  $100 \Omega$ , but the filter had weak common-mode suppression. Wu et. al. [82] have used half-wavelength stepped impedance resonators to implement a balanced filter. However, the filter suffers from poor common-mode suppression. Shi and Xue [83] designed a balanced filter using center-loaded half-wavelength resonators, and the common-mode suppression was not high. Abbosh [84] has achieved a balanced filter by using tapered microstrip patches coupled via tapered slots in the ground. The ground plane was located in the middle layer. The common-mode signal was suppressed to about 27 dB, which is not very high and having multi-layers, the design is challenging to achieve.

In [85] a balanced filter with enhanced stop-band capabilities is presented. The design utilizes third-order quarter wavelength coupled resonators to achieve the filtering response. Discriminating coupling is then used between the resonator and the feedline. The filter operates at  $2.4 \text{ GHz}$  and has a CM rejection of over 20 dBs. In [25, 86] dual-mode ring resonators and coupled lines loaded with multiple stubs are used to create single-ended and balanced filters. The filter presented works at  $2.1 \text{ GHz}$ . The authors in [25] presented a fourth-order filter they implemented using a symmetric-stub loaded resonator (SSLR). The filter operated at  $1.9 \text{ GHz}$  and  $4.9 \text{ GHz}$ .

In ref. [87] a balanced substrate integrated waveguide dual-band filter is presented. In this work, the authors use the TE<sub>102</sub> mode in the cavity. The filter operated at center frequencies of  $9.42 \text{ GHz}$  and  $9.99 \text{ GHz}$ . In ref. [81, 88] the authors presented a balanced band-pass filter. The design of the filter was based on an integration scheme between capacitively loaded coaxial and microstrip resonators to form a hybrid system. The operation frequency was between  $2.2 \text{ GHz}$  and  $2.4 \text{ GHz}$ . The authors in [81] presented a balanced filter based on a resonator composed of two closed loop transmission lines of characteristic impedance  $50 \Omega$  and electrical length  $53.13^\circ$  and another line of characteristic impedance  $100 \Omega$  and electrical length  $53.13^\circ$ . The filter operated at a center frequency of  $1.029 \text{ GHz}$ . In ref. [89], the authors presented a compact band-pass filter with a wide stop band. A pair of shunt-connected coupled line resonators were used to design the filter. To achieve common-mode signal suppression, the middle point of one side of the shunt-

connected coupled line resonator is short-circuited. The filter operates at  $2.4\text{ GHz}$  with an insertion loss of 1dB and a return loss of 16 dBs.

In many instances, the balanced filters are limited in common-mode rejection and are of big size. In ref. [90, 91] the authors worked on a balanced filter based on simple square patch resonators. *Jankovic and Bengin* [90, 91] [12] have designed the balanced band-pass filter using two square patches and the filter operated at  $1.8\text{ GHz}$ ; however, the selectivity of the filter was not very satisfactory. *Zheng et. al.* [90, 91] [13] have introduced open-stubs and spur-lines to improve the selectivity of the filter and increase the common-mode rejection ratio. *Shi and Xue* [92] have designed a balanced filter based on Stepped-Impedance Resonators (SIRs). A total of eight quarter wavelength-type coupled SIRs were used. The eight SIRs were arranged in a symmetrical structure, and an acceptable differential mode operation was achieved; however, the common-mode suppression was unsatisfactory. *Abbosh* [84] used a broadside-coupled structure where the top and bottom layers of the structure contain tapered microstrip patches. The patches are coupled using tapered slots in the ground plane. *Perieto et. al.* [93] have used conventional open-loop resonators and folded stepped-impedance resonators. In this work, magnetic coupling was used instead of electrical coupling, which is commonly used.

Substrate Integrated Waveguide (SIW) technology has also been employed to design different types of filters [94–99]. The advantages of substrate integrated waveguide filters stem from their use, operation, and application, similar to the conventional rectangular waveguide. SIW has the advantages of the rectangular waveguide, which include high-quality factors, high power handling capabilities, fewer losses etc.[93]. At the same time, they overcome the disadvantages of the rectangular waveguide being bulky. Also, SIW technology is easy to integrate with planar technology and can easily be implemented on PCBs. *Xu et. al.* [94] have designed a Ku-band balanced filter on a single-layer substrate. This method used SIW resonators that are properly arranged in a suitable topology. In this method, CM signals are suppressed by the phenomenon from even and odd mode analysis [80], where the common-mode signals are converted into two signals in parallel, being out of phase and canceling out each other, and DM signals are allowed to pass. This method used TE<sub>101</sub> and TE<sub>102</sub> resonators to achieve the balanced band-pass filter. The major issue was to deal with the common-mode suppression without affecting selectivity since there was a need to remove the desired two transmission zeros to increase the common-mode suppression.

*Chu et. al.* [95] have presented a balanced SIW filter. In this work, they utilized the horizontal and vertical symmetry of the SIW to design a balanced filter operating around  $10\text{ GHz}$ . This filter had better CM suppression performance; however, the selectivity was not very good. *Chen et. al.* [96] have designed a balanced band-pass filter using SIW technology. Two square-shaped SIW cavities are arranged side by side, and the vias on the common side are removed. Paired microstrip lines are used to couple the power into the cavities and slots to perturb the degenerated TE<sub>102</sub> and TE<sub>201</sub> modes. The filter operates at around  $12\text{ GHz}$ , and better CM suppression was achieved by employing a short section of vias on the inputs and outputs; however, the selectivity was not as good on the higher side of the pass-band.

*Zhou et. al.*[97] have designed a compact SIW balanced band-pass filter operating around  $9.5\text{ GHz}$ , which was realized through two substrate layers. The circle coupling slots etched on the layer interface achieved negative coupling to introduce transmission zeros. *Shen et. al.* [98] reported a balanced band-pass filter operating using SIW technology at a frequency of  $3.5\text{ GHz}$ . In this work, transverse slots are etched on the top metal of the SIW structure. The SIW structure between the slots then became resonators operating at TE<sub>20 $\delta$</sub>  for DM operation and TE<sub>10 $\delta$</sub>  and TE<sub>30 $\delta$</sub>  modes for CM operation. The structure had a small footprint since the TE<sub>20 $\delta$</sub>  resonator was much smaller than the TE<sub>201</sub> mode resonator and had wider bandwidth due to the strong electric coupling formed by the slots. *Ji et. al.* [99] have realized a single-layer SIW filter using the eighth mode SIW cavities. In this work, cross-coupling paths are adopted, and the nature of the coupled open ends of the cavities realizes negative coupling. The filter operates at a frequency of  $2.4\text{ GHz}$ .

## **2.5. Common Mode Suppression**

To have high noise immunity, higher quality factors, and higher power handling capability, SIW technology employing the balanced technique has also come into play in implementing dual-band balanced filters. *Wang et. al.* [100] have realized a SIW dual band-pass filter using multi-mode resonators to operate at  $10.25\text{ GHz}$  and  $14.6\text{ GHz}$ . Four slot lines are etched at the bottom/ground metal to improve the common-mode rejection. The common-mode suppression was to the tune of  $40\text{ dBs}$ . Qian [87] designed a dual-band filter operating at  $9.42\text{ GHz}$  and  $9.99\text{ GHz}$  center frequencies using six SIW resonators. The common-mode suppression reached  $50\text{ dBs}$ . Shen et. al. [101] have achieved a dual band-

pass filter using four SIW resonators to operate at  $9.23\text{ GHz}$  and  $14.05\text{ GHz}$ . Four slot lines were etched on the top metal surface to improve the CM rejection capability of the proposed filter. The CM signal suppression reached 40 dBs. Zhang et. al. [28] have realized a dual band-pass filter using SIW resonators loaded with two complementary split-ring resonators etched on the top metal surface. The CM suppression reached 40 dBs. Zhang et. al. [102] employed six SIW resonators to realize a dual-band filter. The CM rejection reached about 55 dBs. In all these cases, it can be seen that the common-mode rejection is not very high, which might compromise the integrity of the wanted signal. On the other hand, the filters are also bulky since most of the work employs several resonators.

The work that has been proposed in ref. [28, 87, 100–102] falls short on either the size of the filter being large through the use of many resonators or common-mode suppression being not high.

## 2.6. Reconfigurability of Filters

Tunability of filters has become necessary in modern filters to avoid costly reinstallation of devices or modification of physical communication systems. In literature, vast research has been done to achieve tunability or reconfigurability. Yuan et. al. [29] have presented a balanced dual-band filter, which could only tune the first pass-band. The filter was constructed using Stepped Impedance Resonators (SIRs) with varactor diodes as tuning elements. The second band is implemented using an Eighth-Mode SIW etched on the bottom layer of the filter. The center frequency varies from  $1.23\text{ GHz}$  to  $1.53\text{ GHz}$ , while the insertion loss varies from  $0.5\text{ dB}$  to  $4\text{ dB}$ . Pal et. al. [30] have presented a dual-band filter made up of a stub-loaded ring resonator. A varactor diode is placed in the ring to control the odd mode resonant frequency. A second varactor diode that connects the stub to the ring controls the even mode frequency. The first band was tuned from  $0.69\text{ GHz}$  to  $0.88\text{ GHz}$  with  $1.83\text{ dB}$  maximum insertion loss. The second band is tuned from  $2.67\text{ GHz}$  to  $3.78\text{ GHz}$  with  $2.02\text{ dB}$  maximum insertion loss. Fan et. al. [31] have designed a reconfigurable band-pass to band-stop filter using a pin diode. Two pairs of varactor diodes are also employed to control the center frequency and external quality factor. The center frequency can be tuned from  $0.79\text{ GHz}$  to  $1.59\text{ GHz}$ . The stop-band is tunable from  $0.7\text{ GHz}$  to  $1.47\text{ GHz}$ .

Brown and Saavedra [103] used Eutectic Gallium Indium (EGaIn) for frequency tuning. A SIW quasi elliptic band-pass filter was presented using reconfigurable  $\text{TE}_{101}$ -made

cavity resonators. Four cavities were designed with vias on the corners, selectively filled with EGaIn for frequency tuning. The frequency can be changed from 7.96 GHz to 8.39 GHz. *Brown and Saavedra* [104] used fluidic pockets with different dimensions and geometrics for tuning the frequency of substrate integrated waveguide cavities. The center frequency was changed over a range of 170 MHz. The center frequency was 2.4 GHz, and the insertion loss reached -5 dB during tuning.

*Sun et. al.* [105] present a filter based on combined SIW resonators loaded with varactors for center frequency tuning. Varactor diodes are surface mounted between two coupled resonators to control the inter-resonator coupling and tune the bandwidth. The center frequency is tuned by varactors loaded on the compline resonators. The 3 dB bandwidth range around the center frequency of 4.5 GHz is between 82 MHz – 260 MHz, around the center frequency of 3.5 GHz, the 3 dB bandwidth range is between 40 MHz – 170 MHz and lastly, around the center frequency of 3 GHz, the 3 dB bandwidth is between 75 MHz – 90 MHz. *Sirci et. al.* [106] have designed an electronically reconfigurable C-dual band mode coaxial SIW resonator. Back-to-back varactor diodes tune the center frequency, bandwidth, and return loss levels. Tuning occurs over the range of 5.54 GHz to 6.3 GHz with a worst-case insertion loss of 5 dB.

*Abdelfattah and Peroulis* [107] used two dual-mode SIW cavity resonators to design a second-order band-pass filter. A contactless tuner is then used for center frequency tuning, which occurs from 2.2 GHz to 3.4 GHz with an insertion loss of 1.36 dB. *Alterkawi et. al.* [108] have presented an embedded suspended stripline in PCB, where a direct copper-to-copper connection joins the metalized cavity walls on the ground layer. The filter is based on a dual-mode patch.

## 2.7. Graphene Tuning

Microwave filters are an important component of communication systems. With recent advances in technology, tunable/reconfigurable filters are becoming necessary to achieve a modern filter's requirements. Beyond 5G, communication systems are required to operate at high frequencies in the region of THz. A good amount of available filters use planar technologies [75, 109–115], which suffer huge losses in the THz region. Substrate integrated waveguide (SIW) filters were introduced to solve the problem of high losses at

high frequencies suffered by planar circuits. SIW has the same characteristics of high power handling and lower losses at high frequencies as the conventional waveguide [13, 116].

In terms of tuning the filters, different ways have been explored in literature [30, 106, 117–122]. In [117], a liquid metal, GaInSn was used to tune the center frequency. The volume of the cavity was reduced by filling the cavity with this alloy, which reduced the internal wall distance. Frequency tuning was between  $7\text{ GHz}$  and  $8\text{ GHz}$ . In [118] a multi-layer periodic structure is presented whereby tuning is achieved by liquid metal. A thickness-controlling aperture separates the Frequency Selective Surfaces (FSS). The liquid metal layers are combined with the elastomeric substrate to realize a flexible and fluid-tunable device. The filter was tuned between  $13.5\text{ GHz}$  and  $17\text{ GHz}$ . *Alkaraki et. al.* [119] presented a method for allowing or preventing wave propagation using a removable wall built from several drill holes. To form a wall, the vias were filled with a gallium liquid metal; when not required, the vias were emptied. Tuning occurred from  $4.7\text{ GHz}$  to  $7.2\text{ GHz}$ .

In [120], liquid metal - Eutectic gallium indium (EGaIn) was used to design a reconfigurable meta-surface antenna. Distinct reflective phase response was achieved by melting and rotating the element structure, which changed the liquid metal's shape and hence achieved reconfigurability. *Alex* [121] has presented a liquid-based tuned filter. Square substrate integrated waveguide resonators were capacitively loaded with liquid metal posts, which meant changing the loading capacitance. The resonant frequencies were changed between  $3.4\text{ GHz}$  and  $5.83\text{ GHz}$  using this technique. In [106] varactor diodes were used in a back-to-back setup to tune the center frequency and bandwidth of the filter as well as the return loss. Ten varactor diodes were used to implement a two-pole tunable band-pass filter with two transmission zeros. The tuning occurred in the range of  $5.65\text{ GHz}$  to  $6.35\text{ GHz}$ .

In [122] the authors placed varactor diodes along the open side of a half-mode SIW and microstrip feeding line to construct in-band notches. They then controlled the biasing voltage and reconfigurability was achieved. The frequency and bandwidth of the filter were successfully tuned independently. Frequency tuning was achieved in the range of  $5.99\text{ GHz}$  to  $10.15\text{ GHz}$ . *Biswajit and Marinal* [30] have presented a stub-loaded resonator. A varactor diode was placed in the ring to control the odd-mode resonant frequency. Frequency was tuned from  $0.69\text{ GHz}$  to  $0.88\text{ GHz}$  with a maximum insertion loss  $1.83\text{ dB}$ .

For high-frequency structures in the THz region, Graphene has been used for frequency and bandwidth tuning [37, 38, 123–126]. This is achievable because Graphene as

a material has superior structural, mechanical, and electrical properties [127]. In ref. [123], the authors used Graphene for the tunability of a THz duplexing MIMO antenna. The antenna can tune the frequency at the two ports independently. By changing the Graphene's chemical potential, the radiators can be tuned. In [124], square patch microstrip antennas are studied. Graphene material was used to control and regulate the antenna's polarization. By controlling the fermi energy level, right-hand, left-hand circular polarization, and linear polarization can be displayed. This changes the chemical potential of Graphene. In [125] Ram et.al simulated a planar THz filter designed based on Graphene. A Graphene layer was inserted between the conductor layer and the dielectric to support the propagation of plasmonic waves. The Graphene's chemical potential was varied to tune the resonant frequency of the band stop filter over the range of  $0.1 THz$ . *Naghizade and Saghaei* [37] have presented Graphene On Insulator (GOI) band stop filter operating in the mid-infrared region. To achieve tunability of the filter, some physical parameters, such as the number of overlapped filters and the number of graphene layers were changed together with the applied voltage.

*Moazami et. al.* [126] have presented a plasmonic tunable single stub filter. A thin Graphene layer was used to tune the filter in the THz region. By applying a gate voltage between the gate graphene sheet and the Indium antimonide (InSb) substrate, the center frequency was shifted by  $32 GHz$ . The filter's bandwidth was also improved by 33% by increasing the number of stubs. *Guarev* [38] has presented a single/dual band notch filter for THz applications. A graphene patch is inserted in the filter for tunability. The aspect ratio of the graphene patch was changed to determine the different  $TM_{mn}$  modes to be excited from the structure – which helped the filter to be configured as a single or dual-band notch filter. The variation of the chemical potential of Graphene also changed the center frequency.

## 2.8. Filter Background Theory

For a two-port filter network shown in Fig. 2.1, the design starts with identifying the approximate transfer function suitable for the specified requirements. The transfer function is simply a mathematical description of the network response characteristics given as  $S_{21}$  in Eq. (2.1) [5] where  $S_{21}$  = power that reaches port 2 from port 1, and  $S_{11}$ ,  $S_{22}$  are the reflection coefficients,  $S_{21}$  and  $S_{12}$  are transmission coefficients.

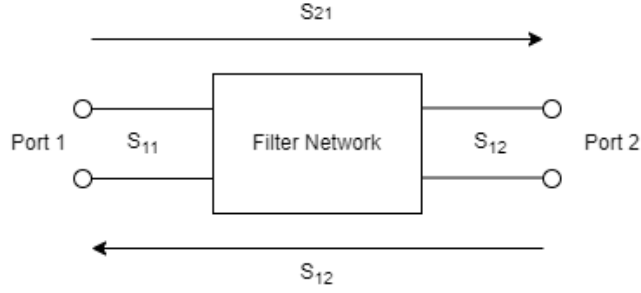


Figure 2.1 Two-port filter network

$$|S_{21}(j\omega)|^2 = \frac{1}{1 + \varepsilon^2 F_n^2(\omega)} \quad (2.1)$$

where  $\varepsilon$  is the ripple factor,  $\omega$  is a frequency variable, and  $F(\omega)$  is the filtering or characteristic function. For linear time-invariant systems, the characteristic function is defined as:

$$S_{21}(p) = \frac{N(p)}{D(p)} \quad (2.2)$$

where,  $N(p)$  and  $D(p)$  are complex polynomials and  $p = \delta + j\omega$  and for lossless filter networks,  $\delta = 0$  and  $p = j\omega$ . For a given transfer function of Eq. (2.1) the insertion loss of the filter is given by:

$$L_A(\omega) = 10 \log \frac{1}{10|S_{21}(j\omega)|^2} \text{ dB} \quad (2.3)$$

For a lossless network  $|S_{21}|^2 + |S_{11}|^2 = 1$  meaning the power reflected + power transmitted is equal to the input power, the return loss of the filter is then given by

$$L_R(\omega) = 10 \log[1 - |S_{21}(j\omega)|^2] \text{ dB} \quad (2.4)$$

### 2.8.1 Butterworth (Maximally flat) Approximation

The Butterworth response gives the simplest frequency response approximation to an ideal filter, the S-parameters of this kind of filter are given by:

$$|S_{21}(j\omega)|^2 = \frac{1}{1+\omega^{2n}} \quad (2.5)$$

$$|S_{11}(j\omega)|^2 = \frac{\omega^{2n}}{1+\omega^{2n}} \quad (2.6)$$

where  $n$  is the order of the filter, which represents the number of reactive elements required in the low-pass prototype filter. And the insertion loss is computed as:

$$L_A(\omega) = 10 \log_{10}[1 + \omega^{2n}] \text{ dB} \quad (2.7)$$

A typical Butterworth filter response is shown in Fig. 2.2 [4] with low pass amplitude response of a 3-pole Butterworth filter. The more reactive elements, the higher the selectivity of the filter.

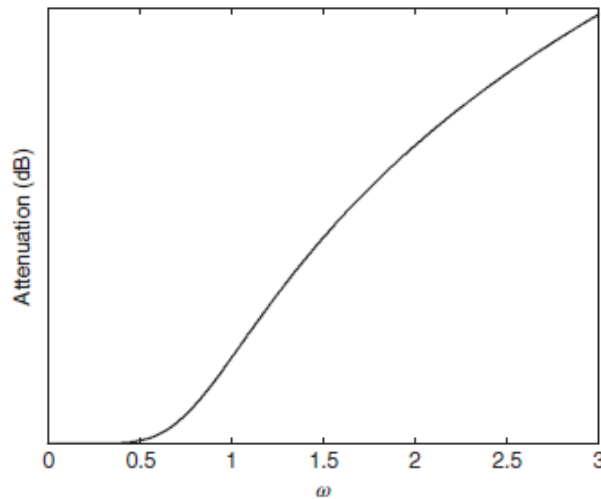


Figure 2.2 Butterworth filter response [4].

### 2.8.2 Chebyshev Approximation

For this approximation, all the transmission zeroes are located at infinity. This is a more improved approximation than the maximally flat roll-off from pass-band to stop-band. The S-parameters of this kind of filter are given as:

$$|S_{21}(j\omega)|^2 = \frac{1}{1+\varepsilon^2 T_n^2(\omega)} \quad (2.8)$$

where the ripple constant is related to the pass-band  $L_{Ar}$  in dB by;

$$\varepsilon = \sqrt{10^{\frac{L_{Ar}}{10}} - 1} \quad (2.9)$$

And  $L_{Ar}$  is computed by:

$$L_A(\omega) = 10 \log_{10}[1 + \varepsilon^2 T_n^2(\omega)] \quad (2.10)$$

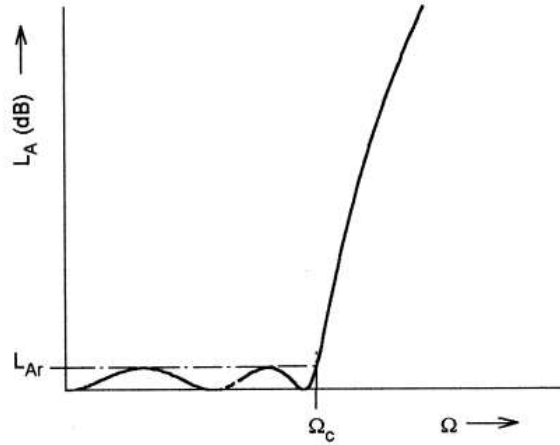


Figure 2.3 Chebyshev frequency response [5].

A Chebyshev function's low-pass prototype frequency response is shown in Fig. 2.3 [5]. It has a sharp roll-off after the cut-off frequency as compared to the maximally flat frequency response.

### 2.8.3 Elliptic Approximation

The transmission roles of Chebyshev and Maximally flat filters are located at infinity. They are also referred as all-pole filters [5, 128], where one of the elliptic approximation transmission zeroes can be placed at the finite frequency to ensure an improved roll-off. This kind of approximation has an equal ripple in the pass-band and stop-band. The transfer function is given by [5]:

$$|S_{21}(j\omega)|^2 = \frac{1}{1 + \varepsilon^2 F_n^2(\omega)} \quad (2.11)$$

where

$$F_n(\omega) = \begin{cases} \frac{M \prod_{i=1}^{\frac{n}{2}} (\omega_i^2 - \omega^2)}{\prod_{i=1}^{\frac{n}{2}} (\frac{\omega_s^2}{\omega_i^2} - \omega^2)}, & \text{for } n \text{ even} \\ \frac{N \omega \prod_{i=1}^{\frac{(n-1)}{2}} (\omega_i^2 - \omega^2)}{\prod_{i=1}^{\frac{(n-1)}{2}} (\frac{\omega_s^2}{\omega_i^2} - \omega^2)}, & \text{for } n(\geq 3) \text{ odd} \end{cases} \quad (2.12)$$

and  $\omega_i$  ( $0 < \omega_i < 1$ ) and  $\omega_s > 1$  represent a critical frequency, M and N are constants. The low-pass prototype frequency response of the elliptic function is given in Fig. 2.4 [4].

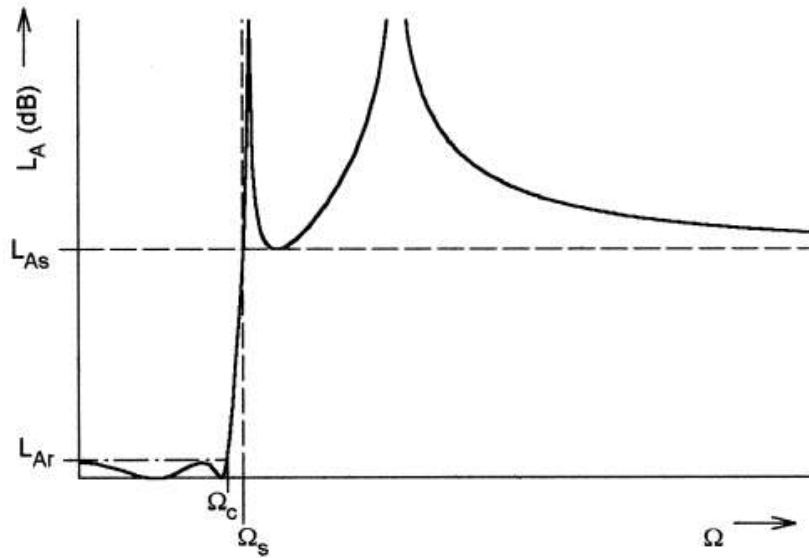


Figure 2.4 Elliptic function frequency response. [4]

## 2.9. Low-pass Filter Prototype Networks

A low-pass prototype filter or equivalent network is required to realize filters with approximate response functions as discussed above [5, 128]. The normalized filter prototype is used, where the source resistance or conductance is equal to one denoted by  $g_0 = 1$  and the cut-off angular frequency is equal to one as well represented by  $\Omega_c = 1$  rad/s. A possible prototype filter is the ladder network which consists of alternating series and parallel impedances shown in Fig. 2.5. This prototype filter can be used to realize maximally flat or Chebyshev filters.

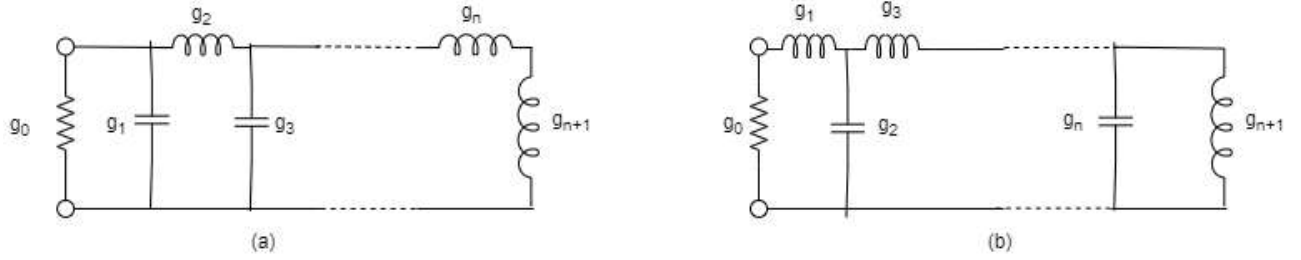


Figure 2.5 Low-pass filter prototype for all poles with (a) Ladder network (b) Dual network. [4]

The order of the filter to specify given specifications can be given by Eq. (2.13):

$$n \geq \frac{\log_{10}(10^{0.1L_{AS}} - 1)}{2 \log_{10} \Omega_s} \frac{L_{AR} + L_{AS}}{20 \left( \log_{10} \frac{\Omega_s}{\Omega_p} \right)} \quad (2.13)$$

Where  $\Omega = \Omega_s$  and  $\Omega_s$  and  $\Omega_p > 1$  represent some critical frequency.

### 2.9.1 Maximally Flat Low-Pass Filter Prototype

The maximally flat filter or Butterworth filter with a transfer function given by Eq. (2.5) with an insertion loss of 3.01 dB and  $\Omega_c = 1$  rad/s can be given by:

$$g_0 = 1.0$$

$$g_i = 2 \sin \left( \frac{(2i-1)\pi}{2n} \right), \text{ for } i = 1 \dots n \quad (2.14)$$

$$g_{n+1} = 1$$

To find the order of the filter to satisfy the given specification Eq. (2.15) and be used

$$n \geq \frac{\log(10^{0.1L_{AS}} - 1)}{2 \log \Omega_s} \quad (2.15)$$

### 2.9.2 Chebyshev Low-pass Filter Prototype

For a Chebyshev filter with pass-band ripple  $L_{Ar}$  dB and cut-off frequency,  $\Omega_c = 1$ , the element values of the ladder network can be computed as follows [5], [128]:

$$g_0 = 1.0 \quad (2.16)$$

$$g_1 = \frac{2}{\gamma} \sin\left(\frac{\pi}{2n}\right) \quad (2.17)$$

$$g_i = \frac{1}{g_{i-1}} \frac{4 \sin\left[\frac{(2i-1)\pi}{2n}\right] \cdot \sin\left[\frac{(2i-3)\pi}{2n}\right]}{\gamma^2 + \sin^2\left[\frac{(i-1)\pi}{n}\right]} \quad (2.18)$$

$$g_{n+1} = f(x) = \begin{cases} 1.0, & \text{for } n \text{ odd} \\ \coth^2\left(\frac{\beta}{4}\right), & \text{for } n \text{ even} \end{cases} \quad (2.19)$$

And,

$$\beta = \ln \left[ \coth \left( \frac{L_{Af}}{17.37} \right) \right] \quad (2.20)$$

$$\gamma = \sinh \left( \frac{\beta}{2n} \right) \quad (2.21)$$

The order/degree of the filter to satisfy the given specifications when given pass-band ripple  $L_{Ar}$  dB and minimum stop-band attenuation  $L_{As}$  at  $\Omega = \Omega_s$  can be computed by

$$n \geq \frac{\cosh^{-1} \sqrt{\frac{10^{0.1L_{As}-1}}{10^{0.1L_{Ar}-1}}}}{\cosh^{-1}\Omega_s} \quad (2.22)$$

### 2.9.3 Elliptic Low-pass Filter Prototype

For the elliptic low-pass filter prototype, the ladder network introduced in the previous two sections is modified to introduce transmission zeroes at finite frequencies as shown in Fig. 2.6(a). The series of branches of parallel resonators introduce transmission zeroes. The parallel resonators block transmission since it has infinite impedance at resonance. The dual realization is shown in Fig. 2.6(b).

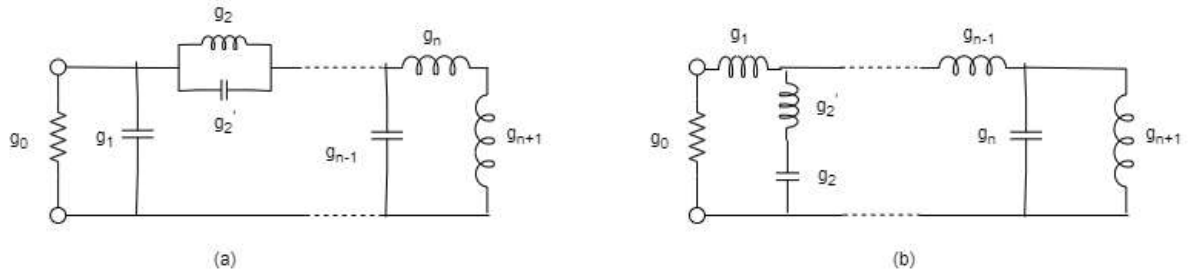


Figure 2.6 LPF prototype for the elliptic filter (a) Ladder network and (b) Dual network [4].

## 2.10. Transformation of the LPF

The LPF prototype considered in the previous sections only applies to source resistance/conductance  $g_0 = 1$  and a cut-off frequency  $\Omega_c = 1$ . Frequency and element transformation are required to set the practical values for building physical filters. The frequency transformation changes the value of reactive elements but does not affect the resistive elements. For impedance transformation:

$$\gamma_0 = \begin{cases} z_0/g_0, & g_0 = \text{resistance} \\ g_0/Y_0, & g_0 = \text{conductance} \end{cases} \quad (2.23)$$

where,  $\gamma_0$  is the impedance scaling factor and  $Y_0 = 1/Z_0$  is the source admittance. Then:

$$L \rightarrow \gamma_0 L \quad (2.24.1)$$

$$C = C/\gamma_0 \quad (2.24.2)$$

$$R = \gamma_0 R \quad (2.24.3)$$

$$G = G/\gamma_0 \quad (2.24.4)$$

### 2.10.1 Low-pass Filter Transformation

To transform a low-pass prototype filter to a practical LPF with a cut-off frequency  $\omega_c$  in the angular frequency axis  $\omega$  Eq. (2.25) can be used

$$\Omega = \frac{\Omega_c}{\omega_c} \omega \quad (2.25)$$

$$L = \left( \frac{\Omega_c}{\omega_c} \right) \gamma_0 g \quad (2.26)$$

$$C = \left( \frac{\Omega_c}{\omega_c} \right) \frac{g}{\gamma_0} \quad (2.27)$$

This can be shown in Fig. 2.7

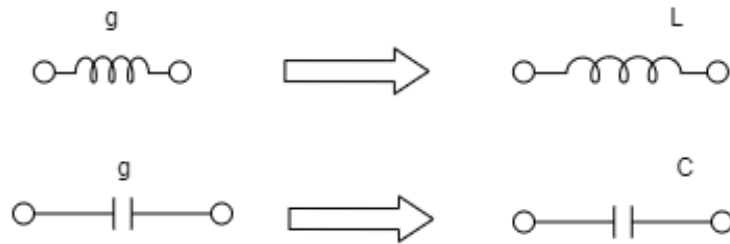


Figure 2.7 LPF prototype transformation

### 2.10.2 High-pass Filter Transformation

The transformation of a LPF prototype to a practical HPF with a cut-off frequency  $\omega_c$  is given by Eq. (2.28):

$$\Omega = \frac{-\omega_c}{\omega} \Omega_c \quad (2.28)$$

$$C = \left( \frac{1}{\omega_c \Omega_c} \right) \frac{1}{\gamma_0 g}, \quad g \text{ representing inductance} \quad (2.29)$$

$$L = \left( \frac{1}{\omega_c \Omega_c} \right) \frac{\gamma_0}{g}, \quad \text{for } g \text{ representing capacitance} \quad (2.30)$$

In this case, the capacitance is transformed into an inductor, and the inductor will become a capacitor as shown in Fig. 2.8.

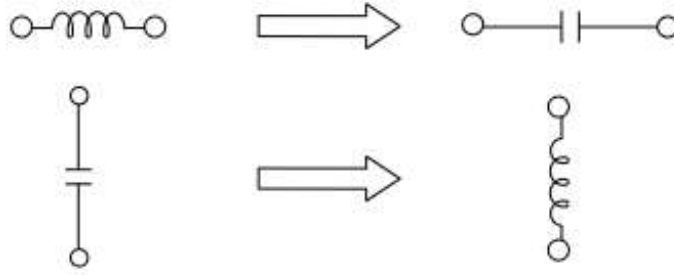


Figure 2.8 HPF prototype transformation

### 2.10.3 Band-pass Filter Transformation

Assuming  $\omega_2$  and  $\omega_1$  represent the pass-band edge angular frequency and pass-band being equal to  $(\omega_2 - \omega_1)$ , the transformation from LPF prototype to practical BPF is given as:

$$\Omega = \frac{\Omega_c}{FBW} \left( \frac{\omega}{\omega_0} - \frac{\omega_0}{\omega} \right) \quad (2.31)$$

$$FBW = \frac{\omega_2 - \omega_1}{\omega_0} \quad (2.32)$$

$$\omega_0 = \sqrt{\omega_1 \omega_2} \quad (2.33)$$

Where  $\omega_0$  denotes the center frequency

$$L_s = \left( \frac{\Omega_c}{(FBW)\omega_0} \right) \gamma_0 g, \text{ for } g \text{ representing the inductance} \quad (2.34)$$

$$C_s = \left( \frac{FBW}{\omega_0 \Omega_c} \right) \frac{1}{\gamma_0 g} \quad (2.35)$$

$$C_p = \left( \frac{\Omega_c}{FBW \omega_0} \right) \frac{g}{\gamma_0}, \text{ for } g \text{ representing the capacitance} \quad (2.36)$$

$$L_s = \left( \frac{FBW}{\omega_0 \Omega_c} \right) \frac{\gamma_0}{g} \quad (2.37)$$

This transformation is represented as in Fig. 2.9:

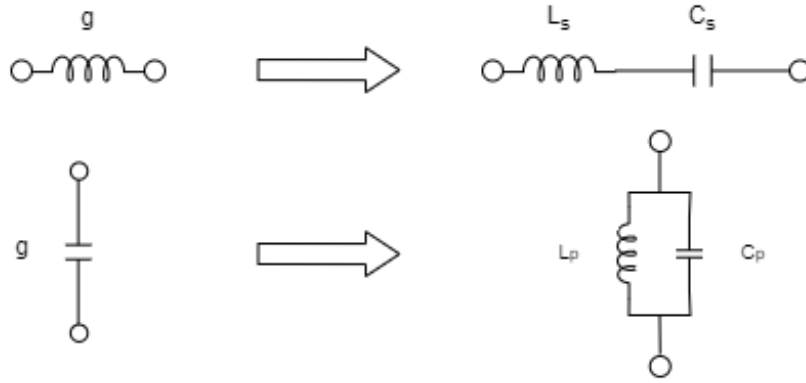


Fig. 2.9 BPF prototype transformation

### 2.10.4 Band-Stop Filter Transformation

To transform from LPF prototype to a practical BPF the following Eq.s are used:

$$\Omega = \frac{\Omega_c FBW}{\left(\frac{\omega_0 - \omega}{\omega - \omega_0}\right)} \quad (2.38)$$

where,  $\omega$  and FBW are defined in Eq. (2.32) and Eq. (2.33), respectively.

$$C_p = \left(\frac{1}{(FBW)\omega_0\Omega_c}\right)\frac{1}{\gamma_0 g}, \text{ for } g \text{ representing the inductance} \quad (2.39)$$

$$L_p = \left(\frac{\Omega_c FBW}{\omega_0}\right)\gamma_0 g \quad (2.40)$$

$$L_s = \left(\frac{1}{(FBW)\omega_0\Omega_c}\right)\frac{\gamma_0}{g} \quad (2.41)$$

$$C_s = \left(\frac{\Omega_c FBW}{\omega_0}\right)\frac{g}{\gamma_0}, \text{ for } g \text{ representing the capacitance} \quad (2.42)$$

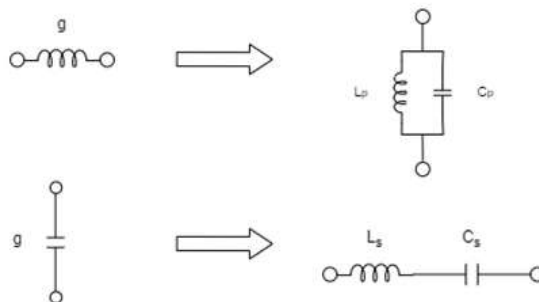


Fig. 2.10 BSF prototype transformation

## 2.11. Immittance, Impedance, and Admittance Inverters

The LPF prototype described in the previous section uses lumped LC components. Implementing filters at high frequencies using lumped elements without incurring large radiation losses is difficult. The resonators in the LPF prototype can operate at different frequencies and thus makes it difficult to realize a practical filter; hence all resonators need to be adjusted to work at the same frequency. This is achieved through the use of immittance inverters. Immittance inverters can be implemented as either impedance or admittance inverters. An immittance inverter has the ability to convert the lumped elements for example, from inductance to capacitance and vice versa, as shown in Fig. 2.11 [5].

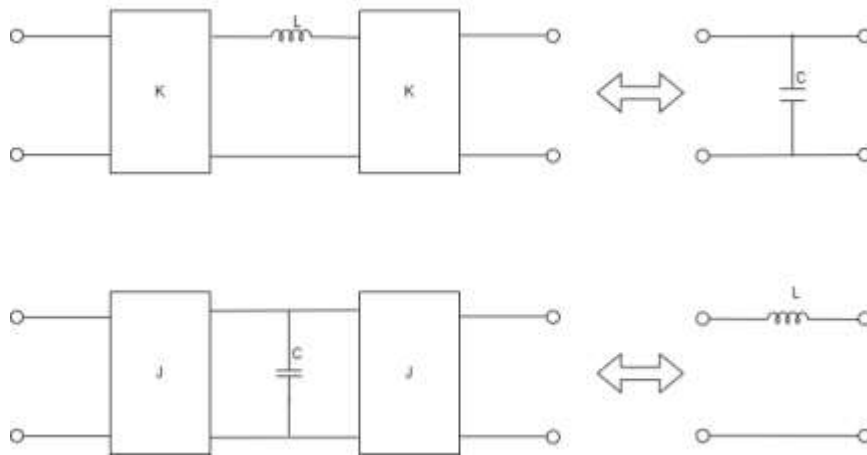


Figure 2.11 Immittance inverter used to convert (a) inductor to a capacitor, (b) capacitor to an inductor.

For an ideal two-port impedance inverter terminated by an impedance  $Z_2$  on one port, the impedance  $Z_1$  looking from the other port is computed as:

$$Z_1 = \frac{K^2}{Z_2} \quad (2.43)$$

where  $K$  is the characteristic impedance of the inverter. In terms of the admittance, the two-port network admittance is inverted when  $Y_2$  is connected to one port, and the other port admittance becomes:

$$Y_1 = \frac{J^2}{Y_2} \quad (2.44)$$

where  $J$  is the characteristic admittance of the inverter.

### 2.11.1 Using Immittance Inverters

The filter in Fig. 2.5 may be converted using immittance inverters to one as shown in Fig. 2.12 [5].

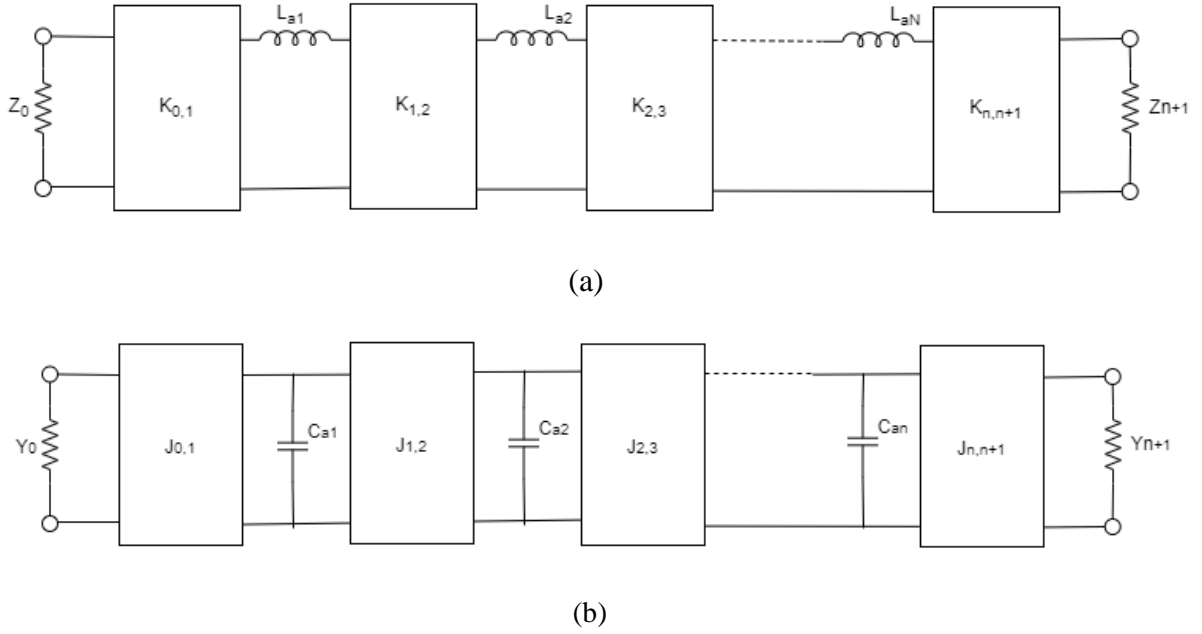


Figure 2.12(a) Immittance inverters (b) The dual

$$K_{0,1} = \sqrt{\frac{Z_0 L_{a1}}{g_0 g_1}} \quad (2.45)$$

$$K_{i,i+1} = \sqrt{\frac{L_{ai} L_{a(i+1)}}{g_i g_{i+1}}}$$

$$K_{n,n+1} = \sqrt{\frac{L_{an} Z_{n+1}}{g_n g_{n+1}}}$$

Using the J inverters, we obtain:

$$J_{0,1} = \sqrt{\frac{Y_0 C_{a1}}{g_0 g_1}}$$

$$j_{i,i+1} = \sqrt{\frac{C_{ai} C_{a(i+1)}}{g_i g_{i+1}}} \quad |_{i=1 \text{ to } n-1} \quad (2.46)$$

$$J_{n,n+1} = \sqrt{\frac{C_{an}Y_{n+1}}{g_n g_{n+1}}}$$

where  $g_i$  is the original prototype values, it can be seen that the equivalent circuit consists of lumped elements of the same type connected by J or K inverters. The values  $Z_0, Z_{n+1}, L_{ai}, C_{ai}, Y_0, Y_{n+1}$  can be chosen arbitrarily; however, for the equivalent circuit's filter response to be the same as the original prototype, the immittance inverter parameters must be defined as in eq. (18) and (19).

### 2.11.2 Band-pass Filter Using Immittance Inverters

To transform the LPF with inverters to other types of filters, the element transformation, as described in section 2.11.1 can be applied. Figure 2.13 shows a band-pass filter using immittance inverters.

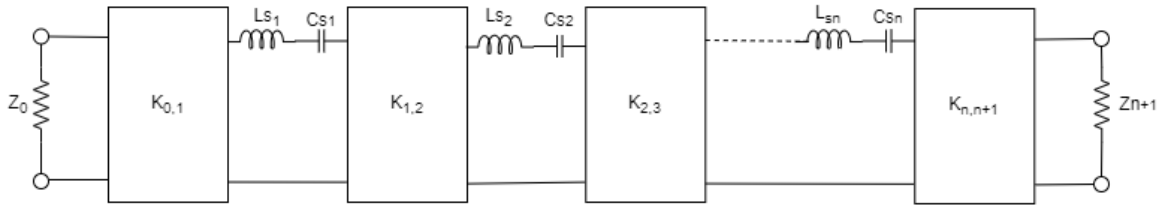


Figure 2.13 BPF transformation.

$$K_{0,1} = \sqrt{\frac{Z_0 FBW \omega_0 L_{s1}}{\Omega_c g_0 g_1}}$$

$$K_{i,i+1} = \frac{FBW \omega_0}{\Omega_c} \sqrt{\frac{L_{si} L_{s(i+1)}}{g_i g_{i+1}}} \quad (2.47)$$

$$K_{n,n+1} = \sqrt{\frac{FBW \omega_0 L_{sn} Z_{n+1}}{\Omega_c g_n g_{n+1}}}$$

$$C_{si} = \frac{1}{\omega_0^2 L_{si}} \Big|_{i=1 \text{ to } n}$$

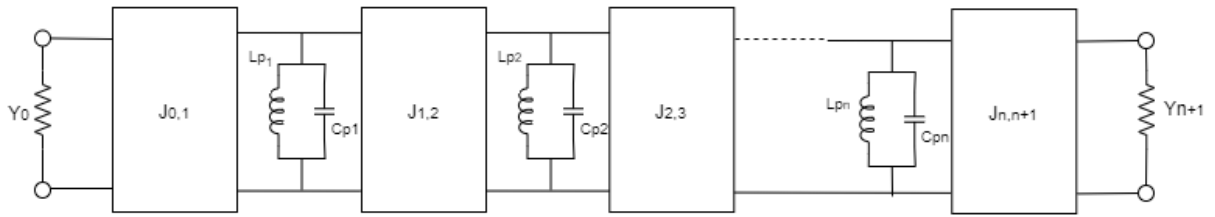


Figure 2.14 Transformed filter using J -inverters.

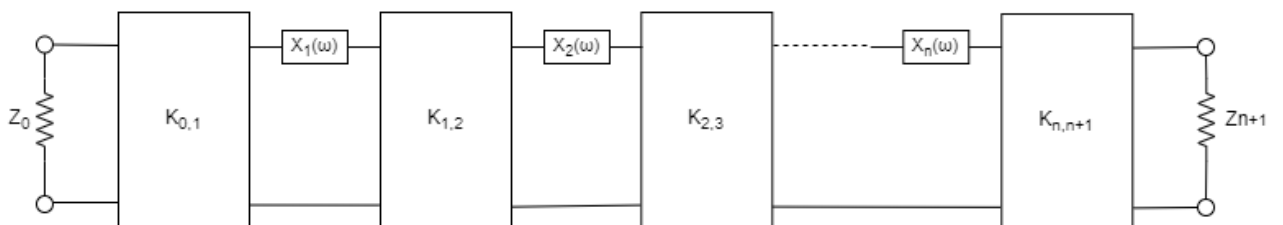
$$J_{0,1} = \sqrt{\frac{Y_0 FBW \omega_0 C_{p1}}{\Omega_c g_0 g_1}}$$

$$J_{i,i+1} = \frac{FBW}{\Omega_c} \sqrt{\frac{C_{pi} C_{p(i+1)}}{g_i g_{i+1}}} \Big|_{i=1 \text{ to } n-1} \quad (2.48)$$

$$J_{n,n+1} = \sqrt{\frac{FBW \omega_0 C_{pn} Y_{n+1}}{\Omega_c g_n g_{n+1}}}$$

$$L_{pi} = \frac{1}{\omega_0^2 C_{pi}} \Big|_{i=1 \text{ to } n}$$

To be able to design a filter that can operate at high frequencies, lumped LC components must be replaced with distributed circuits. Distributed circuits can be, among other things, microstrip resonators, microwave cavities or other suitable resonant structures. These distributed resonators are shown in Fig. 2.15.



(a)

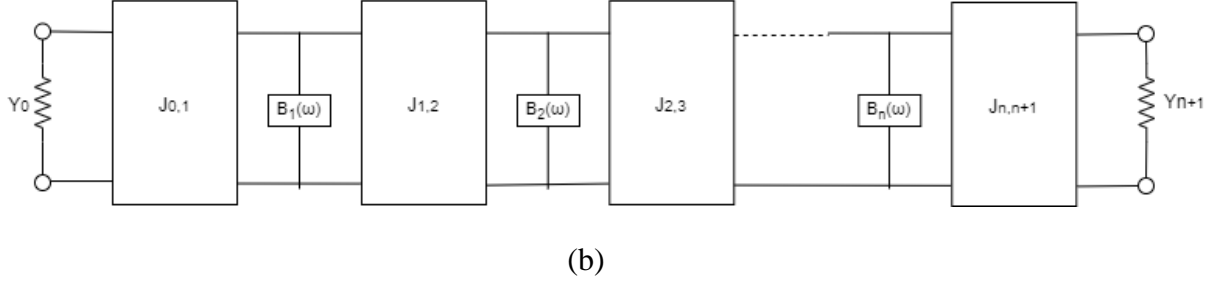


Fig. 2.15(a) Band pass filter using K inverters and distributed resonators (b) Band pass filter using J inverters and distributed resonators.

Using the K inverters:

$$K_{0,1} = \sqrt{\frac{Z_0 FBW x_1}{\Omega_c g_0 g_1}}$$

$$K_{i,i+1} = \frac{FBW}{\Omega_c} \sqrt{\frac{x_i x_{i+1}}{g_i g_{i+1}}}$$

(2.49)

$$K_{n,n+1} = \sqrt{\frac{FBW x_n Z_{n+1}}{\Omega_c g_n g_{n+1}}}$$

$$x_i = \omega_0 \left. \frac{d X_i(\omega)}{d\omega} \right|_{\omega=\omega_0}$$

Using the J inverters:

$$J_{0,1} = \sqrt{\frac{Y_0 FBW b_1}{\Omega_c g_0 g_1}}$$

$$J_{i,i+1} = \frac{FBW}{\Omega_c} \sqrt{\frac{b_i b_{i+1}}{g_i g_{i+1}}}$$

(2.50)

$$J_{n,n+1} = \sqrt{\frac{FBW b_n Y_{n+1}}{\Omega_c g_n g_{n+1}}}$$

$$b_i = \frac{\omega_0}{2} \frac{d B_i(\omega)}{d\omega} \Big|_{\omega=\omega_0}$$

where:

$x = \frac{\omega_0}{2} \frac{d X_i(\omega)}{d\omega} \Big|_{\omega=\omega_0}$  is the reactance slope parameter for resonators having zero reactance

at center frequency  $\omega_0$ .  $X(\omega)$  is the reactance of the distributed resonator. In the dual case:

$b = \frac{\omega_0}{2} \frac{d B_i(\omega)}{d\omega} \Big|_{\omega=\omega_0}$  where  $B(\omega)$  is the susceptance of the distributed resonator. The

reactance slope parameter of a lumped LC series resonator is equal to  $\omega_0 L$ , while the susceptance slope parameter of the lumped LC resonator is  $\omega_0 C$ .

## 2.12. Chapter Summary

This chapter discusses different types of technologies used to design microwave filters. The advantages and disadvantages of planar technologies are presented. Conventional rectangular waveguide technology is also discussed, and its shortfalls are highlighted. This chapter also looks at the need for a compromise between planar technologies and the conventional rectangular waveguide to harness the advantages of each technology while minimizing the effects of their shortfalls. Substrate integrated waveguide is introduced and its benefits are discussed. This chapter also deals with the background and need for microwave devices to have a small footprint. Work done in the field of miniaturization is presented and various methods for microwave device miniaturization are presented. The need for multi-band filters in a modern communication system is also discussed, and various methods of multi-band filters are presented. In light of the need to maintain high communication integrity, the balanced filter circuits theory is presented in this chapter, the advantages of balanced circuits are also discussed, and ways for common noise suppression are also discussed. This chapter also discusses the need for reconfigurability in a modern communication system and presents ways to achieve tunability. Tuning using semiconductors, liquid metal, and Graphene, among other methods, are discussed in this chapter.

The background of microwave filter design and its theory was presented as well. The two-port filter network is discussed together with its theoretical design background.

The Butterworth (maximally flat), Chebyshev, and Elliptic response functions illustrate the ideal filter's frequency response approximation. Low pass filter prototypes are presented regarding the normalized components and angular frequency,  $\Omega_c = 1$  rad/s. The chapter also presents the techniques for transformation from the low pass filter prototype to practical realizable filters. High pass, band-pass, and band-stop filter transformations are discussed. The effect of high radiation losses at high frequencies when using lumped LC elements is discussed and ways to implement filters using distributed elements are presented. Impedance and admittance inverters are then used to implement filters using distributed elements to design practical filters that operate at high frequencies.

## Chapter-3

# SUBSTRATE INTEGRATED WAVEGUIDE (SIW) FILTER DESIGN

---

### 3.1. Rectangular Waveguide

The Substrate Integrated Waveguide (SIW) is derived directly from the conventional rectangular waveguide [50, 62, 129–133]. In the early days of the transmission of microwave signals, rectangular waveguides were the most popular medium of transmission. However, because of the large size and the trend in which technology has been advancing, there became a need for the miniaturization of microwave devices such as filters, couplers, dividers etc. [13, 58, 134, 135]. Nowadays, most microwave devices are manufactured using planar transmission lines, which occupy less space and are easy to fabricate and integrate with other circuit components. Figure 3.1 shows the geometry of a rectangular waveguide. This waveguide can only propagate TM and TE modes with one conductor [1]. This section reviews the theory behind the operation of a rectangular waveguide.

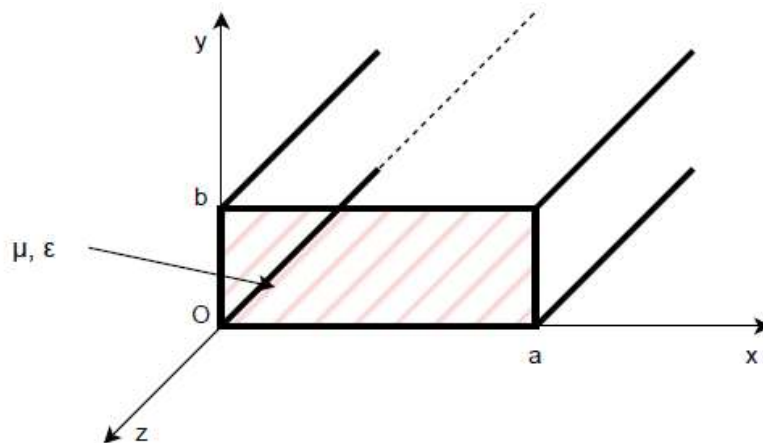


Figure 3.1 Rectangular Waveguide

The waveguide is filled with a material of permittivity  $\epsilon$  and permeability  $\mu$ . For the  $TE_{mn}$  mode, the field distribution components can be expressed as [1]:

$$H_z = A_{mn} \cos \frac{m\pi x}{a} \cos \frac{n\pi y}{b} e^{-j\beta z} \quad (3.1)$$

$$E_x = \frac{j\omega\mu n\pi}{k_c^2 b} A_{mn} \cos \frac{m\pi x}{a} \sin \frac{n\pi y}{b} e^{-j\beta z} \quad (3.2)$$

$$E_y = \frac{-j\omega\mu m\pi}{k_c^2 a} A_{mn} \sin \frac{m\pi x}{a} \cos \frac{n\pi y}{b} e^{-j\beta z} \quad (3.3)$$

$$H_x = \frac{j\beta m\pi}{k_c^2 a} A_{mn} \sin \frac{m\pi x}{a} \cos \frac{n\pi y}{b} e^{-j\beta z} \quad (3.4)$$

$$H_y = \frac{j\beta n\pi}{k_c^2 b} A_{mn} \cos \frac{m\pi x}{a} \sin \frac{n\pi y}{b} e^{-j\beta z} \quad (3.5)$$

where  $A_{mn}$  is an arbitrary amplitude constant and  $\beta$  is the propagation constant given by:

$$\beta = \sqrt{k^2 - k_c^2} = \sqrt{k^2 - \left(\frac{m\pi}{a}\right)^2 - \left(\frac{n\pi}{b}\right)^2} \quad (3.6)$$

where  $a$  and  $b$  represent the width and height of the waveguide and

$$k > k_c = \sqrt{\left(\frac{m\pi}{a}\right)^2 + \left(\frac{n\pi}{b}\right)^2} \quad (3.7)$$

where  $k_c$  is the cut-off wavenumber. Each mode has a cut-off frequency  $f_{cmn}$  given as:

$$f_{cmn} = \frac{k_c}{2\pi\sqrt{\mu\epsilon}} = \frac{1}{2\pi\sqrt{\mu\epsilon}} \sqrt{\left(\frac{m\pi}{a}\right)^2 + \left(\frac{n\pi}{b}\right)^2} \quad (3.8)$$

The dominant mode has a cut-off frequency of

$$f_{c10} = \frac{1}{2a\sqrt{\mu\epsilon}}, \text{ where } \mu = 1, n = 0 \quad (3.9)$$

Most waveguides are designed for the dominant mode. The field components of the dominant mode are given:

$$H_z = A_{10} \cos \frac{\pi x}{a} e^{-j\beta z} \quad (3.10)$$

$$E_y = \frac{-j\omega\mu a}{\pi} A_{10} \sin \frac{\pi x}{a} e^{-j\beta z} \quad (3.11)$$

$$H_x = \frac{j\beta a}{\pi} A_{10} \sin \frac{\pi x}{a} e^{-j\beta z} \quad (3.12)$$

$$E_x = E_z = H_y = 0 \quad (3.13)$$

For the  $TM_{mn}$  mode, the field distribution components are given by:

$$E_z = B_{mn} \sin \frac{m\pi x}{a} \sin \frac{n\pi y}{b} e^{-j\beta z} \quad (3.14)$$

$$E_x = \frac{-j\beta m\pi}{ak_c^2} B_{mn} \cos \frac{m\pi x}{a} \sin \frac{n\pi y}{b} e^{-j\beta z} \quad (3.15)$$

$$E_y = \frac{-j\beta n\pi}{bk_c^2} B_{mn} \sin \frac{m\pi x}{a} \cos \frac{n\pi y}{b} e^{-j\beta z} \quad (3.16)$$

$$H_x = \frac{j\omega\epsilon n\pi}{bk_c^2} B_{mn} \sin \frac{m\pi x}{a} \cos \frac{n\pi y}{b} e^{-j\beta z} \quad (3.17)$$

$$H_y = \frac{-j\omega\epsilon m\pi}{ak_c^2} B_{mn} \cos \frac{m\pi x}{a} \sin \frac{n\pi y}{b} e^{-j\beta z} \quad (3.18)$$

where  $B_{mn}$  is an arbitrary amplitude constant.

The magnetic field lines of the lower TE and TM modes which helps us to visualize the electric field are shown in Fig. 3.2 as derived from Eq. (3.14) through Eq. (3.18). They show the direction of fields for the modes as indicated by the arrowhead. The line density represents the magnitude of the field. The closer the field lines, the more the field magnitude at that place and the further apart the field lines are, the smaller the electric field strength at that point.

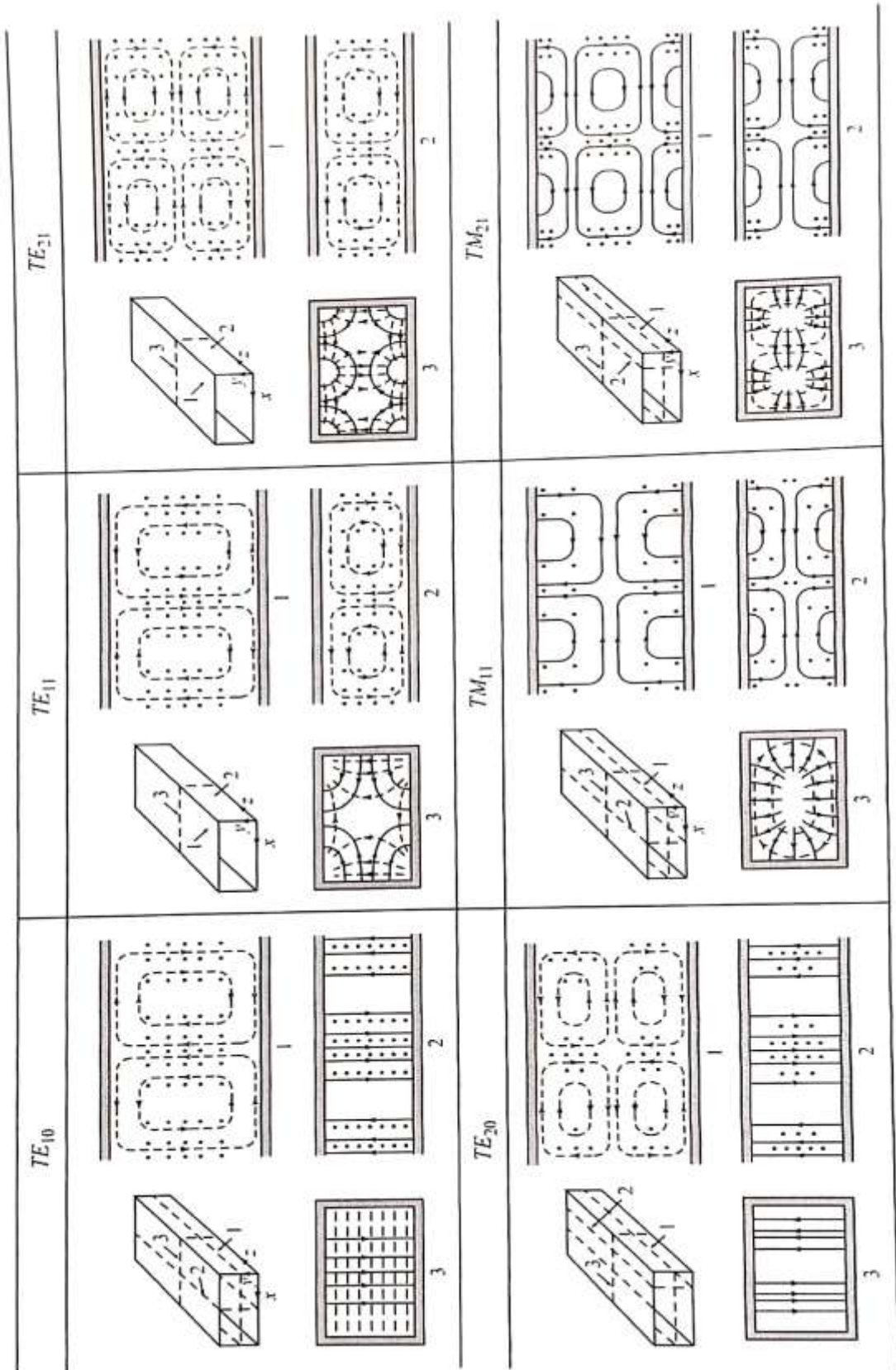


Figure 3.2 Field line distribution of lower TE and TM modes [1].

### 3.2. Rectangular Waveguide Cavity Resonators

A resonator or cavity can be achieved by short-circuiting both ends of the open-ended waveguide of Fig 3.1 to get a cavity as represented in Fig 3.3 (b) with width indicated as  $a$ , height  $b$  and length  $d$ . Electric and magnetic energy can then be stored within the cavity enclosure. A small loop or probe can then be used for coupling signals into the resonator. The  $TE_{101}$  and  $TE_{102}$  modes are as shown in Fig. 3.3(a) whilst the cavity resonator is shown in Fig. 3.3(b)

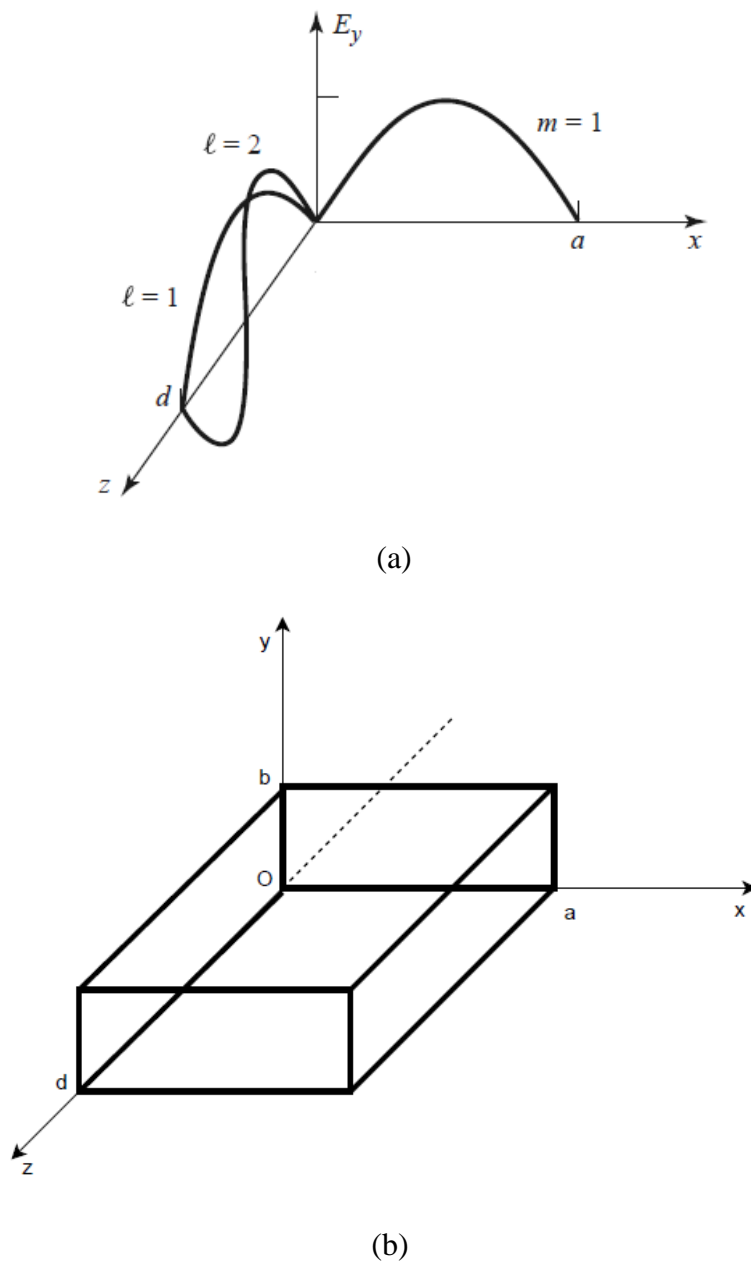


Figure 3.3 (a) Field variations for  $TE_{101}$  and  $TE_{102}$  and (b) Cavity resonator [1].

The transverse electric fields ( $E_x, E_y$ ) of  $TE_{mn}$  and  $TM_{mn}$  of a rectangular waveguide are given by:

$$\bar{E}_t = \bar{e}(x, y)(A^+ e^{-j\beta_{mn}z} + A^- e^{j\beta_{mn}z}) \quad (3.19)$$

where  $\bar{e}(x, y)$  is the mode variation and  $A^+$  and  $A^-$  are arbitrary amplitudes of the forward and backward traveling waves.  $\beta_{mn}$  is the propagation constant. At resonance, the wave number is given as:

$$k_{mnl} = \sqrt{\left(\frac{m\pi}{a}\right)^2 + \left(\frac{n\pi}{b}\right)^2 + \left(\frac{l\pi}{d}\right)^2} \quad (3.20)$$

and the resonant frequency of the  $TE_{mnl}$  or  $TM_{mnl}$  mode is given by:

$$f_{mnl} = \frac{ck_{mnl}}{2\pi\sqrt{\mu_r\epsilon_r}} = \frac{c}{2\pi\sqrt{\mu_r\epsilon_r}} \sqrt{\left(\frac{m\pi}{a}\right)^2 + \left(\frac{n\pi}{b}\right)^2 + \left(\frac{l\pi}{d}\right)^2} \quad (3.21)$$

For  $b < a < d$ , the dominant TE mode is the  $TE_{101}$  mode and the dominant TM mode is  $TM_{110}$  mode. The fields of the dominant mode can be given by:

$$E_y = E_0 \sin \frac{\pi x}{a} \sin \frac{l\pi z}{d} \quad (3.22)$$

$$H_x = \frac{-jE_0}{z_{TE}} \sin \frac{\pi x}{a} \cos \frac{l\pi z}{d} \quad (3.23)$$

$$H_x = \frac{-j\pi E_0}{k\eta a} \sin \frac{\pi x}{a} \cos \frac{l\pi z}{d} \quad (3.24)$$

and this indicates that the fields form standing waves inside the resonator.  $z_{TE}$  and  $\eta$  represent.

### 3.3. Substrate Integrated Waveguide

The substrate integrated waveguide operates almost similar to the conventional rectangular waveguide. It eliminates the sidewalls of the rectangular waveguide and

replaces them with a column of vias in the form of metal posts. For the past decade, SIW technology has seen a steep increase in usage, and research work has also seen a tremendous increase [21, 43–45, 136]. The SIW technology compromises the well-established rectangular waveguide and planar technology. Rectangular waveguides can handle high powers, exhibit tremendously lower losses, and have high Q factors but have the disadvantage of large size being too bulky in such a way that it becomes difficult to handle and integrate with other microwave circuit components [7].

On the other hand, planar technology devices such as micro-strip lines have smaller sizes than rectangular waveguides. Still, they have less power handling capabilities, lower Q factors, and higher insertion losses. SIW trades in the middle of the two mentioned structures above [8]. The SIW size is smaller than that of the conventional rectangular waveguide. It is easier to integrate with other microwave components but has higher losses and less power handling capability than the rectangular waveguide [16, 17]. The SIW is a bit larger than equivalent planar structures but can handle higher powers and operate at higher frequencies than planar structures; it also has a high Q factor and its easy to integrate with other microwave components. Many principles that guide the design of rectangular waveguides also apply to the SIW with slight modifications, and the characteristics such as field patterns and dissipation properties are also similar [14, 15]. SIW supports the  $TE_{m,0}$  modes, including the dominant mode  $TE_{1,0}$ , also found in the conventional rectangular waveguide. However, for the TM and  $TE_{mn}$  modes (where  $n \neq 0$ ), the SIW cannot maintain these modes because of the discontinuous sidewalls.

Figure 3.4 shows the structure of a substrate integrated waveguide. The conventional rectangular waveguide is modified by replacing the air with a substrate of dielectric constant  $\epsilon_r$ . The top and bottom plates are made of metal, such as copper. Copper is used to constructing the sidewalls via holes, which cut through from the top to the bottom of copper plates. The fundamental parameters to be considered when designing a SIW are the diameter of the via hole,  $d$ , pitch representing the center-to-center distance between two adjacent via holes,  $p$ , and the width,  $w$  of the structure. The width is proportional to the frequency at which the waveguide operates. The  $d$  and  $p$  are the diameter and pitch of the via holes, respectively. The  $h$ ,  $a_{sw}$ , and  $L$  are the substrate's height, width, and length, respectively. The operation and field distribution is similar to the conventional rectangular waveguide [14, 137].

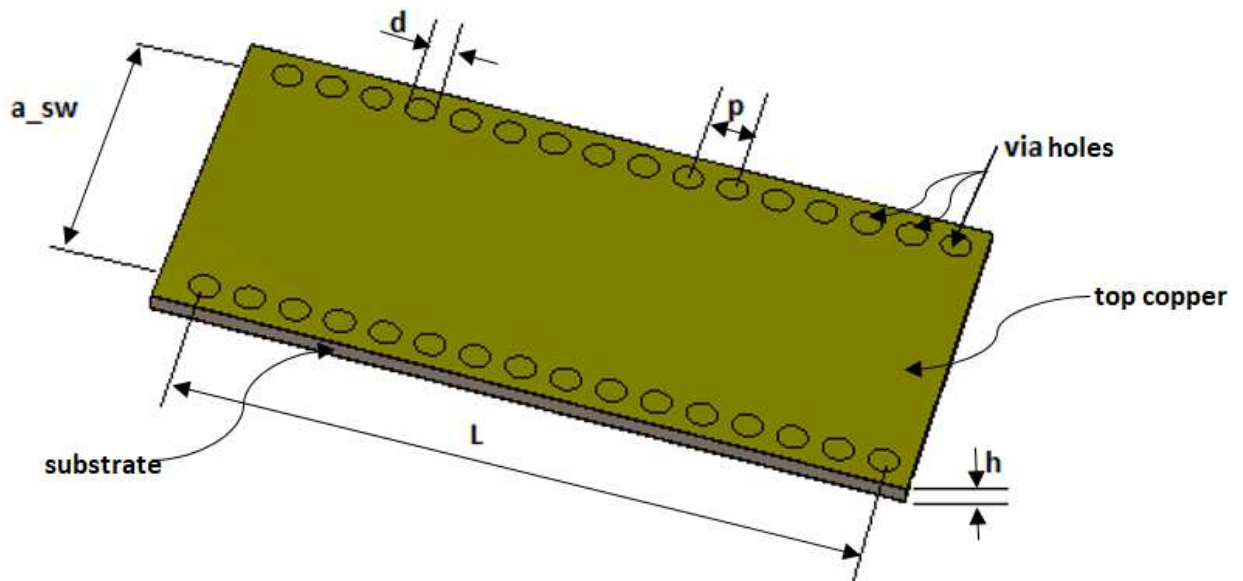


Figure 3.4 SIW structure.

### 3.4. SIW Transitions

To integrate the SIW and other microwave components, there is a need for a transition mechanism. The transition or interconnections of the traditional waveguide can be adopted with some modifications. However, the most popular mechanism is using methods that work with PCB techniques.

#### 3.4.1 Micro-strip to SIW Transition

A microstrip to SIW transition mechanism is one of the most used methods for integration due to its easiness in design and fabrication. The SIW and the micro-strip line are interconnected through a taper [110, 138]. Figure 3.5 shows the design whereby a 50Ω microstrip line interconnects with the SIW.

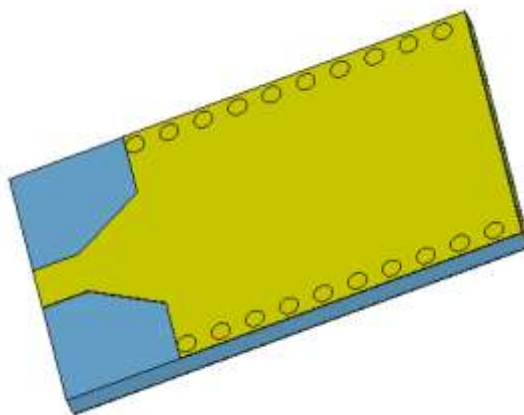


Figure 3.5 Microstrip to SIW transition.

To achieve lower conductor losses, the substrate height can be increased; however, it comes with the disadvantage of increasing radiation losses. This reduces the suitability of the transition mechanism to operate at higher frequencies.

### 3.4.2 Co-planar waveguide (CPW) to SIW Transition

Another method for interconnecting SIW to other circuit components is through the use of a co-planar waveguide (CPW) to get a co-planar to SIW transition [139, 140]. The co-planar waveguide is designed with a  $90^\circ$  angle and a slot inside the SIW structure. Fig. 3.6 shows the co-planar SIW transition.

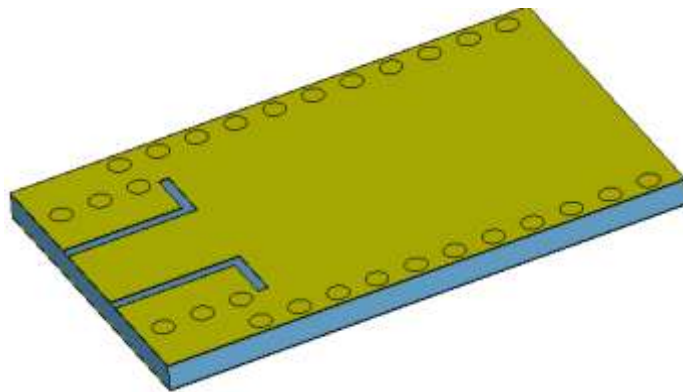


Figure 3.6 CPW to SIW transition.

This interconnection mechanism is not affected much by a change in the substrate height compared to the tapered microstrip – SIW transition. Hence conductor losses can be minimized by increasing the height while not incurring many penalties in terms of radiation losses and its more suitable for operation at higher frequencies. The CPW-SIW transition mechanism can also be implemented using a current probe, as shown in Fig. 3.7 [141].

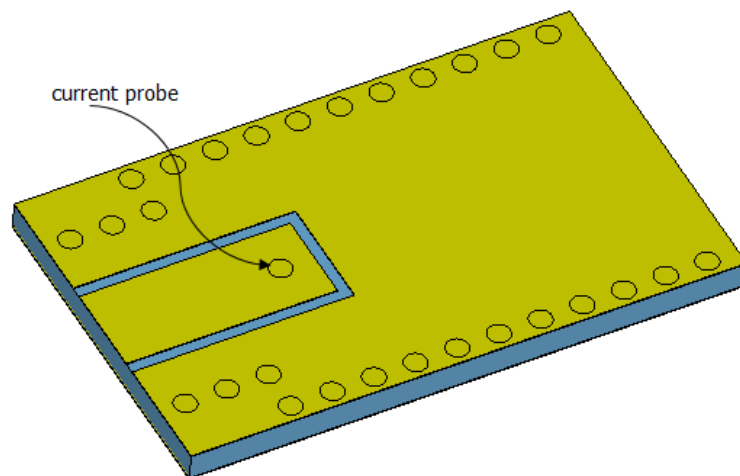


Figure 3.7 CPW-SIW transition with current probe.

A magnetic field is created by the current flowing through the grounded co-planar waveguide (GCPW) when it passes through the coupling probe. This magnetic field can match the magnetic field inside the SIW, and the coupling is achieved through this action.

### 3.5. Losses in SIW

Because of the similarities between the SIW and rectangular waveguides, the operation modalities are similar, save for minor adjustments [142]. This also applies to the losses that occur in both structures they tend to be similar. In rectangular waveguides, there are two main types of losses: conductor losses and dielectric losses [141, 143]. The conductor losses arise due to the metallic walls, while the dielectric losses arise due to the dielectric material used. The dielectric loss,  $\alpha_d$ , and conductor loss,  $\alpha_c$  can be expressed as [142]:

$$A_d = \frac{k^2 \tan \delta}{2\beta} \quad (3.25)$$

$$\alpha_c = R_s \frac{(2h\pi^2 + l^3 k^2)}{l^3 h \beta k \eta} \quad (3.26)$$

where  $k$  is the free space wave number,  $\beta$  is the phase constant,  $\tan \delta$  is the dielectric loss tangent and  $\eta$  is the intrinsic impedance of the medium:

$$\eta = \sqrt{\frac{\mu_0}{\epsilon_0 \epsilon_r}} \quad \text{and} \quad R_s = \sqrt{\frac{w \mu_0}{2\sigma}} \quad (3.27)$$

where  $\sigma$  represents the conductivity of metal,  $R_s$  is the surface resistance of the conductor,  $\epsilon_0$  represents the free space dielectric constant and  $\epsilon_r$  represents the substrate dielectric constant. The total losses will be the summation of the dielectric and conductor losses.

The SIW also has radiation or leakage losses and conductor and dielectric losses. These losses are present due to the non-presence of a solid wall on the vertical sides of the SIW structure. The solid metallic wall of the traditional waveguide is replaced by a fence or row of vias of a certain diameter and separated by a distance known as the pitch,  $p$ . Through these spacings, some radiation can leak from the structure and hence introduce additional losses known as radiation or leakage losses. The total losses in a SIW structure are given from this leakage by adding the conductor, dielectric, and leakage losses. In a SIW structure, the conductor losses,  $\alpha_{c\_siw}$  can be investigated by [141]:

$$\alpha_{c\_siw} = \frac{\sqrt{\pi f \epsilon_0 \epsilon_r} \frac{1+2(\frac{f_0}{f})^2 * \frac{h}{w\_siw}}{h\sqrt{\sigma_c}}}{\sqrt{1-(\frac{f_0}{f})^2}} \quad (3.28)$$

where  $w\_siw$  is the effective width of the SIW,  $h$  is the height of the substrate,  $f$  is a specific frequency,  $f_0$  is the cut-off frequency of the SIW,  $\epsilon_0$  represents free space dielectric constant, and  $\epsilon_r$  represents the substrate dielectric constant. The dielectric losses of the SIW structure,  $\alpha_{d\_siw}$ , can be given by:

$$\alpha_{d\_siw} = \frac{\pi f \sqrt{\epsilon_r}}{c_0 \sqrt{1-(\frac{f_0}{f})^2}} \tan \delta \quad (3.29)$$

where  $\tan \delta$  is the loss tangent and  $c_0$  is the speed of light in a vacuum. The radiation loss is merely related to the structural design of the SIW and happens due to the spacings between the vias. The energy that escapes through these gaps contributes to radiation or leakage losses,  $\alpha_r$  and these losses can be analyzed through the use of [144]:

$$\alpha_r = \frac{\frac{1}{w}(\frac{d}{w})^{2.84} (\frac{s}{d}-1)^{6.28}}{4.85 \sqrt{(\frac{2w}{\lambda})^2 - 1}} \quad (3.30)$$

where  $\lambda$  is the SIW propagation wavelength and  $w$  is the width of the SIW resonator.  $s$  is a unit cell which is equivalent to the pitch in dimensions.

### 3.6. Design of a SIW Filter With High Selectivity

This work uses SIW technology to design a high-selectivity BPF that operates in the Ka-band of the electromagnetic spectrum. Agilent ADS was used for circuit simulation, and CST microwave studio was used for the implementation. This work presents a BPF that is very small in size compared to other filters in the same category. The filter's insertion loss is also very small and has high selectivity compared to other filters, as shown in the following sections. The first step is to design a suitable resonator with  $30 \text{ GHz}$  frequency. The conventional waveguide design Equations can be used to calculate the filter dimensions. The cut-off frequency is given by [47]:

$$f_{cmn} = \frac{1}{2\pi\sqrt{\mu\epsilon}} \sqrt{\left(\frac{m\pi}{a}\right)^2 + \left(\frac{n\pi}{b}\right)^2} \quad (3.31)$$

where  $a$  and  $b$  are the rectangular waveguide dimensions [7] and  $m$  and  $n$  are the mode numbers. For the  $TE_{10}$  mode, which is the dominant mode of the rectangular waveguide, Eq. (3.31) reduces to [47]:

$$f_{c10} = \frac{1}{2a\sqrt{\mu\epsilon}} = \frac{c}{2a} \quad (3.32)$$

where  $c$  is the speed of light. The authors have calculated the waveguide width given the center frequency. Since the SIW is filled with a substrate with permittivity ( $\epsilon_r$ ), it needs to use the equivalent width of a rectangular waveguide filled with a dielectric given by:

$$a_f = \frac{a}{\sqrt{\epsilon_r}} \quad (3.33)$$

Then the width of the SIW is determined from [7]:

$$a_{sw} = a_f + \frac{d^2}{0.95p} \quad (3.34)$$

For efficient operation of the SIW,  $d < \frac{\lambda_g}{5}$  and  $p < 2d$  where  $\lambda_g$  is the guided wavelength given by:

$$\lambda_g = \frac{2\pi}{\sqrt{\frac{(2\pi f)^2 \epsilon_r}{c^2} - \left(\frac{\pi}{a}\right)^2}} \quad (3.35)$$

The length of the SIW should be multiples of half wavelength of the center frequency [1] and by closing both ends, a cavity resonator can be realized. For this design,  $width = 3.88 \text{ mm}$ ,  $length = 9.78 \text{ mm}$ ,  $d = 0.4 \text{ mm}$ ,  $p = 0.6 \text{ mm}$ , and  $h = 0.22 \text{ mm}$ .

### 3.6.1 Filter Implementation

In this work, coupled resonators were used to realize the filter. The topology diagram is shown in Fig 3.8. In the diagram, 5 resonating nodes {R1-R5} and 2 none resonating nodes {S & L} are the source and load, respectively.  $Q_e$  is the external quality factor, and  $C_{i,i+1}$  is the mutual coupling coefficients given by Eq. (3.36) and Eq. (3.37).

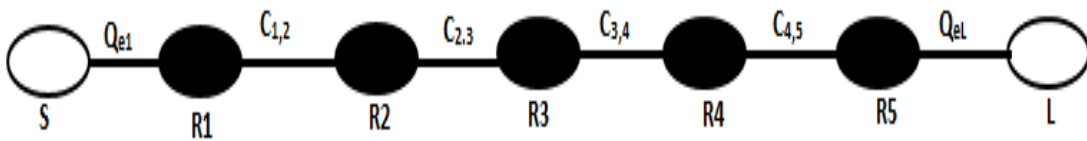


Figure 3.8 Illustration of resonators topology.

Each resonating node represents a SIW cavity resonator. The  $g$  parameters can be derived using the equations in ref. [23] or the tables with predefined  $g$  values to obtain a Chebyshev filter. This 5-pole filter design is designed with an insertion loss of 0.01 dB. The  $g$  parameters [23] are  $g_0 = 1$ ,  $g_1 = 0.7563$ ,  $g_2 = 1.3049$ ,  $g_3 = 1.5773$ ,  $g_4 = 1.3049$ ,  $g_5 = 0.7563$  and  $g_6 = 1$ . The theoretical mutual coupling coefficients are calculated as [24]:

$$c_{i,i+1} = \frac{fbw}{g_i g_{i+1}} \quad (3.36)$$

$$Q_{e1} = Q_{en} = \frac{g_0 g_1}{fbw} \quad (3.37)$$

where  $f_{bw}$  is the fractional bandwidth of the filter. In this design,  $f_{bw} = 9\%$ . This wider fractional bandwidth helps systems to transmit high data rates while consuming less power and makes it suitable for high-speed wireless applications [25].  $c_{12} = c_{45} = 0.0912$  and  $c_{23} = c_{34} = 0.0437$  then  $Q_{e1} = Q_{en} = 8.4$ . The simulated values of  $c_{i, i+1}$  were obtained by the technique shown in the diagram, Fig 3.9. The distance  $l_s$  was varied and from the two eigenmodes observed on the  $S_{21}$  parameters, the coupling coefficient was determined by [5, 145]:

$$c_{i,i+1} = \frac{f_2^2 - f_1^2}{f_2^2 + f_1^2} \quad (3.38)$$

The value for  $l_s$  was determined to be 1.8 mm, which gave a coupling coefficient of 0.052, close to the theoretical value of 0.0912. It was noted that this same value provided satisfactory results for all the coupling slots.

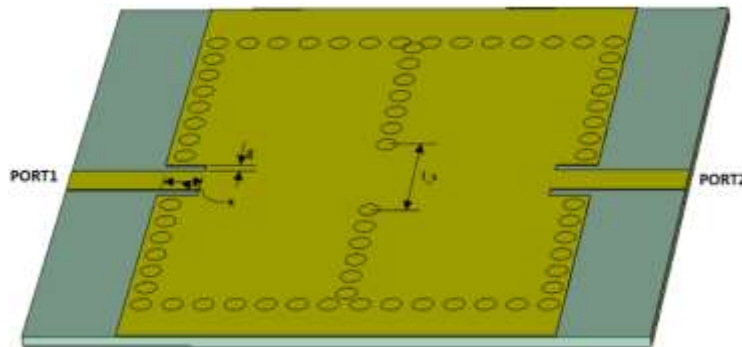


Figure 3.9 Extraction of the coupling coefficient.

To determine the value for the external quality factor,  $Q_{e1}$ , Fig 3.10 was used, the distance  $g$  and  $x$  were varied, and Eq. (3.39) was used [45]:

$$Q_{e1} = \frac{f_0}{fbw_{\pm 90^\circ}} \quad (3.39)$$

where  $f_0$  is the frequency at which group delay of  $S_{11}$  reaches the max and  $fbw_{\pm 90^\circ}$  is the bandwidth between  $\pm 90^\circ$  with respect to the absolute phase of  $S_{11}$  at  $f_0$ . The values for  $x$  and  $g$ , which gave a  $Q$  value of 9.2, which is close to the theoretical value, were  $x = 2.0$  mm and  $g = 0.2$  mm.

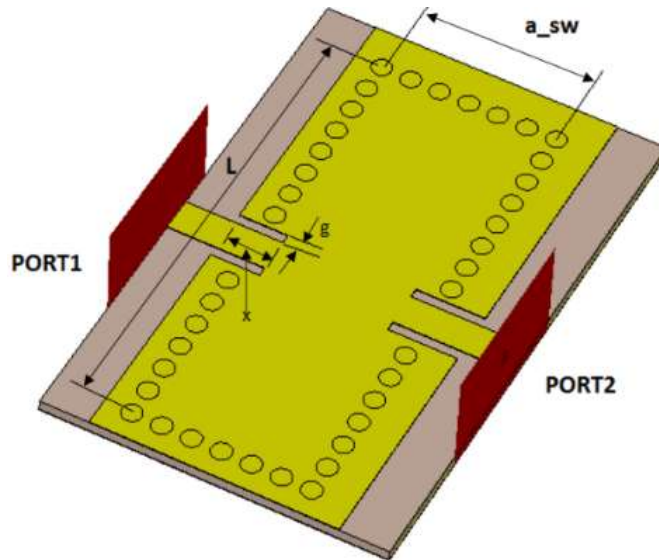


Figure 3.10 Extraction of the external quality factor.

The five resonators were combined using these dimensions as shown in Fig 3.11. The filter size is  $19.4 \times 9.68$  cm<sup>2</sup>. Table 3.1 shows the final dimensions used.

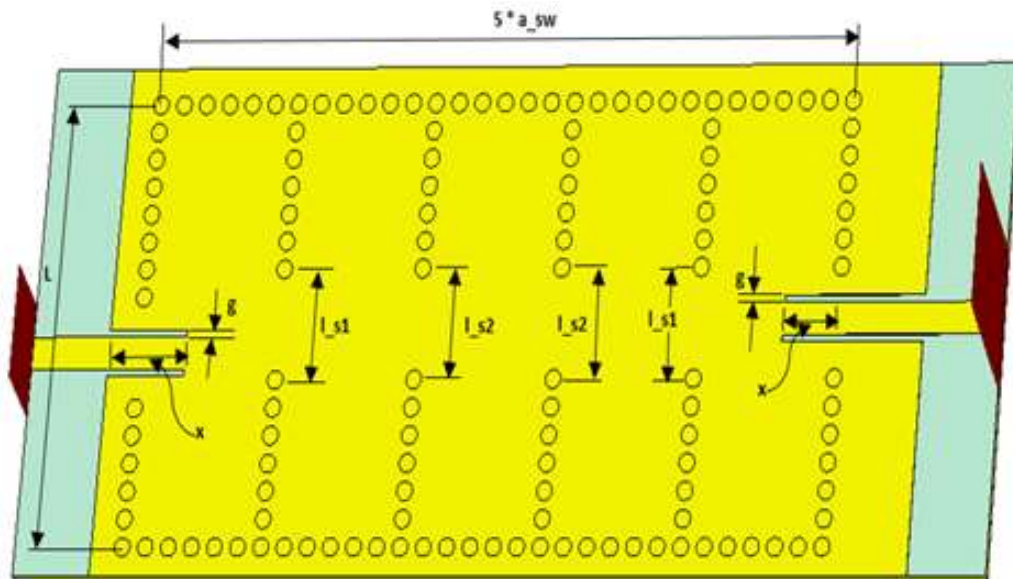


Figure 3.11 Fifth-order SIW filter.

Table 3.1 Filter dimensions

Parameter	Length(mm)
x	2
g	0.2
l <sub>s</sub>	1.8
a <sub>sw</sub>	3.88
L	9.78

### 3.7. Results Analysis and Discussion

The simulated results are as Fig. 4.12. The filter achieves a return loss better than -10 dB and an insertion loss of  $-0.9$  dB throughout the pass-band. The loss in dB between the 3dB cut-off frequency i.e. at  $32$  GHz and a frequency of  $33$  GHz is of  $-30$  dB. This illustrates very high selectivity as the roll-off is very high. The pass-band has a little ripple indicating the filter's Chebyshev characteristics, and the ripple in the stop-band indicates the quasi-elliptic filter characteristics. The bandwidth can be adjusted slightly by changing the values of x and g as shown in Fig 3.11.

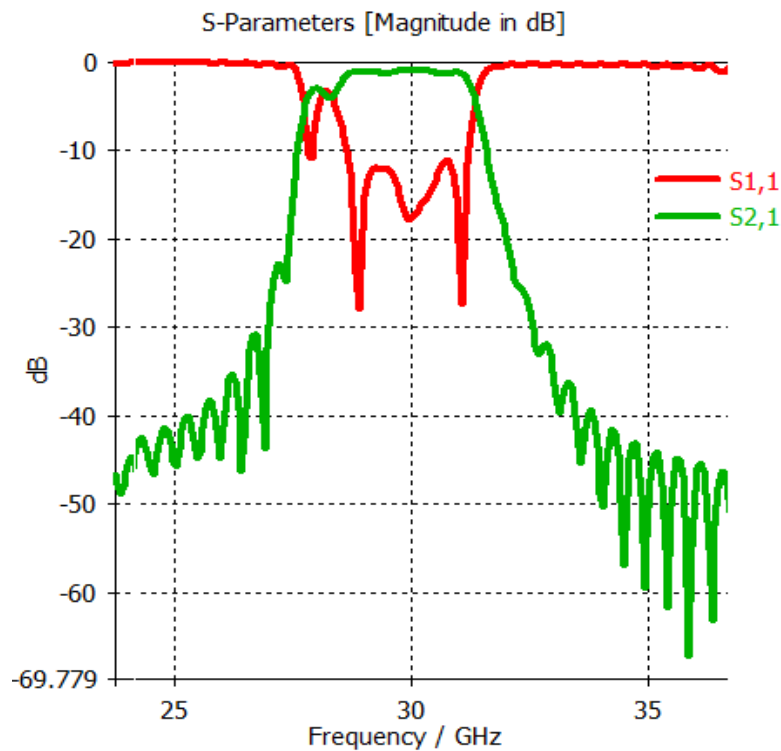


Fig 3.12 Output results of the 5<sup>th</sup>-order SIW filter.

Table 3.2 Comparison with the other existing works

Ref.	Technology	S <sub>21</sub> (dB)	Freq (GHz)	Size (mm <sup>2</sup> )	Selectivity
[7]	SIW	1.4	14.25	30x30	Medium
[8]	SIW	0.95	2.4	--	Low
[21]	SIW with CR	1.5	15	12.6x60	Low
[146]	SIW air-filled	1.15	27.92	7.04x46.5	High
[146]	SIW dielectric-filled	2.13	28.03	4.13x28.5	High
[22]	SIW	1.81	13	--	Low
[23]	SIW	3.3	2.4	45x160	Low
[19]	SIW	0.65	9.5	12.3x25.2 3	Low
[6]	SIW CMRC	N/S	4.5	10x48.1	Medium
This Work	SIW	0.9	30	9.6x19.4	High

CR – circular ring, CMRC - compact microstrip resonant cell

The filter has a small VSWR of almost 1 within the range 28 GHz – 32 GHz as shown in Figure 3.13. This is quite an appreciably low return loss within the range, which is desirable for the efficient operation of the designed filter.

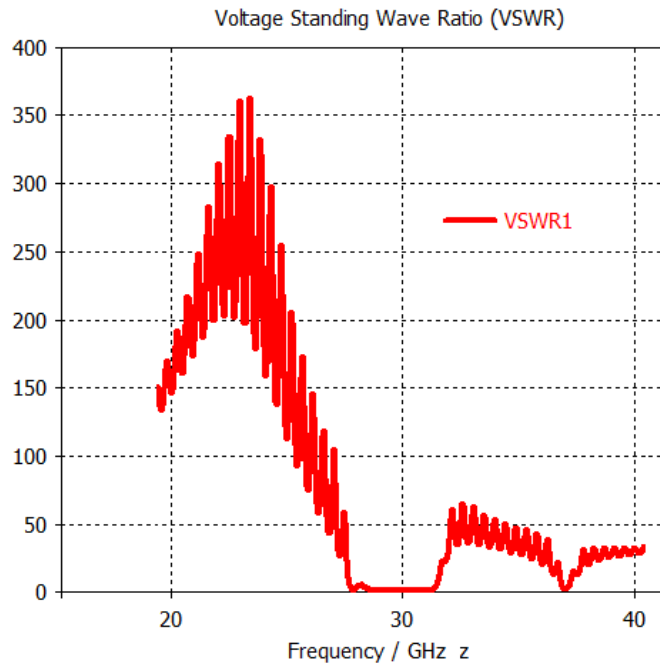


Figure 3.13 Voltage standing wave ratio (VSWR)

The five-pole Chebyshev filter can be further reduced in size by half by cutting it through the  $x$ -plane, illustrating half-mode operation, as shown in Fig 3.14. The electric field is maximum at the vertical center plane and can be viewed as a magnetic wall. This allows it to be cut into half and maintain its field distribution properties[147]. This in turn, reduces the size by 50% but still maintains the same field distribution. In Fig. 3.15, the output of  $S_{22}$  and  $S_{12}$  is shown. Due to the fields not being confined in the waveguide, the insertion loss and return loss become more impoverished than the complete structure. Better  $S_{22}$  and  $S_{12}$  properties can be obtained by increasing the substrate height. Figure 3.16 shows the VSWR of the filter operating in half mode. The results show an acceptable return loss of below 1.8, which shows that the designed filter can still operate satisfactorily in the half mode.

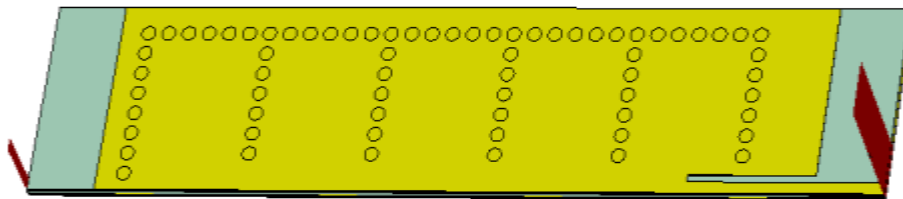


Figure 3.14 SIW filter cut in half.

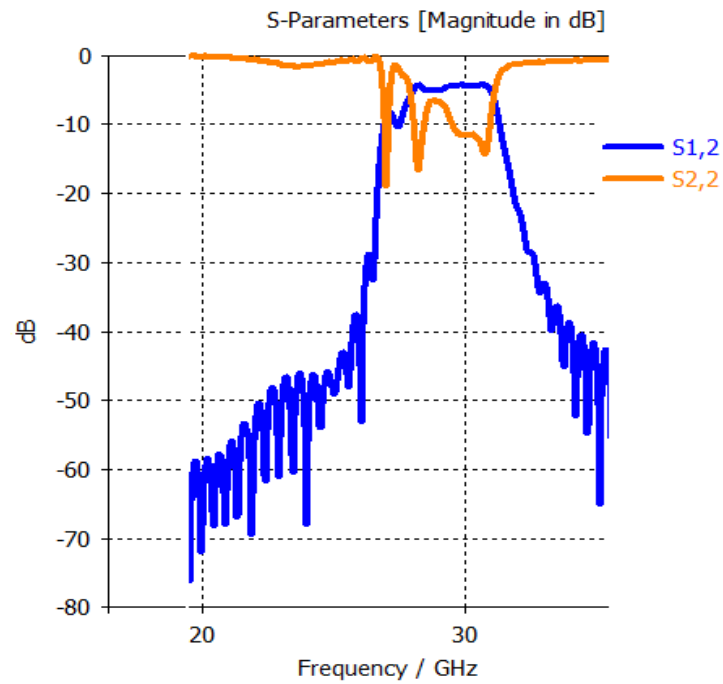


Figure 3.15 Output results of the half-mode filter.

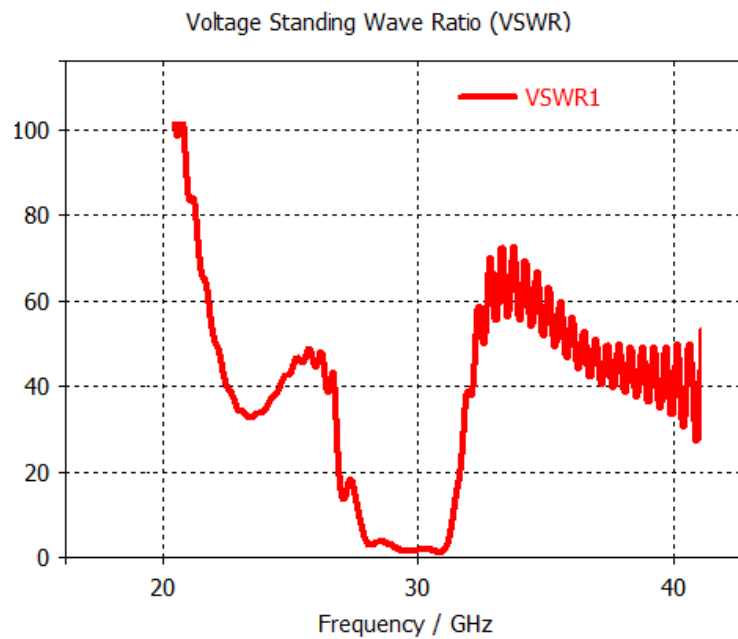


Figure 3.16 The VSWR in half mode

### 3.8. Chapter Summary

This chapter discusses the theory and background of the rectangular waveguide. The design Eq.s are presented, and the propagating and non-propagating modes in the waveguide are illustrated. A brief discussion of the rectangular cavity resonator is presented and how it is derived from the rectangular waveguide by short-circuiting both ends of the waveguide is illustrated. The resonant frequencies in the rectangular waveguide cavity are also

discussed. This chapter also introduces the substrate integrated waveguide (SIW) as a compromise between planar technologies and the conventional rectangular waveguide. The background and history of the SIW were discussed. The SIW structure, its parameters, operation and construction are presented. Different SIW transition mechanisms include microstrip to SIW transition and CPW to SIW transition. The losses associated with the SIW technology are presented with their mathematical models. Finally, a SIW band-pass filter design with high selectivity is presented. The design procedure and practical implementation of the filter are illustrated.

## Chapter-4

# SIW MINIATURIZATION

---

### 4.1. Introduction

With technological advancement, substrate integrated waveguides must be miniaturized to give a small footprint structure. A smaller footprint implies low cost as less material is used and can be incorporated in many integrated circuits as many applications are being developed and added to the communication system. In wireless technology, various functionalities must be added to mobile phones and other electronic gadgets. This has necessitated miniaturizing microwave components such as filters [8]. On the other hand, the amount of traffic conveyed by these communication devices is increasing tremendously, leading devices to operate at high frequencies and filter devices needing sharp edges or high selectivity to reduce interference between different applications [18]. The SIW structures are more beneficial due to their high-power handling capabilities, low loss, high-quality factor, etc., than conventional planar structures [13, 148, 149]. Their structures are similar to the traditional waveguide; however, it is easier to integrate with planar circuits [8]. The field distribution and propagation modes are the same as in the conventional waveguide [13]. Even though the structure has its advantages, SIW has the disadvantage of being bulky. In this regard, it becomes imperative to find ways to reduce the structure so that it becomes more compact while at the same time maintaining an acceptable level of operation in terms of low radiation losses and high efficiency. Many techniques have been considered for miniaturization in literature.

### 4.2. Ridged Substrate Integrated Waveguide

To reduce the width of the rectangular waveguide structure, ridges can be placed inside the waveguide to increase capacitance at the ridge step, as shown in Fig. 4.1 [150], [151]. This capacitance lowers the cut-off frequency of the  $TE_{10}$  mode of the waveguide [152, 153]. Compared to the rectangular waveguide of the same dimensions, the ridge waveguide can operate at a much lower frequency of the fundamental mode [154, 155].

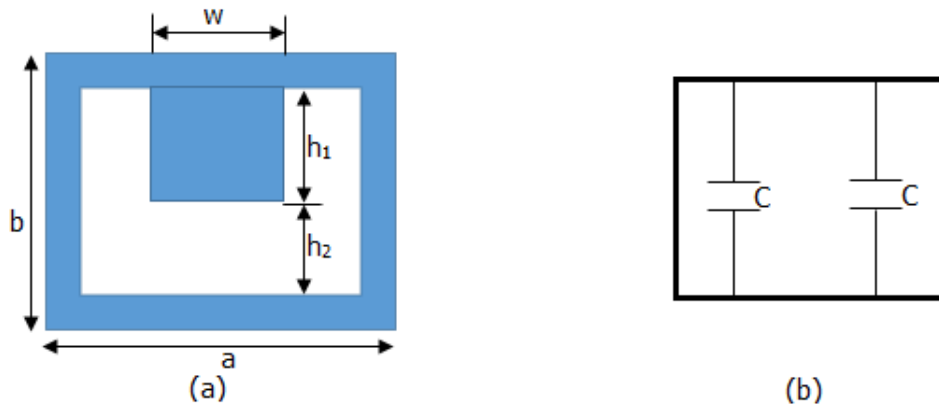


Figure 4.1 (a) Ridged waveguide (b) Equivalent circuit.

Introducing the ridge means that the physical structure of the rectangular waveguide will be reduced, which plays an important role in component miniaturization. The other benefit of the ridge waveguide comes when there is a proper selection of the dimensions  $w$  and  $h_2$  from Fig. 4.1. This tends to push the higher modes frequency further from the fundamental frequency, which is desirable in filter design to avoid spurious pass-bands associated with higher order modes. This, in turn, increases the single-mode bandwidth of the filter. To build a ridged SIW, a row of vias that do not connect to the ground (blind vias) is placed in the middle of the SIW structure, as shown in Fig. 4.2.

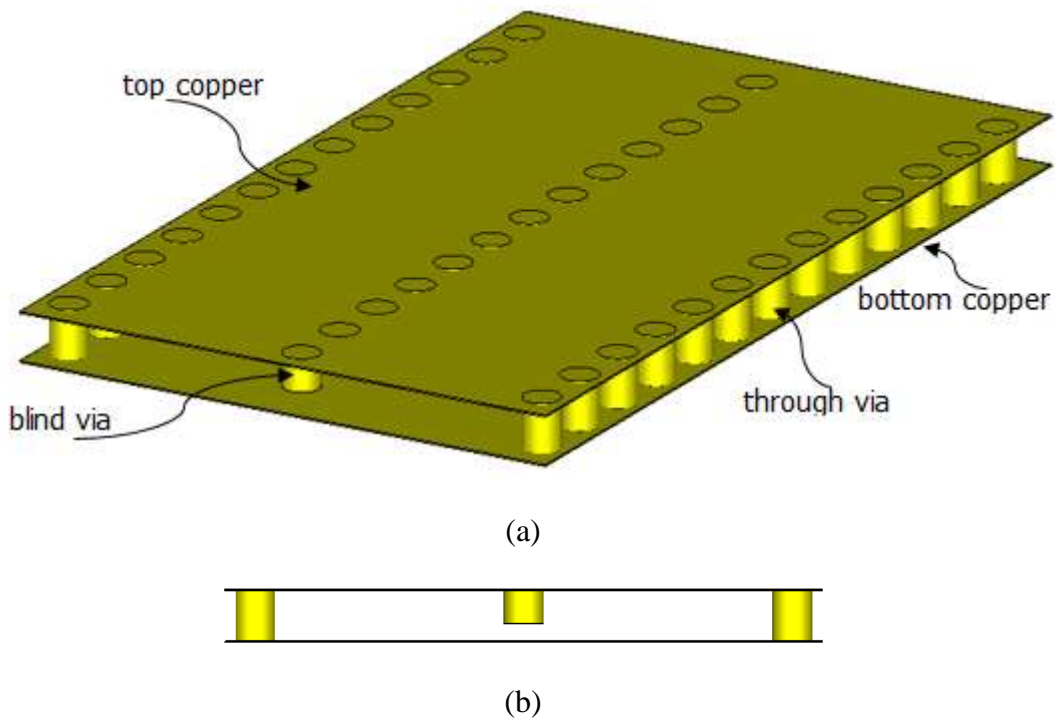


Figure 4.2 Ridged SIW. (a) 2-D view (b) front view

The middle row of vias introduces capacitance the same way as the ridge rectangular waveguide, which decreases the cut-off frequency of the fundamental  $TE_{10}$  mode. To improve the performance of the ridge SIW structure, a metal strip can be added to the bottom of the middle via row, as shown in Fig. 4.3. The metal strip connects all the metal vias at the bottom. The bandwidth of this modified structure improves three-fold [156].

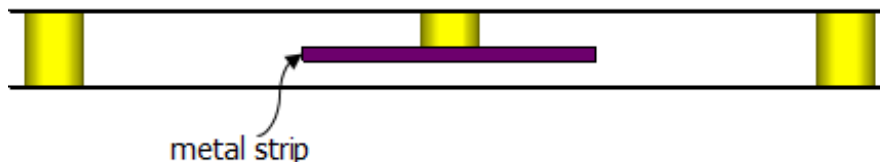


Figure 4.3 Ridged SIW with a metal strip.

A half-mode ridge SIW structure can further reduce the size of the SIW by cutting the original SIW structure into half along its length and placing the ridge, as shown in Fig. 4.4(a). One line of the through vias is cut out and the half structure still exhibits a propagation pattern similar to the full structure. At the same time, a significant amount of size reduction of up to 50% is achieved compared to the original structure [155]. The ridge can be moved inside the main waveguide channel to form the folded ridge, as shown in Fig. 4.4(b) [156, 157]. This now produces a folded ridge half-mode SIW structure, which can further reduce the footprint by 56.7% [156].

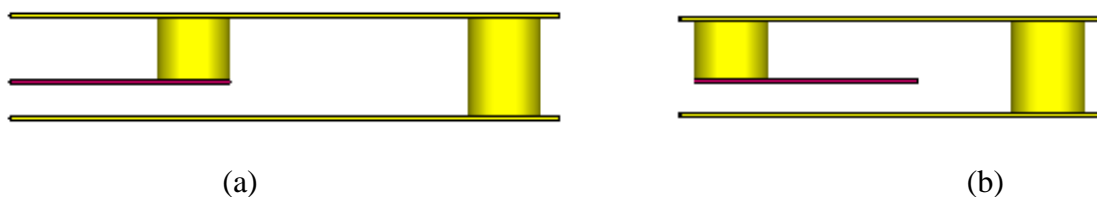


Figure 4.4 (a) Half mode ridged SIW and (b) Folded Half mode ridged SIW.

### 4.3. Using Complementary Slip Ring Resonator (CSRR)

The reduction of SIW footprint can also be achieved by using slip ring resonators (SRR) which were first introduced by *Pendry et. al.* [158, 159]. The SRR is formed by conducting rings coupled by the capacitance between the rings. An SRR structure is shown in Fig. 4.5 alongside its equivalent circuit.

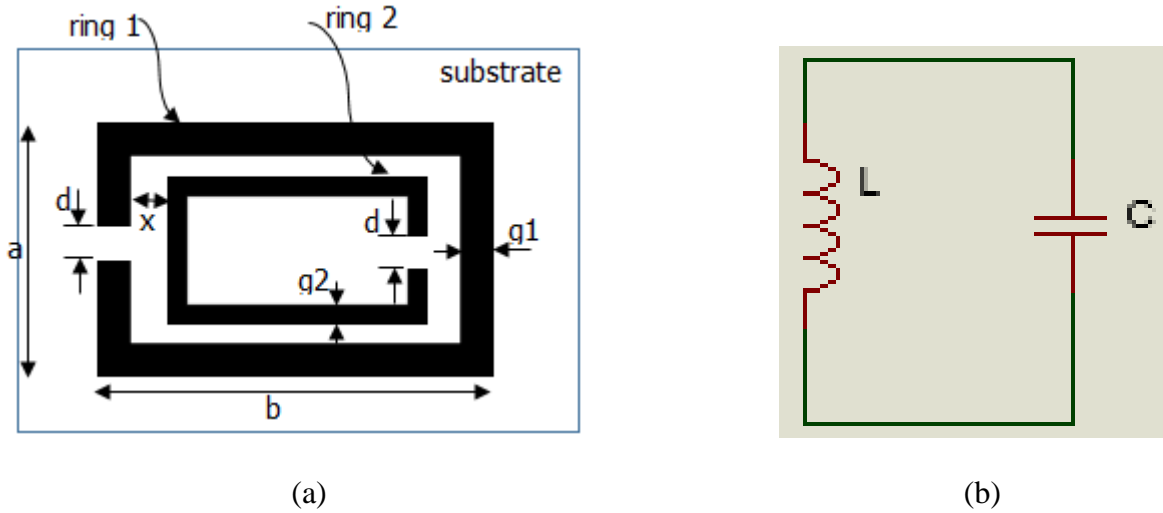


Figure 4.5 (a) SRR and (b) Equivalent circuit.

According to the equivalent circuit, it can be observed that the SRR operates as a tuned circuit with a resonant frequency given as:

$$f_r = \frac{1}{2\pi\sqrt{LC}} \quad (4.1)$$

The dimensions  $g_1$  and  $g_2$  are used to determine the inductance of the SRR, while the distance  $d$  is used to determine the equivalent capacitance. The SRR loaded waveguides provide a stop band when their resonance frequency is above the cut-off frequency and behaves as a pass-band when their resonance frequency is below the cut-off frequency of the waveguide. SRR are considered as resonant magnetic dipoles [159]. By introducing a time-varying magnetic field near the rings, the current is induced in the split rings. The induced current is directly proportional to the capacitance [158].

Complementary split ring resonators (CSRR) are the dual of the SRR and can be viewed as electric dipoles. CSRR can be used in the design of stop band filters when their resonant frequency is greater than the cut-off frequency of the waveguide [159]. The structure of the CSRR is shown in Fig. 4.6(a) and its equivalent circuit is in Fig. 4.6 (b). When the resonant frequency of the CSRR is below the cut-off frequency of the waveguide, then a pass-band can be realized. The resonant frequency of the CSRR is given by Eq. (4.1), which is the same as the resonant frequency of the SRR. CSRR was applied in [159] to design a miniaturized filter.

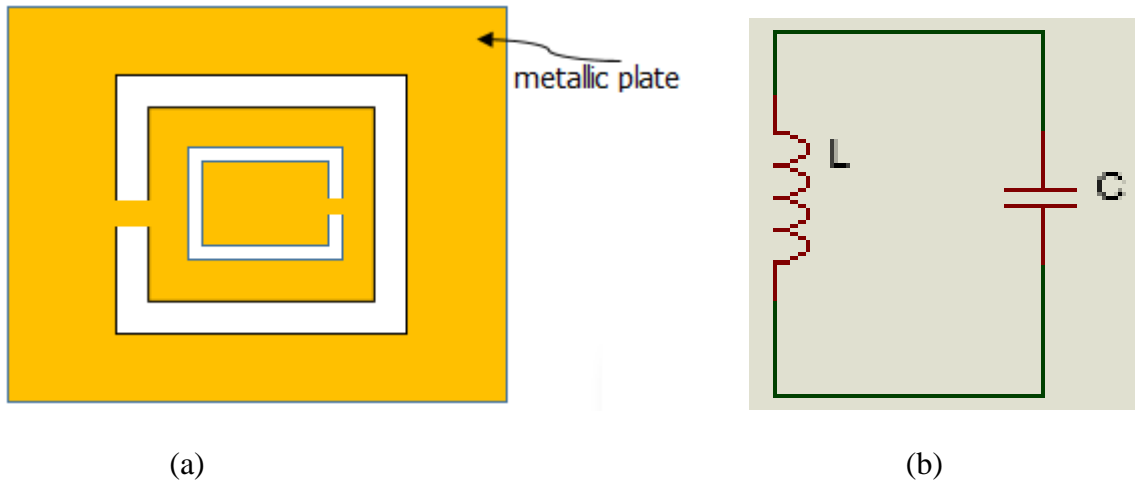


Fig. 4.6 (a) CSRR (b) Equivalent circuit.

A square CSRR was etched on top of the SIW resonator and different orientations of the square CSRR were implemented to vary the pass-band characteristics. The pass-band center frequency was below the cut-off frequency of the original waveguide and this showed that miniaturization was achieved through the square CSRR. The shape of the SRR / CSRR was also changed in work done by [160]. In this work, the square CSRR was replaced by a diamond-shaped CSRR. Two diamond CSRRs were used to implement a two-stage / second-order filter operating at a center frequency of  $8.86 \text{ GHz}$ . The filter was found to operate at a lower frequency than that of a SIW with similar dimensions. In ref. [161] a miniaturized SIW filter was also designed using a modified CSRR in the form of an "S" shape. The CPW-SIW interconnection mechanism was used to improve impedance matching, and the filter worked below the operating frequency of the waveguide. This also generated a pair of transmission zeros on both sides of the pass-band.

#### 4.4. Bisecting the SIW Structure

The structure can be divided through the symmetry lines to achieve further miniaturization to the SIW waveguide, as shown in Fig. 6. The structures derived from these divisions have the same propagation characteristics as the full wave structure. Fig. 2 [162] shows the electric field distribution of the full SIW structure as simulated in the electronic simulator. There are four symmetric lines as indicated by A-A', B-B', C-C' and D-D', which can be regarded as virtual magnetic walls [59, 162, 163]. By bisecting this structure through the symmetry line A-A', a Half-Mode SIW (HMSIW) as shown in Fig. 4.7 (b) resonator is achieved. If the structure is further dissected through the B-B' symmetry line a Quarter

Mode (QMSIW) resonator is achieved as indicated in Fig. 4.7(c). By further bisecting the quarter-wave resonator through the line O-C' or similarly, an EMSIW resonator is obtained as shown in Fig. 4.7(d). The EMSIW is only 12.5% the size of the original structure, which implies a smaller final design as required. To get a sixteenth mode structure, the EMSIW is further bisected through the line O-E' illustrated in Fig. 4.7(e). It has been demonstrated that the field distribution of the HMSIW, QMSIW, and EMSIW resonators is the same as the conventional full SIW structure and they resonate at almost the same frequency [58, 164].

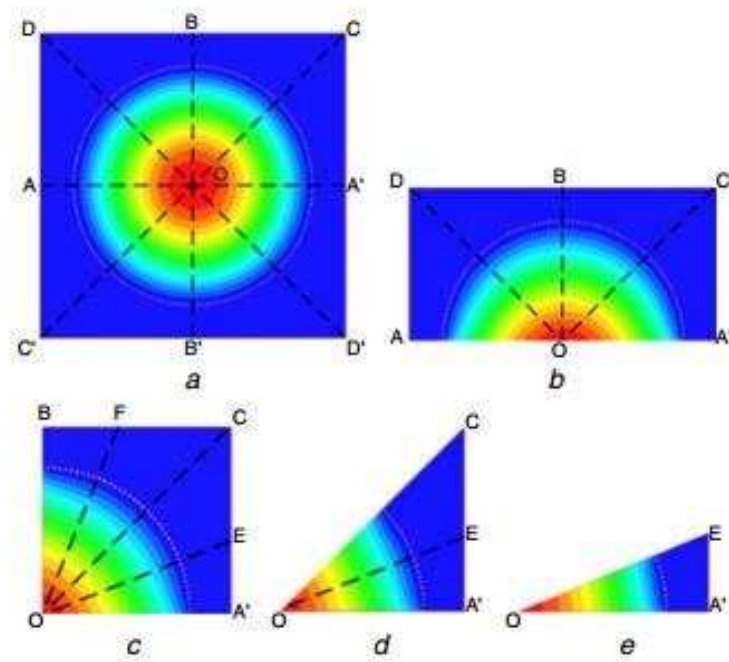


Figure 4.7 (a) Full SIW resonator structure (b) HMSIW (c) QMSIW (d) EMSIW (e) SMSIW [162]

#### 4.5. Miniaturized Filter Design 1

This research work used QMSIW to design a fourth-order high-selectivity filter.



Figure 4.8 Electric field distribution of EMSIW resonator (a) First orientation, and (b) second orientation.

Fig 4.8(a) and (b) show the two orientations used in the design, with field intensity observed to be highest towards the center that is point O. Dimensions of  $a_{EMSIW}$  and  $b_{EMSIW}$  are  $7.5\text{ mm}$  and  $20\text{ mm}$ , respectively. The resonant frequency of the  $TE_{101}$  mode,  $f_{TE_{101}}$  of the EMSIW, can be approximated by [165, 166]:

$$f_{TE_{101}} = \frac{c}{2\pi\sqrt{\epsilon_r\mu_r}} \sqrt{\left(\frac{\pi}{a_{eff}}\right)^2 + \left(\frac{\pi}{b_{eff}}\right)^2} \quad (4.2)$$

$$a_{EMSIW} = a_{eff} + \left(\frac{d}{0.95 * p}\right)^2 - \Delta w \quad (4.3)$$

$$b_{EMSIW} = b_{eff} + \left(\frac{d}{0.95 * p}\right)^2 - \Delta w \quad (4.4)$$

$$\frac{\Delta w}{h} = \left(0.05 + \frac{0.3}{\epsilon_r}\right) * \ln\left(0.79 \frac{(a_{eff}/2)^2}{h^3} + 104 \frac{(a_{eff}/2)}{h^2} + \frac{38}{h} + 2.77\right) \quad (4.5)$$

where  $\epsilon_r$  and  $\mu_r$  are the relative permittivity and permeability, respectively, and  $c$  is the speed of light in a vacuum.  $a_{EMSIW}$  and  $b_{EMSIW}$  are the initial sizes of the EMSIW, while  $a_{eff}$  and  $b_{eff}$  are the edges of the equivalent EMSIW resonator.  $d$  and  $p$  are the via diameter and the distance between centers of two adjacent vias (also known as the pitch) and the substrate's height, respectively. Lastly,  $\Delta w$  is the effect of the fringing field of the equivalent magnetic walls. From Fig. 4.7 extracted EMSIW cavity resonators as presented in Fig. 4.8. However, due to the magnetic walls and fringing effects associated with the EMSIW resonator, the dimensions of  $a$  and  $b$  need to be modified according to Eq. (4.2) through Eq. (4.5) and use the values of  $a_{eff}$  and  $b_{eff}$ , respectively in the fourth-order filter.

#### 4.5.1 Proposed Fourth-Order Filter Design

Using the EMSIW resonator (as proposed in previous sections), a fourth-order SIW band-pass filter has been designed. Rogers-5880 substrate with  $\epsilon_r = 2.2$  and a thickness  $0.3\text{ mm}$  was used. Four-EMSIW resonators are placed in topology as indicated in Fig. 4.9, where  $R_1$ - $R_4$  represent the four-EMSIW cavity resonators,  $c_{i,i+1}$  represent the coupling coefficient and  $Q_e$  represent the quality factor,  $i = 1$  to  $4$  and  $n = 1$  and  $4$ . The physical implementation of the filter is shown in Fig. 4.10.

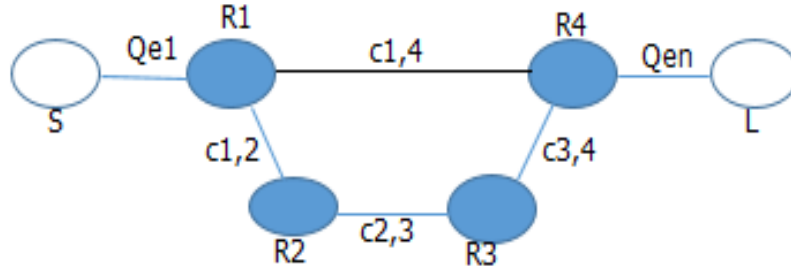


Figure 4.9 EMSIW filter topology.

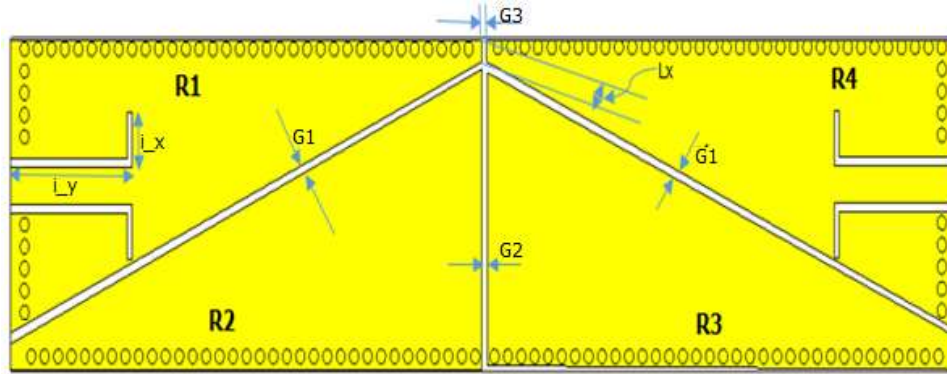


Figure 4.10 Forth order EMSIW filter.

For a fourth-order Chebyshev band pass filter with  $0.1 \text{ dB}$  ripple, the  $g$  parameters are as follows;  $g_0 = 1$ ,  $g_1 = 1.1088$ ,  $g_2 = 1.3062$ ,  $g_3 = 1.7704$ ,  $g_4 = 0.8181$ , and  $g_5 = 1.3554$ . The coupling matrix of the filter in Fig. 4.10 can be determined by [4], [5]:

$$c_{i,i+1} = \frac{fbw}{\sqrt{g_i * g_{i+1}}} \quad (4.6)$$

$$Q_{en} = \frac{g_0 g_n}{fbw} \quad (4.7)$$

Because of the shape of EMSIW resonator, two of such resonators can be arranged in different orientations to achieve various electrical coupling schemes, as shown in Fig. 4.10. The coupling between  $R_1$  &  $R_2$  and  $R_3$  &  $R_4$  is achieved by a varied separation distance, shown as  $G1$ . The coupling between  $R_2$  and  $R_3$  is achieved by varying gap  $G2$ . Then the coupling between  $R_1$  and  $R_4$  is achieved by varying gap  $G3$ . To enhance the degrees of freedom for coupling, instead of having a pointed edge of the EMSIW cavity, an edge is introduced with a distance indicated as  $l_x$  in Fig. 4.10. From the field pattern, the intensity is highest at the origin ( $O$ ). Hence by manipulating the distance  $l_x$  and the gap  $G3$ , the appropriate coupling can be achieved through simulation, which is equal to the theoretical value. In Fig. 4.10, the  $R_1$  &  $R_2$ ,  $R_2$  &  $R_3$ , and  $R_1$  &  $R_4$  are simulated, and two split frequencies

are observed on the  $S_{12}$  parameters, with peaks  $f_1$  and  $f_2$  being the lower and upper frequencies, respectively. The structure used to extract the coupling coefficient between  $R_1$  and  $R_2$  is shown in Fig. 4.11. The other resonators' coupling factors can be extracted following the same procedure [13, 166].

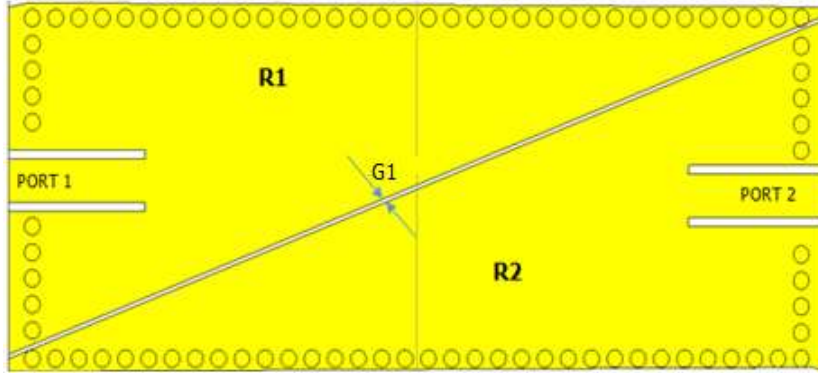


Figure 4.11 Coupling factor extraction.

Table 4.1 Design Parameters

Parameter	Dimension (mm)
G1	0.20
G2	0.25
G3	0.10
$i_x$	1.40
$i_y$	5.40

The coupling coefficient can be calculated by:

$$c_{i,i+1} = \frac{f_2^2 - f_1^2}{f_2^2 + f_1^2} \quad (4.9)$$

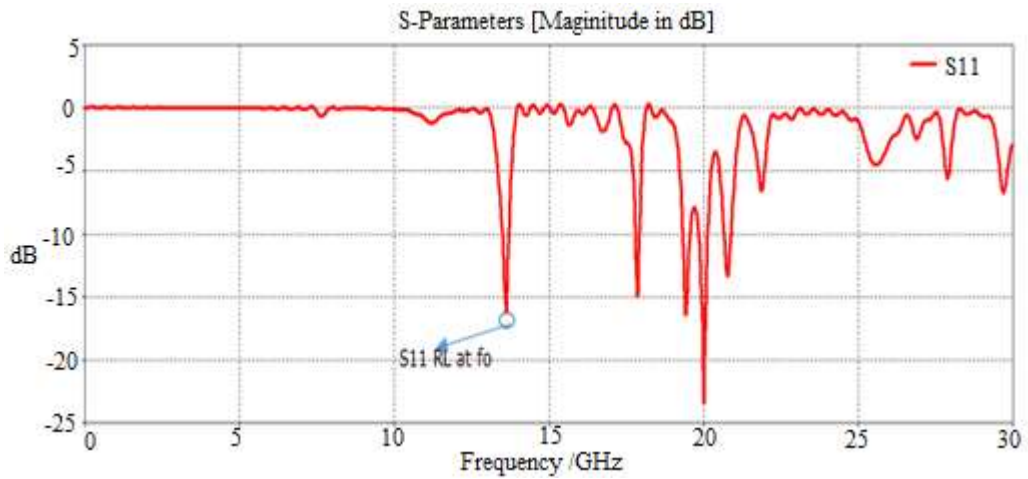
The respective gaps are varied to adjust the electrical coupling until the simulation value derived by Eq. (4.9) is equal to the theoretical value determined by Eq. (4.7). The quality factor can be extracted by varying the distance  $i_x$  and  $i_y$  indicated in Fig. 4.10 and then applying:

$$Q_e = \frac{2f_o}{\Delta f_{3dB}} \quad (4.10)$$

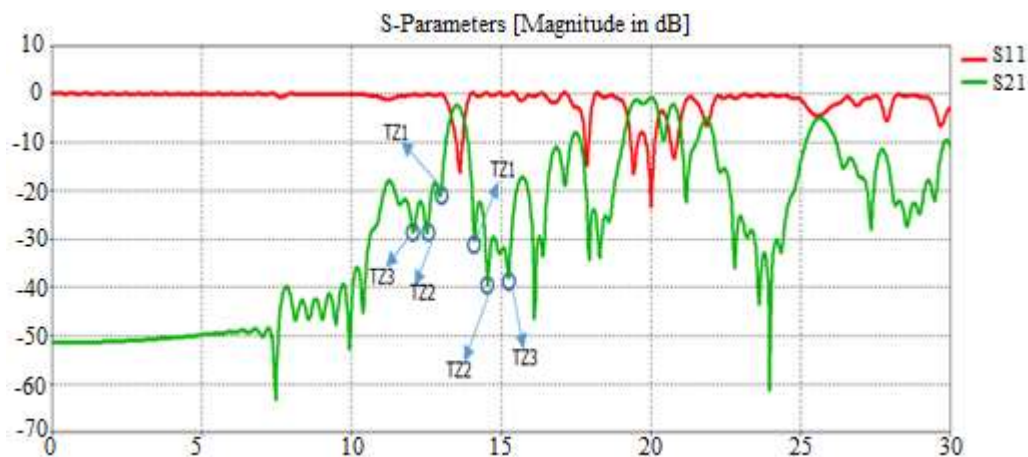
where  $f_0$  is the frequency at which  $S_{21}$  gets maximum and  $\Delta f_{3dB}$  is the  $3dB$  bandwidth when  $S_{21}$  is maximum. The values for  $i_x$  and  $i_y$  are varied until the simulated  $Qe$ , according to Eq. (4.10) is equal to the theoretical value given by Eq. (4.8).

#### 4.6. Results Analysis and Discussions

The pass-band is centered at  $13.5\text{ GHz}$  with a  $3dB$  bandwidth of  $0.5\text{ GHz}$ , as shown in Fig. 4.12. An insertion loss better than  $-2\text{ dBs}$  with a return loss of  $-17\text{ dBs}$  has been achieved. The source-to-load coupling leads to three transmission zeros on each side of the pass-band labeled in Fig. 7 as  $TZ_1 - TZ_3$ . These transmission zeros increase the filter's high selectivity on either side of the pass-band, achieving high out-of-band rejection.



(a)



(b)

Figure 4.12 Output results of the proposed filter (a)  $S_{11}$  output and (b) Combined  $S_{11}$  and  $S_{12}$  output.

From comparative Table 4.2, it can be concluded that this filter has higher selectivity than filters of the same category and also has the highest order of operation, fourth-order. The proposed filter has the highest number of transmission zeros on either side of the pass-band, as shown in Fig. 4.12. It operates at a higher frequency as compared to the other work.

Table 4.2 Comparison of the proposed design with existing work

Ref.	No. of Layers	Order of filter	Frequency, fo (GHz)	TZs	Selectivity
[51]	single	--	8.5	2	low
[52]	single	3 <sup>rd</sup>	1	1	high
[53]	single	3 <sup>rd</sup>	28.5	2	low
[7]	single	--	4	0	low
[60]	single	--	6.8	2	low
[54]	double	4 <sup>th</sup>	2.8	3	high
[20]	double	4 <sup>th</sup>	3.52	4	high
This work	single	4 <sup>th</sup>	13.5	6	high

With a filter operating at this frequency, applications requiring higher frequency operation can be achieved satisfactorily. With a size reduction of 87.5% compared to the conventional SIW resonators, a device with a much smaller size can be designed and operated, which helps in the miniaturization of devices. The source-to-load coupling increases the number of transmission zeros, increasing selectivity, which is required for efficient operation since the pass-band will have much sharper edges.

#### 4.7. Proposed Miniaturized Filter Design-2

A Chebyshev filter was designed with transmission zeros at  $\pm 1.1258$  and  $\pm 1.6050$  and 20 dB return loss. For these given specifications, the general objective transfer and reflection functions of the Chebyshev filtering function may be expressed as a ratio of two  $N^{\text{th}}$ -degree polynomials as [167, 168]:

$$S_{11}(w) = \frac{F_N(w)}{E_N(w)}, S_{21}(w) = \frac{P_N(w)}{\varepsilon E_N(w)} \quad (4.11)$$

where  $w$  is the real frequency variable related to the complex plane  $s$  by  $s = j(w)$ . The  $\varepsilon$  is a constant normalizing  $S_{21}$  to the equi-ripple level at  $w = \pm 1$  as:

$$\varepsilon = \frac{1}{\sqrt{\frac{R_L}{10^{RL/10}} - 1}} \frac{P_N(w)}{E_N(w)} (w = 1) \quad (4.12)$$

where  $R_L$  is the return loss in dBs, all polynomials are assumed normalized, whereby their highest degree polynomial is 1. The  $P_N(w)$  contains the  $n_{fz}$  prescribed transmission zeros. The  $F_N(w)$  is an  $N^{\text{th}}$ -degree polynomial with  $E_N(w)$ , also a Hurwitz polynomial. Using the procedure highlighted in [4] the coefficients of the numerator and denominator polynomials of  $S_{11}(s)$  and  $S_{22}(s)$  are shown in Table 1.

Table 4.3 Polynomial normalized coefficients

$s^i, i$	P(s)	F(s)	E(s)
0	+j3.2648	-0.1300	+1.2787
1	—	—	+2.8621
2	+j3.8434	-1.0334	+4.7981
3	—	—	+5.1328
4	+j1.0	-1.8864	+4.3610
5		—	+2.2244
6		-1.0	+1

The polynomials  $F(s)$  and  $E(s)$  can now be used to formulate the complex even and complex odd polynomials as:

$$m_1 + n_1 = E(s) + F(s) \quad (4.13)$$

where  $y_{21}$  and  $y_{22}$  being the short circuit admittance parameters, can be derived as:

$$y_{21}(s) = \frac{P(s)}{\epsilon m_1} \quad y_{22}(s) = \frac{n_1}{m_1} \quad (4.14)$$

$$y_{21} = \frac{P(s)}{\epsilon n_1} \quad y_{22} = \frac{m_1}{n_1} \quad (4.15)$$

and by the use of partial fractions,

$$y_{21}(s) = j \sum_{k=1}^N \frac{T_{Nk} T_{1k}}{w - \lambda_k} \quad (4.16)$$

$$y_{22}(s) = j \sum_{k=1}^N \frac{T_{Nk}^2}{w - \lambda_k}$$

where  $T_{1k}$  and  $T_{Nk}$  are the first and last rows of the orthogonal matrix,  $T$  and  $\lambda_k$  is the Eigen-pole. The Gram-Schmidt orthogonalization process can formulate the orthogonal rows [4]. The coupling matrix can then be deduced, as shown in Table 4.3, after similarity transformation and annihilation of matrix elements. The S and L represent the source and load, respectively; the numbers denote the resonators.

Table 4.4 Coupling Matrix

	s	1	2	3	4	5	6	L
S	0	1.2863						
1	1.2863	0	0.7875		0.8187			
2		0.7875	0	0.8673				
3			0.8673	0	-0.3119		0.8947	
4		0.8187		-0.3119	0	0.8992		
5					0.8992	0	0.6999	
6				0.8947		0.6999	0	1.2863
L							1.2863	0

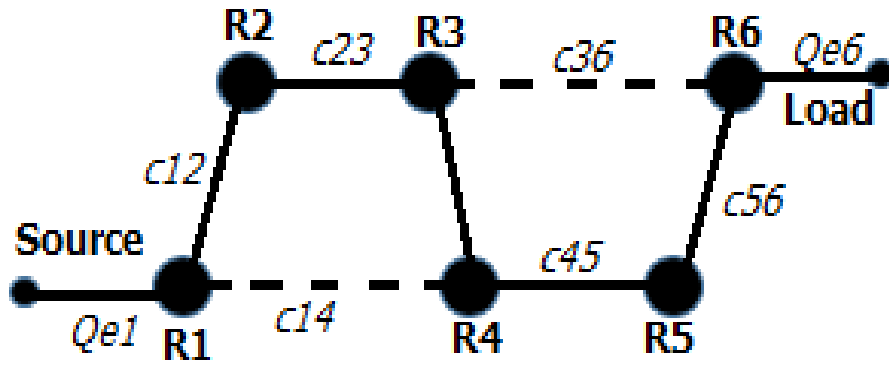


Figure 4.13 Filter topology.

The topology diagram of the designed filter is shown in Fig. 4.13. There are six resonators indicated by  $R_1$  through  $R_6$ . The solid line indicates a direct connection between the resonators and the broken line represents cross-coupling between  $R_1$  and  $R_4$  &  $R_3$  and  $R_6$ . The coupling coefficients are the  $c_{12}$ ,  $c_{23}$ , etc., while  $Q_{e1}$  and  $Q_{e6}$  are the external quality factors to be determined. In Fig. 4.14, the equivalent circuit is shown where the connections between the resonators are illustrated. The admittance inverters are shown by  $J_{i,i+1}$  where  $i=0$  to  $5$ . The admittance inverters  $J_{01}$  represent the coupling between the source and load to the first and last resonators, and the others represent the coupling between the respective resonators.  $C$  and  $L$  are the equivalent capacitance and inductance of the resonators, respectively. The filter derived from the topology diagram in Fig. 4.13 is shown in Fig. 4.14.

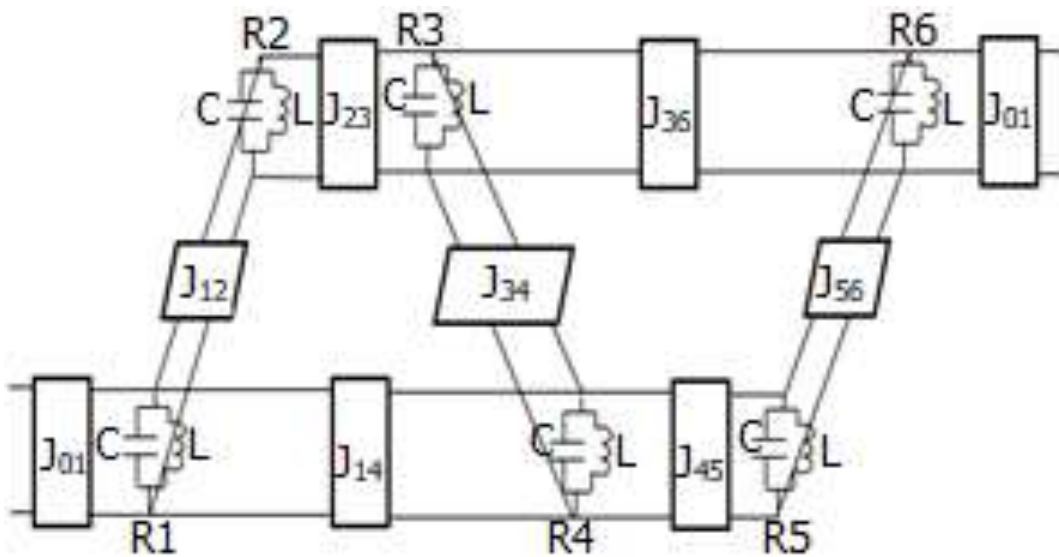


Fig. 4.14 Equivalent circuit of the 6<sup>th</sup> order filter.



The structure in Fig. 4.16 has been simulated to determine the coupling coefficients, keeping the load and source coupling as weak as possible. From the observation of the results, two split frequencies are seen on the S21 parameter plot [5], and the coupling coefficient is calculated as shown in Eq. (4.9). The gap  $g_i$  ( $i = 1$  to 7, as shown in Fig. 4.15) is varied repeatedly and Eq. (4.9) is employed until the value achieved is equal to the value in the coupling matrix. To get the external quality factor,  $L_{in}$  and  $W_{in}$  are varied. The quality factor is determined according to Eq. (4.10). Table 3 shows the distances determined as suitable to give the coupling coefficients from the simulations.

Table 4.5. Parameter values

Parameter	Value(mm)
$L_{in}$	1.7
$W_{in}$	0.5
$g_1$	0.1
$g_2$	0.2
$g_3$	0.05
$g_4$	0.1
$g_5$	0.05
$g_6$	0.2
$g_7$	0.1

#### 4.8. Results and Analysis of second filter design

After determining suitable gap and feedline lengths, the structure in Fig. 4.15 was simulated. The reflection coefficient  $S_{11}$  is achieved as shown in Fig. 4.17. It shows that the filter operates at 33 GHz and has a high return loss of -27 dBs. The results of both  $S_{11}$  and  $S_{21}$  on the same graph are shown in Fig. 4.18. These results indicate a filter operating with a low insertion loss of -1.8 dBs.

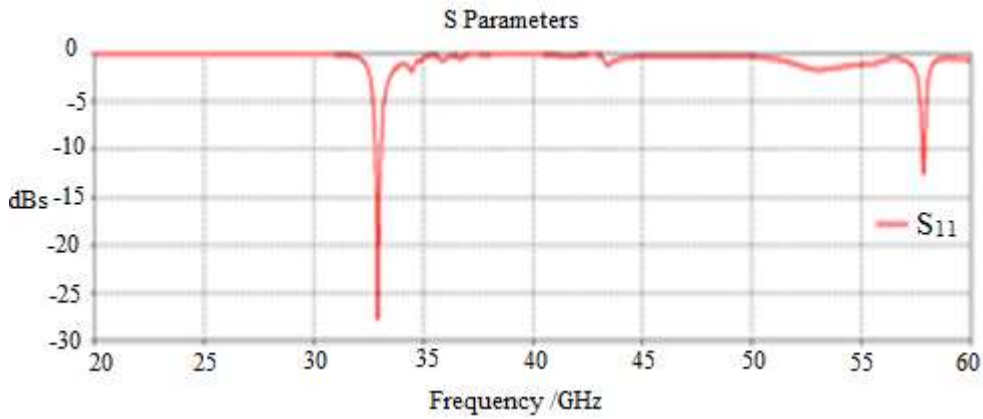


Figure 4.17 S parameter plot,  $S_{11}$ .

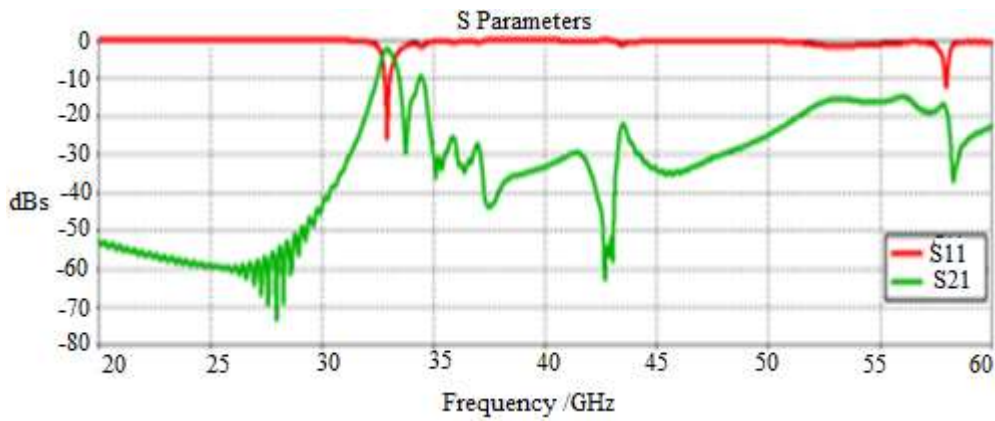


Figure 4.18 S-parameter plot;  $S_{11}$  and  $S_{21}$ .

It can be seen that the filter has an observable wide stop-band, as shown in Fig. 4.18. This helps operate the filter so that it won't pick up some interfering signals that may be within its frequency range. The filter has a bandwidth of  $600\text{ MHz}$ , which translates to a fractional bandwidth of 2%, enabling many devices to operate within this range. The Voltage Standing Wave Ratio (VSWR) graph is shown in Fig. 4.19. The graph shows that at the operation frequency,  $32\text{ GHz}$ , the VSWR is close to 1 or 0 dB; power is being transferred efficiently from the source to the load without much reflection.

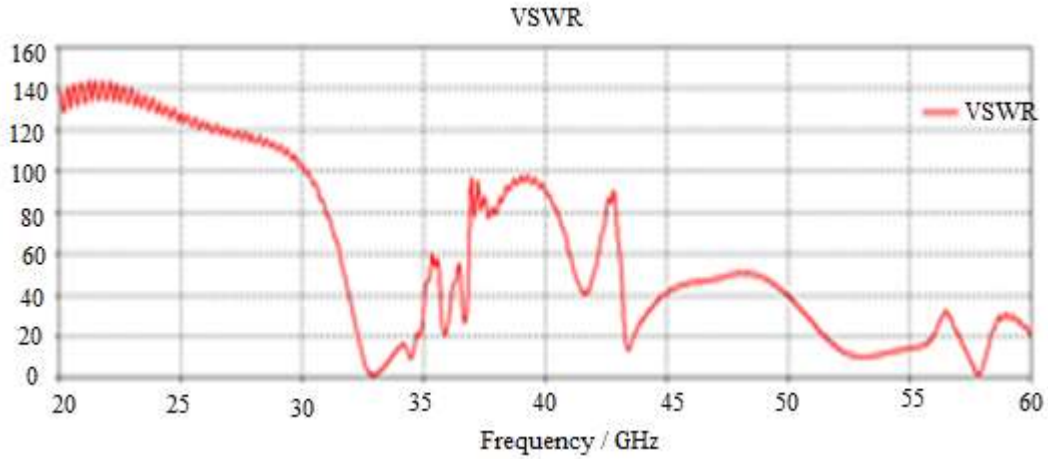


Figure 4.19 The VSWR analysis.

Table 4.6 Comparison with similar work

Ref	fo (GHz)	IL (dB)	R <sub>L</sub> (dB)	Layers	VSWR	size (λ <sub>g</sub> xλ <sub>g</sub> )
[132]	4	1.88	30	multi	--	0.23x0.25
[169]	10	0.8	10	double	--	--
[170]	10.04	1.5	20	single	--	0.48x1.10
[171]	13.2	1.5	20	double	--	0.4x0.4
[115]	10	1.2	20	single	--	0.62x0.62
[172]	3.9	0.9	70	single	1.2	--
This work	32	1.8	27	single	1	0.3x1.25

Compared to other filters of similar nature in the literature (Table 4.4), the filter operates at a high frequency, which means it can be used in modern technology in the mm-wave range. This design fares very well in terms of a small footprint. A single layer makes the design more straightforward, so fabrication will be much easier. The VSWR reaches 1 or 0 dB at the operation frequency, which fares well with related work, and it shows a good match between the input and the output.

## 4.9 Dual Band Filter

Because of many applications that need to be added to the communication networks, different frequency bands are needed to group these applications successfully. This research work uses SIW multi-mode resonators to design a dual-band filter. The mode frequencies and field distributions have been analyzed. The design specifications of the coupling coefficients and external quality factors have been determined. The Rogers-5880 substrate has been used with a permittivity of 2.2. The first design demonstrates the filter using the full-mode SIW resonator cavity and for miniaturization, the half-mode SIW resonator is used in the second design. This in turn, reduces the size of the filter by 50%. To the author's best knowledge, not much work on dual-band filters was reported using the triangular HMSIW resonators using the multi-mode resonance. Compared to similar devices in literature, this fares as one of the smallest filters giving a satisfactory performance.

### 4.9.1 Multi-Mode Dual Band Filter Design

To design the filter, the following steps have been undertaken:

#### A. Filter Topology

An appropriate resonator that operates at the desired frequency should be constructed to design a band-pass filter. Then the resonators can be utilized in different topologies to implement either single, dual, triple, quad-band filters, etc. Coupled resonators, as shown in Fig. 4.20 can be used for a single-band filter. The coupling between the resonators and external Q factors can be determined by Eq. (4.17) and Eq. (4.18), respectively [173]. These parameters can then determine the physical separation distances between the resonators and how the signals can be fed in and brought out of the filter through ports.

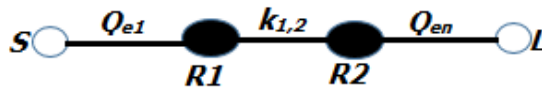


Figure 4.20 Second-order single-band filter topology.

where  $S$  and  $L$  represent the source and load,  $k_{1,2}$  is the coupling coefficient between resonator 1,  $R_1$  and resonator 2,  $R_2$  and  $Q_{e1}$  and  $Q_{en}$  are the load and source external quality factors, respectively. For a second-order filter, the coupling coefficient and external quality factor are given as:

$$k_{1,2} = \frac{FBW}{\sqrt{(g_1 g_2)}} \quad (4.17)$$

$$Q_{e1} = \frac{g_0 g_1}{FBW} \quad (4.18.1)$$

$$Q_{en} = \frac{g_2 g_3}{FBW} \quad (4.18.2)$$

where  $g$  is the element in the low pass filter prototype and  $n$  is the number of resonators in the filter [173]. As shown in Fig. 4.21, a dual or triple band filter can be realized by replacing the single mode resonator in Fig. 4.20 with dual or / triple mode resonators. A dual-mode resonator node now replaces one resonator. The combination of  $R1-R1'$  and  $R2-R2'$  as shown in Fig. 4.21 represents a dual-mode resonator.

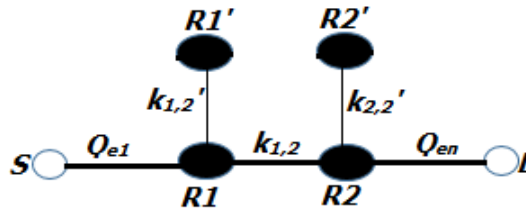


Figure 4.21 Second-order dual-band filter topology.

## B. Resonator Design

The following procedure has been used to determine the initial size of the resonator. Since the SIW resonator has the same properties as the conventional rectangular waveguide, the modified design Eq.s of the rectangular waveguide can be applied. The resonant frequency of the  $TE_{mon}$  in the dielectric rectangular waveguide is given by [1]:

$$f_{TE_{mon}} = \frac{c}{2\sqrt{\mu_r \epsilon_r}} \sqrt{\left(\frac{m}{W}\right)^2 + \left(\frac{n}{L}\right)^2} \quad (4.19)$$

where  $c$  is the speed of light in a vacuum and  $m$  and  $n$  are the mode  $x$ - and  $z$ -directions indices, respectively. Then the sizes of the resonator length and width can be given as:

$$W_{RECT} = \frac{c}{2\sqrt{\mu_r \epsilon_r}} \sqrt{\frac{3}{f^2_{TE_{201}} - f^2_{TE_{101}}}} \quad (4.20)$$

$$L_{RECT} = \frac{c}{2\sqrt{\mu_r \epsilon_r}} \sqrt{\frac{3}{4f^2_{TE101} - f^2_{TE201}}} \quad (4.21)$$

where  $W_{RECT}$  and  $L_{RECT}$  are the width and length of the traditional rectangular waveguide, respectively. Now to get the equivalent length and width of the SIW resonator, Eq. (4.20) and Eq. (4.21) can be modified as:

$$W_{SIW} = W_{RECT} + \frac{via\_d^2}{0.95 * pitch} \quad (4.22)$$

$$L_{SIW} = L_{RECT} + \frac{via\_d^2}{0.95 * pitch} \quad (4.23)$$

where  $L_{SIW}$  and  $W_{SIW}$  denote the length and the width of the SIW cavity resonator, respectively,  $via\_d$  is the via diameter, and  $pitch$  is the distance between two adjacent vias. In this work  $via\_d = 0.4$  mm,  $pitch = 0.6$  mm,  $h = 0.2$  mm,  $L_{SIW} = 12.4$  mm and  $W_{SIW} = 18$  mm. The first four modes in the SIW resonator of the calculated dimensions are shown in Fig. 4.22.

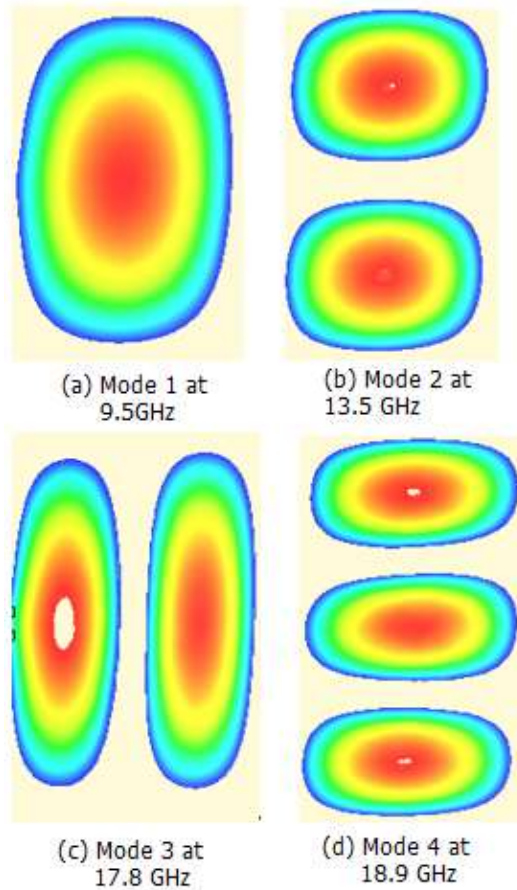


Figure 4.22 Resonator modes field distribution.

The first four modes in the resonator are TE<sub>101</sub> at 9.5 GHz, TE<sub>201</sub> at 13.5 GHz, TE<sub>102</sub> at 17.8 GHz, and TE<sub>301</sub> at 18.9 GHz. From this, by properly coupling the resonators and allowing for the proper selection of the external quality factors, a dual-band filter operating at 9 GHz and 13 GHz can be realized. The input and output coupling are achieved by using a microstrip feedline with two degrees of freedom, as shown in Fig. 4.25 where the parameters labeled *insert\_l* and *feed\_l* are changed one at a time, and a simulation is carried out. Two sharp frequencies are observed on the S<sub>21</sub> parameter output graph to be used to determine the implementation quality factor and compare it to the theoretical one.

### C. Realization of the Filter

This work builds a dual-band filter based on the full- and half-mode SIW structures. Because the two pass-bands can be implemented individually, the synthesis procedure of single-band filters can be applied [174]. Eq. (4.9) and Eq. (4.10) can be used to derive the design parameters. In this work, the two center frequencies are  $f_1 = 9 \text{ GHz}$  and  $f_2 = 13 \text{ GHz}$ , with a fractional bandwidth of 10% and 6% for the first and second pass-band, respectively. For a maximally flat response, the  $g$  parameters as obtained from Tables in [175] are  $g_0 = 1$ ,  $g_1 = 1.414$ ,  $g_2 = 1.414$ ,  $g_3 = 1$ , which gives  $k_{1,2}^I = 0.0707$ ,  $k_{1,2}^{II} = 0.0424$ ,  $Q_e^I = Q_{en}^I = 14.14$ ,  $Q_e^{II} = Q_{en}^{II} = 23.57$  where  $k$  is the coupling coefficient and subscripts <sup>I</sup> and <sup>II</sup> represent pass-band 1 and pass-band 2, respectively.

The filter can be implemented physically after finding the values of the coupling coefficients and the external quality factors. To get  $k_{i,j}$ , weakly coupled input and output ports are employed. Two split resonant frequencies can be observed by simulating the structure in a full wave simulator [5], and the coupling coefficient is given by Eq. (4.9). The distance  $l$  shown in Fig. 4.23 is varied until the desired value of  $k$  is achieved for the full mode resonator filter. The graph of variation of  $k$  and  $l$  is shown in Fig. 4.23 for the full-mode SIW resonator. For the half-mode SIW resonator, in Fig. 4.24, the distance indicated as  $tl$  is varied and in the same graph, the variations of the coupling factor with the distance  $tl$  are also shown. A second-order filter has been designed using Rogers-5880 substrate with permittivity 2.2.

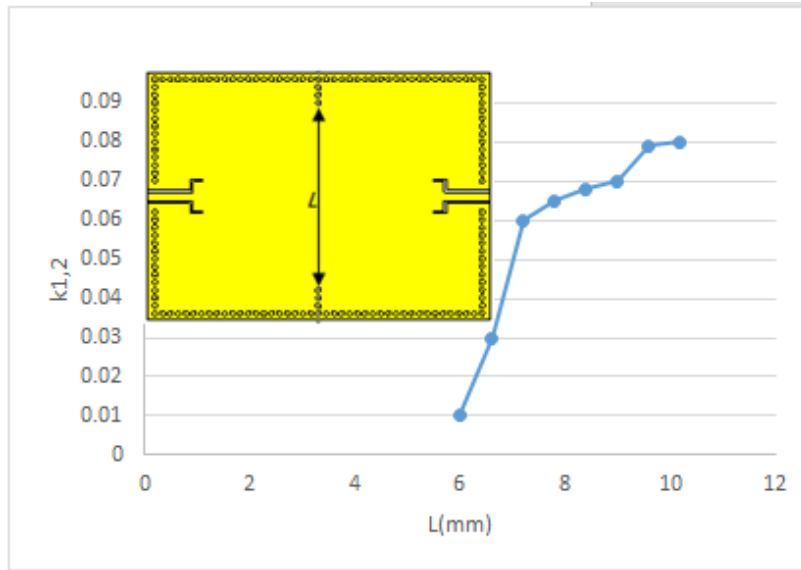


Figure 4.23 Determination of coupling coefficient using full mode resonator.

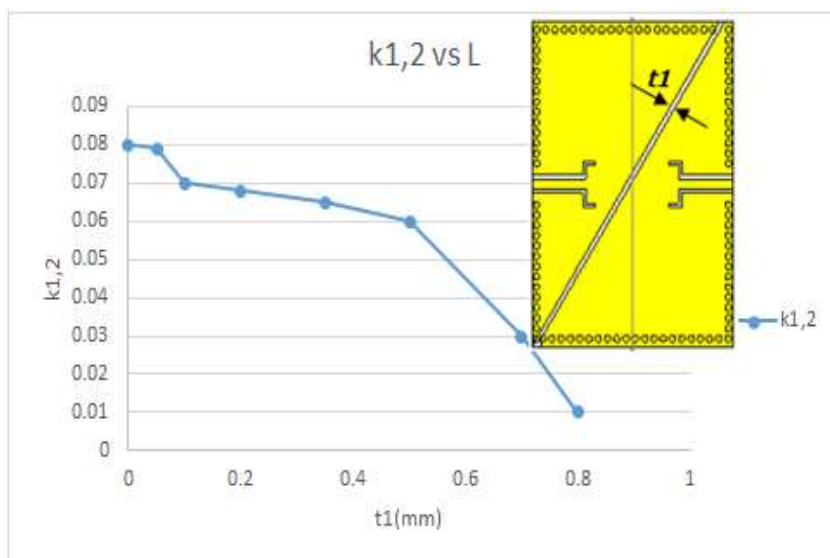


Figure 4.24 Determination of coupling coefficient using half-mode resonator.

The external quality factor is determined according to [98]. Figure 4.25 shows the structure used to determine the external quality factor. The distances labeled *insert<sub>l</sub>*, *feed<sub>l</sub>* and *gap* are varied using a parametric sweep in the simulation software. From the  $S_{11}$  parameter output results, the 3 dB bandwidth is used in Eq. (4.10) and the center frequency to derive the external quality factor.

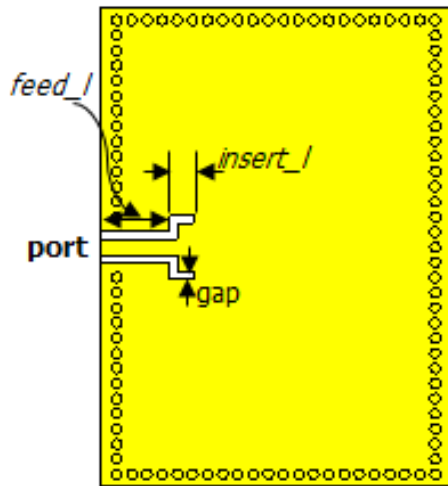


Fig 5.25 Determination of external quality factor.

From these experiments, Table 4.5 shows the optimum values of the parameters, together with all the dimensions used to design the filter.

Table 4.7 Filter dimensions

Parameter	Length (mm)
$W_{SIW}$	18
$L_{SIW}$	12.4
<i>height</i>	0.2
<i>pitch</i>	0.6
<i>via_d</i>	0.4
<i>insert_l</i>	0.5
<i>feed_l</i>	3
<i>gap</i>	0.7
<i>t1</i>	0.2
<i>l</i>	9.4

## 4.10 Results and Analysis of Dual Band Filter

In Fig. 4.26, the results of the filter using full-mode resonators are shown. It can be seen that the dual-band filter operates at the first pass-band of  $9.5\text{ GHz}$  and the second pass-band at  $13.5\text{ GHz}$ . The return loss of the first and second pass-band is  $-12\text{ dB}$  and  $-22\text{ dB}$ , respectively. Insertion loss of the first and second pass-band being  $-3\text{dB}$  and  $-2.2\text{ dB}$ , respectively.

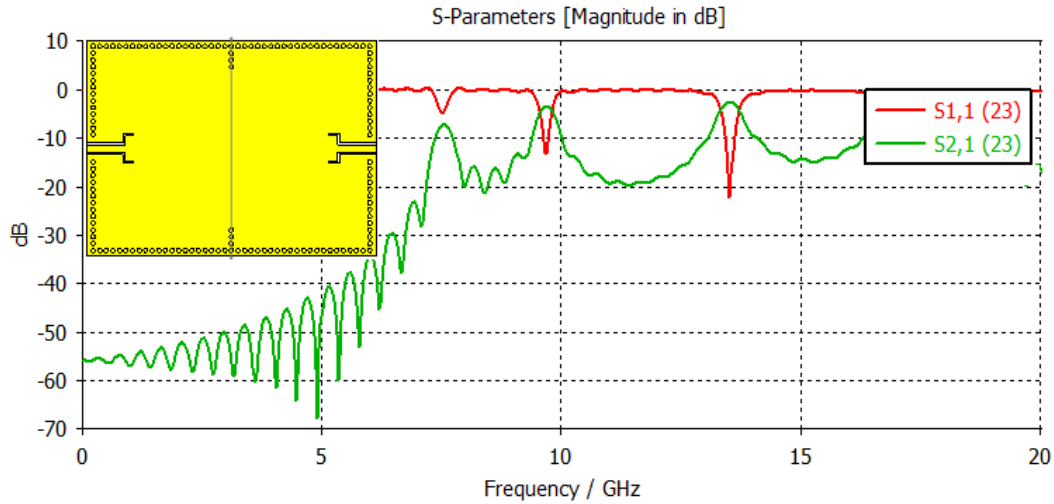


Fig. 4.26 Results of dual-band filter utilizing full mode SIW resonators.

In Fig. 4.27, the filter implemented using half-mode SIW resonators is simulated, and the results are shown. It can be seen that the dual-band filter operates at a first pass-band of  $9\text{ GHz}$  and the second pass-band at  $14\text{ GHz}$ . The return loss of the first and second pass-band is  $-15\text{ dB}$  and  $-19.7\text{ dB}$ , respectively. Insertion loss of the first and second pass-band is  $-1.4\text{ dB}$  and  $-4\text{ dB}$ , respectively.

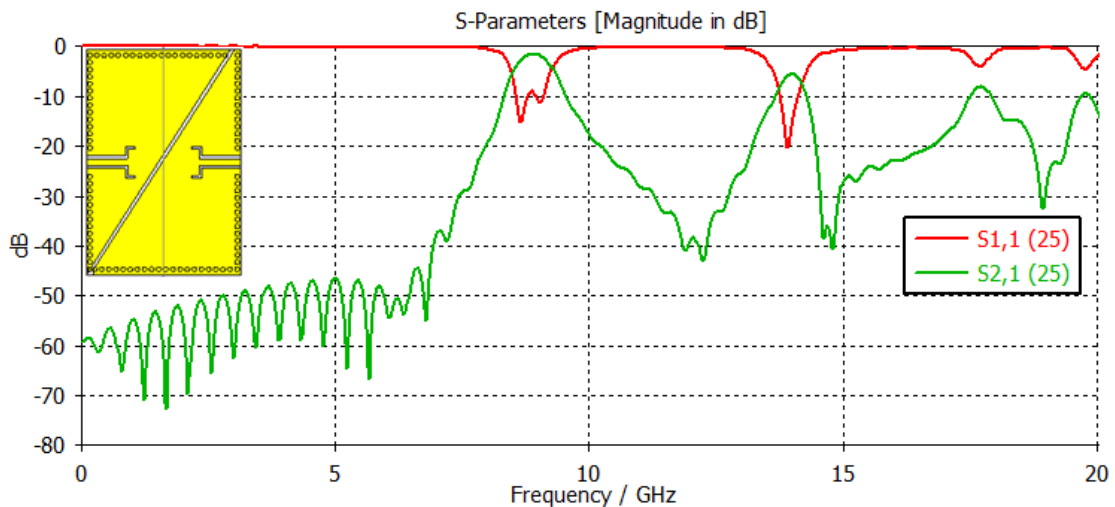


Figure 4.27 Results of dual-band filter utilizing half-mode SIW resonators.

The results of the dual-band filter utilizing multi-mode resonators operating using full-mode SIW resonators and half-mode SIW resonators are in agreement. This shows that the footprint size can be reduced by 50% while maintaining satisfactory filtering performance. And this, in turn, plays a significant role in coming up with smaller miniaturized devices.

Table 4.8 Comparison with existing work

<b>Ref.</b>	<b>Freq (GHz)</b>	<b>IL (dB)</b>	<b>Technology</b>	<b>Size (mm<sup>2</sup>)</b>
[176]	1/1.6	1.6/1.9	DGS*/Hairpin resonator	49x30
[114]	9/11.2	1.4/1.0 2	SIW	26x13.3
[177]	13.47/14.05	1/1	waveguide	40x7.89
[45]	3.6/7.1	1.3/1.8	SIW	48x24
[178]	3.64/8.06	0.8/1.2	SIR	--
[179]	5.50/8.50	2/2	CSRR*	--
[180]	4.48/5.25	1.2/1.2	SIW	28.5x57
<b>This work</b>	9.5/13.8	1/3	SIW	18x12.4

\*Deformed Ground Structure (DGS), Complementary Slip Ring Resonator (CSRR).

From this comparison, Table 4.6 shows that the filter designed from the half-wave SIW resonator has the smallest size compared to similar work. The filter also operates at a higher frequency except for the work [177], which was bulky. Hence for dual-band filter miniaturization, the half-mode dual-mode resonator can be used effectively to reduce the size of the structure by 50%.

## 4.11. Chapter Summary

This chapter deals with miniaturization of microwave system devices in particular microwave filters. The need for miniaturization is explored. Different ways used to achieve miniaturized devices are presented. The ridged and folded ridge SIW filters are presented as a way to reduce microwave resonators. Slip ring resonators (SRR) and Complementary slip ring resonators (CSRR) are also presented and their theory behind explained. Another method for miniaturization presented was through the bisection of the full SIW into, for example, the half, quarter, etc. to get HMWSIW, QMSIW etc. structures. These structures will be small but exhibit the same propagation characteristics as the original structure. This chapter presents a proposed design utilizing Half mode (HM) and eighth-mode (EM) substrate integrated waveguide structures. A second-order filter was presented, operating at  $13.5\text{ GHz}$ . In the proposed second design, a sixth-order cross-coupled filter was presented. EMSIW structures were used to achieve miniaturization. This chapter also presents the theory behind dual-band filters and methods for the filter design of dual-band filters. A proposed second-order dual-band filter utilizing triangular HMSIW structures is presented. The filter operates at center frequencies for the first and second pass-bands of  $9.5\text{ GHz}$  and  $13.8\text{ GHz}$ , respectively.

## Chapter-5

# DESIGN OF BALANCED FILTERS

---

### 5.1. Introduction

In communication systems, it's essential to maintain signal integrity. Balanced circuits can be used for this purpose as they can suppress an undesirable signal while permitting the wanted one. In typical communication systems, one of the two conductors is connected to the ground, one for signal propagation and the other for the return path. However, signals are transmitted as complementary pairs in balanced circuits, also known as differential circuits [80]. In this way, one wire carries a positive voltage while the other carries an equal but opposite polarity signal. Hence the signals on the two wires are  $180^\circ$  out of phase. The signal to be transmitted is the difference between the two signals carried by the two wires. Since the signals in the wires are equal in amplitude but opposite in polarity, a cancellation effect occurs in case there is noise presented on both wires. Noise often appears on the systems as an identical signal on the two signal wires; hence it's common to both wires and this noise is also referred as a common mode (CM) signal. It's imperative to reduce this CM signal as much as possible to maintain the integrity of the communication system. An adequately designed balanced filter offers low electromagnetic interference, high immunity to electromagnetic noise, low cross talk, high out-of-band rejection ratio, and high selectivity. Figure 5.1 shows the different transmission lines representing differential mode transmission [80].

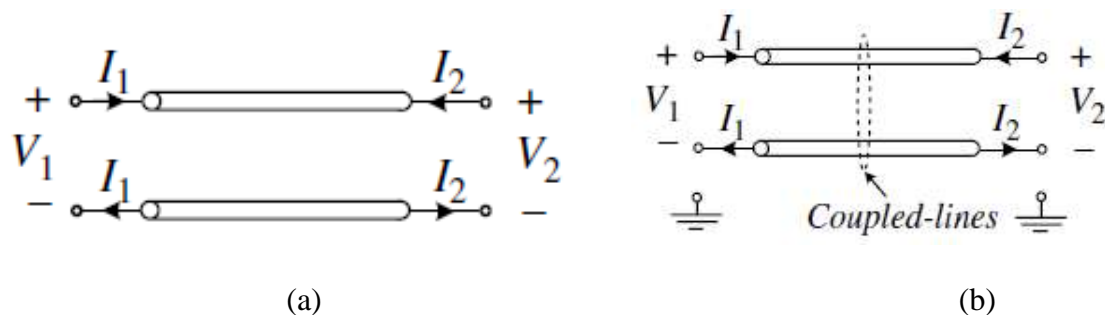


Figure 5.1 Differential mode transmission lines (a) Two conductors and (b) Three conductors.

In balanced or differential transmission systems, as shown in Fig. 5.1(a), the conductors are at the same potential from the ground but with a  $180^\circ$  phase shift. Differential ports feed these lines. The conductors also have the same impedance going to the ground. Most practically, balanced lines use a third conductor to act as ground as shown in Fig. 5.1 (b).

## 5.2. Propagating Modes

The three-wire transmission line can propagate two fundamental modes: the balanced and unbalanced modes. In this case, the balance mode is the fundamental mode, also referred to as the odd mode, and the unbalanced mode is the even mode, also referred to as the common mode. Figure 5.2 shows the single-ended voltages and currents for even and odd modes found in a differential system where  $Z_0$  is the source/ load reference impedance.

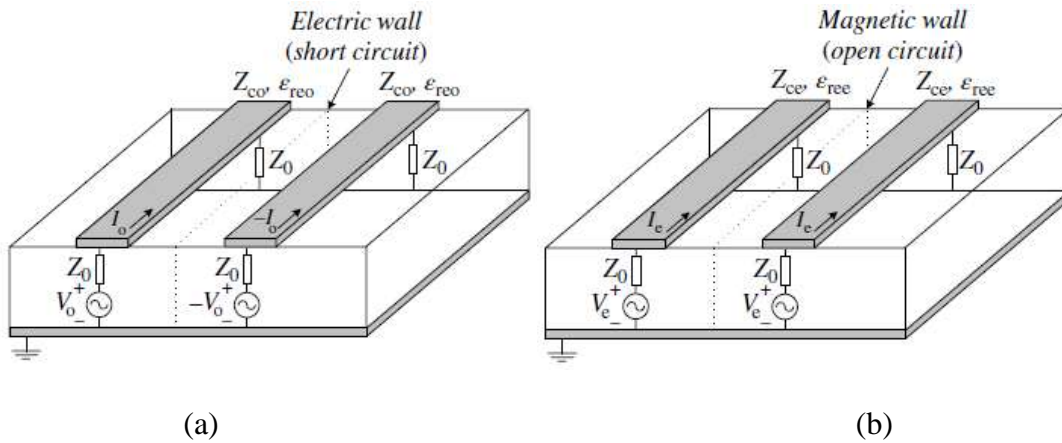


Figure 5.2 Single-ended voltages (a) even mode and (b) odd mode [80].

The odd and even voltages are defined by:

$$v_o = \frac{1}{2}(v_1 - v_2) \quad (5.1)$$

$$v_e = \frac{1}{2}(v_1 + v_2) \quad (5.2)$$

And the odd and even currents are defined as:

$$I_o = \frac{1}{2}(I_1 - I_2) \quad (5.3)$$

$$I_e = \frac{1}{2}(I_1 + I_2) \quad (5.4)$$

The characteristic impedance of each mode is given by:

$$Z_{c0} = \frac{V_o}{I_o} \text{ for the odd mode} \quad (5.5)$$

$$Z_{ce} = \frac{V_e}{I_e} \text{ for the even mode} \quad (5.6)$$

where  $Z_{c0} = \frac{1}{v_{p0}C_o} = \frac{1}{c\sqrt{C_oC_{o0}}}$  and  $Z_{ce} = \frac{1}{v_{pe}C_e} = \frac{1}{c\sqrt{C_eC_{oe}}}$ ,  $c$  being the speed of light,  $C_o$  and  $C_e$  representing the per unit length odd and even capacitances,  $C_{o0}$  and  $C_{oe}$  denote per unit length odd and even capacitances by replacing the relative dielectric constant of the substrate by unity.

$$v_{p0} = \frac{c}{\sqrt{\epsilon_{re,o}}} \quad (5.7)$$

$$v_{pe} = \frac{c}{\sqrt{\epsilon_{re,e}}} \quad (5.8)$$

where  $\epsilon_{re,o}$ ,  $\epsilon_{re,e}$  are the dielectric constants of the odd and even modes given by:

$$\epsilon_{re,e} = \frac{C_o}{C_{o0}} \quad (5.9)$$

$$\epsilon_{re,o} = \frac{C_o}{C_{oe}} \quad (5.10)$$

In this work, a 5<sup>th</sup>-order SIW filter operating at 39 GHz with a fractional bandwidth of 2 % has been designed and analyzed. RFSim99 software has been used to simulate the lumped element circuit, and later on, CST microwave studio has been used to implement the filter using SIW resonators.

### 5.3. Balanced Filter Design

The design of the balanced filter begins with the Low Pass Filter (LPF) prototype. The design specifications are as follows: 0.01 dB ripple and the filter is fifth-order for high selectivity. For such specifications, referring to the tables presented by *Matthaei et. al.* [175]

$g_0 = 1$ ,  $g_1 = 0.7563$ ,  $g_2 = 1.3049$ ,  $g_3 = 1.5773$ ,  $g_4 = 1.3049$ ,  $g_5 = 0.7563$  and  $g_6 = 1$ . With this information, the lumped filter design procedure outlined in [5] has been followed to develop a lumped band-pass filter. Once the lumped band-pass filter is synthesized, the method presented by *Mutepfe and Srivastava* [13] has been followed to determine the resonators' size.

Figure 5.3 shows the SIW resonator with all dimensions and the values are as follows: length ( $l$ ) = 5.77886 mm, width ( $w$ ) = 2.994 mm, the distance between centers of adjacent vias (pitch) = 0.4 mm, via diameter ( $d$ ) = 0.2 mm, the substrate is Rogers 5880, and substrate height ( $h$ ) = 0.5 mm. The electronic device simulator is then used to model this resonator. The designed filter operates at 39 GHz, higher than other filters of the same technology. This helps to have more bandwidth, and more data can be sent using higher frequencies.

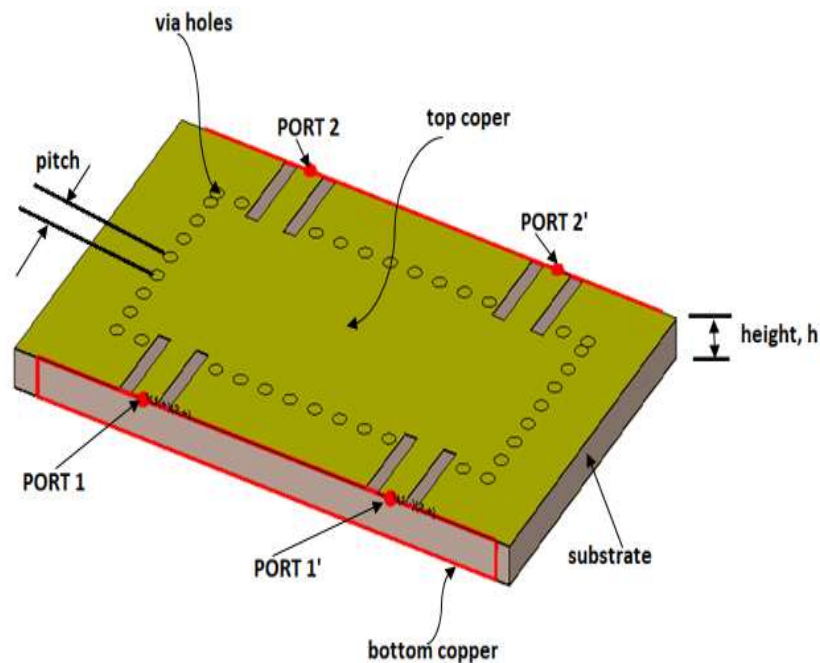


Figure 5.3 Substrate Integrated Waveguide (SIW) resonator.

Using even and odd mode theory [80], the SIW resonator already has a line of symmetry, which is a requirement for implementing a balanced filter. From Fig. 5.4 (a) it can observe a  $TE_{102}$  mode inside the cavity from the field distribution. The field distribution is odd symmetric w.r.t. to the middle symmetric line. From Fig. 5.4 (b) it can be seen (by the field distribution) that the field lines of the  $TE_{102}$  mode have equal and opposite intensities and hence can be excited by a pair of feed lines properly arranged symmetrically

to the symmetry line of the field distribution. That is ports 1 and 1' on the input side and ports 2 and 2' on the output side as shown in Fig. 5.4.

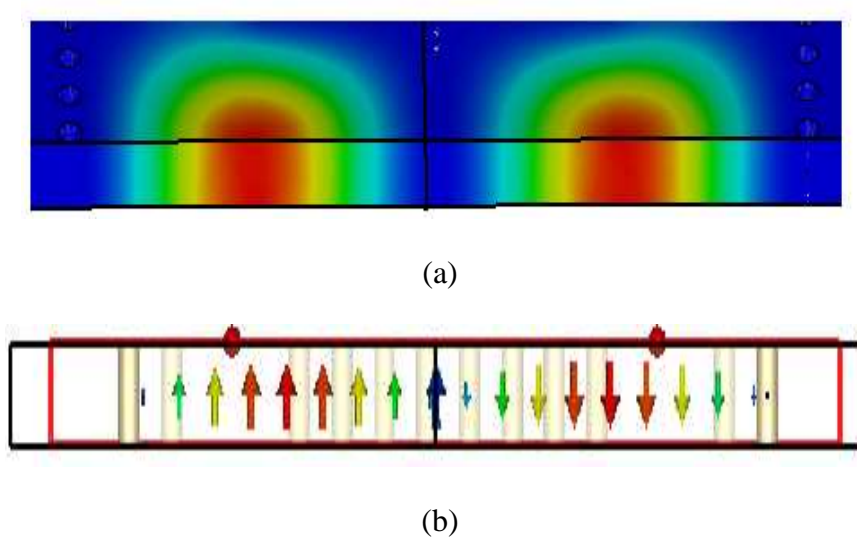


Figure 5.4 TE102 (a) field intensity, and (b) Field pattern.

By simulating the resonator in Fig. 5.3, it can be seen that there is a good suppression of the common-mode signal and good passage of the differential mode signal when the resonator is fed in the balanced mode configuration. This is illustrated in Fig. 5.5, where the subscripts DM and CM represent differential and common modes, respectively.

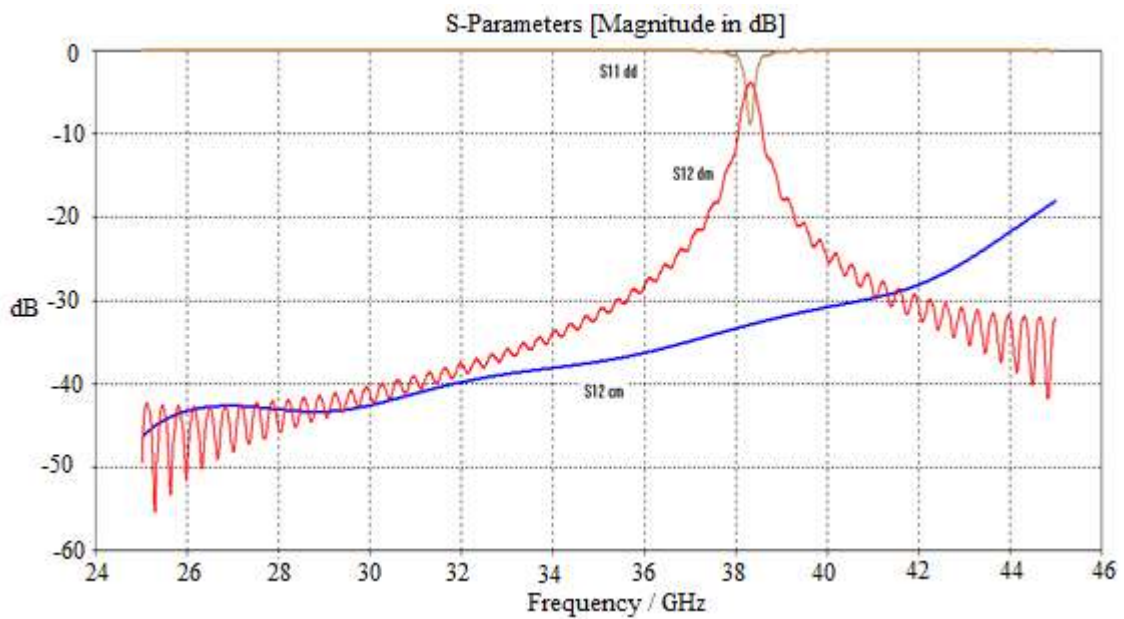


Figure 5.5 The DM and CM S12 response.

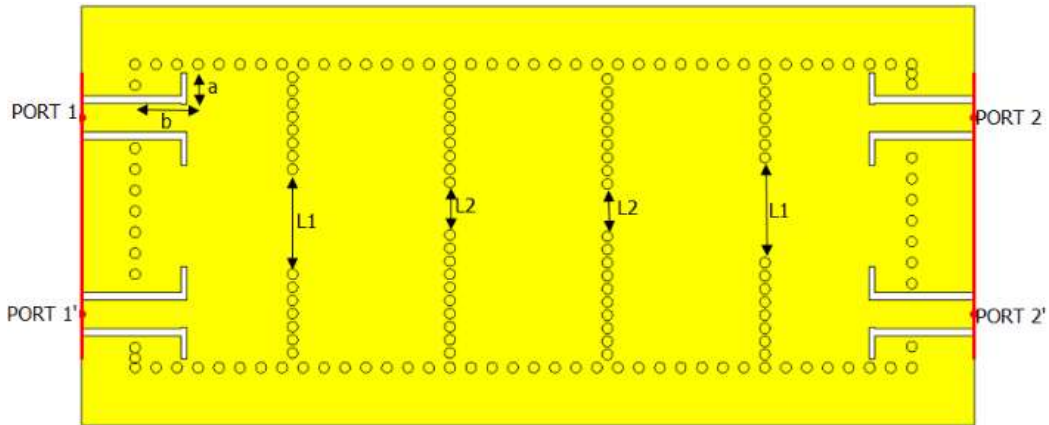


Figure 5.6 Substrate Integrated Waveguide (SIW) filter.

Figure 5.6 illustrates the differential filter. Port 1 and 1' represents the input ports and Port 2 and 2' are the output ports. The coupling between resonators is achieved by the coupling windows represented by L1 and L2. The quality factor is achieved by adjusting distances a and b in Fig. 5.8. This resonator is used in the final design of the filter. Using the method in ref. [5] the coupling between the resonators, as shown in Fig. 5.7,  $C_{i,i+1}$ , where  $i = 1 \dots 5$  can be determined by using:

$$C_{i,i+1} = \frac{fbw}{\sqrt{(g_i g_{i+1})}} \quad (5.11)$$

where  $f_{bw}$  is the fractional bandwidth and  $g$  stands for the  $g$ -parameters.

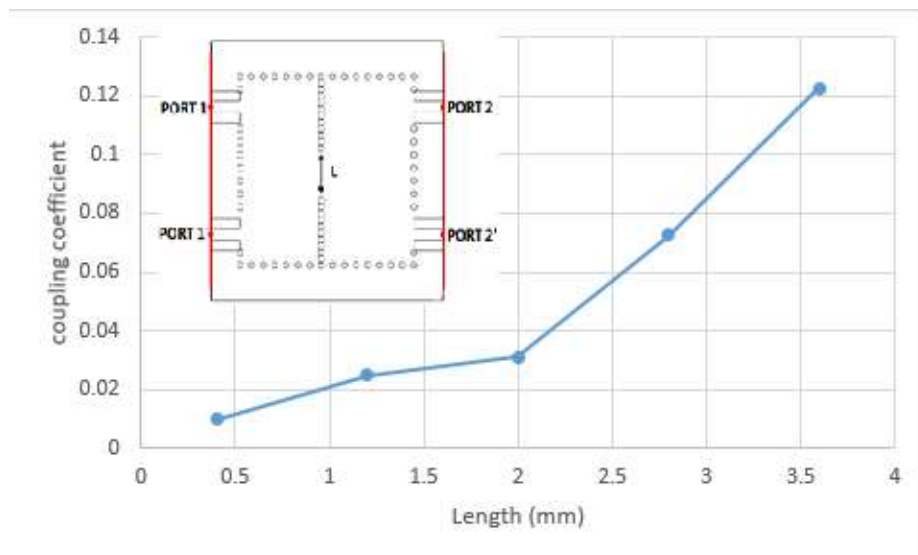


Figure 5.7 Coupling coefficient simulation.

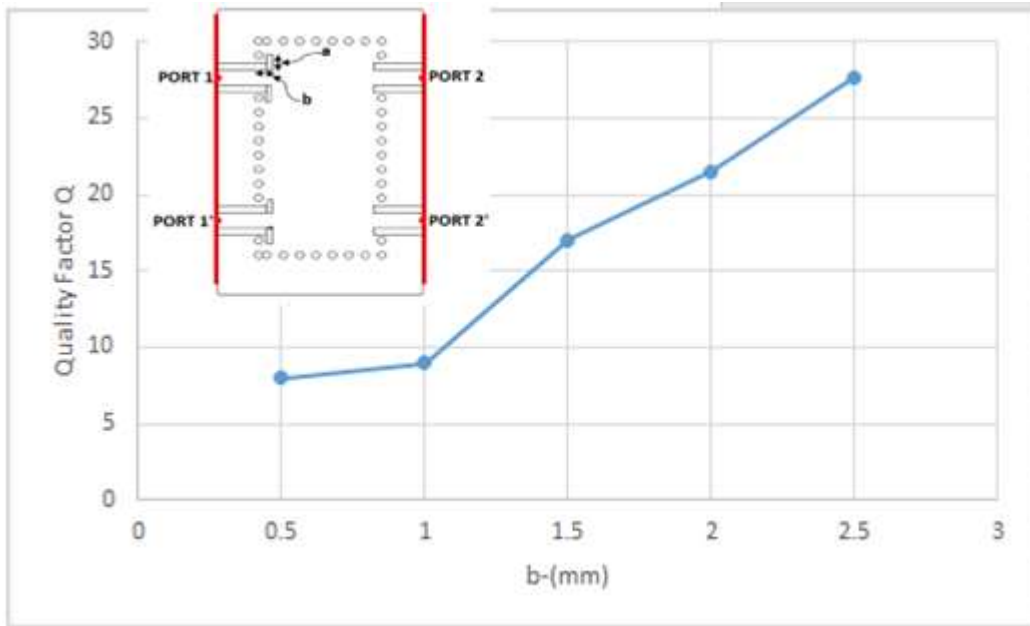


Figure 5.8 External quality factor simulation.

The external quality factor on the input and output ports can then be determined by:

$$Q_{e1} = Q_{en} = \frac{g_0 g_1}{fbw} \quad (5.12)$$

The calculated values are,  $c_{12} = c_{14} = 0.0362$ ,  $c_{23} = c_{34} = 0.0251$ ,  $Q_{e1} = Q_{en} = 21.008$ . CST microwave studio electronic device simulator has been used to determine these couplings in simulation. For the coupling coefficients between the resonators, the width opening,  $L$  between the resonators is varied, and the structure in Fig. 5.7 is used. After simulation, two split frequencies have been observed on the  $S_{21}$  parameters plot; from these two frequencies, the coupling coefficient is calculated using Eq. 5.9 [5]. The graph of how the coupling coefficient varies with the distance  $l$  is shown in Fig. 5.7 and the external couplings are then determined in simulation using the structure in Fig. 5.8. From the output response of the simulation, the quality factor is calculated by Eq. 5.10. The graph on how the external coefficient varies with distances  $a$  and  $b$  are also shown in Fig. 5.8. The optimum distances for  $L_1$ ,  $L_2$ ,  $a$ , and  $b$  are 2 mm, 1.2 mm, 0.3 mm, and 2 mm, respectively.

## 5.4. Results and Analysis of Balanced Filter

Figure 5.9 shows the results, from these, it can be realized that the common-mode signal is suppressed to the tune of at least  $-30$  dB throughout the range of interest. The simulated differential mode pass-band is centered at  $39$  GHz and has a fractional bandwidth of about 2 %. The filter was also simulated in half mode configuration to reduce the size, as shown in Fig. 5.10. The results are shown in Fig. 5.11. These results show that the filter can operate satisfactorily at  $39$  GHz since there is a high return loss and a low insertion loss, as shown in Fig. 5.11. The selectivity around this frequency range is also satisfactory. These results show that the structure can be halved without much performance degradation. This is useful in size reduction.

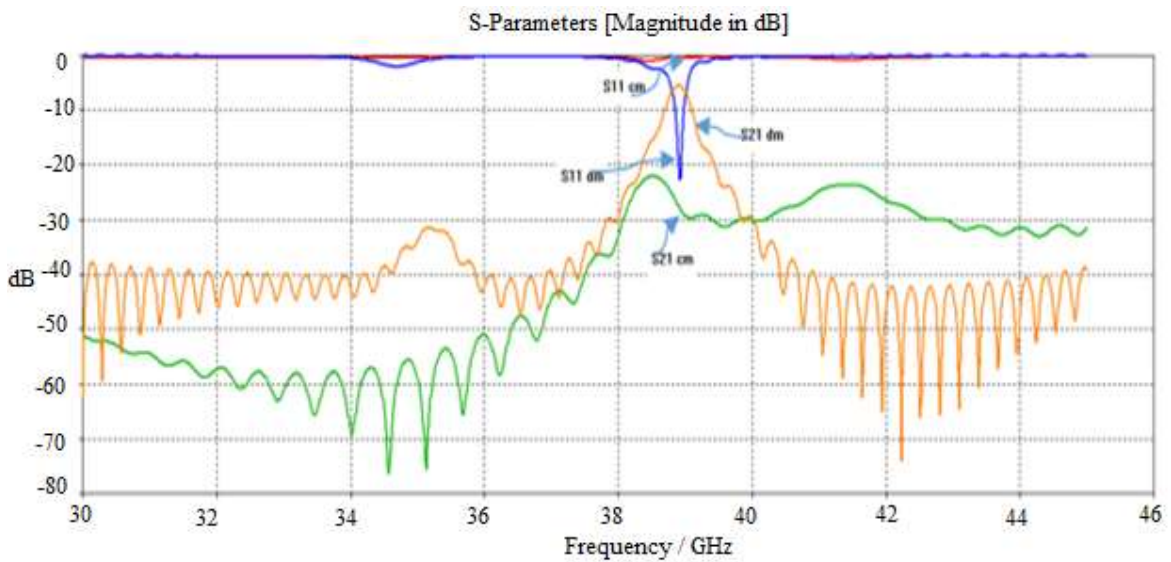


Figure 5.9 Output results.

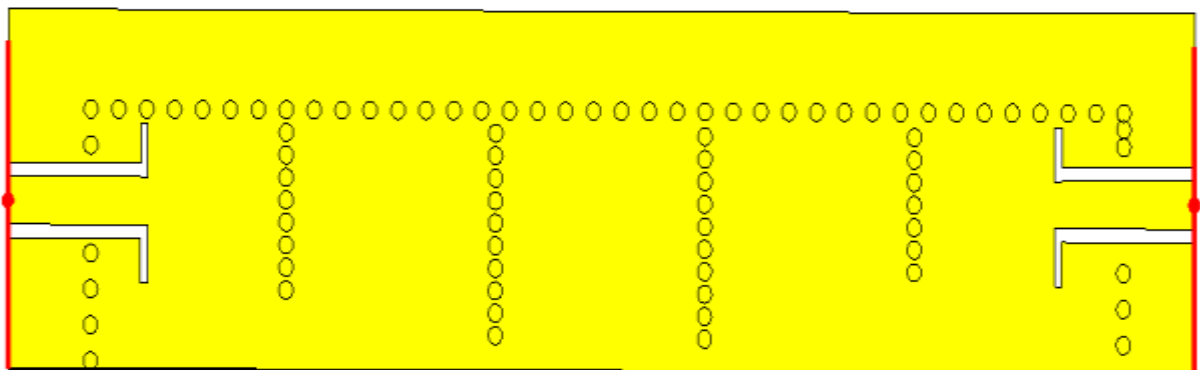


Figure 5.10 Half-mode configuration.

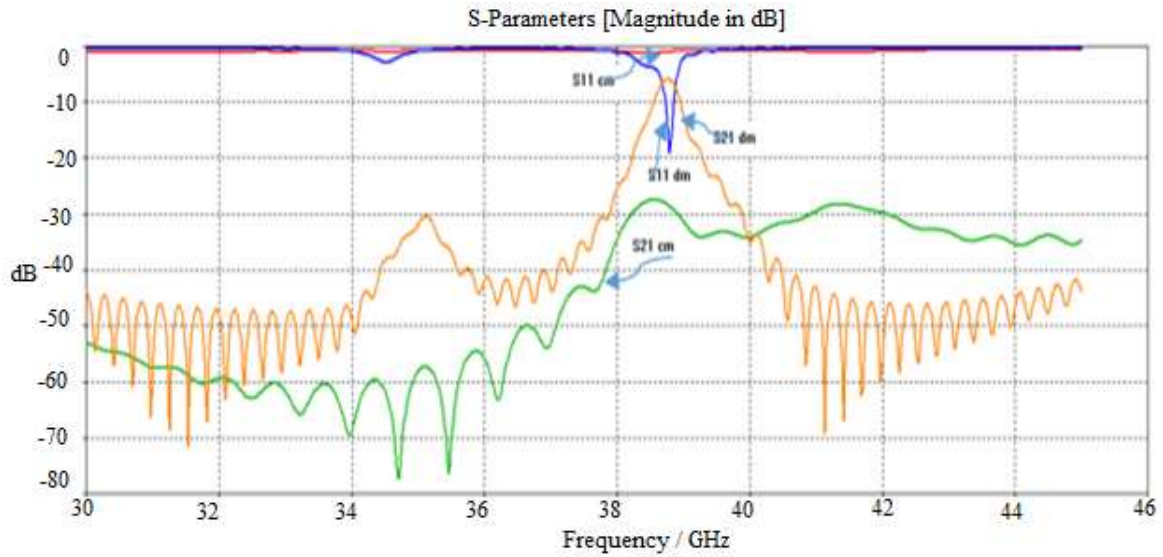


Figure 5.11 Half-mode configuration output results.

A comparison with other single-layered SIW filters is presented in Table 5.1. From this, it can be realized that the filter in this research work operates at a much higher frequency than all its other counterparts. This helps with larger bandwidths which helps to transmit more data in one instant. It also has the highest return loss to the other filters. The size is also small compared to most of the presented filters. This filter also operates at a higher mode than the rest of the filters, which aids in higher selectivity. The common mode signal is suppressed heavily in the differential mode transmission range, ensuring that it doesn't have spurious signals being transmitted.

Table 5.1 Comparison with similar work

Ref.	fo (GHz)	Filter order	IL (dB)	RL (dB)	Size ( $\lambda_g \times \lambda_g$ )
[98]	3.5	3 <sup>rd</sup>	0.9	20	1.2x0.83
[55]	3.09	3 <sup>rd</sup>	1.28	20	0.7x0.7
[181]	10	4 <sup>th</sup>	1.4	11	1.7x2.2
[94]	13.45	4 <sup>th</sup>	2.15	13	1.9x3.5
This work	39	5 <sup>th</sup>	4	28	1x2.4

## 5.5. Common Mode Suppression Techniques

In the design of balanced circuits, the CM signal has to be suppressed as much as possible in the region of interest, known as the differential-mode pass-band. The differential systems must have a high Common Mode Rejection Ratio (CMRR). In some cases, the CMRR in the region of interest is low and has to be improved. In practical applications, CM noise is unavoidable due to the timing skew between the differential lines [182]. Common mode noise suppression is achieved through symmetric resonant elements [80]. If a transmission line is loaded with a resonator coupled to it, a stop band, also known as a transmission zero, is generated at the fundamental frequency of the resonant element. Hence the signal is inhibited from propagating because the injected power is reflected. In this work, a dual-band balanced filter has been implemented using SIW technology. A multi-mode resonator and  $TE_{102}$  and  $TE_{201}$  modes have been used to develop the dual bands. A patterned ground structure is then used for CM signal suppression enhancement. The dumbbell-shaped defective ground structure and conductor patch with meandered lines have been used for the patterned ground.

## 5.6. Common Mode Suppression Filter Design Process

To design the dual Band-Pass Filter (BPF), a Low-Pass Filter (LPF) prototype was developed. The prototype specifications are: 0.01 dB ripple, second-order filter, center frequency  $10\text{ GHz}$ . The  $g$  parameters are as follows:  $g_0 = 1$ ,  $g_1 = 0.4489$ ,  $g_2 = 0.4078$ ,  $g_3 = 1.1008$  [24]. Filter design procedure outlined in ref. [5] has been followed to develop a lumped element LPF and then converted to a band-pass filter. To implement this filter, SIW resonators were used. Fig. 5.12(b) shows the 3D view of a SIW resonator. To develop the resonator size, the procedure in ref. [5] has been used, and for an operating frequency of  $10\text{ GHz}$ , the resonator's dimensions are  $l=27.386\text{ mm}$ ,  $w = 15\text{ mm}$ . The Rogers-3003 substrate has been used with  $\epsilon_r = 3$ , a height of 0.22 mm, a hole diameter of 0.2 mm, and a pitch of 0.4 mm. Figure 5.12 (a) shows the schematic topology of the proposed filter. Here  $R_1$  and  $R_2$  represent the resonators operating at  $TE_{102}$  and  $TE_{201}$  modes. The  $C_{1,2}$  represents the coupling between the resonators, and the quality factor is represented by  $Q_e$ , while Fig. 5.12 (b) shows the 3D view of the whole filter structure.

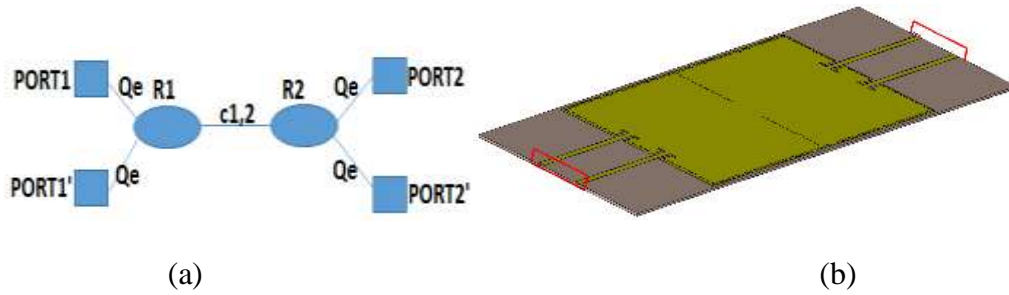
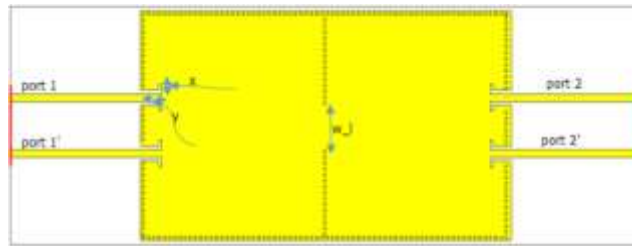
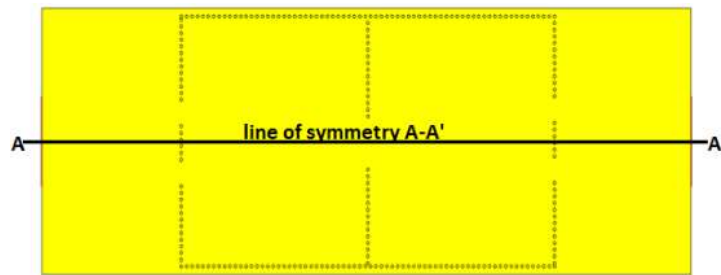


Figure 5.12 (a) Schematic filter topology, and (b) 3D view of the filter structure.



(a)



(b)

Figure 5.13 (a) Top view of the filter, and (b) Bottom view of the filter.

The top and bottom view of the filter are shown in Fig. 5.13. To determine the couplings, the standard method for filter design is followed [5]. From Eq. (5.11) and Eq. (5.12) and for fractional bandwidth (FBW) of 4%,  $c_{1,2} = 0.0935$  and  $Q_e = 11.22$ . Once these values are determined, the CST Microwave Studio suite is used to determine the physical dimensions of the magnetic coupling window length ( $w_l$ ). The procedure in ref. [5] is followed to determine  $c_{1,2}$  and  $Q_e$  through simulation. For  $c_{1,2}$  two split frequencies have been observed once the simulation is done and the coupling factor is calculated using Eq. 4.9 is discussed in chapter 4 [5].

The magnetic coupling window length is then varied until a value of  $c_{1,2} = 0.0935$  is achieved. From the simulation, window length  $w_l = 2.8$  mm gives the desired value for  $c_{1,2}$  according to Eq. (4.6). The  $Q_e$  is then determined by following the procedure in [5] through the use of Eq. (4.10):  $x$  and  $y$  are varied accordingly until a value of  $Q_e = 11.22$  is achieved

according to Eq. (4.7). The simulation values for  $x$  and  $y$  as shown in Fig. 5.13(a) are 0.2 mm and 2.4 mm, respectively. It can be observed from the designed filter that the dual band-pass balanced filter is operating at 8.4 GHz and 13.6 GHz. The CM signal is being suppressed to the tune of 80 dBs. The results of a dual-band filter with no suppression mechanism are shown in Fig. 5.14.

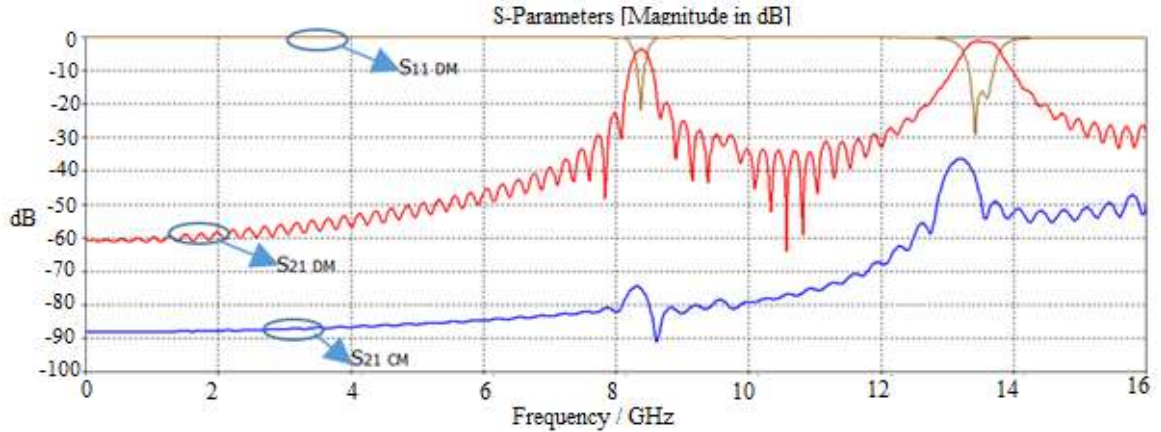


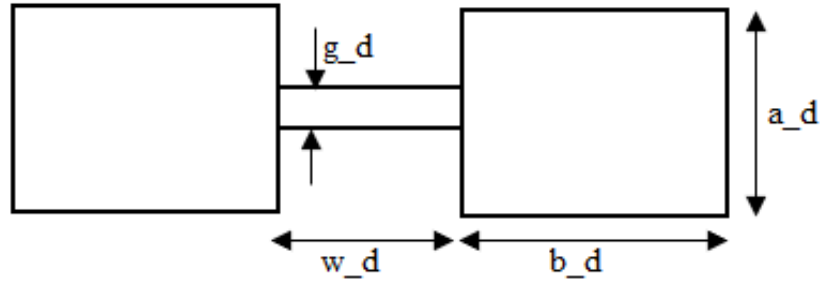
Figure 5.14 Output from the filter without any suppression mechanism.

## 5.7. Common-Mode (CM) Suppression Mechanism

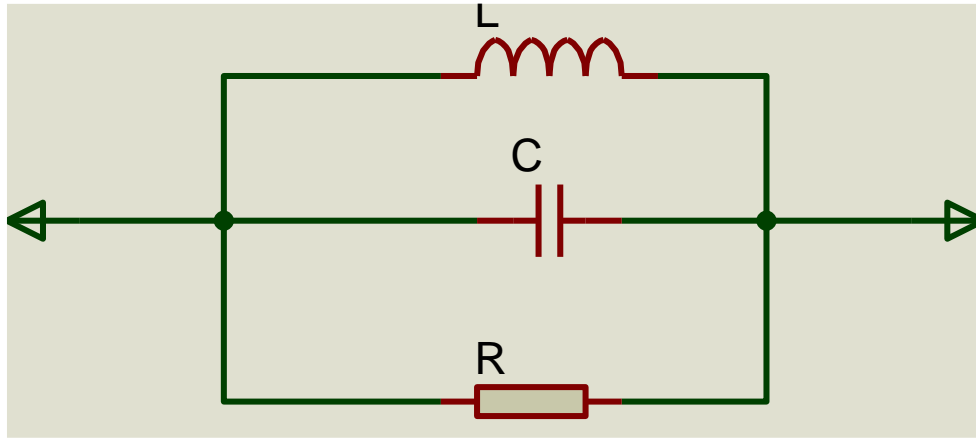
It is of paramount importance to suppress the common-mode signal in balanced circuits. To achieve this, two methods have been employed on the ground plane:

### 5.7.1 Dumbbell Structure

A resonator coupled to a transmission line exhibits a stop-band at its fundamental resonance frequency because the injected power is reflected to the source [80]. When the symmetry planes of the line and the resonant structure are of the same electromagnetic nature, i.e., both electric or magnetic walls simultaneously, the resonator is excited, and CM signal propagation is prohibited. This principle applies in this work, where the dumbbell is used as a resonator. The dumbbell-defected ground structure is shown in Fig. 5.15(a), where  $a$  and  $b$  are the length and width of the rectangular shape,  $g$  = gap,  $l$  = length between the squares. For simplicity of construction  $a_d = b_d$  has been assumed. The dumbbell can be modeled as a parallel resonator, shown in Fig. 5.15(b) [183, 184]. The capacitance is mainly dominated by  $g_d$  and  $w_d$ , while the inductance is dominated by  $a_d$  and  $w_d$ , which results from the electromagnetic field distribution in the defect, and  $R$  represents radiation and conductor losses that occur in the defect [183]. The actual values for  $L$ ,  $C$ , and  $R$  can be extracted using the parameter extraction method highlighted in ref. [185].



(a)



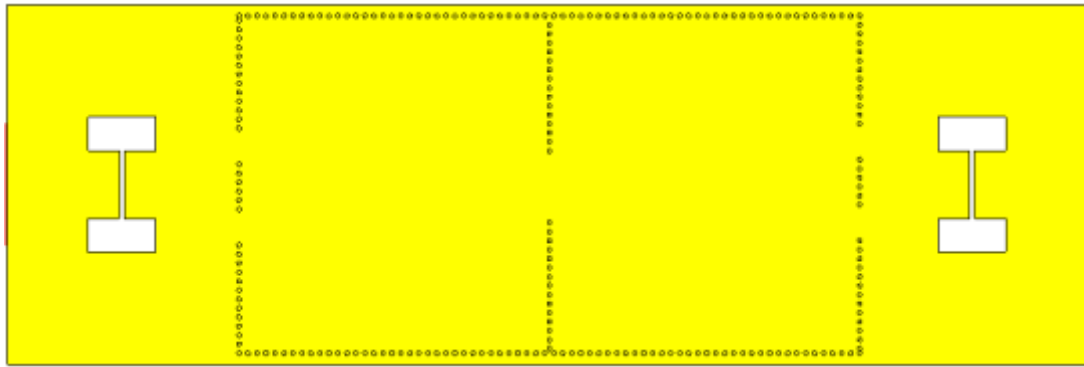
(b)

Figure 5.15 (a) Dumbbell unit cell geometry, and (b) Dumbbell unit cell equivalent circuit.

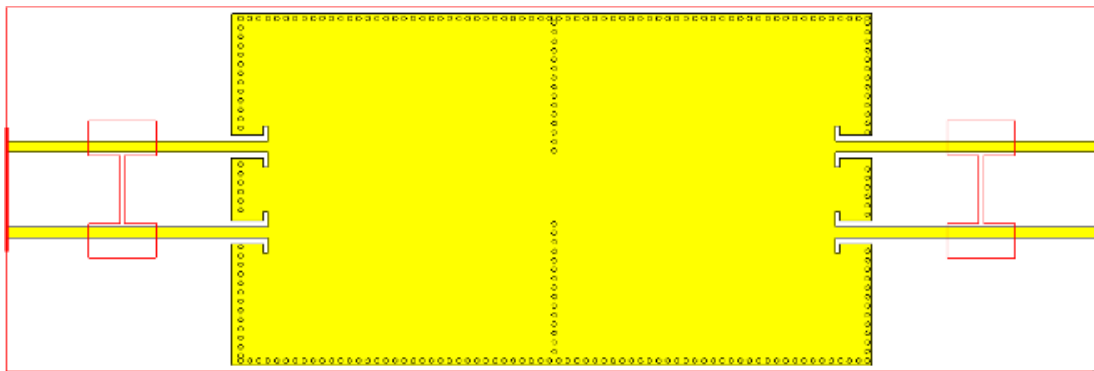
According to ref. [186], the dimensions of the dumbbell Defected Ground Structure (DGS) are determined by choosing the initial value of  $g_d$  from the range 0.2 to 0.5, then  $w_d$  is  $\sim 3g_d$  to  $4g_d$ , and the value of  $a_d$  is calculated as represented as:

$$a_d = 96.44^{0.923} f^{-2.923} \epsilon_r^{-0.9424} w_d^{-0.8896} g_d^{0.0013} h^{-0.4593} \quad (5.13)$$

where  $a_d$ ,  $w_d$ , and  $g_d$  are in mm,  $h$  is in mil and  $f$  is the desired frequency in GHz. The above values are achieved:  $a_d = 3$  mm,  $g_d = 0.2$  mm,  $w_d = 0.8$  mm. Having found the correct dimensions, the dumbbell-defected ground structure is then etched on the ground plane, as shown in Fig. 5.16. The positioning of the dumbbell is such that its symmetry lies on the same line as the symmetry of the whole filter, line A-A' as shown in Fig. 5.13 (b).



(a)

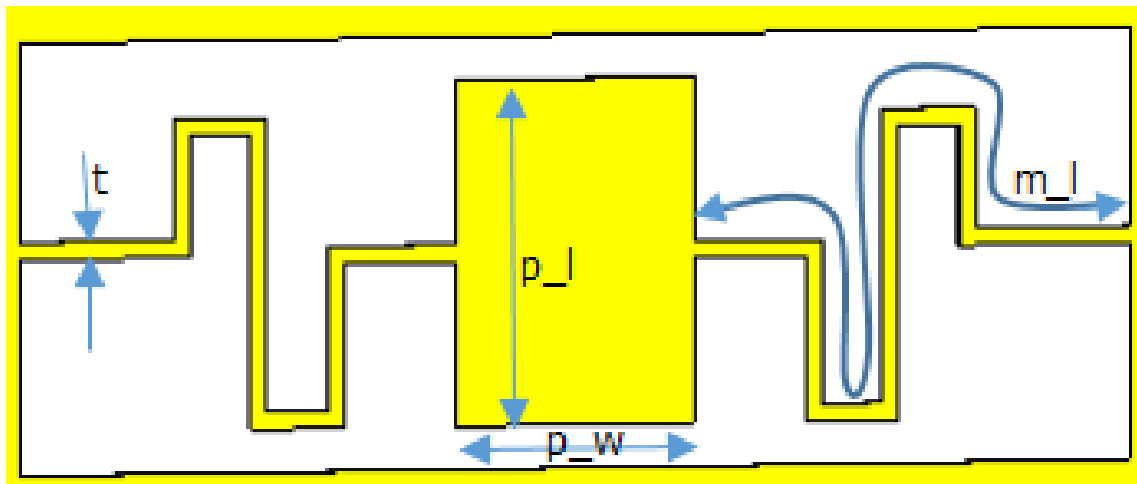


(b)

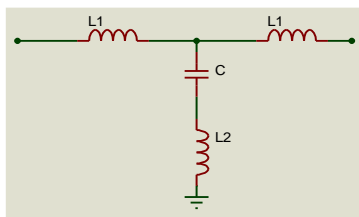
Figure 5.16 (a) Dumbbell DGS etched at the bottom surface of the filter, and (b) The top surface of the filter with a view of the DGS at the bottom.

### 5.7.2 Center conductor patch with meandered line

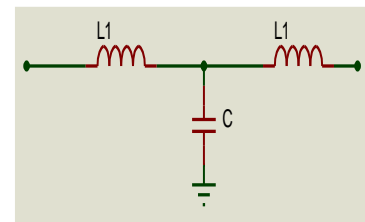
The pair of feed lines attached to the ports are loaded with a centered conductor patch on the ground plane. The patch is then connected to the ground by meandered lines of high impedance, which behave as inductors in a specific frequency range [80]. The structured shape is shown in Fig. 5.17 (a), where  $t$  is the meandered line thickness,  $p_l$  is the patch length,  $p_w$  is the patch width and  $m_l$  is the meandered line length. The transmission lines loaded with the DGS behave as low-pass filters. This implies that the CM signal will be inhibited above a certain frequency range [187]. The equivalent circuit can demonstrate this in Fig. 5.17 (b) and (c), where  $L_1$  is the inductance of the individual feed line.  $L_2$  is the inductance of the meandered strip line and  $C$  is the capacitance between the conductor patch and the individual feed lines. The structure and feed lines operate as low-pass filters for the CM signal. Hence the CM signal will be rejected above a certain frequency. For the DM signal, as shown in Fig. 5.17 (c), the filter operates as an all-pass structure and the DM signal can pass.



(a)



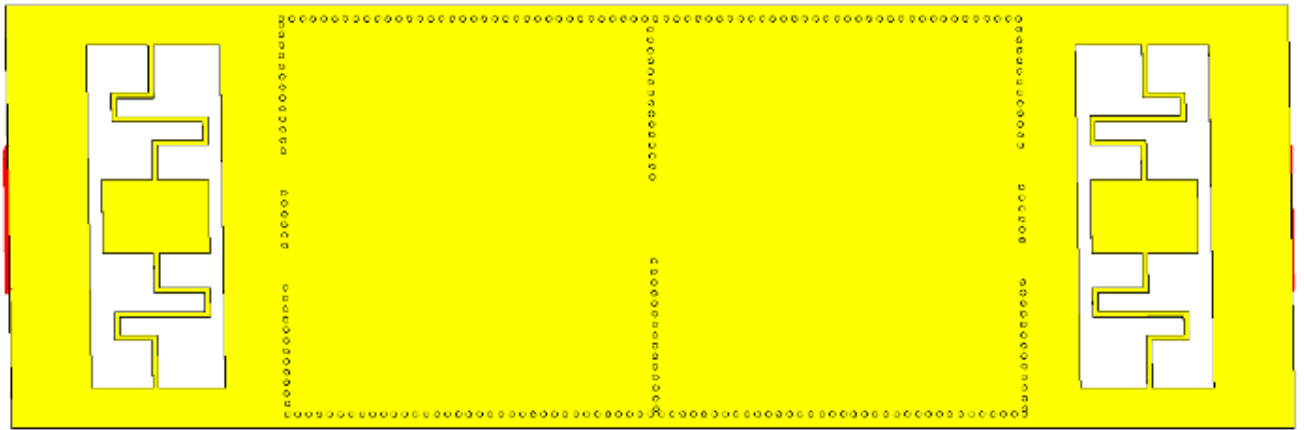
(b)



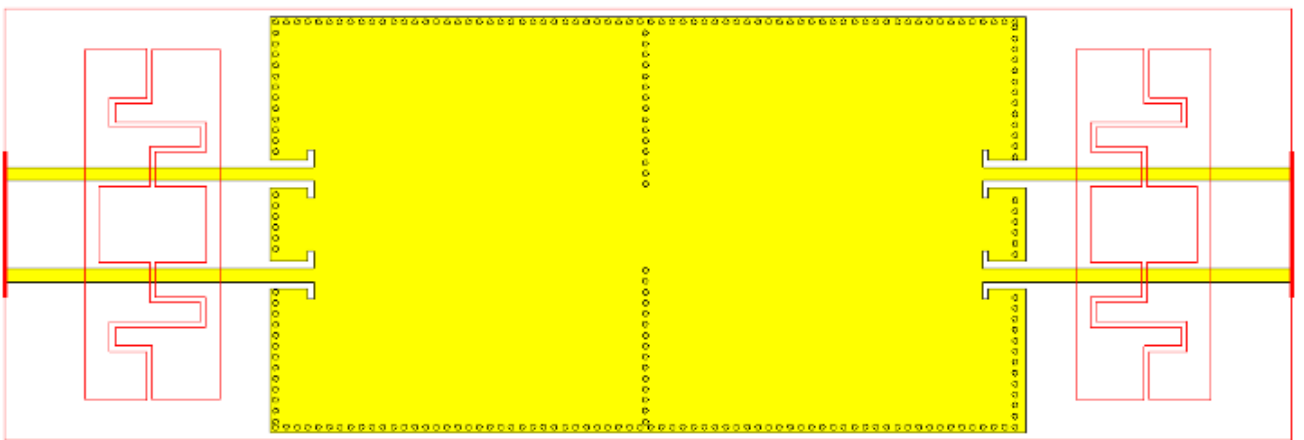
(c)

Figure 5.17 (a) Center patch with meandered loop, (b) Equivalent circuit for common-mode, and (c) Differential-mode.

The dimensions affecting the structure are  $t$ ,  $m_l$ ,  $p_l$ , and  $p_w$ . The procedure to determine the values is highlighted in [188]. The values were  $t = 0.2 \text{ mm}$ ,  $m_l = 10 \text{ mm}$ ,  $p_l = 3 \text{ mm}$ , and  $p_w = 2 \text{ mm}$ . When applied to the dual-band filter, the DGS is shown in Fig. 5.18. The DGS line of symmetry falls on the same line as the filter, A – A' indicated in Fig. 5.13 (b).



(a)

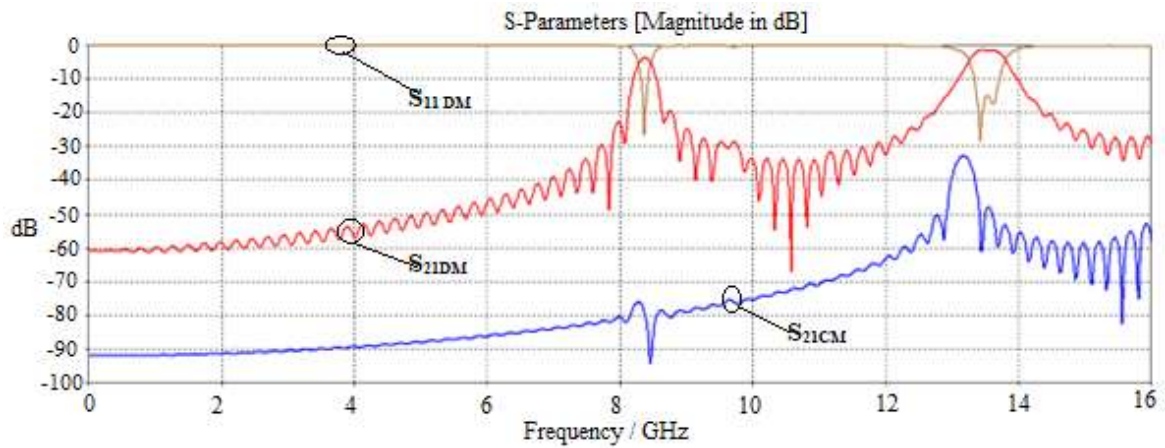


(b)

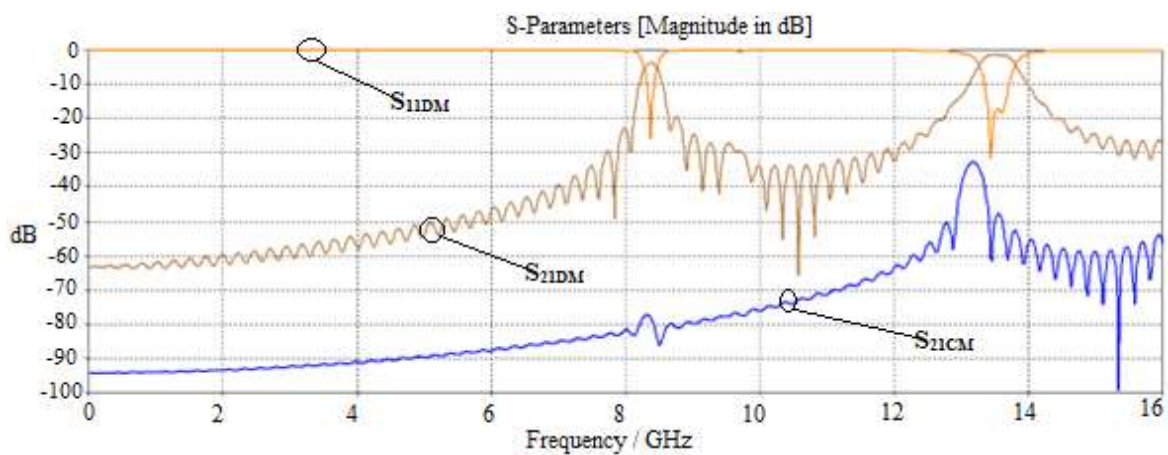
Figure 5.18 (a) The bottom surface of the filter with conductor patch and meandered loop, and (b) Top surface of the filter with a view of the DGS at the bottom.

## 5.8. Results and Analysis of Filter with Common Mode Suppression

As compared to the filter without any DGS, it can be observed that about 5 *dBs* have further suppressed the common-mode signal. At the same time, the differential signal is allowed passage without any degradation. This shows that the dumbbell structure can further enhance the CM signal suppression ratio. The output results of the filter with (a) dumbbell DGS, and (b) conductor patch with the meandered loop are shown in Fig. 5.19, wherein (a) the blue graph represents the CM signal, brown graph is the S11 and red being the S21 of the differential mode. In (b) the blue graph is the CM signal, orange represents S11 and brown represents S21 of the differential mode.



(a)



(b)

Figure 5.19 Output result of the filter with (a) dumbbell DGS, and (b) conductor patch with meandered loop.

This patterned ground structure significantly suppressed the CM signal compared to the filter without a DGS. From these results, it can be seen a further suppression of about 8 dB. The differential signal is not affected, it is allowed to pass without any degradation. The meandered ground pattern has a better suppression magnitude than the dumbbell structure.

Table 5.2 Comparison with similar work for SIW technology

Ref.	Frequency (GHz)	IL (DBS) 1 <sup>st</sup> and 2 <sup>nd</sup> band	S <sub>21CM</sub> (DBS) 1 <sup>st</sup> & 2 <sup>nd</sup> band	No. of resonators
[100]	10.25/14.60	~1/1.5	40/35	2
[87]	9.42/ 9.99	2.2/2.3	41/41	6
[101]	9.23/14.05	2.9/2.7	48/40	4
[28]	6.22/8.24	0.86/1.32	41/36	1
[102]	9.40/9.98	2.24/2.01	55/55	6
This work	8.4/13.6	2.8/1.6	90/40	2

Compared to similar work, as in Table 5.2, of almost the same frequency range, this research work has superior CM signal suppression, especially in the first band with a rejection of up to  $> 90$  dBs in the first band when either of the DGS is used. To increase the rejection ratio in the second band, more DGS unit cells can be employed. The proposed filter also uses two resonators which results in a compact size.

## 5.9. Chapter Summary

In this chapter, the theory behind balanced filters is presented, and the way noise is suppressed using as a way to maintain communication integrity in balanced circuits is explored. The differences between differential and common mode signals is explained. Topologies for differential and common mode transmission lines are presented. The propagating modes and how they get propagated on the transmission lines are explained. The basic principle of balanced filter design is also presented. A proposed balanced filter design utilizing SIW technology is presented in this chapter. The filter passed the differential signal at  $39$  GHz and had a common mode suppression of  $-30$ dB in the pass-band region. Two common mode suppression techniques are presented in this chapter. The first is through

the use of dumbbell defected ground structure and the second is through the use center conductor patch with meandered line. A balanced filter design was presented utilizing these two common mode suppression techniques.

## Chapter-6

# RECONFIGURABLE SIW FILTERS ANALYSIS

---

### 6.1. Introduction

Tunable filters are indispensable in reconfigurable applications in microwave and mm-wave communication systems. They are used to replace bulky filter banks. Most work done on tunable filters is on microstrip technology [75, 113, 189, 190]. However, microstrip filters have low power handling capability, lower quality (Q) factor, and the Q factor degrades when the microstrip filter is integrated with the tuning elements, which limits the practical applications that can be used with microstrip technology [191]. The availability of reconfigurable filters provides efficient means of managing hardware resources while achieving multi-standard requirements [4] and optimizing network capacity. Tunable filters reduce the cost of modifying existing hardware or reinstating the system if there are changes in bandwidth requirements or operating frequency.

Different technologies used for tuning are ferromagnetic materials, ferroelectric materials, semiconductors, and mechanical systems. Below is a comparison in Table 6.1, which shows differences between these technologies in terms of linearity, power consumption, size, and insertion loss.

Table 6.1 Comparison table of tuning technologies [4]

Parameter	Mechanical and piezoelectric	semiconductor	BST	Ferromagnetic	MEMS	PCM
Unloaded Q	High	Low	Medium	High	High	High
Tuning range	Medium	Low	Medium	Wide	Medium	Medium
Power handling	High	Low	Medium	Medium	High	Medium
Tuning speed	Slow	Fast	Fast	Fast	Moderate	Moderate
Size	Large	Small	Small	Very large	Small	Small
Linearity	Excellent	Poor	Good	Good	Excellent	Very good
Frequency range (GHz)	< 20	< 30	< 3	< 20	< 40	< 100

## 6.2. Ferromagnetic Materials

Materials such as Yttrium – iron- granite (YIG) crystal can be used for implementing tuning in microwave filters. The YIG is a ferromagnetic material whose resonant frequency can be changed by applying an external magnetic field. This material exhibits low losses, making it a good candidate for tuning applications [32]. The concept of operation of YIG was first explored in 1961 by *Philip S. Carter* [192]. The basic principle of operation is shown in Fig. 6.1. The axis of the two coils is at right angles. A small sample of YIG ferrite is placed at the filter's center. No power will be transferred between the coils when the ferrite sample is not magnetized because the loop axes are perpendicular.

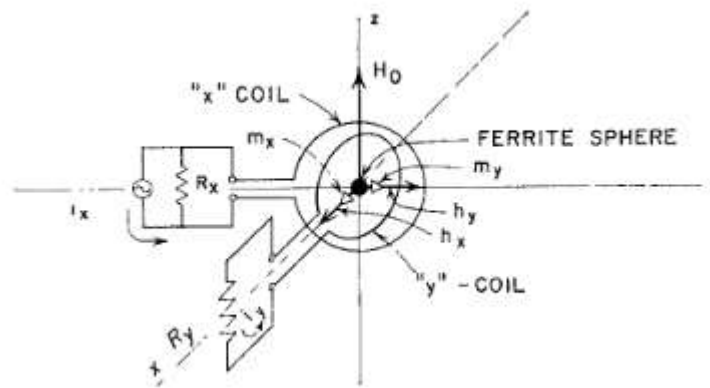


Fig 6.1 Operation principle of YIG [192]

When a magnetizing force is applied to the x-coil, the magnetic moments of electrons in the YIG ferrite precess around the x-axis and produce a moment along the y-axis, which then induces a voltage in the y-circuit [32]. Hence, the filter's resonant frequency can be altered by simply changing the external magnetic field applied to the YIG ferrite. The major drawback of the YIG filter is its large power consumption ranging from 0.75W to 3W [193] during the magnetic field generation. This limits the suitability of YIG filters in portable wireless devices where battery life is crucial.

## 6.3. Ferroelectric Materials

Materials such as Barium Strontium Titanate (BST) fall under the ferroelectric material category [193]. In these materials, spontaneous polarization is reversible in the presence of external electric fields. When the material is polarized by an external field, the induced polarization ( $P$ ) is directly proportional to the external electric field ( $E$ ). Above the Curie temperature  $T_c$ , a nonlinear polarization is present versus an external electric field;

this condition is known as the paraelectric state. Figure 6.2 shows the paraelectric and ferroelectric states [32]. When the temperature goes above  $T_c$ , the material loses its spontaneous polarization. It obtains paraelectric properties – where polarization can occur even when no permanent electric dipole exists in the material. The polarization becomes zero in the absence of an external force. The hysteresis loop, as shown in Fig. 6.2 arises because spontaneous polarization can be reversed by applying a strong external electric field- and it depends on the current electric field and history.

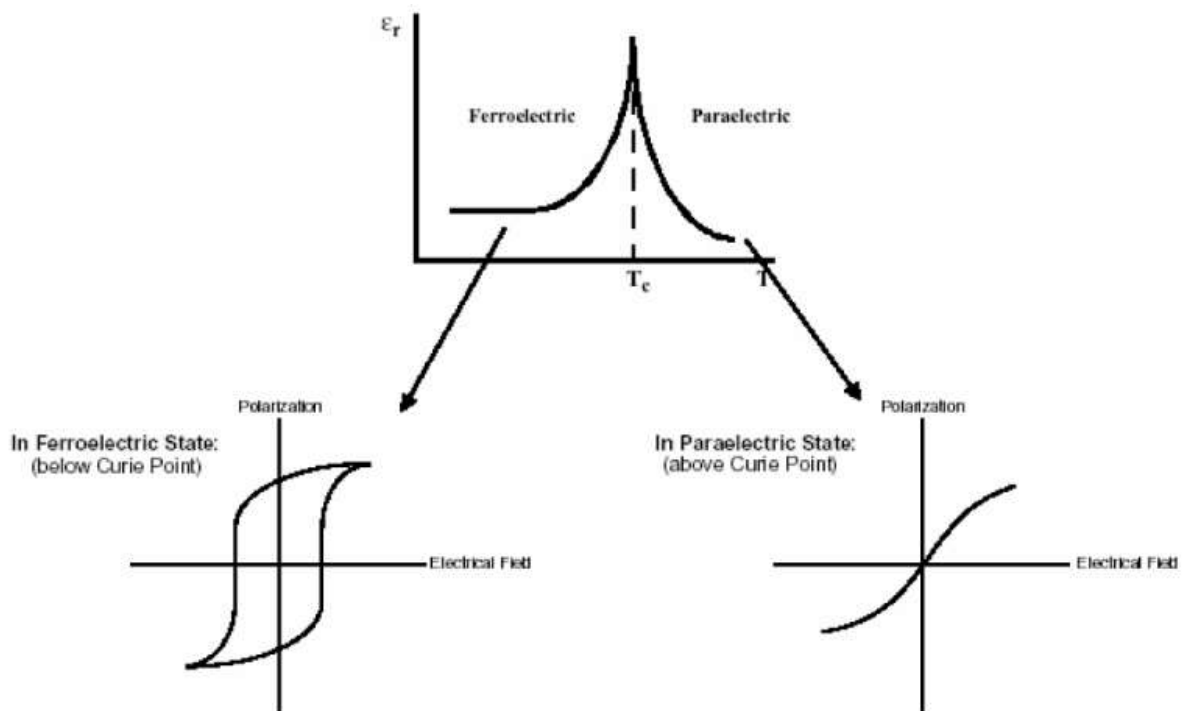


Figure 6.2 Illustration of the ferroelectric, paraelectric region, and hysteresis loop [32].

## 6.4. Semiconductors

Many tunable filters have been reported utilizing semiconductor pin and varactor diodes [30, 194, 195]. These are suitable where high-speed tuning is required [193]. Varactor diodes are p-n junction devices operated with a reverse bias voltage. When the reverse bias is varied, the junction's depletion region changes, which alters the diode capacitance. Figure 6.3 shows a varactor diode.



Figure 6.3 Varactor diode.

The relationship between capacitance and voltage is given as:

$$C = \frac{C_0}{\left(\frac{V}{V_{bi}} + 1\right)^n} \quad (6.1)$$

where  $C_0$  is the zero bias capacitance,  $V$  is the reverse bias voltage,  $V_{bi}$  is the built-in voltage potential and  $n$  represents the slope of  $\log C$  vs  $\log V$ . The disadvantage of semiconductor varactor tuning is low power handling, low-quality factor, and poor linearity.

## 6.5. Mechanical Systems

Microelectromechanical systems (MEMs) is a system that makes use of mechanical and electrical components at the same time. These devices can control, sense, and actuate on the micro-scale [4, 32, 193]. They can be found in medical, automobile, electronic, and defense appliances. MEMs components are illustrated in Fig. 6.4 [196].

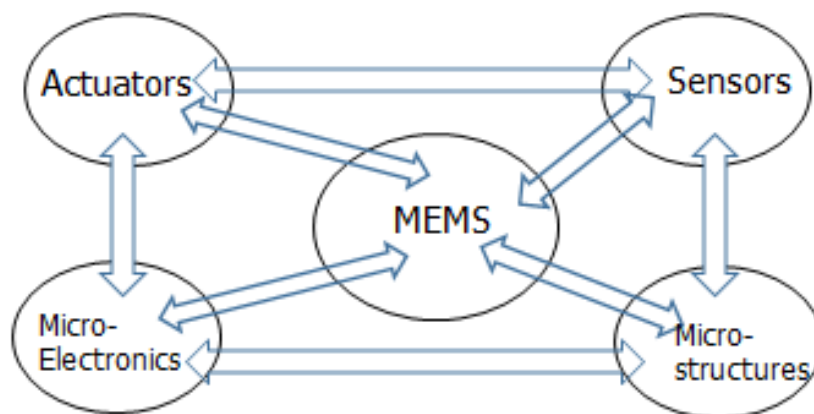


Figure 6.4 The MEMs components.

The MEMs comprise microsensors, actuators, and microelectronics integrated into one chip. MEMs utilize a d.c voltage to control the mechanical structure of the capacitor to

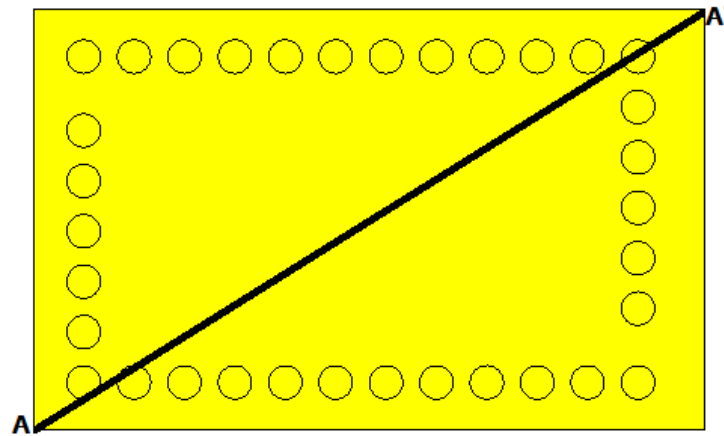
change, for example, the area under the plates or the distance between the plates. By changing these two parameters, the capacitance can be effectively changed and hence the center frequency of operation can also be changed.

## 6.6. Dielectric Rods Tunable Filter

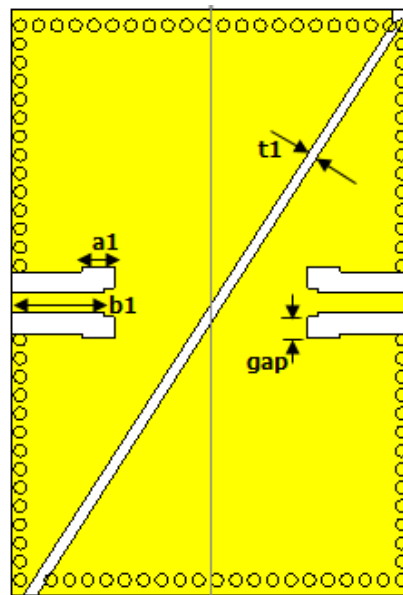
In this work, a second-order dual-band SIW has been designed (based on the triangular half-mode SIW resonator). Dielectric rods have been inserted in the main substrate to alter the structure's overall permittivity. The diameter of the rods is changed simultaneously, and the position of the rods, together with the permittivity of the rods is changed to change the operating frequency of the two pass-bands. Fig 1 shows a SIW structure together with the dimension parameters.

### 6.6.1 Dielectric rod tunable filter design

A dual-band filter operating at a center frequency of  $9\text{ GHz}$  and  $14\text{ GHz}$  first and second pass-band, respectively, has been designed. Dual mode resonators utilize  $TE_{101}$  and  $TE_{201}$  modes for the first and second pass-band. To determine the resonator's dimensions [1], the modified equations of the traditional waveguide can be used. In a dielectric rectangular waveguide, the resonant frequency of the  $TE_{mon}$  mode is given in chapter 4 in Eq. (4.19). Then the resonator length and width sizes can be given as shown in Eq.s (4.20) and (4.21). To get the equivalent length and width of the SIW resonator, Eq.s (4.22) and (4.23) are employed. In this work  $L = 12\text{ mm}$  and  $a_{siw} = 18\text{ mm}$ , via diameter =  $0.4\text{ mm}$ , pitch =  $0.6\text{ mm}$  and  $h = 0.2\text{ mm}$ . To reduce the size of the footprint of the SIW resonator, the structure can be bisected on the diagonal line of symmetry [162] as shown by line A-A' in Fig. 6.5(a). Boundary A-A' becomes an imaginary boundary and the operation of this half structure is still similar to that of the full structure [13].



(a)



(b)

Figure 6.5 (a) Line of symmetry to form HMSIW, and (b) Dual band filter.

A second-order dual-band filter can be constructed by combining two structures, as shown in Fig. 6.5 (b). The coupling between these two resonators can be determined by varying the distance  $t_1$  on Fig. 6.5 (b) [188]. And the quality factor can be determined by varying  $a_1$ ,  $b_1$ , and  $gap$ , as shown in Fig 6.5(b). For this work  $t_1 = 0.1 \text{ mm}$ ,  $a_1 = 0.7 \text{ mm}$ ,  $b_1 = 3 \text{ mm}$ ,  $gap = 0.7 \text{ mm}$ . The s-parameter result of the filter is shown in Fig. 6.6.

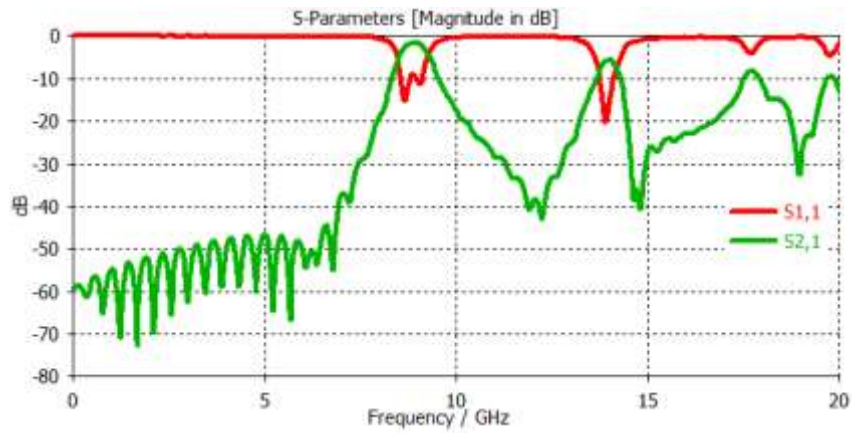


Figure 6.6 The  $S_{11}$  and  $S_{21}$  Parameter.

### 6.6.2 Reconfigurability of the filter

Figure 6.7 illustrates the dual-band filter loaded with dielectric rods. A dielectric rod with a different permittivity from the substrate and having a diameter  $rod\_diam$  is inserted into the main substrate to alter the permittivity of the original structure. Using transmission line theory, the SIW cavity can be taken as a transmission line operating at the corresponding frequency and assuming that the rod is placed at the center of the SIW cavity. The equivalent circuit of the structure is shown in Fig. 6.8.

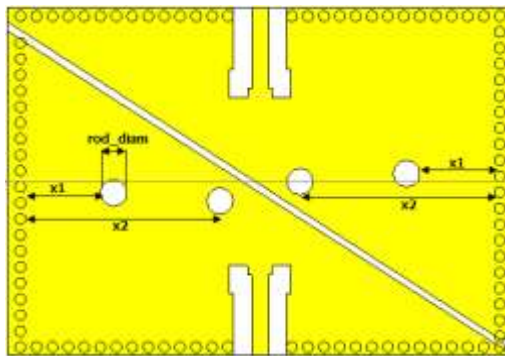


Figure 6.7 Dielectric rod-filled SIW filter.

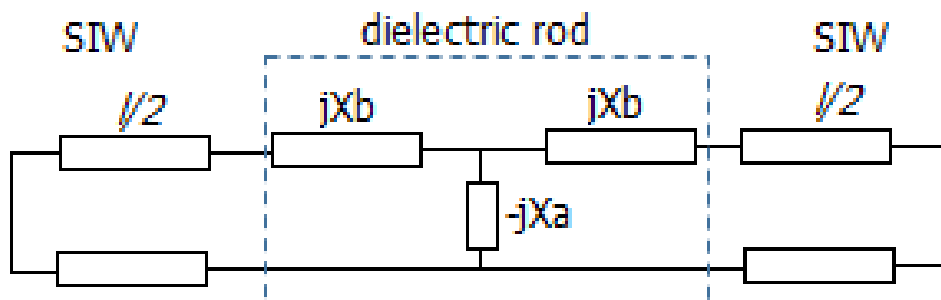


Figure 6.8 Equivalent circuit.

where  $X_a$  and  $X_b$  are the reactances associated with the dielectric rod. From [197, 198] the characteristic Eq. of the SIW resonator with rod is given as:

$$\frac{1}{2} \tan\left(\frac{\pi l}{v}(f^2 - fc^2)^2\right) - \frac{a}{2\lambda}\left(1 - \frac{\lambda}{2a}\right)^{\frac{1}{2}} \operatorname{cosec}^2\left(\frac{\pi x}{a}\right) \quad (6.2)$$

$$\left\{ \begin{aligned} & \frac{2\lambda^2}{(\varepsilon-1)\pi^2 d^2} - \frac{(\varepsilon-3)}{4(\varepsilon-1)} - \ln\left(\frac{4a}{\pi d} \sin\left(\frac{\pi x}{a}\right)\right) * \\ & + 2\sin^2\left(\frac{\pi x}{a}\right) - 2 \sum_{n=2}^{\infty} \sin^2\left(\frac{n\pi x}{a}\right) \left[ \frac{1}{\left(n^2 - \left(\frac{2a}{\lambda}\right)^2\right)^{\frac{1}{2}}} - \frac{1}{n} \right] \end{aligned} \right\} = 0 \quad (6.3)$$

where  $a$  is the width of the SIW resonator,  $x$  is the position,  $\varepsilon$  is the permittivity,  $l$  is the length of the transmission line,  $c$  is the speed of light,  $\lambda$  is the wavelength, and  $f$  is the frequency of operation. Eq. 6.3 can be solved for  $f$ , and by varying the diameter of the rod and its permittivity, the author can change the operating frequency. And in this work, these two parameters have been varied to change the frequency of operation.

## 6.7. Results and Analysis of Filter Tunability

From Eq. 6.3 it can be noticed that the frequency of the filter loaded with dielectric rods depends on the diameter of the rod,  $rod\_diam$ , change of permittivity of the dielectric rod, and change of the position of the electric rods as indicated by  $x1$  and  $x2$  in Fig. 6.7. In this work, the dielectric rod diameter was changed first, followed by the permittivity and then the positions were changed. Figure 6.9 shows the  $S_{11}$  parameter for different dielectric rod diameters.

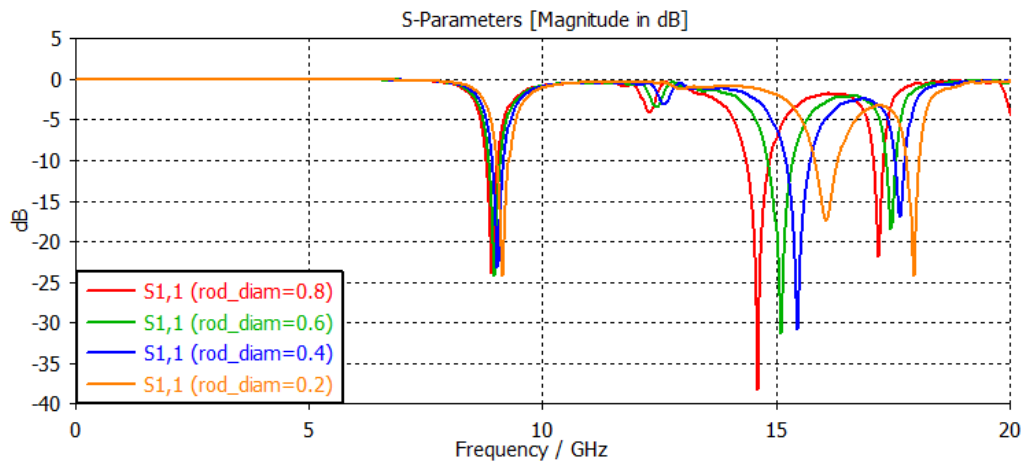


Figure 6.9 Variation of dielectric rod diameter.

In Fig. 6.9, there is a frequency shift as the diameter of the dielectric rod is changed from  $0.2\text{ mm}$  to  $0.8\text{ mm}$ . The first pass-band frequency changed from  $8.91\text{ GHz}$  to  $9.15\text{ GHz}$ , while the second pass-band changed from  $14.61\text{ GHz}$  to  $16.10\text{ GHz}$ . By varying the permittivity of the dielectric rod, the frequency can also be changed, as can be deduced from Eq.8. while the permittivity changes, the dielectric rod diameter,  $rod\_diam$ , is kept constant at  $0.8\text{ mm}$ . Figure 6.10 shows the S-parameters of the filter when the insert dielectric rod is Gallium Arsenide with a permittivity of  $12.94$ . The Center frequency of the first pass-band is  $8.9\text{ GHz}$  and the second pass-band center frequency is  $14.61\text{ GHz}$ .

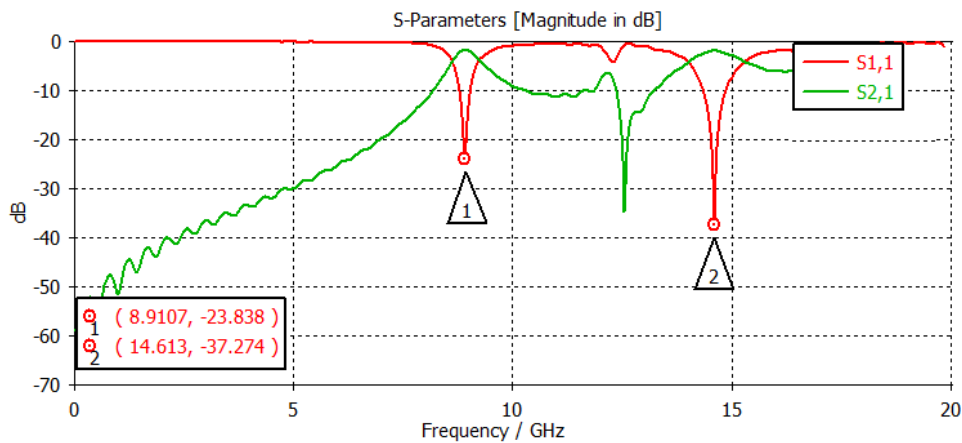


Figure 6.10 S-parameter results for  $\epsilon=12.94$

When the dielectric is perturbed by a dielectric rod with permittivity  $11.2$ , Rogers-3010 substrate, the center frequency for the first pass-band shift to  $9\text{ GHz}$  while that of the second pass-band becomes  $14.65\text{ GHz}$ , as shown in Fig. 6.11.

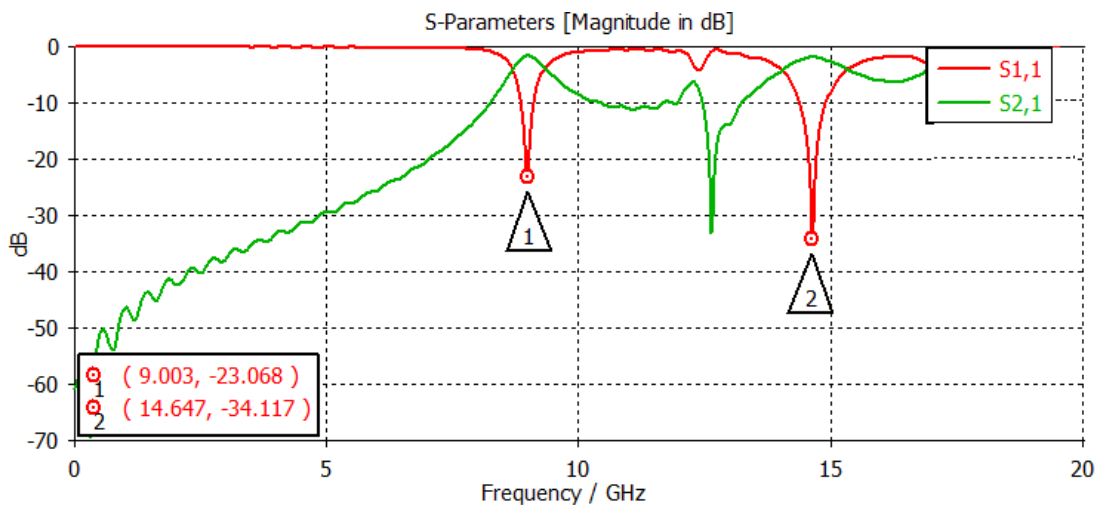


Figure 6.11 S-parameter results for  $\epsilon=11.2$

When the dielectric rod material is changed to Rogers RT6006 with a permittivity of 6.45, the first pass-band center frequency changes to 9.2 GHz, while the center frequency of the second pass-band changes to 14.7 GHz, the results are shown in Fig. 6.12.

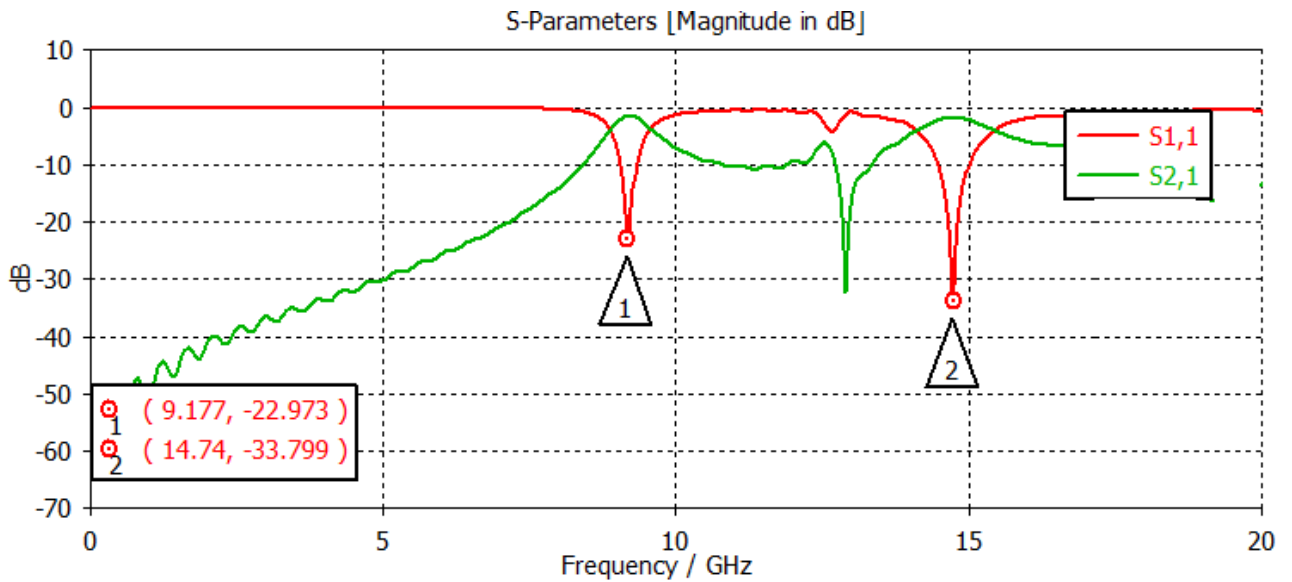


Figure 6.12 S-parameter results for  $\epsilon=6.45$ .

This shows that the center frequency of both pass-bands can be reconfigured by changing the perturbing material used by the dielectric rod.

## 6.8. Chapter Summary

In this work, a miniaturized dual-band filter was designed and implemented. For miniaturization, triangular HMSIW resonators were used to build a second-order filter with Roger-5880 substrate with a permittivity of 2.2. The operation frequency of the first and second pass-band is 9 GHz and 14 GHz, respectively. Dielectric rods were used to perturb the structure for reconfiguring the center frequency of operation. Firstly, the diameter of the perturbing dielectric rods varied from 0.2 mm to 0.8 mm, and the center frequency for the first pass-band changed from 8.1 GHz to 9.15 GHz, while the center frequency of the second pass-band changed from 14.61 GHz to 16.10 GHz. The second change was made on the permittivity of the dielectric rod, Gallium Arsenide with a permittivity of 12.94, followed by Rogers-3010 substrate with a permittivity of 11.2, and Rogers RT6006 with a

permittivity of 6.45 was used. With the electric rods' permittivity change, the center frequency for the first and second pass-band changed from 8.1 GHz to 9.1 GHz and 14.61 GHz to 14.74 GHz, respectively. For future work, the authors will build the physical structure and expand the filter to become a multi-band-pass filter.

## Chapter-7

# TERA HERTZ FREQUENCY BAND TUNING USING GRAPHENE

---

### 7.1. Graphene Material

Graphene is a material that has excellent electrical, optical, and chemical properties [199, 200]. This makes such material find many uses in various applications, including tunable filters. With the advent of new technologies and many applications having to be added to the communication system, devices must operate at high frequencies in the terahertz (THz) region to increase bandwidth. Conducting surfaces mainly used at microwave and RF frequency ranges have diminishing conductivity at the THz frequency region; hence other materials, such as graphene, are being explored as a substitute [38, 125]. From chapter 6, Table 6.1 shows that most technologies used for frequency tuning are only suitable for frequencies less than  $100\text{ GHz}$ . And as such suitable tuning, mechanisms need to be explored. Graphene was exfoliated for the first time from graphite by Andre Geim and Konstantin Novoselov in 2004 [199]. Graphene is a two-dimensional (2D) material with semi-metallic properties [201]. It is a single layer of graphite crystal with a single atomic layer of covalently bonded hexagonal carbon atoms. Fig. 7.1 shows the lattice structure of graphene.

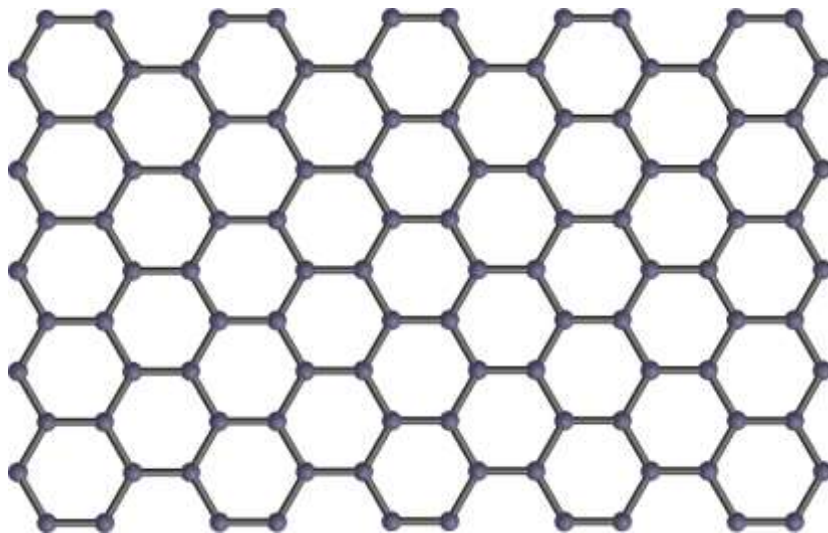


Figure 7.1 The lattice structure of Graphene [202].

Due to its ability to support surface plasmon polaritons (SPPs), graphene is tremendously good in electrical tunability and has low ohmic losses [200]. This is made possible through the change in the chemical potential of graphene, which can be achieved by doping or simply applying an external DC voltage. Various components have been developed using these electrical properties together with the optical properties of graphene, including phase shifters, antennas, modulators, etc. [37, 127, 201, 203–205].

## 7.2. Graphene Conductivity

The tunability of graphene occurs due to the configurability of the surface charge conductivity defined by Kubo's model [38, 206]. Surface conductivity,  $\sigma_g$  is a function of chemical potential,  $\mu_c$ , which is a function of the applied external electrostatic field,  $E_0$ . Surface conductivity is due to the contribution of inter and intraband transitions through which the real part of the interband conductivity is negligible in the THz region of operation. This leaves only the intraband being the contributor to surface conductivity. The intraband conductivity can be represented by [38]:

$$\sigma_{g1} = -j \frac{e^2 k_b T}{\pi \hbar^2 (w - j2T)} \left( \frac{\mu_c}{k_b T} + 2 \ln \left( e^{-\frac{\mu_c}{k_b T}} + 1 \right) \right) \quad (7.1)$$

where  $w$  is the angular frequency,  $\mu_c$  is the chemical potential,  $T$  is temperature,  $e$  is the electron charge,  $\hbar$  is the reduced Planck's constant and  $k_b$  is Boltzmann's constant. The interband conductivity can be investigated by:

$$\sigma_{g2} = \frac{-je^2}{4\pi\hbar} \ln \left( \frac{2|\mu_c| - (w - j\Gamma)\hbar}{2|\mu_c| + (w - j\Gamma)\hbar} \right) \quad (7.2)$$

where  $\Gamma$  is the scattering rate, at lower frequencies  $0.5 \text{ THz}$  to  $5 \text{ THz}$  the interband conductivity of graphene remains negligible and the surface conductivity is only due to intraband transitions. However, the  $\sigma_{g2}$  term at higher frequencies becomes complex with a negative imaginary part. Graphene material can be characterized by the displacement vector

$D_n = \varepsilon_b E_0 = e n_s / 2$ , where  $n_s$  is the two-sided surface charge density of graphene, and  $\varepsilon_b$  is the dielectric permittivity:

$$n_s = \frac{2}{\pi \hbar^2 v_f^2} \int_0^\infty E (f_d(E) - f_d(E + 2\mu_c)) dE \quad (7.3)$$

Where  $f_d(E)$  is the fermi – Dirac function as a function of energy,  $v_f$  is the fermi – velocity ( $\sim 10^8$  cm/s) and

$$f_d(E) = \left( e^{\frac{E - \mu_c}{k_b T}} + 1 \right)^{-1} \quad (7.4)$$

The relationship between the surface conductivity and chemical potential is given below in Fig. 7.2.

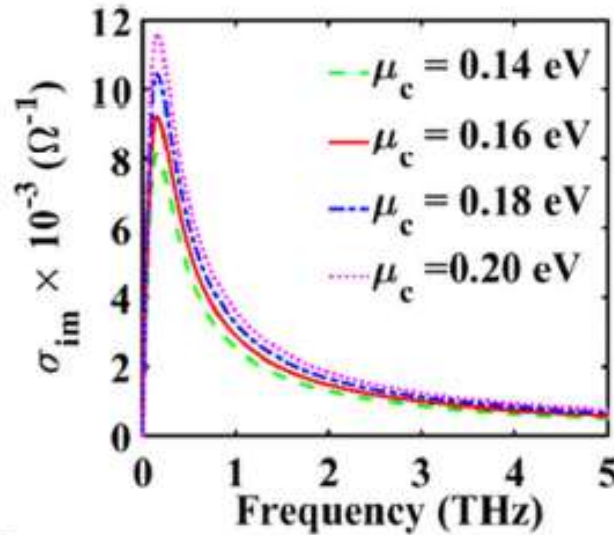


Figure 7.2 Relationship between chemical potential and center frequency [38].

The filter tuning can be achieved by changing the voltage across the graphene sheet. This gives us an easier alternative method for changing the filter's center frequency than changing the filter's entire geometry. The geometry of the filter can be changed in case there is a need to operate in a dual-band mode. The relationship between surface conductivity and chemical potential is given as [207]:

$$\mu_c = \hbar v_f \sqrt{\frac{\pi \varepsilon_r \varepsilon_0 V b}{e t}} \quad (7.5)$$

where  $V_b$  is the bias voltage and  $t$  the substrate thickness, the relationship in Eq. (7.5) shows that as the external bias voltage is changed, the chemical potential is also changed; hence it can control the chemical potential of graphene using an external bias voltage which in turn can be used to vary the center frequency.

### 7.3. Graphene Tunable Filter Design

Figure 7.3 shows the 3D image of the designed second-order SIW filter. The dimensions of the filter are arrived at by following the procedure in [13], [78] where it can be seen that the width of the structure is proportional to the center frequency, hence by changing  $W$ , the width of the resonator, the operational center frequency of the filter can be changed. The magnetic iris of length indicated as  $d_1$ , according to the procedure in [13], provides the coupling between the two resonators. The external quality factor can be determined by a varying distance  $a_1$  and  $gap$ , as shown in Fig. 7.3.

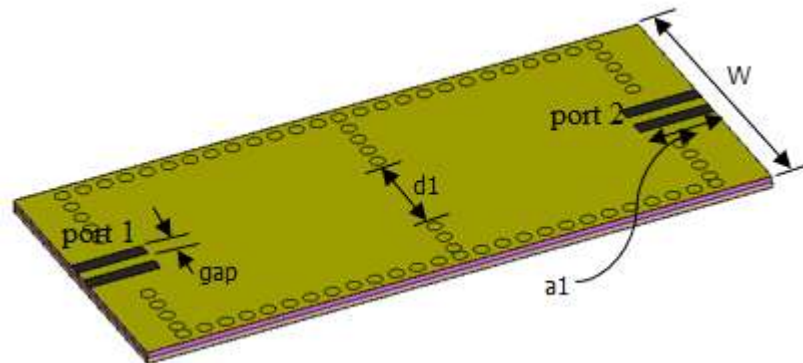


Figure 7.3 Second-order SIW filter 3D image.

A band-pass filter is designed for operation at a resonant frequency of  $1.2 THz$ . Fig. 7.4 is the cross-sectional side view of the proposed filter. The top and ground plane are made up of gold of thickness  $0.17 \mu m$ . A double layer of silicon (Si) and silicon dioxide (SiO<sub>2</sub>) permittivity of 11.9 and 3.9, respectively, is used. Graphene of thickness  $0.0034 \mu m$  is placed between the SiO<sub>2</sub> substrate and the top gold plate. The applied external DC bias voltage is indicated as  $V_b$ . Table 7.1 shows the dimensions of the parameters indicated in the cross-sectional diagram of Fig. 7.4.

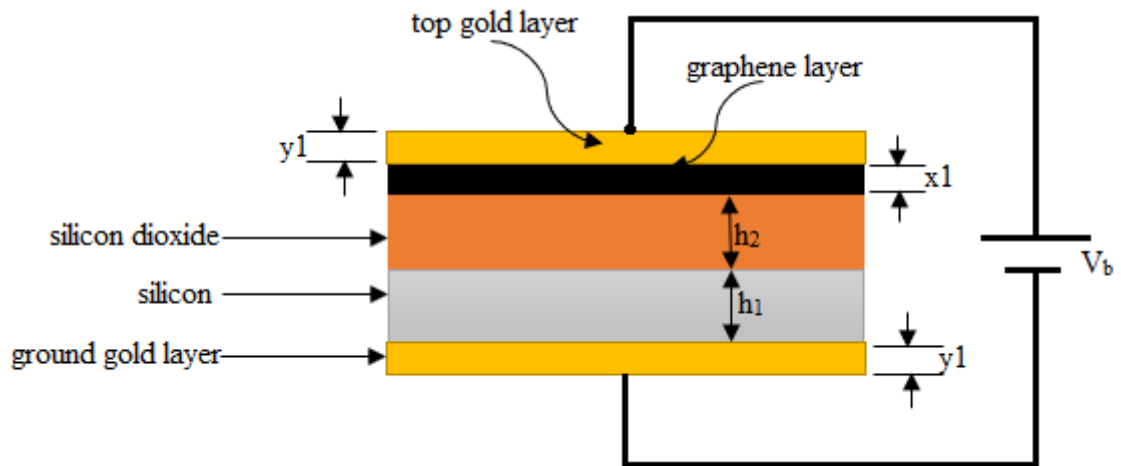


Figure 7.4 Cross-sectional side view of second-order SIW filter.

Table 7.1 SIW filter parameters

Parameter	Dimension ( $\mu\text{m}$ )
h1	4
h2	4
x1	0.0034
y1	0.17
W	210
a1	50
d1	60
gap	10

## 7.4. Results

The CST Microwave Studio was used to simulate the structure in Fig. 7.3. The structure was simulated at first with no graphene and the results are as shown in Fig. 7.5. The group delay is shown in Fig. 7.6. The surface current of the filter is shown in Fig. 7.7, while Fig. 7.8 shows the impedance plot of the filter which confirms resonance of the two frequencies.

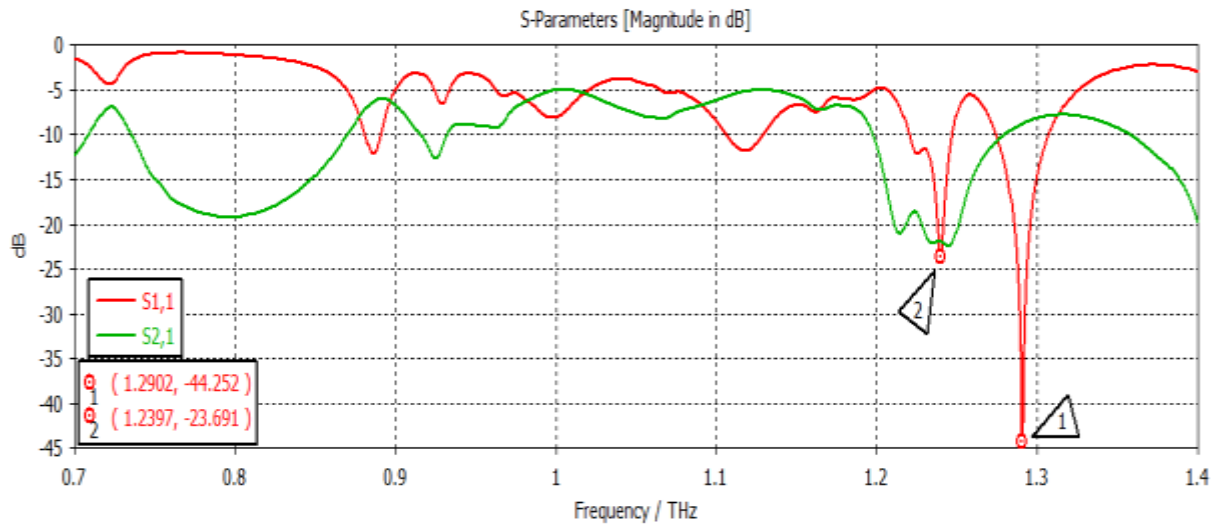


Figure 7.5 The S-parameter results.

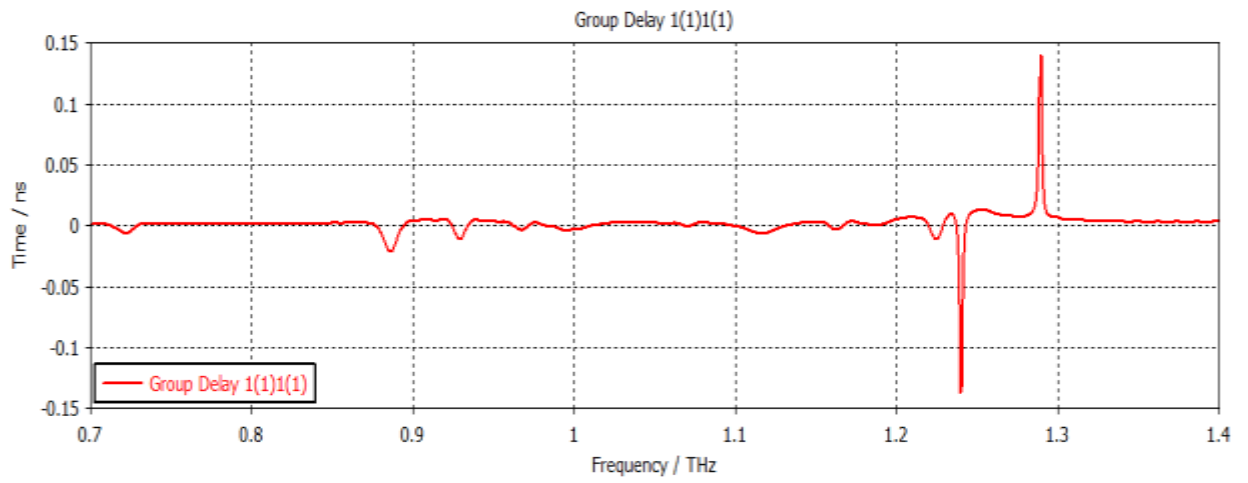


Figure 7.6 Group delay.

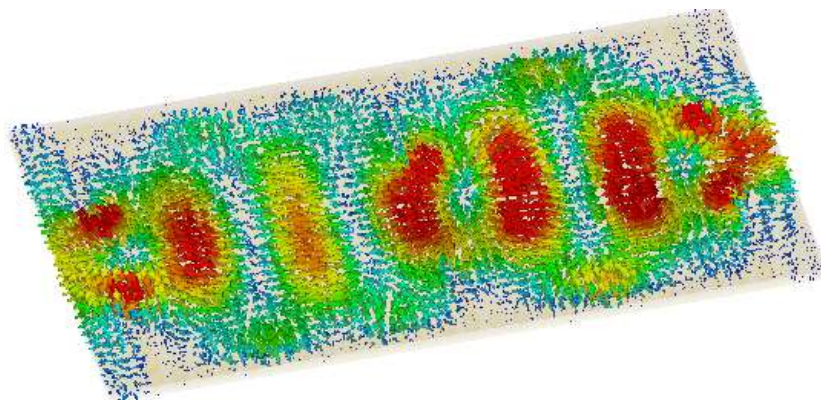


Figure 7.6 Current distribution.

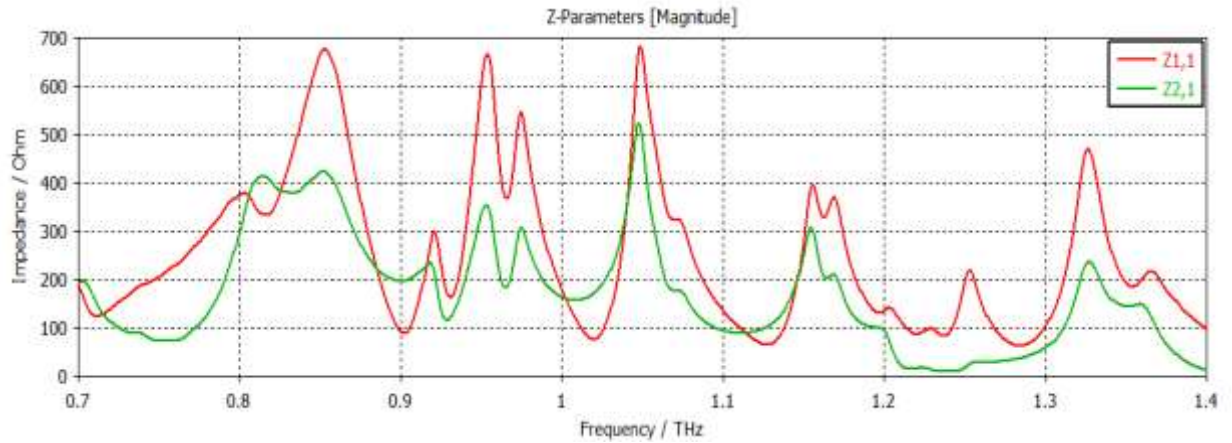


Figure 7.8 Impedance plot.

In this work, external voltage bias  $V_b$ , was used to change the chemical potential of graphene as shown in Fig. 7.4. The chemical potential values started from 0.04 eV to 0.4eV. The other parameters of graphene are as shown in Table 7.2. The change of the chemical potential was used to change the filter's center frequency; the results are presented in the following sub-sections.

Table 7.2 Graphene parameters

Parameter	Value
Temperature	293 K
Relaxation time	0.1 ps
Thickness	0.00034 $\mu\text{m}$

When the chemical potential is 0.1 eV, it was found that the SIW filter was resonating at first and second frequencies of  $1.2894 \text{ THz}$  and  $1.2398 \text{ THz}$ , respectively, with a return loss of -36.441 dB and -28.502 dB respectively, as shown in Fig. 7.9. When the chemical potential was changed to 0.2 eV as shown in Fig. 7.10, the first and second frequencies were at  $1.2967 \text{ THz}$  and  $1.2439 \text{ THz}$  respectively with a return loss of -13.323 dB and -19.508 dB respectively. In Fig. 7.11, the chemical potential was changed to 0.4eV and the results show that the first and second frequencies were at  $1.2894 \text{ THz}$  and  $1.2397 \text{ THz}$ , respectively, while the return loss was -39.787 dB and -26.247 dB, respectively. Lastly, the chemical potential was set at 0.6eV as shown in Fig. 7.12. For this instance, the first and second frequencies were observed at  $1.296 \text{ THz}$  and  $1.244 \text{ THz}$ , with a return loss of -13.288 dB and -18.983 dB, respectively.

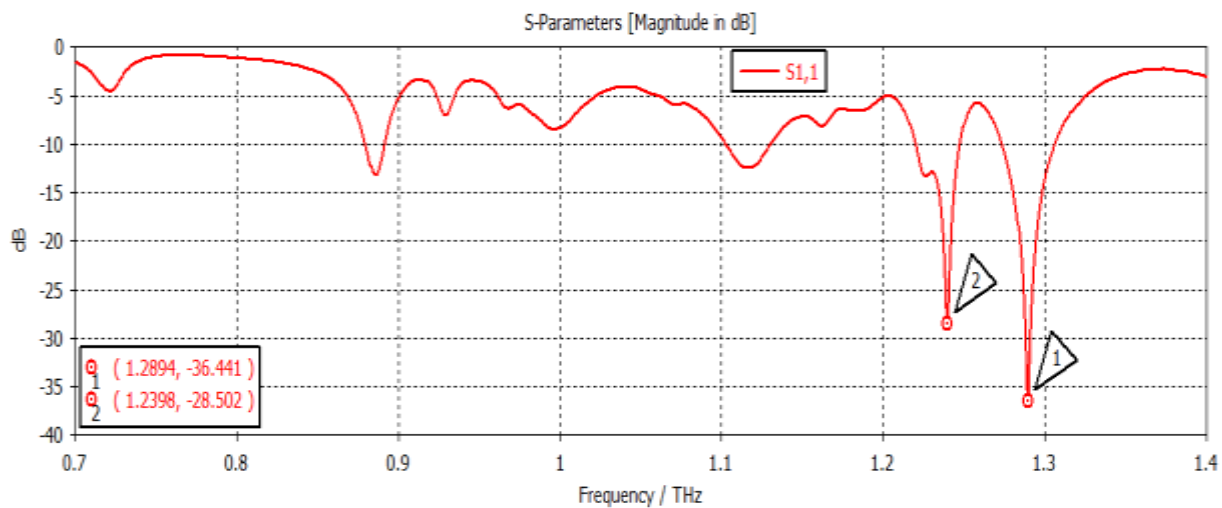


Figure 7.9 Chemical potential = 0.1 eV.

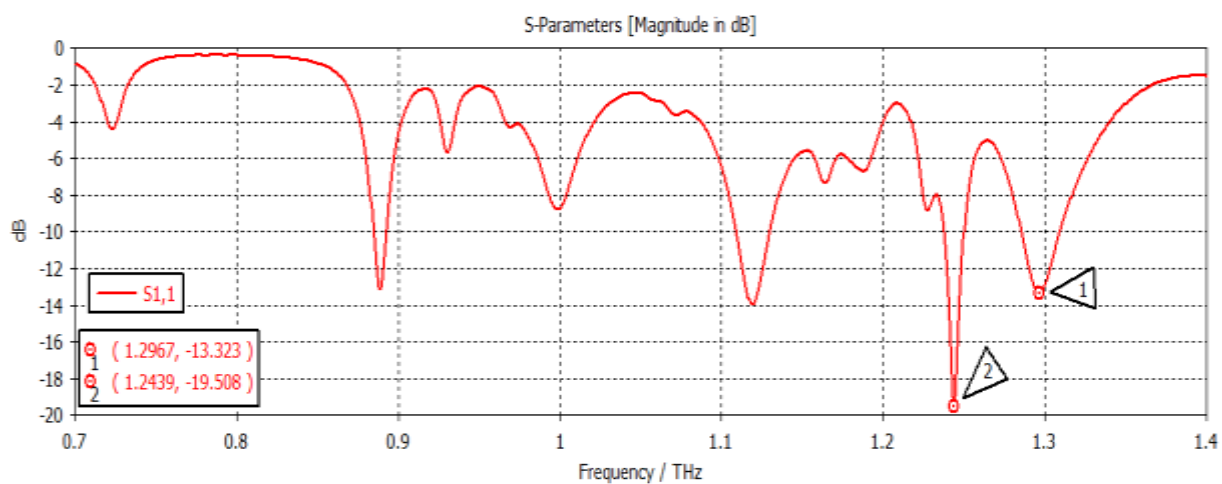


Figure 7.10 Chemical potential=0.2 eV.

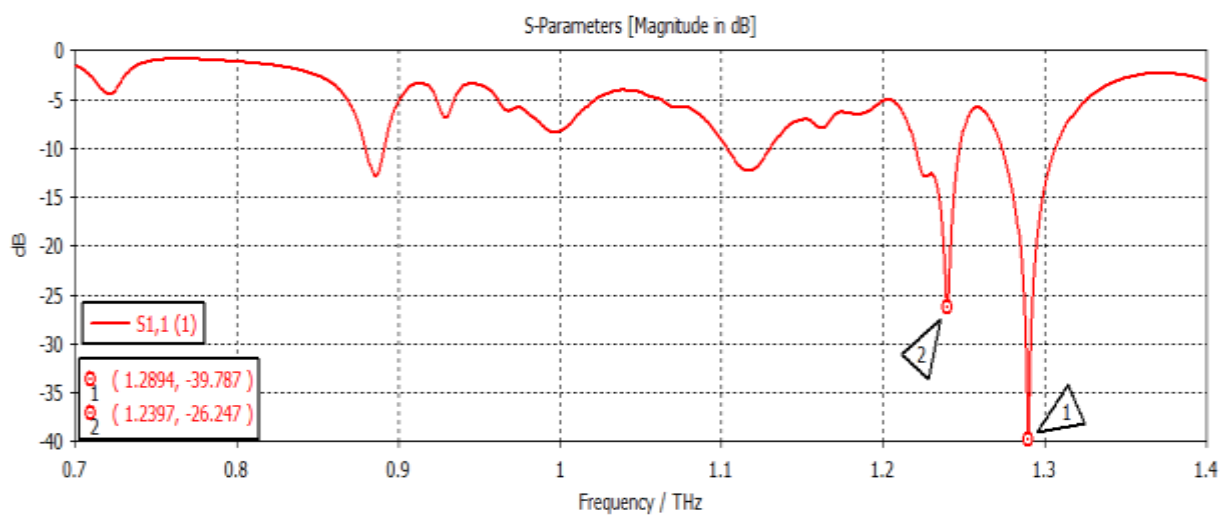


Figure 7.11 Chemical potential = 0.4 eV.

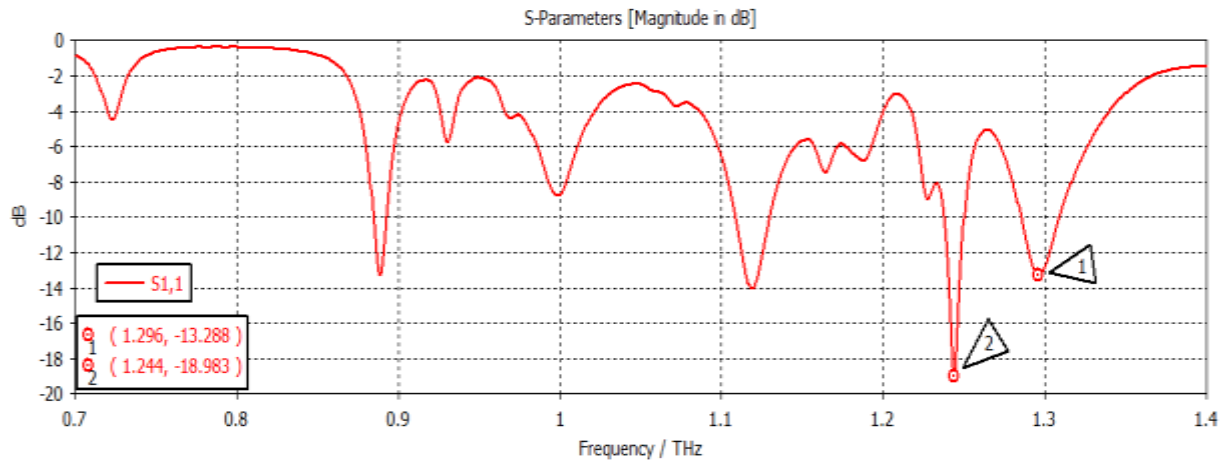


Figure 7.12 Chemical potential = 0.6 eV.

As shown in Eq. (7.5), the chemical potential of graphene is proportional to the applied bias  $V_b$ ; hence the external voltage is varied to get different chemical potential values and, in turn, the center frequency is changed.

### 7.5. Effect of Graphene Aspect Ratio on the Center Frequency

The length and width of graphene as shown in Fig. 7.13, are changed simultaneously and the effect on the center frequency is presented here. The top layer of copper as shown in Fig. 7.3 is removed to expose the graphene sheet, as shown in Fig. 7.13 as the grey patch with dimensions  $w_1$  and  $z_1$ .

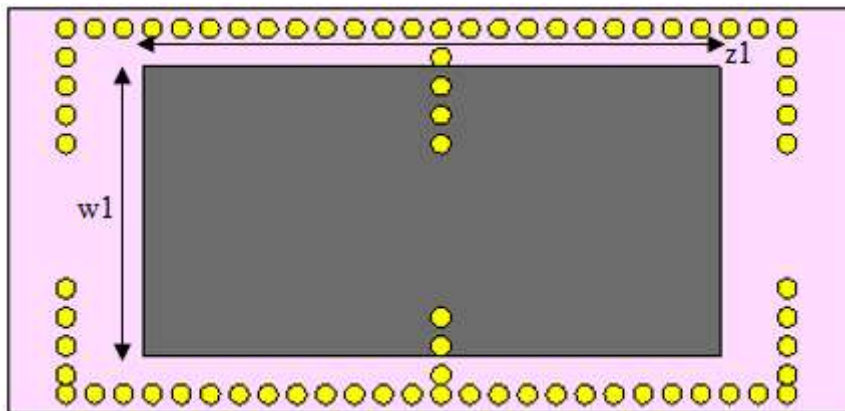


Figure 7.13 Length and width of graphene.

The chemical potential is kept constant at 0.1 eV. The parameters  $w_1$  representing the width and  $z_1$ , representing the length of the graphene patch are changed and the results are shown. When  $w_1 = 50 \mu\text{m}$  and  $z_1 = 100 \mu\text{m}$ , as shown in Fig. 7.14, the first and second

frequencies are  $1.2908 \text{ THz}$  with a return loss of  $-46.9 \text{ dB}$  and  $1.2397 \text{ THz}$  with a return loss of  $-31 \text{ dB}$ . When the length is changed to  $300 \mu\text{m}$  keeping  $w_1$  constant, as indicated in Fig. 7.15, the frequencies of operation changed to  $1.2915 \text{ THz}$  with a return loss of  $-43.327 \text{ dB}$  while the second frequency became  $1.2416 \text{ THz}$  with a return loss of  $-23.963 \text{ dB}$ . When both  $w_1$  and  $z_1$  are changed to  $100 \mu\text{m}$  and  $300 \mu\text{m}$  respectively, Fig. 7.16, the first and second frequencies changed to  $1.2929 \text{ THz}$  and  $1.2425 \text{ THz}$ , respectively, while the return loss was  $-39.182 \text{ dB}$  and  $-22.342 \text{ dB}$  respectively. Lastly in this experiment, the width and length were set at  $150 \mu\text{m}$  and  $100 \mu\text{m}$  respectively, and the first and second frequencies as indicated in Fig. 7.17 changed to  $1.2908 \text{ THz}$  and  $1.2408 \text{ THz}$ , while the return loss was  $-38.426 \text{ dB}$  and  $-23.348 \text{ dB}$ , respectively.

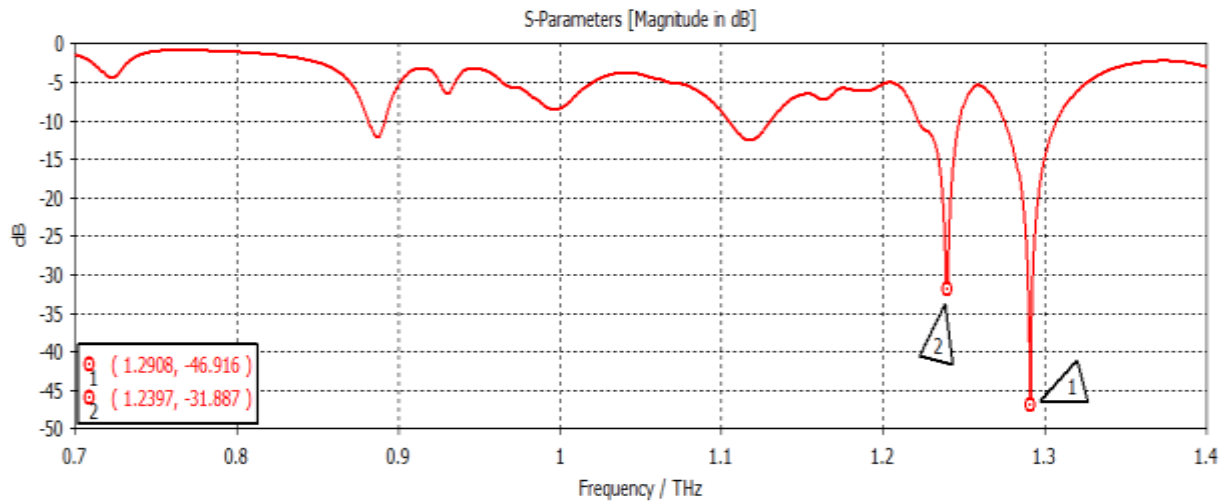


Figure 7.14 For  $w_1 = 50 \mu\text{m}$  and  $z_1 = 100 \mu\text{m}$ .

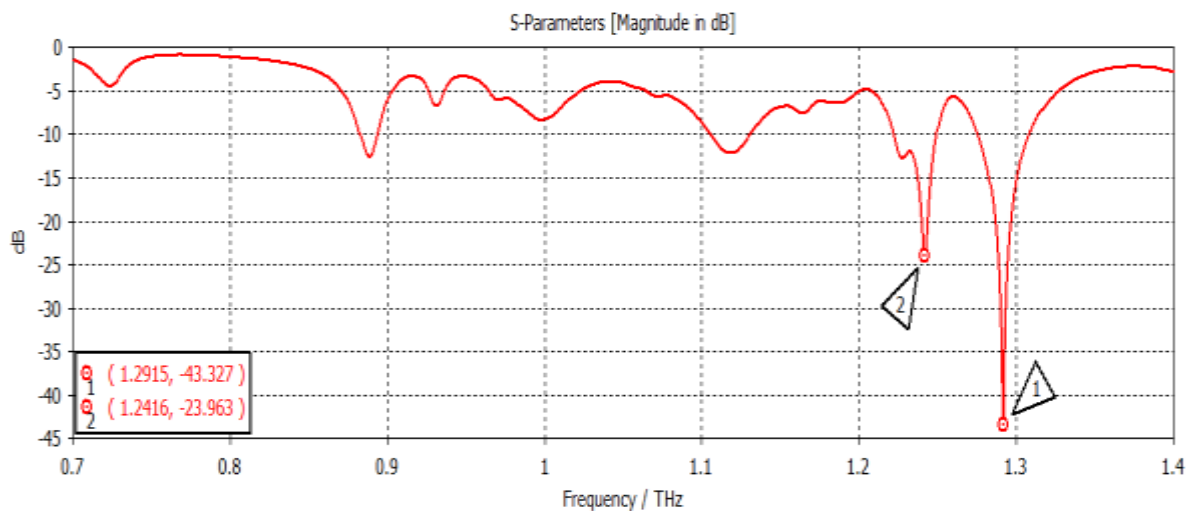


Figure 7.15 For  $w_1 = 50 \mu\text{m}$  and  $z_1 = 300 \mu\text{m}$ .

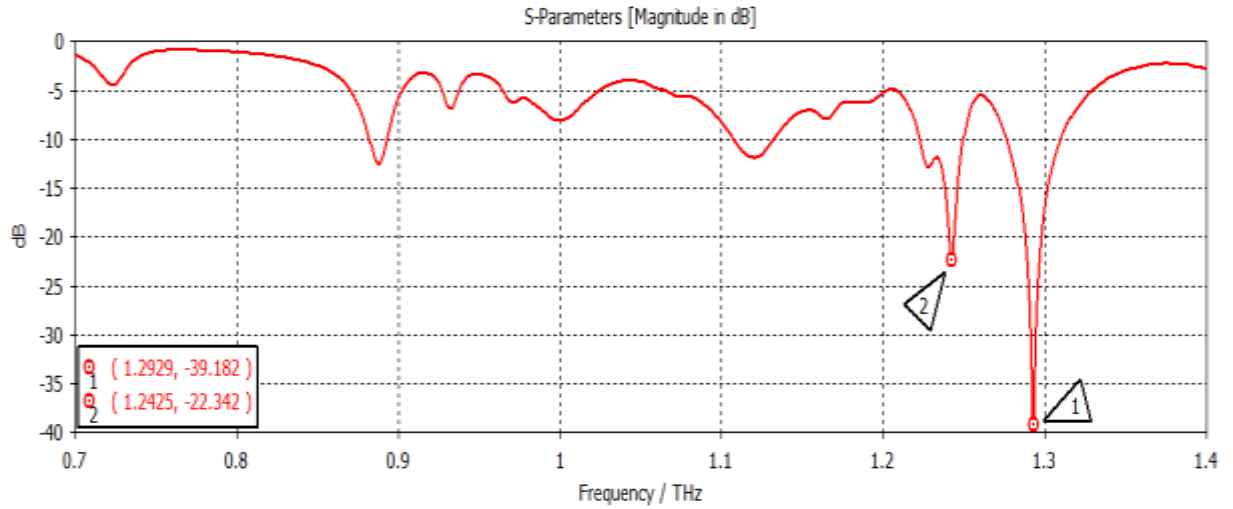


Figure 7.16 For  $w_1 = 100 \mu\text{m}$  and  $z_1 = 300 \mu\text{m}$

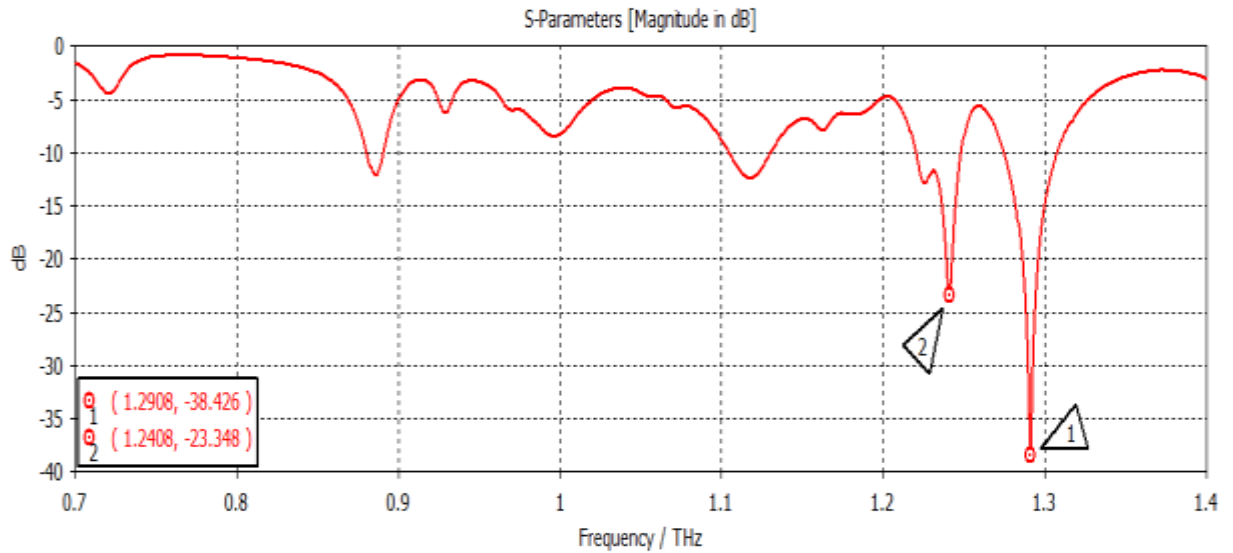


Figure 7.17 For  $w_1 = 150 \mu\text{m}$  and  $z_1 = 100 \mu\text{m}$

## 7.6. Discussion of Results

In this work, a second-order SIW filter was built to operate at  $1.2 \text{ THz}$ . Two SIW resonators were coupled together by the magnetic iris of length  $d_1$  as shown in Fig. 7.3. For frequency tunability, Graphene material was embedded into the substrate. The filter is made up of two layers of substrate, the first one being silicon with a permittivity of 11.9 and the second substrate on top of the silicon substrate being silicon dioxide with a permittivity of 3.9. The ground and top planes of the filter are gold plates. A thin graphene sheet is placed underneath the top gold plate to become sandwiched between the top gold plate and the silicon dioxide substrate. An external bias is applied between the top gold plate and the

ground plate. This was so as to be able to change the chemical potential of graphene. As the chemical potential of graphene was changed, the center frequency of the designed filter change at every instance. The aspect ratio of the graphene sheet was also changed so as to change the frequency of the filter as well. As the with and the length of the graphene patch changed, the center frequency also changed, however, this method means modifying the physical filter structure for change of frequency which may be undesirable, as compared to the change of the frequency by simply changed an external voltage without changing the geometrics of the physical filter structure.

## **7.7. Chapter Summary**

This chapter explores the need for reconfigurability or tunability of filters. Different ways for achieving tunability are presented. Semiconductors in the form of varactor diodes, ferroelectric and magnetic and MEMs methods of filter tuning are examined. To cater for high radiation losses incurred through these methods at high frequencies of operation, graphene material was investigated in this chapter as a substitute material to achieve the tunability of filters in the THz region. The lattice structure of graphene and the theoretical and mathematical models of graphene are presented. The conductivity of graphene is also explored under different operational conditions. Relationships between the chemical potential of graphene and frequency change are also presented. This chapter presents two proposed filter designs with the capability of tuning. The first design used dielectric rods of different permittivity, and the second used graphene material to achieve tunability.

## Chapter-8

# RESULTS AND CONCLUSIONS

---

### 8.1. Introduction

This chapter gives the summary of the results from the conducted research work and the conclusions drawn from these results are discussed, further work that is proposed from this research is presented as well.

### 8.2. Summary of Results

In this thesis, substrate integrated waveguide technology is used to design and develop microwave band-pass filters. The main aim of the research was to develop miniaturized high selectivity band-pass filters that are reconfigurable and can operate at very high frequencies going into the terahertz region. This was achieved in stages were, techniques for miniaturization were explored, and tunability was then effected. The work done in the thesis is summarized as follows:

Firstly, in chapter 3, a high selectivity fifth-order band-pass filter operating at  $30\text{ GHz}$  was illustrated. The filter was built using a single-layer substrate integrated waveguide technology. The performance of the filter was analyzed and its S-parameter results were presented. A similar work was compared, and the filter fared well in size, selectivity, and fractional bandwidth.

In chapter 4, different techniques used to peruse miniaturization are discussed. To achieve miniaturization, a fourth-order substrate integrated waveguide filter was designed four EMSIW cavity resonators were electrically coupled and the source-to-load coupling was achieved by modification of the of the first and last EMSIW resonators. The filter operated at a center frequency of  $13.5\text{ GHz}$  and it was found out that a size reduction of 87.5% was achieved. In the same line of miniaturization, a second design is presented in the form of a sixth-order cross-coupled filter. HMSIW and EMSIW cavity resonators were employed to develop the SIW band-pass filter. A novel cross-coupling technique was introduced between the resonators so as to achieve as to introduce transmission zeros that

will enhance the selectivity of the filter. This chapter presented a second order dual-band filter utilizing triangular-shaped SIW half-mode cavity resonators. The filter operated at center frequencies of  $9.5\text{ GHz}$  and  $13.8\text{ GHz}$  for the first-second pass-bands, respectively. The results were presented and analyzed and it could be proven that the designed dual-band filter offered the smallest size and operated at a high frequency compared to similar work.

In chapter 5, in pursuit of improving information signal integrity in communication networks, balanced filter circuits were presented. SIW resonators were used to design a fifth-order balanced band-pass filter operating at  $39\text{ GHz}$ . The resonators were magnetically coupled through iris windows. Satisfactory roll off at either end of the pass band was achieved and CM suppression as the common mode signal was heavily attenuated while passing the DM signal. To further increase the suppression rate of the CM signal, another design utilizing dumbbell defected ground structure and conductor patches with meandered loops was presented. Results showed a significant improvement of the CM signal suppression, reaching  $-90\text{ dBs}$  in the first pass-band and  $-40\text{ dBs}$  in the second pass-band.

In chapter 6, different ways of tuning are presented, there advantages and disadvantages are discussed. A second dual band design is then presented. Tunability was provided by dielectric rods of varying permittivities. The operating frequencies were  $9\text{ GHz}$  and  $14\text{ GHz}$  for the first and second pass-bands. To reconfigure the center frequencies of the pass-bands, the diameter of the perturbing dielectric rods was changed and secondly, dielectrics of different permittivities were used. The center frequency of the first pass-band changed from  $8.1\text{ GHz}$  to  $9.1\text{ GHz}$  and the second pass band changed from  $14.61\text{ GHz}$  to  $14.74\text{ GHz}$ .

Finally, in chapter 7, the tunability of filters at high frequencies in the tera hertz region is explored. In this work, a second-order SIW filter operating at  $1.2\text{ THz}$  was presented. The filter substrate was made up of two layers, silicon and silicon diode. Graphene sheet was then placed on top of the silicon dioxide layer. An external bias voltage was then applied to change the chemical potential of the graphene sheet. This in turn changed the operational center frequency of the filter, it was observed that the center frequency changed from  $1.289\text{ THz}$  to  $1.298\text{ THz}$  giving a bandwidth of  $8\text{ GHz}$ . The aspect ratio of graphene was also changed to bring about filter tunability. From this a frequency change from  $1.2908\text{ THz}$  to  $1.2929\text{ THz}$  was observed which is about  $2.1\text{ GHz}$  bandwidth.

### **8.3. Conclusions and Future Recommendations**

In this work, miniaturization of substrate integrated waveguide filters through the use of bisected structures in the form of HMSIW, QMSIW, EMSIW resonator structures was carried out. Satisfactory results were achieved without major degradation of the signal, however more work can be done to minimize the footprint of the structures by using much smaller cavity SIW resonators of different shapes and combining the technologies to achieve even higher selectivity of the filters. On the issue of selectivity, more cross-couplings can be introduced and the coupling matrix method can be used to establish the resonators that can possibly be cross-coupled together with their coupling coefficients.

In this thesis, work was done on tuning and reconfigurability of the filter and dielectric rods were used for tuning the center frequency of a dual-band filter. In contrast, graphene material was used to achieve tuning at high-frequency range in the Terahertz band. Future work can be done in identifying alternative nano-materials with superior electrical, mechanical, and optical behavior, which can be embedded in the substrate of the filters such that when their characteristics change, a change in frequency is also achieved.

## REFERENCES

---

- [1] Pozar D M, *Microwave Engineering*, 4th ed. New York, NY, USA: John Wiley & Sons, Inc, 2012.
- [2] A. Salcedo and E. Martinez, "Analysis of the electromagnetic spectrum under the extremely low frequency band: Frequency sub-bands classification," in *Proceedings - 2017 International Conference on Mechatronics, Electronics, and Automotive Engineering, ICMEAE 2017*, Dec. 2017, vol. 2017-January, pp. 157–162. doi: 10.1109/ICMEAE.2017.15.
- [3] W. Jiang, B. Han, M. A. Habibi, and H. D. Schotten, "The road towards 6G: A comprehensive survey," *IEEE Open Journal of the Communications Society*, vol. 2. Institute of Electrical and Electronics Engineers Inc., pp. 334–366, 2021. doi: 10.1109/OJCOMS.2021.3057679.
- [4] Cameron R. J., Kudsia C. M, and Mansour R. R, *Microwave filters for communication systems: fundamentals, design, and applications*, 2nd ed. NJ 07030, USA: John Wiley & Sons Inc, 2018.
- [5] J. S. Hong and M. J. Lancaster, *Microstrip filters for RF/microwave applications*. Chichester, New York: Wiley, 2001.
- [6] L. Huang, W. Wu, X. Zhang, and N. Yuan, "A Compact Bandpass Substrate Integrated Waveguide (SIW) Filter with Compact Microstrip Resonant Cell (CMRC) Resonators," *2017 Progress in Electromagnetics Research Symposium - Fall (PIERS - FALL)*, Singapore, 2017, pp. 06-310, doi: 10.1109/PIERS-FALL.2017.8293154.
- [7] N. Delmonte, M. Bozzi, L. Perreggini, and C. Tomassoni, "Miniaturized SIW Filters Based on Shielded Quarter-Mode Cavities," in *2019 IEEE MTT-S International Conference on Numerical Electromagnetic and Multiphysics Modeling and Optimization (NEMO)*, May 2019, pp. 1–3. doi: 10.1109/NEMO.2019.8853746.
- [8] Y. Li, Z. Zhang, X. Wu, and W. Yu, "A New Compact Quarter-Mode SIW Bandpass Filter Utilising Coaxial Cavity; A New Compact Quarter-Mode SIW Bandpass Filter Utilising Coaxial Cavity," 2018.
- [9] Z. Zakaria and B. H. Ahmad, "Design of SIW bandpass filter with 6 dB offset," in *2011 IEEE International RF and Microwave Conference, RFM 2011 - Proceedings*, 2011, pp. 87–90. doi: 10.1109/RFM.2011.6168702.
- [10] L. Huang, "Novel Substrate Integrated Waveguide Filters and Circuits," University of Leeds, School of Electrical and Electronic Engineering, July 2013.
- [11] W. Hong *et al.*, "The Role of Millimeter-Wave Technologies in 5G/6G Wireless Communications," *IEEE Journal of Microwaves*, vol. 1, no. 1, pp. 101–122, Jan. 2021, doi: 10.1109/jmw.2020.3035541.
- [12] M. Inomata *et al.*, "Terahertz Propagation Characteristics for 6G Mobile Communication Systems," in *15th European Conference on Antennas and Propagation, EuCAP 2021*, Mar. 2021. doi: 10.23919/EuCAP51087.2021.9411143.

- [13] C. D. K. Mutepfe and V. M. Srivastava, "An Approach to High Selectivity Substrate Integrated Waveguide Band-Pass Filter for mm-Wave Applications," *International Journal of Microwave and Optical Technology*, vol. 15, no. 6, pp. 592–598, Nov. 2020.
- [14] Y. D. Parmar and S. C. Bera, "Investigation of substrate integrated waveguide filters and construction technique," in *2017 International Conference on Computing Methodologies and Communication (ICCMC)*, Jul. 2017, pp. 738–740. doi: 10.1109/ICCMC.2017.8282564.
- [15] S. Moitra, P. S. Bhowmik, and A. Muvvala, "Design and Characterization of Angular Bend Substrate Integrated Waveguide (SIW) Bandpass Filter for Microwave Ku-Band Applications," in *2018 International Conference on Communication, Computing and Internet of Things (IC3IoT)*, Feb. 2018, pp. 224–228. doi: 10.1109/IC3IoT.2018.8668172.
- [16] A. el Mostrah, B. Potelon, E. Rius, C. Quendo, J. F. Favennec, and H. Leblond, "Comparative study of Two C-band SIW filter topologies for a space application," in *European Microwave Week 2012: "Space for Microwaves", EuMW 2012, Conference Proceedings - 42nd European Microwave Conference, EuMC 2012*, 2012, pp. 368–371. doi: 10.23919/eumc.2012.6459412.
- [17] X. Chen, T. Cui, W. Hong, J. Chen, and K. Wu, "Substrate Integrated Waveguide (SIW) linear phase filter," *IEEE Microwave and Wireless Components Letters*, vol. 15, no. 11, pp. 787–789, Nov. 2005, doi: 10.1109/LMWC.2005.859021.
- [18] A. A. Khan and M. K. Mandal, "Narrowband Substrate Integrated Waveguide Bandpass Filter with High Selectivity," *IEEE Microwave and Wireless Components Letters*, vol. 28, no. 5, pp. 416–418, May 2018, doi: 10.1109/LMWC.2018.2820605.
- [19] F. Grine, M. T. Benhabiles, R. Khalef, T. Djerafi, and M. L. Riabi, "Substrate Integrated Waveguide with Tapered Electromagnetic Bandgap Structures for Bandpass Filter Design," in *2018 IEEE MTT-S International Conference on Numerical Electromagnetic and Multiphysics Modeling and Optimization, NEMO 2018*, Oct. 2018. doi: 10.1109/NEMO.2018.8503195.
- [20] X. Lu and X. W. Zhu, "Bandpass Filter Design based on Eighth-Mode SIW," in *2020 IEEE Asia-Pacific Conference on Antennas and Propagation, APCAP 2020 - Proceedings*, Aug. 2020. doi: 10.1109/APCAP50217.2020.9245990.
- [21] S. Saeedi and H. H. Sigmarsson, "Miniaturized evanescent-mode cavity SIW bandpass filter with spurious suppression," in *IEEE Radio and Wireless Symposium, RWS*, Feb. 2018, vol. 2018-January, pp. 234–236. doi: 10.1109/RWS.2018.8304996.
- [22] B. Shi and G. Zhai, "A CPW-SIW Filter With Wide Stopband Performance Using Grounded Metallic Vias," in *TENCON 2018 - 2018 IEEE Region 10 Conference*, Oct. 2018, pp. 0346–0349. doi: 10.1109/TENCON.2018.8650283.
- [23] M. P. dos Santos *et al.*, "Design of a SIW Chebyshev Bandpass Filter with Inductive Coupling," in *2018 IEEE MTT-S Latin America Microwave Conference (LAMC 2018)*, Dec. 2018, pp. 1–3. doi: 10.1109/LAMC.2018.8699015.

- [24] Z. Qian, "Design of a Dual-Band Balanced SIW Bandpass Filter with High Common-Mode Suppression," in *2019 International Applied Computational Electromagnetics Society Symposium - China (ACES)*, Aug. 2019, vol. 1, pp. 1–2. doi: 10.23919/ACES48530.2019.9060581.
- [25] B. Ren, Z. Ma, H. Liu, M. Ohira, and X. Guan, "Design of Balanced Dual-Band Superconducting Bandpass Filter With High Selectivity and Deep Common-Mode Suppression," *2018 Asia-Pacific Microwave Conference (APMC)*, Kyoto, Japan, 2018, pp. 423-425, doi: 10.23919/APMC.2018.8617383. .
- [26] Y. Shen, H. Wang, W. Kang, and W. Wu, "Dual-band SIW differential bandpass filter with improved common-mode suppression," *IEEE Microwave and Wireless Components Letters*, vol. 25, no. 2, pp. 100–102, Feb. 2015, doi: 10.1109/LMWC.2014.2382683.
- [27] H. Zhang, W. Kang, and W. Wu, "Miniaturized Dual-Band Differential Filter Based on CSRR-Loaded Dual-Mode SIW Cavity," *IEEE Microwave and Wireless Components Letters*, vol. 28, no. 10, pp. 897–899, Oct. 2018, doi: 10.1109/LMWC.2018.2867082.
- [28] H. Zhang, W. Kang, and W. Wu, "Miniaturized Dual-Band Differential Filter Based on CSRR-Loaded Dual-Mode SIW Cavity," *IEEE Microwave and Wireless Components Letters*, vol. 28, no. 10, pp. 897–899, Oct. 2018, doi: 10.1109/LMWC.2018.2867082.
- [29] X. Yuan, W. Kang, H. Zhang, and J. Gao, "Design of tunable balanced dual-band filter using SIR and EMSIW," in *2019 IEEE 3rd International Conference on Electronic Information Technology and Computer Engineering, EITCE 2019*, Oct. 2019, pp. 1646–1650. doi: 10.1109/EITCE47263.2019.9094969.
- [30] B. Pal, M. K. Mandal, and S. Dwari, "Varactor Tuned Dual-Band Bandpass Filter with Independently Tunable Band Positions," *IEEE Microwave and Wireless Components Letters*, vol. 29, no. 4, pp. 255–257, Apr. 2019, doi: 10.1109/LMWC.2019.2898725.
- [31] M. Fan, K. Song, Y. Zhu, and Y. Fan, "Compact Bandpass-to-Bandstop Reconfigurable Filter with Wide Tuning Range," *IEEE Microwave and Wireless Components Letters*, vol. 29, no. 3, pp. 198–200, Mar. 2019, doi: 10.1109/LMWC.2019.2892846.
- [32] Thilagavathi K and Balakumar B, "Review on RF Tunable Filters," *International Journal of Innovations in Engineering and Technology*, vol. 8, no. 2, 2017, doi: 10.21172/ijiet.82.007.
- [33] S. De, S. K. Koul, and K. K. Samanta, "Tunable SIW band pass filters," in *2019 IEEE MTT-S International Microwave and RF Conference, IMARC 2019*, Dec. 2019. doi: 10.1109/IMaRC45935.2019.9118649.
- [34] K. Entesari, A. P. Saghati, V. Sekar, and M. Armendariz, "Tunable SIW structures: Antennas, VCOs, and filters," *IEEE Microw Mag*, vol. 16, no. 5, pp. 34–54, Jun. 2015, doi: 10.1109/MMM.2015.2408273.

- [35] V. Sekar, M. Armendariz, and K. Entesari, "A 1.2-1.6-GHz substrate-integrated-waveguide RF MEMS tunable filter," *IEEE Trans Microw Theory Tech*, vol. 59, no. 4 PART 1, pp. 866–876, Apr. 2011, doi: 10.1109/TMTT.2011.2109006.
- [36] Q. Li *et al.*, "Active graphene-silicon hybrid diode for terahertz waves," *Nat Commun*, vol. 6, May 2015, doi: 10.1038/ncomms8082.
- [37] S. Naghizade and H. Saghaei, "Tunable graphene-on-insulator band-stop filter at the mid-infrared region," *Opt Quantum Electron*, vol. 52, no. 4, Apr. 2020, doi: 10.1007/s11082-020-02350-4.
- [38] G. Varshney, S. Gotra, V. S. Pandey, and R. S. Yaduvanshi, "Proximity-Coupled Graphene-Patch-Based Tunable Single-/Dual-Band Notch Filter for THz Applications," *J Electron Mater*, vol. 48, no. 8, pp. 4818–4829, Aug. 2019, doi: 10.1007/s11664-019-07274-8.
- [39] M. Kong, Y. Wu, Z. Zhuang, W. Wang, and Y. Liu, "Graphene-Based THz Tunable Bandstop Filter with Constant Absolute Bandwidth," *Progress In Electromagnetics Research Letters*, vol. 71, pp. 141–147, 2017.
- [40] D. Correas-Serrano, J. S. Gomez-Diaz, J. Perruisseau-Carrier, and A. Alvarez-Melcon, "Graphene-based plasmonic tunable low-pass filters in the terahertz band," *IEEE Trans Nanotechnol*, vol. 13, no. 6, pp. 1145–1153, Nov. 2014, doi: 10.1109/TNANO.2014.2344973.
- [41] H. Abunahla, R. Gadhafi, B. Mohammad, A. Alazzam, M. Kebe, and M. Sanduleanu, "Integrated graphene oxide resistive element in tunable RF filters," *Sci Rep*, vol. 10, no. 1, Dec. 2020, doi: 10.1038/s41598-020-70041-x.
- [42] M. Bozzi, L. Perregrini, and C. Tomassoni, "A Review of Compact Substrate Integrated Waveguide (SIW) Interconnects and Components," *2019 IEEE 23rd Workshop on Signal and Power Integrity, SPI 2019 - Proceedings*, Jun. 2019, doi: 10.1109/SAPIW.2019.8781646.
- [43] P. Li, H. Chu, D. Zhao, and R. S. Chen, "Compact Dual-Band Balanced SIW Bandpass Filter with Improved Common-Mode Suppression," *IEEE Microwave and Wireless Components Letters*, vol. 27, no. 4, pp. 347–349, Apr. 2017, doi: 10.1109/LMWC.2017.2678428.
- [44] M. H. Ho, J. C. Li, and Y. C. Chen, "Miniaturized SIW Cavity Resonator and Its Application in Filter Design," *IEEE Microwave and Wireless Components Letters*, vol. 28, no. 8, pp. 651–653, Aug. 2018, doi: 10.1109/LMWC.2018.2845101.
- [45] H. Zhang, W. Kang, and W. Wu, "Miniaturized Dual-Band SIW Filters Using E-Shaped Slotlines with Controllable Center Frequencies," *IEEE Microwave and Wireless Components Letters*, vol. 28, no. 4, pp. 311–313, Apr. 2018, doi: 10.1109/LMWC.2018.2811251.
- [46] C. Devika, K. Karthika, N. Raj, K. Swetha, and P. R. Lal, "Substrate Integrated Waveguide Based Rectangular Cavity Resonator Filter for WiFi Applications," in *2018 9th International Conference on Computing, Communication and Networking Technologies (ICCCNT)*, Jul. 2018, pp. 1–4. doi: 10.1109/ICCCNT.2018.8494083.

- [47] A. Gopinath and P. R. Lal, "Substrate integrated waveguide based hybrid cavity filter for ku band applications," in *Proceedings of the 2017 IEEE International Conference on Communication and Signal Processing, ICCSP 2017*, Feb. 2018, vol. 2018-January, pp. 1563–1566. doi: 10.1109/ICCSP.2017.8286651.
- [48] T. Martin, A. Ghiotto, F. Lotz, and T. P. Vuong, "Air-Filled SIW Filters for K-to E-Band Substrate Integrated Systems," *2018 IEEE MTT-S International Conference on Numerical Electromagnetic and Multiphysics Modeling and Optimization, NEMO 2018*, Oct. 2018, doi: 10.1109/NEMO.2018.8503392.
- [49] S. Moitra *et al.*, "Design of substrate integrated waveguide (SIW) BPF using circular ring, split ring and inductive posts," *2018 2nd International Conference on Electronics, Materials Engineering and Nano-Technology, IEMENTech 2018*, Sep. 2018, doi: 10.1109/IEMENTECH.2018.8465311.
- [50] M. H. Ho and K. H. Tang, "Miniaturized SIW Cavity Tri-Band Filter Design," *IEEE Microwave and Wireless Components Letters*, vol. 30, no. 6, pp. 589–592, Jun. 2020, doi: 10.1109/LMWC.2020.2987172.
- [51] A. J. Salim, A. N. Alkhafaji, T. A. Elwi, H. T. Ziboon, S. Mutashar, and J. K. Ali, "Miniaturized SIW Wideband BPF Based on Folded Ring and Meander Line Slot for Wireless Applications; Miniaturized SIW Wideband BPF Based on Folded Ring and Meander Line Slot for Wireless Applications," *2017 Second Al-Sadiq International Conference on Multidisciplinary in IT and Communication Science and Applications (AIC-MITCSA)*, Baghdad, Iraq, 2017, pp. 136-139, doi: 10.1109/AIC-MITCSA.2017.8722992..
- [52] H. Y. Xie, B. Wu, L. Xia, J. Z. Chen, and T. Su, "Miniaturized Half-Mode Fan-Shaped SIW Filter with Extensible Order and Wide Stopband," *IEEE Microwave and Wireless Components Letters*, vol. 30, no. 8, pp. 749–752, Aug. 2020, doi: 10.1109/LMWC.2020.3001092.
- [53] Z. Wang and Y. Dong, "Miniaturized Substrate Integrated Waveguide Filters with Stepped-Impedance Slot Resonators for Millimeter-Wave Application," in *2019 IEEE MTT-S International Microwave Symposium (IMS)*, Jun. 2019, pp. 1038–1041. doi: 10.1109/MWSYM.2019.8700884.
- [54] P. Li, D. Zhao, Y. Rui, and R. Xie, "Design of Compact Bandpass Filter Based on EMSIW Cavities," in *2017 International Applied Computational Electromagnetics Society Symposium (ACES)*, Aug. 2017.
- [55] P. Li, H. Chu, and R. S. Chen, "Design of compact bandpass filters using quarter-mode and eighth-mode SIW cavities," *IEEE Trans Compon Packaging Manuf Technol*, vol. 7, no. 6, pp. 956–963, Jun. 2017, doi: 10.1109/TCPMT.2017.2677958.
- [56] J. Guo, B. You, and G. Q. Luo, "A Miniaturized Eighth-Mode Substrate-Integrated Waveguide Filter with Both Tunable Center Frequency and Bandwidth," *IEEE Microwave and Wireless Components Letters*, vol. 29, no. 7, pp. 450–452, Jul. 2019, doi: 10.1109/LMWC.2019.2916780.

- [57] X. Lu and X. W. Zhu, "Third-order Bandpass Filter Design by EMSIW and QMSIW Cavity," in *2020 International Conference on Microwave and Millimeter Wave Technology, ICMMT 2020 - Proceedings*, Sep. 2020. doi: 10.1109/ICMMT49418.2020.9386811.
- [58] X.-H. Nie and W. Hong, "Miniaturized EMSIW Filter with High out of Band Rejection," in *2018 Asia-Pacific Microwave Conference (APMC)*, Nov. 2018, pp. 1357–1359. doi: 10.23919/APMC.2018.8617542.
- [59] P. Li, Z. Rao, D. Zhao, R. Xie, Y. Rui, and H. Chu, "Design of Compact Bandpass Filter With Enhanced Frequency Selectivity Based on EMSIW Cavities," in *2019 IEEE Asia-Pacific Microwave Conference (APMC)*, Dec. 2019, pp. 1718–1720. doi: 10.1109/APMC46564.2019.9038662.
- [60] Z. Troudi and L. Osman, "Design of Miniaturized Half Mode SIW BandPass Filter Using Metamaterial Unit Cell," in *2019 IEEE 19th Mediterranean Microwave Symposium (MMS)*, Oct. 2019, pp. 1–4. doi: 10.1109/MMS48040.2019.9157268.
- [61] F. Zhu, G. Q. Luo, Z. Liao, X. W. Dai, and K. Wu, "Compact Dual-Mode Bandpass Filters Based on Half-Mode Substrate-Integrated Waveguide Cavities," *IEEE Microwave and Wireless Components Letters*, vol. 31, no. 5, pp. 441–444, May 2021, doi: 10.1109/LMWC.2021.3066569.
- [62] M. Nosrati, Z. Abbasi, and M. Daneshmand, "Single-layer substrate-integrated waveguide evanescent-mode filter," *IEEE Microwave and Wireless Components Letters*, vol. 28, no. 12, pp. 1107–1109, Dec. 2018, doi: 10.1109/LMWC.2018.2875313.
- [63] M. Dong *et al.*, "Substrate Integrated Gap Waveguide Bandpass Filters with High Selectivity and Wide Stopband," in *IEEE MTT-S International Microwave Symposium Digest*, Aug. 2018, vol. 2018-June, pp. 285–288. doi: 10.1109/MWSYM.2018.8439506.
- [64] F. Grine, H. Ammari, M. T. Benhabiles, and M. L. Riabi, "Double-layer Sixteenth-mode Substrate Integrated Waveguide Filter based on Defected Ground Structure," *IMWS-AMP 2019 - 2019 IEEE MTT-S International Microwave Workshop Series on Advanced Materials and Processes for RF and THz Applications*, pp. 55–57, Jul. 2019, doi: 10.1109/IMWS-AMP.2019.8880138.
- [65] M. Li, C. Chen, X. Zhang, and W. Chen, "Multi-mode bandpass filters using triangular half-mode substrate integrated waveguide," in *2016 Progress In Electromagnetics Research Symposium, PIERS 2016 - Proceedings*, Nov. 2016, pp. 3809–3813. doi: 10.1109/PIERS.2016.7735430.
- [66] R. Zhang and L. Zhu, "Synthesis and Design of Wideband Dual-Band Bandpass Filters With Controllable In-Band Ripple Factor and Dual-Band Isolation," *IEEE Trans Microw Theory Tech*, vol. 61, no. 5, pp. 1820–1828, May 2013, doi: 10.1109/TMTT.2013.2256145.
- [67] G. Shen, W. Che, and Q. Xue, "Novel Tri-Band Bandpass Filter With Independently Controllable Frequencies, Bandwidths, and Return Losses," *IEEE Microwave and Wireless Components Letters*, vol. 27, no. 6, pp. 560–562, Jun. 2017, doi: 10.1109/LMWC.2017.2701302.

- [68] S. Zhang and L. Zhu, "Compact Tri-Band Bandpass Filter Based on  $\lambda/4$  Resonators With U-Folded Coupled-Line," *IEEE Microwave and Wireless Components Letters*, vol. 23, no. 5, pp. 258–260, May 2013, doi: 10.1109/LMWC.2013.2255868.
- [69] Y. Zhang, G. Li, and X. Yin Zhang, "Compact Quad-Band Bandpass Filter for DCS/WLAN/WiMAX/5G Wi-Fi Application" *IEEE MICROWAVE AND WIRELESS COMPONENTS LETTERS*, vol. 25, no. 10, 2015, doi: 10.1109/LMWC.2015.2463227.
- [70] S. A. Shakib, V. Sekar, and K. Entesari, *A Compact Triple-band Bandpass Filter Based on Half-mode Substrate Integrated Waveguides*. 2012. doi: 10.23919/EuMC.2012.6459144.
- [71] W.-L. Tsai, T.-M. Shen, B.-J. Chen, T.-Y. Huang, and R.-B. Wu, "Triband Filter Design Using Laminated Waveguide Cavity in LTCC," *IEEE Trans Compon Packaging Manuf Technol*, vol. 4, no. 6, 2014, doi: 10.1109/TCPMT.2014.2319299.
- [72] M. Esmaili and J. Bornemann, "Substrate Integrated Waveguide Triple-Passband Dual-Stopband Filter Using Six Cascaded Singlets," *IEEE Microwave and Wireless Components Letters*, vol. 24, no. 7, p. 439, 2014, doi: 10.1109/LMWC.2014.2316242.
- [73] L. Gao, Y. Zhang, and Q. Xue, "Compact Tri-Band Bandpass Filter Using Novel Eight-Mode Resonator for 5G WiFi Application; Compact Tri-Band Bandpass Filter Using Novel Eight-Mode Resonator for 5G WiFi Application," *IEEE Microwave and Wireless Components Letters*, vol. 25, no. 10, 2015, doi: 10.1109/LMWC.2015.2421298.
- [74] D. Li, D. Wang, Y. Liu, X. Chen, and H. Wu, "Compact Tri-Band Bandpass Filter Based on Ring Multi-Mode Resonator," in *2019 IEEE MTT-S International Wireless Symposium (IWS)*, May 2019, pp. 1–3. doi: 10.1109/IEEE-IWS.2019.8804094.
- [75] B. Ren, Z. Ma, H. Liu, X. Guan, P. Wen, and M. Ohira, "Compact Multi-Band Differential Bandpass Filters Using Microstrip Multi-mode Resonators," in *2019 IEEE MTT-S International Wireless Symposium (IWS)*, 2019. Accessed: Nov. 10, 2022. [Online]. Available: <https://ieeexplore.ieee.org/document/8804107/>
- [76] B. Ren, X. Guan, and H. Liu, "Multi-Band HTS Bandpass Filters Using Multimode Square Ring Loaded Resonators," *2020 Cross Strait Radio Science and Wireless Technology Conference, CSRSWTC 2020 - Proceedings*, Dec. 2020, doi: 10.1109/CSRSWTC50769.2020.9372554.
- [77] H. Xie, K. Zhou, C. Zhou, and W. Wu, "Compact Substrate-Integrated Waveguide Triplexer Based on a Common Triple-Mode Cavity," in *2018 IEEE/MTT-S International Microwave Symposium - IMS*, 2018. Accessed: Nov. 10, 2022. [Online]. Available: <https://ieeexplore.ieee.org/document/8439574/>
- [78] C. D. K. Mutepfe and V. M. Srivastava, "Design and Analysis of Compact 5th Mode Balanced Substrate Integrated Waveguide Band-Pass Filter for 39 GHz," *International Journal on Communications Antenna and Propagation (IRECAP)*, vol. 11, no. 6, p. 401, Dec. 2021, doi: 10.15866/irecap.v11i6.20981.

- [79] C. H. Wu, C. H. Wang, and C. H. Chen, "Novel balanced coupled-line bandpass filters with common-mode noise suppression," *IEEE Trans Microw Theory Tech*, vol. 55, no. 2, pp. 287–294, Feb. 2007, doi: 10.1109/TMTT.2006.889147.
- [80] F. Martín, L. Zhu, J.-S. Hong, and F. Medina, *Balanced microwave filters*. Hoboken, NJ 07030, USA: John Wiley & Sons, Inc, 2018. Accessed: Nov. 10, 2022. [Online]. Available: <https://www.wiley.com/en-us/Balanced+Microwave+Filters-p-9781119237617>
- [81] J. L. Olvera-Cervantes and A. Corona-Chavez, "Microstrip balanced bandpass filter with compact size, extended-stopband and common-mode noise suppression," *IEEE Microwave and Wireless Components Letters*, vol. 23, no. 10, pp. 530–532, 2013, doi: 10.1109/LMWC.2013.2279096.
- [82] C. H. Wu, C. H. Wang, and C. H. Chen, "Stopband-extended balanced bandpass filter using coupled stepped-impedance resonators," *IEEE Microwave and Wireless Components Letters*, vol. 17, no. 7, pp. 507–509, Jul. 2007, doi: 10.1109/LMWC.2007.899311.
- [83] J. Shi and Q. Xue, "Balanced bandpass filters using center-loaded half-wavelength resonators," *IEEE Trans Microw Theory Tech*, vol. 58, no. 4, pp. 970–977, Apr. 2010, doi: 10.1109/TMTT.2010.2042839.
- [84] A. M. Abbosh, "Ultrawideband balanced bandpass filter," *IEEE Microwave and Wireless Components Letters*, vol. 21, no. 9, pp. 480–482, Sep. 2011, doi: 10.1109/LMWC.2011.2162620.
- [85] Q. Cao, H. Liu, and L. Gao, "Design of Balanced Filter with Wide Stopband by Using Discriminating Coupling," *Frequenz*, vol. 73, no. 3–4, pp. 117–122, Mar. 2019, doi: 10.1515/FREQ-2018-0174/MACHINEREADABLECITATION/RIS.
- [86] K. da Xu, Z. Luo, Y. Liu, and Q. H. Liu, "High-selectivity single-ended and balanced bandpass filters using ring resonators and coupled lines loaded with multiple stubs," *AEU - International Journal of Electronics and Communications*, vol. 96, pp. 193–198, Nov. 2018, doi: 10.1016/J.AEUE.2018.09.021.
- [87] Z. Qian, "Design of a dual-band balanced SIW bandpass filter with high common-mode suppression," *2019 International Applied Computational Electromagnetics Society Symposium-China, ACES 2019*, Aug. 2019, doi: 10.23919/ACES48530.2019.9060581.
- [88] D. Simpson and D. Psychogiou, "High-Order Fully-Reconfigurable Balanced Bandpass Filters Using Mixed Technology Resonators," in *2020 50th European Microwave Conference, EuMC 2020*, Jan. 2021, pp. 897–900. doi: 10.23919/EuMC48046.2021.9338195.
- [89] W. Nie, Y. B. Pang, X. H. Tan, and Y. H. Wang, "Compact wide-stopband balanced bandpass filter with intrinsic common-mode suppression," *AEU - International Journal of Electronics and Communications*, vol. 127, p. 153456, Dec. 2020, doi: 10.1016/J.AEUE.2020.153456.
- [90] N. Janković and V. Crnojević-Bengin, "Balanced bandpass filter based on square patch resonators," in *2015 12th International Conference on Telecommunications in Modern Satellite, Cable and*

*Broadcasting Services, TELSIKS 2015*, Dec. 2015, pp. 189–192. doi: 10.1109/TELSKS.2015.7357766.

- [91] S. Y. Zheng, R. T. Wu, and Z. W. Liu, “A balanced bandpass filter with two transmission zeros based on square patch resonators,” in *2016 IEEE International Conference on Ubiquitous Wireless Broadband, ICUWB 2016*, Dec. 2016. doi: 10.1109/ICUWB.2016.7790443.
- [92] J. Shi and Q. Xue, “Novel balanced dual-band bandpass filter using coupled stepped-impedance resonators,” *IEEE Microwave and Wireless Components Letters*, vol. 20, no. 1, pp. 19–21, Jan. 2010, doi: 10.1109/LMWC.2009.2035954.
- [93] A. Fernández-Prieto, A. Lujambio, J. Martel, F. Medina, F. Mesa, and R. R. Boix, “Simple and compact balanced bandpass filters based on magnetically coupled resonators,” *IEEE Trans Microw Theory Tech*, vol. 63, no. 6, pp. 1843–1853, Jun. 2015, doi: 10.1109/TMTT.2015.2424229.
- [94] X. Xu, J. Wang, and L. Zhu, “A new approach to design differential-mode bandpass filters on SIW structure,” *IEEE Microwave and Wireless Components Letters*, vol. 23, no. 12, pp. 635–637, Dec. 2013, doi: 10.1109/LMWC.2013.2283859.
- [95] P. Chu *et al.*, “Balanced substrate integrated waveguide filter,” *IEEE Trans Microw Theory Tech*, vol. 62, no. 4, pp. 824–831, 2014, doi: 10.1109/TMTT.2014.2307055.
- [96] M. Y. Chen, W. Hong, and M. H. Ho, “Balanced BPF design using the substrate integrated waveguide,” in *Asia-Pacific Microwave Conference Proceedings, APMC*, 2012, pp. 25–27. doi: 10.1109/APMC.2012.6421486.
- [97] K. Zhou, W. Kang, and W. Wu, “A compact SIW balanced bandpass filter with high selectivity and good common-mode suppression,” in *9th International Conference on Microwave and Millimeter Wave Technology, ICMMT 2016 - Proceedings*, Nov. 2016, vol. 1, pp. 76–78. doi: 10.1109/ICMMT.2016.7761682.
- [98] Z. Shen, K. Xu, G. M. Mbongo, J. Shi, and Y. Yang, “Compact Balanced Substrate Integrated Waveguide Filter with Low Insertion Loss,” *IEEE Access*, vol. 7, pp. 126111–126115, 2019, doi: 10.1109/ACCESS.2019.2937349.
- [99] X.-B. Ji, Q. Liu, and M. Yang, “Compact Single-Layer Balanced Eighth-Mode Substrate Integrated Waveguide Bandpass Filter with High Selectivity,” *Progress In Electromagnetics Research Letters*, vol. 87, pp. 131–136, 2019.
- [100] S. Wang, K. Zhou, W. Kang, and W. Wu, “SIW Dual-Mode Dual-Band Balanced Filter With Good Common-Mode Suppression,” in *2019 International Conference on Microwave and Millimeter Wave Technology (ICMMT)*, 2019. Accessed: Nov. 10, 2022. [Online]. Available: <https://ieeexplore.ieee.org/document/8992551/>
- [101] Y. Shen, H. Wang, W. Kang, and W. Wu, “Dual-Band SIW Differential Bandpass Filter With Improved Common-Mode Suppression,” *IEEE Microwave and Wireless Components Letters*, vol. 25,

- no. 2, 2015, Accessed: Nov. 10, 2022. [Online]. Available: <https://ieeexplore.ieee.org/document/7000581/>
- [102] G. Zhang, J. Wang, S. Ge, and W. Wu, "A new balanced dual-band SIW bandpass filter with high common-mode suppression," in *Asia-Pacific Microwave Conference Proceedings, APMC*, Feb. 2016, vol. 2. doi: 10.1109/APMC.2015.7413144.
- [103] M. Brown and C. E. Saavedra, "Frequency-Tunable Quasi-Elliptic Filter Using Liquid Metal," *Proceedings of 2020 IEEE Asia Pacific Conference on Circuits and Systems, APCCAS 2020*, pp. 110–113, Dec. 2020, doi: 10.1109/APCCAS50809.2020.9301676.
- [104] M. Brown and C. E. Saavedra, "Reconfigurable Substrate Integrated Waveguide Circuits Using Dielectric Fluids," in *2020 50th European Microwave Conference, EuMC 2020*, Jan. 2021, pp. 542–545. doi: 10.23919/EuMC48046.2021.9338183.
- [105] M. Sun, J. Zhang, Z. Zheng, J. Yang, X. Zhu, and R. Leng, "A 3-4.5 GHz electrically reconfigurable bandpass filter based on substrate integrated waveguide," *IEEE International Symposium on Electromagnetic Compatibility*, vol. 2019-November, Nov. 2019, doi: 10.1109/ISEMC48616.2019.8986147.
- [106] S. Sirci, M. A. Sanchez-Soriano, J. D. Martinez, and V. E. Boria, "Electronically Reconfigurable Doublet in Dual-Mode Coaxial SIW," in *2019 IEEE MTT-S International Microwave Symposium (IMS)*, Jun. 2019, pp. 17–20. doi: 10.1109/MWSYM.2019.8700912.
- [107] M. Abdelfattah and D. Peroulis, "A 2.2 - 3.4 GHz Constant Bandwidth High-Selectivity Tunable Filter Based on Dual-Mode SIW Resonators," *IEEE MTT-S International Microwave Symposium Digest*, vol. 2019-June, pp. 98–101, Jun. 2019, doi: 10.1109/MWSYM.2019.8701126.
- [108] A. B. Alothman Alterkawi, S. W. Sattler, R. Teschl, and W. Bosch, "A reconfigurable dual-mode Filter in Embedded Suspended Stripline Substrate Technology (ESSS)," in *2021 IEEE MTT-S International Microwave Filter Workshop, IMFW 2021*, 2021, pp. 306–308. doi: 10.1109/IMFW49589.2021.9642296.
- [109] J. C. Bohorquez *et al.*, "Reconfigurable Planar SIW Cavity Resonator and Filter," in *2006 IEEE MTT-S International Microwave Symposium Digest*, Jun. 2006, pp. 947–950. doi: 10.1109/MWSYM.2006.249873.
- [110] B. Scheiner *et al.*, "Microstrip-to-waveguide transition in planar form using a substrate integrated waveguide," in *IEEE Radio and Wireless Symposium, RWS*, Feb. 2018, vol. 2018-January, pp. 18–20. doi: 10.1109/RWS.2018.8304934.
- [111] Y. Wu, E. Fourn, and P. Besnier, "A Planar Quad-band Band-Pass Filter Employing Dual-Mode Band-Stop Resonators," in *2021 IEEE MTT-S International Microwave Filter Workshop, IMFW 2021*, 2021, pp. 79–81. doi: 10.1109/IMFW49589.2021.9642378.
- [112] Y. X. Tu, "Design, modelling and implementation of several multi-standard high performance single-wideband and multi-wideband microwave planar filters," University of Bradford, Bradford, 2016.

- [113] S. A. Khodenkov, B. A. Belyaev, and V. v. Ivanin, "Investigation of irregular microstrip resonators and wideband filters based on them," in *2016 13th International Scientific-Technical Conference on Actual Problems of Electronic Instrument Engineering, APEIE 2016 - Proceedings*, Dec. 2016, vol. 1, pp. 482–486. doi: 10.1109/APEIE.2016.7802210.
- [114] Y. Zheng and Y. Dong, "Dual-Band, Dual-Mode, Microstrip Resonator Loaded, Compact Hybrid SIW Bandpass Filter," in *IEEE MTT-S International Microwave Symposium Digest*, Jun. 2021, vol. 2021-June, pp. 50–53. doi: 10.1109/IMS19712.2021.9574892.
- [115] Y. Zheng, Y. Zhu, Z. Wang, and Y. Dong, "Compact, Wide Stopband, Shielded Hybrid Filter Based on Quarter-Mode Substrate Integrated Waveguide and Microstrip Line Resonators," *IEEE Microwave and Wireless Components Letters*, vol. 31, no. 3, pp. 245–248, Mar. 2021, doi: 10.1109/LMWC.2020.3049048.
- [116] S. Wang, D. Zhang, J. Jiang, Q. Yuan, L. Liu, and L. Wang, "SIW Dual-Mode Dual-Band Balanced Filter with Closely Spaced Passbands," in *2020 Cross Strait Radio Science and Wireless Technology Conference, CSRSWTC 2020 - Proceedings*, Dec. 2020. doi: 10.1109/CSRSWTC50769.2020.9372524.
- [117] C. S. Gallo *et al.*, "Microwave cavity tuned with liquid metal and its application to Electron Paramagnetic Resonance," Apr. 2018, [Online]. Available: <http://arxiv.org/abs/1804.03443>
- [118] K. Xu and J. H. Choi, "Flexible Liquid-Metal-Tuned Higher-Order Bandpass Frequency Selective Surfaces," in *Asia-Pacific Microwave Conference Proceedings, APMC*, Dec. 2020, vol. 2020-December, pp. 296–298. doi: 10.1109/APMC47863.2020.9331351.
- [119] S. Alkaraki, J. Kelly, A. L. Borja, R. Mittra, and Y. Wang, "Gallium-Based Liquid Metal Substrate Integrated Waveguide Switches," *IEEE Microwave and Wireless Components Letters*, vol. 31, no. 3, pp. 257–260, Mar. 2021, doi: 10.1109/LMWC.2020.3040795.
- [120] T. Qian, "Reconfigurable metasurface antenna based on the liquid metal for flexible scattering fields manipulation," *Micromachines (Basel)*, vol. 12, no. 3, pp. 1–8, Mar. 2021, doi: 10.3390/mi12030243.
- [121] A. E. Prasetyadi *et al.*, "Continuously tunable substrate integrated waveguide bandpass filter in liquid crystal technology with magnetic biasing," *Electron Lett*, vol. 51, no. 20, pp. 1584–1585, Oct. 2015, doi: 10.1049/el.2015.2494.
- [122] Q. Li and T. Yang, "Compact UWB Half-Mode SIW Bandpass Filter with Fully Reconfigurable Single and Dual Notched Bands," *IEEE Trans Microw Theory Tech*, vol. 69, no. 1, pp. 65–74, Jan. 2021, doi: 10.1109/TMTT.2020.3033830.
- [123] M. F. Ali, R. Bhattacharya, and G. Varshney, "Graphene-based tunable terahertz self-diplexing/MIMO-STAR antenna with pattern diversity," *Nano Commun Netw*, vol. 30, Dec. 2021, doi: 10.1016/j.nancom.2021.100378.

- [124] N. Kiani, F. T. Hamedani, and P. Rezaei, "Polarization controlling plan in graphene-based reconfigurable microstrip patch antenna," *Optik (Stuttg)*, vol. 244, Oct. 2021, doi: 10.1016/j.ijleo.2021.167595.
- [125] G. Challa Ram, P. Sambaiah, S. Yuvaraj, and M. v. Kartikeyan, "Tunable bandstop filter using graphene in terahertz frequency band," *AEU - International Journal of Electronics and Communications*, vol. 144, Feb. 2022, doi: 10.1016/j.aeue.2021.154047.
- [126] A. Moazami, M. Hashemi, and N. C. Shirazi, "High Efficiency Tunable Graphene-Based Plasmonic Filter in the THz Frequency Range," *Plasmonics*, vol. 14, no. 2, pp. 359–363, Apr. 2019, doi: 10.1007/s11468-018-0812-5.
- [127] A. Ilić, B. Bukvić, M. M. Ilić, and D. Budimir, "Graphene-based waveguide resonators for submillimeter-wave applications," *J Phys D Appl Phys*, vol. 49, no. 32, Jul. 2016, doi: 10.1088/0022-3727/49/32/325105.
- [128] I. Hunter, "Theory and design of microwave filters," Milton Keynes, 2006.
- [129] P. N. Choubey and W. Hong, "Dual-Band bandpass filter designed by exploiting the second-order degenerated modes of the siw-Cavity," in *Asia-Pacific Microwave Conference Proceedings, APMC*, Feb. 2016, vol. 1. doi: 10.1109/APMC.2015.7411657.
- [130] A. O. Nwajana and E. R. Obi, "A Review on SIW and Its Applications to Microwave Components," *Electronics (Switzerland)*, vol. 11, no. 7. MDPI, Apr. 01, 2022. doi: 10.3390/electronics11071160.
- [131] W. Peng, Q. Xiao, and J. Zhang, "Design of Compact SIW Bandpass Filter for Millimeter-Wave Applications," in *2018 International Conference on Microwave and Millimeter Wave Technology (ICMMT)*, 2018.
- [132] M. Li, C. Chen, and W. Chen, "Miniaturized Dual-Band Filter Using Dual-Capacitively Loaded SIW Cavities," *IEEE Microwave and Wireless Components Letters*, vol. 27, no. 4, pp. 344–346, Apr. 2017, doi: 10.1109/LMWC.2017.2678435.
- [133] W. Shen, W. Y. Yin, X. W. Sun, and L. S. Wu, "Substrate-integrated waveguide bandpass filters with planar resonators for system-on-package," *IEEE Trans Compon Packaging Manuf Technol*, vol. 3, no. 2, pp. 253–261, 2013, doi: 10.1109/TCPMT.2012.2224348.
- [134] A. Iqbal, J. J. Tiang, S. K. Wong, M. Alibakhshikenari, F. Falcone, and E. Limiti, "Miniaturization Trends in Substrate Integrated Waveguide (SIW) Filters: A Review," *IEEE Access*, vol. 8, pp. 223287–223305, 2020, doi: 10.1109/ACCESS.2020.3044088.
- [135] T.-Y. Huang, T.-M. Shen, B.-J. Chen, H.-Y. Chien, and R.-B. Wu, *Design of miniaturized vertically stacked SIW filters in LTCC; Design of miniaturized vertically stacked SIW filters in LTCC*. 2009. doi: 10.23919/EUMC.2009.5296500.
- [136] M. Bozzi, L. Perregrini, and C. Tomassoni, "A Review of Compact Substrate Integrated Waveguide (SIW) Interconnects and Components," in *2019 IEEE 23rd Workshop on Signal and Power Integrity (SPI)*, Jun. 2019, pp. 1–4. doi: 10.1109/SaPIW.2019.8781646.

- [137] G. Romo, Ac. Scogna, O. Connecticut Path, and U. antoniocicomancini cst co, *Substrate in:tegrated waveguide (SIW) filter. design methodology and performance study Inde rms-substrate integrate-d waveguide (SIW), band pass filter, EBG, dispersion diagrams.* 2009. doi: 10.1109/IMWS.2009.4814901.
- [138] D. Deslandes and K. Wu, "Integrated microstrip and rectangular waveguide in planar form," *IEEE Microwave and Wireless Components Letters*, vol. 11, no. 2, pp. 68–70, Feb. 2001, doi: 10.1109/7260.914305.
- [139] F. Taringou and J. Bornemann, *New Substrate-Integrated to Coplanar Waveguide Transition.* Proceedings of the 41st European Microwave Conference 2011. doi: 10.23919/EuMC.2011.6101767.
- [140] D. Lorente, M. Limbach, H. Esteban, and V. Boria, "Compact Ultrawideband Grounded Coplanar Waveguide to Substrate Integrated Waveguide Tapered V-Slot Transition," *IEEE Microwave and Wireless Components Letters*, vol. 30, no. 12, pp. 1137–1140, Dec. 2020, doi: 10.1109/LMWC.2020.3031025.
- [141] A. O. Nwajana and E. R. Obi, "A Review on SIW and Its Applications to Microwave Components," *Electronics (Switzerland)*, vol. 11, no. 7. MDPI, Apr. 01, 2022. doi: 10.3390/electronics11071160.
- [142] Sheelu Kumari and Shweta Srivastava, "Losses in Waveguide and Substrate Integrated Waveguide (SIW) For Ku Band: A Comparison," *International Journal of Modern Engineering Research (IJMER)*, vol. 3, no. 1, pp. 53–57, Jan. 2013.
- [143] M. Bozzi, M. Pasian, L. Perregriani, and K. Wu, "On the losses in substrate integrated waveguides," in *2007 European Microwave Conference*, Oct. 2007, pp. 384–387. doi: 10.1109/EUMC.2007.4405207.
- [144] M. Pasian, M. Bozzi, and L. Perregriani, "Radiation losses in Substrate Integrated Waveguides: A semi-analytical approach for a quantitative determination," *IEEE MTT-S International Microwave Symposium Digest*, 2013, doi: 10.1109/MWSYM.2013.6697593.
- [145] K. Zhou, C. X. Zhou, and W. Wu, "Substrate-Integrated Waveguide Dual-Mode Dual-Band Bandpass Filters with Widely Controllable Bandwidth Ratios," *IEEE Trans Microw Theory Tech*, vol. 65, no. 10, pp. 3801–3812, Oct. 2017, doi: 10.1109/TMTT.2017.2694827.
- [146] N. H. Nguyen, F. Parment, A. Ghiotto, K. Wu, and T. P. Vuong, "A fifth-order air-filled SIW filter for future 5G applications," in *2017 IEEE MTT-S International Microwave Workshop Series on Advanced Materials and Processes for RF and THz Applications (IMWS-AMP)*, Sep. 2017, pp. 1–3. doi: 10.1109/IMWS-AMP.2017.8247355.
- [147] W. Hong *et al.*, "Half mode substrate integrated waveguide: A new guided wave structure for microwave and millimeter wave application," in *IRMMW-THz 2006 - 31st International Conference on Infrared and Millimeter Waves and 14th International Conference on Terahertz Electronics*, 2006, p. 219. doi: 10.1109/ICIMW.2006.368427.

- [148] F. Zhu, W. Hong, J. X. Chen, and K. Wu, "Cross-coupled substrate integrated waveguide filters with improved stopband performance," *IEEE Microwave and Wireless Components Letters*, vol. 22, no. 12, pp. 633–635, 2012, doi: 10.1109/LMWC.2012.2228174.
- [149] D. Deslandes and K. Wu, "Single-substrate integration technique of planar circuits and waveguide filters," *IEEE Trans Microw Theory Tech*, vol. 51, no. 2 I, pp. 593–596, Feb. 2003, doi: 10.1109/TMTT.2002.807820.
- [150] F. Oktafiani and A. Munir, "Cut-Off Frequency Analysis of Ridged Rectangular Waveguide Based on Its Equivalent Circuit," in *TENSYP 2021 - 2021 IEEE Region 10 Symposium*, Aug. 2021. doi: 10.1109/TENSYP52854.2021.9550849.
- [151] L. Xiu-Zhen and T. Ke-Jun, "A novel ridge substrate integrated waveguide antenna for WLAN application," in *Final Program and Book of Abstracts - iWAT 2011: 2011 IEEE International Workshop on Antenna Technology: Small Antennas, Novel Structures and Innovative Metamaterials*, 2011, pp. 302–305. doi: 10.1109/IWAT.2011.5752334.
- [152] B. Chen, S. K. Thapa, A. Barakat, and R. K. Pokharel, "A 100GHz Bandpass Filter Employing Shielded Folded Ridged Quarter-Mode SIW Resonator in CMOS Technology," in *2021 51st European Microwave Conference, EuMC 2021*, 2021, pp. 853–856. doi: 10.23919/EuMC50147.2022.9784336.
- [153] Thomas. R. Jones and M. Daneshmand, "Miniaturized Reconfigurable Dual-Band Bandstop Filter with Independent Stopband Control using Folded Ridged Quarter-Mode Substrate Integrated Waveguide," in *2019 IEEE MTT-S International Microwave Symposium (IMS)*, Jun. 2019, pp. 102–105. doi: 10.1109/MWSYM.2019.8701129.
- [154] F. Young and J. Hohmank, "Characteristics of ridge waveguides," *Applied Scientific Research, Section B*, vol. 8, no. 1, pp. 321–336, Dec. 1960, doi: 10.1007/BF02920066.
- [155] L. Huang and H. Cha, "Compact Ridged Half-Mode Substrate Integrated Waveguide Bandpass Filter," *IEEE Microwave and Wireless Components Letters*, vol. 25, no. 4, pp. 223–225, Apr. 2015, doi: 10.1109/LMWC.2015.2400921.
- [156] T. R. Jones and M. Daneshmand, "Miniaturized folded ridged half-mode substrate integrated waveguide," in *2017 47th European Microwave Conference (EuMC)*, Oct. 2017, pp. 528–531. doi: 10.23919/EuMC.2017.8230906.
- [157] L. S. Wu, X. L. Zhou, and W. Y. Yin, "Evanescent-mode bandpass filters using folded and ridge substrate integrated waveguides (SIWs)," *IEEE Microwave and Wireless Components Letters*, vol. 19, no. 3, pp. 161–163, Mar. 2009, doi: 10.1109/LMWC.2009.2013739.
- [158] J. B. Pendry, A. J. Holden, D. J. Robbins, and W. J. Stewart, "Magnetism from Conductors and Enhanced Nonlinear Phenomena," *IEEE Trans Microw Theory Tech*, vol. 47, no. 11, 1999.
- [159] Y. D. Dong, T. Yang, and T. Itoh, "Substrate integrated waveguide loaded by complementary splitting resonators and its applications to miniaturized waveguide filters," in *IEEE Transactions on*

- Microwave Theory and Techniques*, Jan. 2009, vol. 57, no. 1, pp. 2211–2223. doi: 10.1109/TMTT.2009.2027156.
- [160] N. Muchhal and S. Srivastava, “Design of Miniaturized Diamond Shaped Substrate Integrated Waveguide CSRR Band Pass Filter for X Band Applications,” in *2019 International Conference on Signal Processing and Communication (ICSC)*, Mar. 2019, pp. 113–116. doi: 10.1109/ICSC45622.2019.8938373.
- [161] J. Pu, F. Xu, and Y. Li, “Miniaturized Substrate Integrated Waveguide Bandpass Filters Based on Novel Complementary Split Ring Resonators,” in *IEEE MTT-S 2019 International Microwave Biomedical Conference, IMBioC 2019 - Proceedings*, May 2019. doi: 10.1109/IMBIOC.2019.8777795.
- [162] F. Z. Siabah, F. Grine, M. T. Benhabiles, and M. L. Riab, “Sixteenth-Mode Substrate-Integrated-Waveguide (SMSIW) Resonator for Dielectric Characterization of Liquid Mixtures,” *Journal of Microwaves, Optoelectronics and Electromagnetic Applications*, vol. 19, no. 1, pp. 129–136, Mar. 2020, doi: 10.1590/2179-10742020v19i11805.
- [163] P. Li, H. Chu, and R. S. Chen, “Design of compact bandpass filters using quarter-mode and eighth-mode SIW cavities,” *IEEE Trans Compon Packaging Manuf Technol*, vol. 7, no. 6, pp. 956–963, Jun. 2017, doi: 10.1109/TCPMT.2017.2677958.
- [164] Z. Zhang, N. Yang, and K. Wu, “5-GHz bandpass filter demonstration using quarter-mode substrate integrated waveguide cavity for wireless systems,” in *RWS 2009 IEEE Radio and Wireless Symposium, Proceedings*, 2009, pp. 95–98. doi: 10.1109/RWS.2009.4957293.
- [165] P. Li, H. Chu, and R. S. Chen, “Design of compact bandpass filters using quarter-mode and eighth-mode SIW cavities,” *IEEE Trans Compon Packaging Manuf Technol*, vol. 7, no. 6, pp. 956–963, Jun. 2017, doi: 10.1109/TCPMT.2017.2677958.
- [166] X. Wang, X. W. Zhu, Z. H. Jiang, Z. C. Hao, Y. W. Wu, and W. Hong, “Analysis of Eighth-Mode Substrate-Integrated Waveguide Cavity and Flexible Filter Design,” *IEEE Trans Microw Theory Tech*, vol. 67, no. 7, pp. 2701–2712, Jul. 2019, doi: 10.1109/TMTT.2019.2913646.
- [167] R. J. Cameron and S. Member, “General Coupling Matrix Synthesis Methods for Chebyshev Filtering Functions,” *IEEE Trans Microw Theory Tech*, vol. 47, no. 4, p. 433, 1999.
- [168] C. Ge, X. W. Zhu, X. Jiang, and X. J. Xu, “A General Synthesis Approach of Coupling Matrix With Arbitrary Reference Impedances,” *IEEE Microwave and Wireless Components Letters*, vol. 25, no. 6, pp. 349–351, Jun. 2015, doi: 10.1109/LMWC.2015.2421327.
- [169] Y. Zhu and Y. Dong, “Double-Layer SIW Filters with Higher-Order Mode Suppression,” in *2019 IEEE Asia-Pacific Microwave Conference (APMC)*, Dec. 2019, pp. 780–782. doi: 10.1109/APMC46564.2019.9038886.

- [170] A. R. Azad and A. Mohan, "Substrate Integrated Waveguide Dual-Band and Wide-Stopband Bandpass Filters," *IEEE Microwave and Wireless Components Letters*, vol. 28, no. 8, pp. 660–662, Aug. 2018, doi: 10.1109/LMWC.2018.2844103.
- [171] D. Jia, Q. Feng, Q. Xiang, and K. Wu, "Multilayer Substrate Integrated Waveguide (SIW) Filters with Higher-Order Mode Suppression," *IEEE Microwave and Wireless Components Letters*, vol. 26, no. 9, pp. 678–680, Sep. 2016, doi: 10.1109/LMWC.2016.2597222.
- [172] Y. Yu and Y. Li, "Design of a small size C-band cavity bandpass filter," *Microw Opt Technol Lett*, vol. 64, no. 9, pp. 1507–1512, Sep. 2022, doi: 10.1002/mop.33307.
- [173] X. Guo, L. Zhu, and W. Wu, "Design Method for Multiband Filters with Compact Configuration in Substrate Integrated Waveguide," *IEEE Trans Microw Theory Tech*, vol. 66, no. 6, pp. 3011–3018, Jun. 2018, doi: 10.1109/TMTT.2018.2830337.
- [174] K. Zhou, C.-X. Zhou, and W. Wu, "Substrate-Integrated Waveguide Dual-Mode Dual-Band Bandpass Filters With Widely Controllable Bandwidth Ratios," *IEEE Trans Microw Theory Tech*, vol. 65, no. 10, 2017, Accessed: Nov. 10, 2022. [Online]. Available: <https://ieeexplore.ieee.org/document/7913695/>
- [175] G. L. Matthaei, L. Young, and E. M. T. Jones, "MICROWAVE FILTERS, IMPEDANCE-MATCHING NETWORKS, AND COUPLING STRUCTURES Technology for Communications International Mountain View, CA ARTECH HOUSE," 1980.
- [176] P. Ma, Y. Yao, and G. Wu, "Design of Lossy Dual-mode Dual-band Bandpass Filters Using Defected Ground Structure," in *2021 International Conference on Microwave and Millimeter Wave Technology, ICMMT 2021 - Proceedings*, 2021. doi: 10.1109/ICMMT52847.2021.9618527.
- [177] P. Boe, D. Miek, F. Kamrath, and M. Höft, "Dual-Band Filter Composed of Dielectric and Waveguide Resonators with In-Band Transmission Zeros," in *2021 IEEE MTT-S International Microwave Filter Workshop (IMFW)*, 2021. Accessed: Nov. 10, 2022. [Online]. Available: <https://ieeexplore.ieee.org/document/9642369/>
- [178] S. Litvintsev and S. Rozenko, "Synthesis of Dual-band Filter with Improved Functionality Based on Dual-mode Resonator," in *2021 IEEE 26th International Seminar/Workshop on Direct and Inverse Problems of Electromagnetic and Acoustic Wave Theory (DIPED)*, 2021. Accessed: Nov. 10, 2022. [Online]. Available: <https://ieeexplore.ieee.org/document/9552281/>
- [179] Y. M. Huang *et al.*, "Miniaturized dual-band filters based on quarter-mode substrate integrated waveguide loaded with double-sided stepped-impedance complementary split-ring resonators," in *2017 IEEE MTT-S International Microwave Symposium (IMS)*, 2017. Accessed: Nov. 10, 2022. [Online]. Available: <https://ieeexplore.ieee.org/document/8059036/>
- [180] B. Maheshwari and D. K. Panda, "Design of single and dual band pass filter using substrate integrated waveguide with DGS," in *2017 International Conference on Information, Communication, Instrumentation and Control (ICICIC)*, Aug. 2017, pp. 1–5. doi: 10.1109/ICOMICON.2017.8279024.

- [181] H. Chu, P. Li, and J. X. Chen, "Balanced substrate integrated waveguide bandpass filter with high selectivity and common-mode suppression," *IET Microwaves, Antennas and Propagation*, vol. 9, no. 2, pp. 133–141, Jan. 2015, doi: 10.1049/iet-map.2013.0708.
- [182] C. R. Paul, "Comparison of the contributions of common-mode and differential-mode currents in radiated emissions," *IEEE Trans Electromagn Compat*, vol. 31, no. 2, pp. 189–193, May 1989, doi: 10.1109/15.18789.
- [183] A. M. E. Safwat, F. Podevin, P. Ferrari, and A. Vilcot, "Tunable bandstop defected ground structure resonator using reconfigurable dumbbell-shaped coplanar waveguide," *IEEE Trans Microw Theory Tech*, vol. 54, no. 9, pp. 3559–3564, Sep. 2006, doi: 10.1109/TMTT.2006.880654.
- [184] H. B. El-Shaarawy, F. Coccetti, and R. Plana, "A novel compact reconfigurable defected ground structure resonator on coplanar waveguide technology for filter applications," in *2010 IEEE Antennas and Propagation Society International Symposium*, 2010. Accessed: Nov. 10, 2022. [Online]. Available: <https://ieeexplore.ieee.org/document/5561177/>
- [185] D. Ahn, J.-S. Park, C.-S. Kim, J. Kim, Y. Qian, and T. Itoh, "A Design of the Low-Pass Filter Using the Novel Microstrip Defected Ground Structure," *IEEE Trans Microw Theory Tech*, vol. 49, no. 1, 2001.
- [186] H. Moghadas and A. Tavakoli, "A design procedure for Defected Ground Structure in antenna arrays based on Genetic Algorithm," in *IEEE Antennas and Propagation Society, AP-S International Symposium (Digest)*, 2012. doi: 10.1109/APS.2012.6347951.
- [187] A. Fernández-Prieto, J. Martel, J. S. Hong, F. Medina, S. Qian, and F. Mesa, *Differential transmission line for common-mode suppression using double side MIC technology*. 2011. doi: 10.23919/EuMC.2011.6101743.
- [188] C. D. K. Mutepe and V. M. Srivastava, "Designing of Novel Eighth-Mode Forth-Order Substrate Integrated Waveguide Band-Pass Filter with High Selectivity," *Journal of Communications*, pp. 553–558, 2021, doi: 10.12720/jcm.16.12.553-558.
- [189] C. U. Ndujiuba, S. N. John, and T. O. Bello, "Duplexer, Microstrip filter, Fractional bandwidth, Resonators; Duplexer, Microstrip filter, Fractional bandwidth, Resonators," *International Journal of Electromagnetics and Applications*, vol. 6, no. 1, pp. 7–12, 2016, doi: 10.5923/j.ijea.20160601.02.
- [190] G. M. Rafiqzaman, A. T. Sadi, and M. N. Mollah, "Design of the novel defected ground structure assisted microstrip low pass filter," in *2nd International Conference on Electrical Engineering and Information and Communication Technology, iCEEiCT 2015*, Oct. 2015. doi: 10.1109/ICEEICT.2015.7307477.
- [191] L. Huang, W. Wu, X. Zhang, and N. Yuan, "A compact bandpass substrate integrated waveguide (SIW) filter with compact microstrip resonant cell (CMRC) resonators," in *2017 Progress in Electromagnetics Research Symposium - Fall (PIERS - FALL)*, Nov. 2017, pp. 306–310. doi: 10.1109/PIERS-FALL.2017.8293154.

- [192] P. S. Carter, "Magnetically-Tunable Microwave Filters Using Single-Crystal Yttrium-Iron-Garnet Resonators," *IRE Transactions on Microwave Theory and Techniques*, vol. 9, no. 3, pp. 252–260, 1961, doi: 10.1109/TMTT.1961.1125316.
- [193] X. Liu, "Tunable RF and microwave filters," in *2015 IEEE 16th Annual Wireless and Microwave Technology Conference, WAMICON 2015*, Jun. 2015. doi: 10.1109/WAMICON.2015.7120436.
- [194] W. Y. Sam, Z. Zakaria, and M. A. Mutalib, "The investigation of reconfigurable SIW filter using varactor diodes," in *2016 IEEE 5th Asia-Pacific Conference on Antennas and Propagation (APCAP)*, Jul. 2016, pp. 167–168. doi: 10.1109/APCAP.2016.7843151.
- [195] W. Y. Sam, Z. Zakaria, and M. A. Mutalib, "The investigation of reconfigurable SIW filter using varactor diodes," in *2016 IEEE 5th Asia-Pacific Conference on Antennas and Propagation (APCAP)*, Jul. 2016, pp. 167–168. doi: 10.1109/APCAP.2016.7843151.
- [196] S. Krishnaveni and D. S. Ravi, "MEMS POWER SWITCH IMPLEMENTATION USING SUGAR SIMULATOR 1," *J Theor Appl Inf Technol*, vol. 31, no. 3, 2014, Accessed: Nov. 11, 2022. [Online]. Available: [www.jatit.org](http://www.jatit.org)
- [197] S. De, S. K. Koul, and K. K. Samanta, "Low Profile Dielectric Rod Tuned Reconfigurable Band Pass Filters," *IEEE Journal of Microwaves*, vol. 2, no. 3, pp. 507–521, May 2022, doi: 10.1109/jmw.2022.3170060.
- [198] "Waveguide handbook | WorldCat.org." <https://www.worldcat.org/title/680485> (accessed Nov. 11, 2022).
- [199] A. Razaq, F. Bibi, X. Zheng, R. Papadakis, S. H. M. Jafri, and H. Li, "Review on Graphene-, Graphene Oxide-, Reduced Graphene Oxide-Based Flexible Composites: From Fabrication to Applications," *Materials*, vol. 15, no. 3. MDPI, Feb. 01, 2022. doi: 10.3390/ma15031012.
- [200] Q. Wang, Z. Ouyang, M. Lin, and Y. Zheng, "High-quality graphene-based tunable absorber based on double-side coupled-cavity effect," *Nanomaterials*, vol. 11, no. 11, Nov. 2021, doi: 10.3390/nano11112824.
- [201] A. S. Vorobev, G. V. Bianco, G. Bruno, A. D'orazio, L. O'faolain, and M. Grande, "Tuning of graphene-based optical devices operating in the near-infrared," *Applied Sciences (Switzerland)*, vol. 11, no. 18, Sep. 2021, doi: 10.3390/app11188367.
- [202] "Three-dimensional graphene could be used to make bone implants - Spinal News International." <https://spinalnewsinternational.com/three-dimensional-graphene-could-be-used-to-make-bone-implants/> (accessed Nov. 28, 2022).
- [203] A.-Q. Zhang, W.-B. Lu, Z.-G. Liu, Y. Yi, H. Chen, and B.-H. Huang, "A tunable attenuator on graphene-based substrate integrated waveguide' *2017 Sixth Asia-Pacific Conference on Antennas and Propagation (APCAP)*, Xi'an, China, 2017, pp. 1-3, doi: 10.1109/APCAP.2017.8420631. .

- [204] M. Esfandiyari, A. Lalbakhsh, S. Jarchi, M. Ghaffari-Miab, H. N. Mahtaj, and R. B. V. B. Simorangkir, "Tunable terahertz filter/antenna-sensor using graphene-based metamaterials," *Mater Des*, vol. 220, Aug. 2022, doi: 10.1016/j.matdes.2022.110855.
- [205] H. Chen, Z. G. Liu, W. B. Lu, and A. Q. Zhang, "A SIW Horn Antenna with Dynamically Tunable Graphene-Based Attenuator," in *2018 Cross Strait Quad-Regional Radio Science and Wireless Technology Conference, CSQRWC 2018*, Sep. 2018. doi: 10.1109/CSQRWC.2018.8455839.
- [206] G. Varshney, A. Verma, V. S. Pandey, R. S. Yaduvanshi, and R. Bala, "A proximity coupled wideband graphene antenna with the generation of higher order TM modes for THz applications," *Opt Mater (Amst)*, vol. 85, pp. 456–463, Nov. 2018, doi: 10.1016/j.optmat.2018.09.015.
- [207] G. C. Ram, P. Sambaiah, S. Yuvaraj, and M. v. Kartikeyan, "Graphene based tunable bandpass filter for terahertz spectroscopy of polymers," *Optik (Stuttg)*, vol. 268, p. 169792, Oct. 2022, doi: 10.1016/J.IJLEO.2022.169792.

## NOTES

---

## NOTES

---